A Multi-Domain Continuum Model of Electrical Stimulation of Healthy and Degenerate Retina

ABDULRAHMAN ALQAHTANI

Supervised by:

A/Prof. Socrates Dokos

Scientia Prof. Nigel H. Lovell

Dr. Amr Al Abed

A thesis in fulfilment of the requirements for the degree of

Doctor of Philosophy

GRADUATE SCHOOL OF BIOMEDICAL ENGINEERING

FACULTY OF ENGINEERING

07 SEPTEMBER 2018

Thesis/Dissertation Sheet

Surname/Family Name	:	**ALQAHTANI**
Given Name/s	:	**ABDULRAHMAN MANA**
Abbreviation for degree as give in the University calendar	:	**PhD**
Faculty	:	**ENGINEERING**
School	:	**GRADUATE SCHOOL OF BIOMEDICAL ENGINEERING**
Thesis Title	:	**A Multi-Domain Continuum Model of Electrical Stimulation of Healthy and Degenerate Retina**

Abstract 350 words maximum: (PLEASE TYPE)

Visual neuroprostheses aim to restore vision to patients suffering from degenerative retinal diseases such as retinitis pigmentosa and age-related macular degeneration. Development of visual implants faces a great number of challenges in both device design and stimulation strategy. Computational modelling is a powerful tool for exploring and testing new visual prostheses design and stimulation strategies.

In this thesis, we have proposed and validated a new version of the classical cable equation valid for any fibre morphology, electrode configuration, or non-uniformity in ion channel expression, implemented using a finite element approach. Moreover, we developed the first continuum multi-domain model of retinal electrical stimulation to represent all main retinal ganglion cell (RGC) compartments. The continuum model was validated against discrete morphologically-realistic OFF and ON RGC models as well as RGC excitation thresholds reported in recently published in vitro experimental studies using intra- and extra-cellular electrical stimulation. The continuum model reproduced the same results as that of the discrete model and in vitro experimental studies.

Furthermore, the first degenerate model of retinal electrical stimulation accounting for observed changes occurring in the whole retina was developed, using a detailed model of electrical stimulation of OFF and ON RGCs. Interestingly, the model predicted that suprachoroidal stimulation of the degenerate retina exhibited increased current thresholds, mainly due to the presence of the glial scar layer. In contrast, epiretinal stimulation thresholds were almost similar for both healthy and degenerate models, implying epiretinal prostheses can bypass the influence of the glial scar layer.

Various stimulation strategies were examined for both healthy and degenerate retinal models. No significant difference among the three return electrode configurations (monopolar, quasi-monopolar and hexapolar) was found when the distance between electrodes and RGCs was less than the electrode diameter. Electrode spacing was the significant factor underlying increased current thresholds, where electrode size had a marginal impact among all three return electrode configurations. Stimulus pulse polarities and durations were found to have a significant impact on the localisation of evoked phosphenes. Moreover, virtual electrodes could be elicited by using an appropriate time shift between two stimulus waveforms applied to the active electrodes.

FOR OFFICE USE ONLY Date of completion of requirements for Award:

ORIGINALITY STATEMENT

‘I hereby declare that this submission is my own work and to the best of my knowledge it contains no materials previously published or written by another person, or substantial proportions of material which have been accepted for the award of any other degree or diploma at UNSW or any other educational institution, except where due acknowledgement is made in the thesis. Any contribution made to the research by others, with whom I have worked at UNSW or elsewhere, is explicitly acknowledged in the thesis. I also declare that the intellectual content of this thesis is the product of my own work, except to the extent that assistance from others in the project's design and conception or in style, presentation and linguistic expression is acknowledged.’

Signed …….....

Date …….....

INCLUSION OF PUBLICATIONS STATEMENT

UNSW is supportive of candidates publishing their research results during their candidature as detailed in the UNSW Thesis Examination Procedure.

Publications can be used in their thesis in lieu of a Chapter if:

- The student contributed greater than 50% of the content in the publication and is the "primary author", ie. the student was responsible primarily for the planning, execution and preparation of the work for publication
- The student has approval to include the publication in their thesis in lieu of a Chapter from their supervisor and Postgraduate Coordinator.
- The publication is not subject to any obligations or contractual agreements with a third party that would constrain its inclusion in the thesis

Please indicate whether this thesis contains published material or not.

☐ *This thesis contains no publications, either published or submitted for publication (if this box is checked, you may delete all the material on page 2)*

☒ *Some of the work described in this thesis has been published and it has been documented in the relevant Chapters with acknowledgement (if this box is checked, you may delete all the material on page 2)*

☐ *This thesis has publications (either published or submitted for publication) incorporated into it in lieu of a chapter and the details are presented below*

CANDIDATE'S DECLARATION

I declare that:

- I have complied with the Thesis Examination Procedure
- where I have used a publication in lieu of a Chapter, the listed publication(s) below meet(s) the requirements to be included in the thesis.

Name	Signature	Date (dd/mm/yy)

Dedicated

To

My respected parents who never stop supporting in countless ways

My dearest wife and childen for cheering me up

My beloved brothers and sisters for always being by my side

Acknowledgment

All praise is due to Allah, the lord of the worlds, who created me, showered me with immense bounties, and gave me the opportunity to attend UNSW and pursue a PhD.

My thesis journey has been a rewarding experience with many ups and downs. I am indebted to a number of people without whom this thesis would not have been completed.

First and foremost, I would like to express my sincere gratitude to my supervisor A/Prof. Socrates Dokos who truly made my journey enjoyable. Socrates gave me the independence in research, while keeping me focused and motivated. He provided me a rigorous supervision and ensured that I can develop myself. His expertise in modelling and mathematics and careful editorial suggestions greatly benefited this thesis. I really appreciate his endless support during my PhD. I am also grateful to my co-supervisor Prof. Nigel Lovell for his guidance and being there always for answering my questions. His critical comments and recommendations helped a lot to fine tune many aspects and improve my work. Special thanks to my co-supervisor Dr. Amr Al Abed for sitting with me patiently and providing me scientific guidance every time I needed him. We had a lot of meetings which lasted for a long time. I would also like to thank him for his emotional support during my PhD. I feel really lucky to have the well-known scholars and very kind people as my supervisors.

I would also like to thank my companions in the Modelling Group, Yousef Alharbi and Azam Bakir for useful discussion along the way, solving software issues, and having a great time together. Special thank goes to our Bionic Group for their support and helpful suggestions. I thank my friend Lutful Amin for his time with me during long-day modelling works and for his accompany to all the Middle Eastern restaurants.

I am also thankful to the faculty and staff members at GSBmE, especially to

Stephen Redmond, for creating a friendly and positive environment.

Abstract

Visual neuroprostheses aim to restore vision to patients suffering from degenerative retinal diseases such as retinitis pigmentosa and age-related macular degeneration. Development of visual implants faces a great number of challenges in both device design and stimulation strategy. Computational modelling is a powerful tool for exploring and testing new visual prostheses design and stimulation strategies.

In this thesis, we have proposed and validated a new version of the classical cable equation valid for any fibre morphology, electrode configuration, or non-uniformity in ion channel expression, implemented using a finite element approach. Moreover, we developed the first continuum multi-domain model of retinal electrical stimulation to represent all main retinal ganglion cell (RGC) compartments. The continuum model was validated against discrete morphologically-realistic OFF and ON RGC models as well as RGC excitation thresholds reported in recently published *in vitro* experimental studies using intra- and extra-cellular electrical stimulation. The continuum model reproduced the same results as that of the discrete model and *in vitro* experimental studies.

Furthermore, the first degenerate model of retinal electrical stimulation accounting for observed changes occurring in the whole retina was developed, using a detailed model of electrical stimulation of OFF and ON RGCs. Interestingly, the model predicted that suprachoroidal stimulation of the degenerate retina exhibited increased current thresholds, mainly due to the presence of the glial scar layer. In contrast, epiretinal stimulation thresholds were almost similar for both healthy and degenerate models, implying epiretinal prostheses can bypass the influence of the glial scar layer.

Various stimulation strategies were examined for both healthy and degenerate retinal models. No significant difference among the three return electrode configurations (monopolar, quasi-monopolar and hexapolar) was found when the

distance between electrodes and RGCs was less than the electrode diameter. Electrode spacing was the significant factor underlying increased current thresholds, where electrode size had a marginal impact among all three return electrode configurations. Stimulus pulse polarities and durations were found to have a significant impact on the localisation of evoked phosphenes. Moreover, virtual electrodes could be elicited by using an appropriate time shift between two stimulus waveforms applied to the active electrodes.

Table of Contents

List of Figures

List of Tables

Abbreviations

AIS	Axon Initial Segment
AMD	Age-Related Macular Degeneration
AP	Action Potential
FEM	Finite Element Method
FM	Fohlmeister and Miller
Hex	Hexapolar
IPL	Inner Plexiform Layer
MEA	Micro Electrodes Array
ONL	Outer Nuclear Layer
OPL	Outer Plexiform Layer
QMP	Quasi-Monopolar
RGC	Retinal Ganglion Cell
RP	Retinitis Pigmentosa
RPE	Retinal Pigment Epithelium
VE	Virtual Electrode

1 Introduction

Vision is arguably the most important sense among all human senses. Vision processing consumes almost half of the brain more than any another sense (Van Essen, 2003). Vision enables us to perform daily tasks and perceive the environment around us. The loss of this sense can lead to complicated medical and psychological issues. Blind people are always reliant on other people or assistive technology to do daily activities. Photoreceptor degeneration is considered to be one of the most common reasons of blindness and it accounts for nearly 50% of blind cases (Bunce and Wormald, 2006). Age-related macular degeneration (AMD) and retinitis pigmentosa (RP) represent the most common diseases that cause photoreceptor death and consequently causing approximately 1.2 million people worldwide to be blind. Fortunately, despite the death of photoreceptors, a significant proportion of inner retinal neurons, especially retinal ganglion cells (RGCs), largely remain intact and functional. With improvements in technology, there is a possibility of restoring rudimentary vision in blind patients by using artificial electrical stimulation. Depending on which part of the visual system is electrically stimulated, different types of visual implants have been proposed. These involve optic nerve, cortical and retinal prostheses, and all of these approaches have allowed generation to some extent of visual perception in blind subjects.

The existing retinal prostheses mainly target RGCs, which are the final stage of retinal circuitry neurons that transmit information to the brain via the optic nerve. Anatomical and physiological experimental studies have indicated that there are more than 20 different kinds of RGCs providing the modulation of various aspects of visual information such as colour, edges and contrast. It has been demonstrated that most of these types differ in their intrinsic properties and their response to light or electrical stimulation. The current designs of retinal implants have presented promising results such as performing navigation or reading simple words (Dumm et al., 2014). However, advanced levels of visual perception,

such as facial recognition or fluent reading, warrants the necessity to develop a high resolution retinal prosthesis. To do so, we need to expand our understanding of the response of different types of RGCs to electrical stimulation.

Computational modelling is a powerful tool complementing experimental neuroscience for understanding the complex behaviour of neuronal circuits that can not be attained using the current state of the experimental approaches. Development of visual prostheses requires repeated and exhaustive experimental testing of electrode designs and stimulation strategies, which can become very costly and prohibitive in terms of the number of stimulus parameters and electrode configurations. Alternatively, computational simulation is a valuable tool for examining and testing new stimulation approaches to enhance the efficacy of visual prostheses.

1.1 Thesis Aims

This thesis was motivated by the need to improve our understanding of the behaviour of RGCs during electrical stimulation to find optimal electrical stimulation strategies for retinal prostheses.

The aims of this thesis are:

a) to develop a novel multi-compartmental continuum model of retinal electrical stimulation, incorporating all the main RGC compartments, in addition to the soma and AIS.

b) to develop, based on the above approach, a model that includes the two prominent kinds of RGCs: OFF and ON types, incorporating up-to-date descriptions of ionic currents observed experimentally.

c) to develop a model of electrical stimulation of the degenerate retina , incorporating ON and OFF RGCs.

d) to investigate various stimulation strategies to optimise the design of retinal implants and understand the response of RGCs to various modes of electrical stimulation.

1.2 Thesis Layout

This thesis details the development of multi-domain continuum models of OFF and ON RGCs in response to extracellular and intracellular electrical stimulation. The thesis chapters are structured as follows:

Chapter 2 provides an overview on the anatomy and physiology of the normal

retina, a brief background of the degenerate retina and some proposed treatments of retinal degenerative diseases.

Chapter 3 presents a critical review of important computational studies of retinal electrical stimulation.

Chapter 4 provides details of the derivation of a modified cable equation and ionic model formulations used to develop the retinal continuum model, including the parameter optimisation algorithms employed for model development.

Chapter 5 presents the efficacy of the modified cable equation compared to the classical cable under different scenarios of electrical stimulation and RGC structures.

Chapter 6 presents the framework development for a multi-domain continuum model and its validation against previous modelling and *in vitro* experimental data.

Chapter 7 presents the development of a degenerate retinal model incorporating both OFF and ON RGCs, and explores the influence of different stimulation strategies on healthy and degenerate models of the retina.

Chapter 8 concludes the main findings presented in this thesis and proposes some improvements to the models for future development.

1.3 Publications

The following refereed conference proceedings arose from work carried out in this thesis:

Alqahtani, A., Al Abed, A., Guo, T., Lovell, N.H. and Dokos, S., 2017, July. A continuum model of electrical stimulation of multi-compartmental retinal ganglion cells. In Engineering in Medicine and Biology Society (EMBC), 2017 39th Annual International Conference of the IEEE (pp. 2716-2719). IEEE.

Alqahtani, A., Al Abed, A., Anderson, Emily., Lovell, N.H. and Dokos, S., 2018, July. A Multi-Domain Continuum Model of Electrical Stimulation of Healthy and Degenerate Retina. In Engineering in Medicine and Biology Society (EMBC), 2018 40th Annual International Conference of the IEEE.

2 Background

2.1 Visual System

In the eye, light is processed within retinal pathways and converted into electrical signals to generate vision. Light enters the eye via the cornea, pupil, lens and vitreous humour and travels to the retina. The amount of light approaching the retina is controlled by the iris, which basically manages the diameter of the pupil. The cornea and lens, which represent the refractive system of the eye, are used to focus the light on the retina. The choroid and blood vessels positioned in the inner retinal layers support retinal metabolism. The sclera protects the sides and back of the eye. In the human visual system, cells are organised retinotopically, which means adjacent cells can feed information from or to other cells in neighbouring areas of the visual pathway (Kolb, 2003; O'Brien, 2012; Weiland et al., 2005). The basic structure of the eye is displayed in Fig. 2.1.

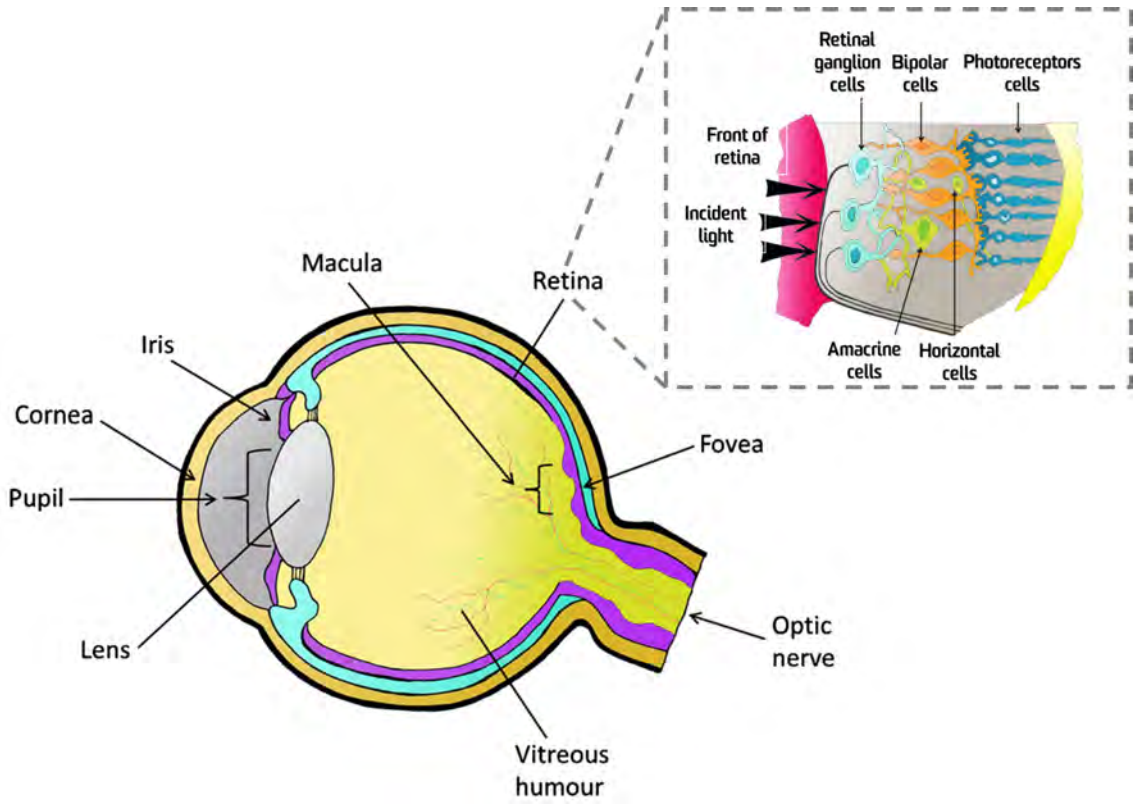

Figure 2.1: Schematic diagram of the human eye (Fitzpatrick, 2014).

2.2 The Retina

Vision is shaped through the retina which has a thickness of approximately 250 μm in vertebrates (Dowling, 2009). Visual perception is accomplished by transducing light to electrical signals via the retina and these signals are interpreted by the brain. The retina is a highly complex tissue containing more than 100 different types of cells (Kolb, 2003), with a well-organised architecture in which all retinal layers can be physically identified and the relationship between these layers and neurons being well-characterised (Masland, 2012). The interconnections between retinal neurons occurs through either gap junctions or synapses (Masland, 2001). In most mammalian retinas, retinal cells are not distributed evenly and there is a region where cells are densely packed. This region is called the macula , and is located near the centre of the retina laterally from the optic disk, known for its absence of blood vessels. The macula contains the fovea which has a high concentration of cone photoreceptors and is specialised for high resolution vision (Cohen, 2007; Kolb, 2003; Wassle and Boycott, 1991).

2.2.1 Retinal Layers

The retina is composed of multiple well-organised layers including several neural cells with different connections and pathways necessary for modulating vision. The retinal pigment epithelium (RPE), which is known as a highly resistive layer (Cohen, 1965), is the outermost structure of the retina. This layer acts as a regulator for transporting nutrients and ions and waste exchange between the retina and blood vessels. Continuing more distally from the sclera, the cell bodies of rod and cone photoreceptors reside in the outer nuclear layer (ONL). The horizontal and bipolar cells have synaptic connections with cone pedicles and rod spherules in the outer plexiform layer (OPL). The splitting of visual signals into two known categories, ON and OFF pathways, takes place in the OPL. The receptive field is constructed from information obtained from the millions of

photoreceptors and the inhibitory influence of horizontal cells. The cell bodies of horizontal cells, amacrine cells (ACs) and bipolar cells (BCs) establish the inner nuclear layer (INL). The inner plexiform layer (IPL) is the place of synaptic connections between the BCs and ACs with the RGCs. In this layer, two sublaminae are formed based on the ON and OFF pathways: the OFF ganglion cells form synaptic connections in sublamina a and the ON ganglion cells in sublamina b. The cell bodies of the RGCs form the final layer, known as the ganglion cell layer (GCL) (Kolb, 1979, 2003; Nelson et al., 1978; Weiland et al., 2005). It has been observed that there is often a displacement between amacrine cells and ganglion cells, in which amacrine cells may be located in the ganglion cell layer and vice versa, however, this only occurs in a small number of all cells in the inner retina (Wassle and Boycott, 1991). The nerve fiber layer, which connects the optic disk, is formed by the axons of ganglion cells. The choroid is separated from the retinal pigmented epithelium (RPE) by Bruch's membrane. The inner limiting membrane separates the retina and vitreous humour whereas the outer limiting membrane separates the photoreceptor layer from the ONL.

Significant preprocessing of visual signals occurs in the ganglion cell layer, which integrates all main visual pathways into ganglion cell outputs capable of generating action potentials (APs). Visual information captured by the eye is encoded by these action potentials and sent along the optic nerve to the brain to interpret it.

In the normal eye, visible light passes the inner retina due to its transparency, reaching the outer segments of photoreceptor cells which absorb most of light. The remaining light is absorbed by the RPE which contains melanin which helps to absorb light and prevents any reflection light back to the retina (Kolb, 2003).

As mentioned earlier, the retina is made up of multiple distinct layers that include the major retinal neurons, as shown in Fig. 2.2. The five major retinal cells which play a role in the visual perception process, will be discussed in some detail below, along with glial cells, which are not included in the visual perception

circuitry but play a significant role in structural support.

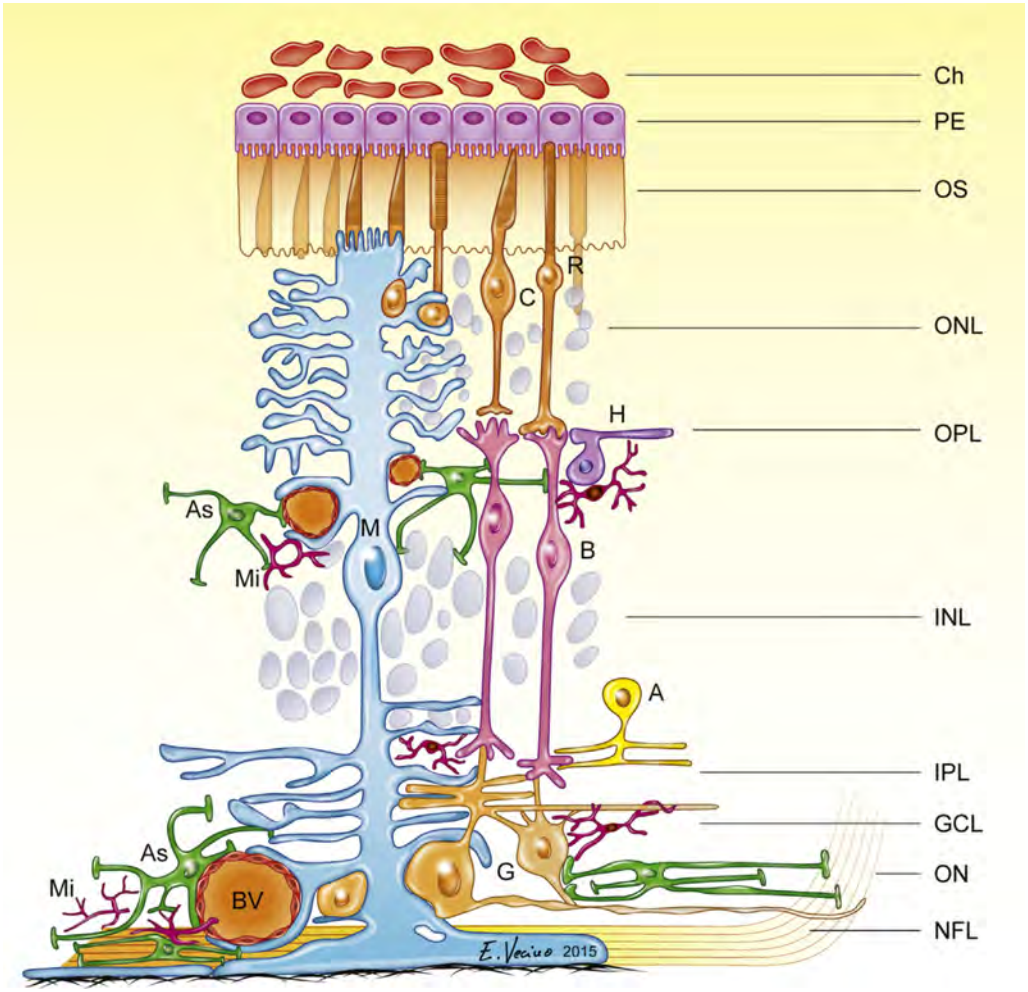

Figure 2.2: Schematic diagram of retinal layer architecture and their cellular components. Retinal neurons which play a significant role in vision processing include rods (R), cones (C), horizontal cells (H), bipolar cells (B), amacrine cells (A) and ganglion cells (G). Glial neurons, which provide structural support, include astrocytes (AS), Müller cells (M) and microglia (Mi). These cells interact with blood vessels (BV), and cells are located in different layers: the choroid (Ch), retinal pigment epithelium (RPE), outer segment layer (OS), outer nuclear layer (ONL), outer plexiform layer (OPL), inner nuclear layer (INL), inner plexiform layer (IPL), ganglion cell layer (GCL), nerve fibre layer (NFL) and the optic nerve (ON). (Vecino et al., 2016)

2.2.2 Photoreceptors

Photoreceptors are the first retinal cells that respond to the incident light and transduce it to a neural signal. There are two basic types of photoreceptors: cones and rods. In the human retina, there are over 130 million rod and cone photoreceptors, which eventually converge into nearly 1 million RGCs (Dowling, 2005). Cones are responsible for colour vision whereas rods are responsible for dim light in order to tackle scotopic vision (Masland, 2012). Unlike most retinal cells, both cones and rods are hyperpolarised in response to light. The foveal region is known as a high-acuity vision area due to the presence of densely packed cones. Rods are absent in the fovea with their density increasing towards the periphery. Rods constitute the major proportion of the mammalian retinal photoreceptor cells with a ratio of 20:1 with respect to cones (Mustafi et al., 2009).

The outer nuclear layer houses the cell bodies of photoreceptors, whereas their synaptic terminals are positioned in the outer plexiform layer. In the human retina, cones are categorised into three spectral subtypes, each detecting wavelengths in specific bands, short (430 nm peak), medium (530 nm peak), and long-wavelength (560 nm peak), to discriminate the detected light, mediating colour vision. In contrast, rods use a single band of wavelength to absorb light peaking at 500 nm (Mustafi et al., 2009).

Anatomically, the four main parts that constitute each photoreceptor are: the nucleus, the synaptic terminal and the inner and outer segments. The outer segments contain visual photopigments, which initiate phototransduction when activated by light, and are located in the distal region of the retina (Baylor, 1987; Steinberg et al., 1980).

2.2.3 Horizontal Cells

Horizontal cells represent the interneurons that provide lateral interactions in the retinal pathway by forming synapses with photoreceptors and modulating their

outputs. The information is transferred vertically through retinal layers and also horizontally parallel to the retinal surface through the horizontal cells. Horizontal cells have connections with both photoreceptors and bipolar cells through synapses (Kolb, 1979) and often hyperpolarise in response to light (Wässle, 2004). The connection between horizontal cells is facilitated mainly through gap junctions and in some cases by synapses.

Horizontal cells are assumed to constitute 5% of the inner nuclear layer cells. Based on morphological shape, there are typically two distinct types of horizontal cells in most mammals, with a third type sometimes proposed. The HI (with axons), HII (axonless) and HIII horizontal cell. In small mammals such as rats and mice, only one type of these cells is present. Horizontal cells play a vital role in adjusting the system's response to the overall level of illumination by keeping the transmitted signal within the inner retinal circuitry operating range (Masland, 2001).

2.2.4 Bipolar Cells

Bipolar cells transfer information from photoreceptors to the other retinal neurons: amacrine, horizontal, and ganglion cells; with extensive synaptic feedback of bipolar cells coming from amacrine cells. Eleven types of bipolar cells can be classified into three main groups based on morphology, physiology, and dendritic contacts: rod bipolar cells and ON and OFF cone bipolar cells. During light stimulation, rod bipolar cells and ON cone bipolar cells are depolarised while OFF cone bipolar cells are hyperpolarised (Boycott and Wässle, 1991). This difference in response is related to the type of glutamate receptor they express: rod bipolar cells and ON cone bipolar cells express a metabotropic receptor (mGluR), while OFF cone bipolar cells express an ionotropic glutamate receptor (iGluR). Bipolar cells play a significant role in visual perception by providing excitatory inputs to ganglion cells (Margalit and Thoreson, 2006). It should be noted that only RGCs generate action potentials while other retinal neurons generate graded re-

sponses.

2.2.5 Amacrine Cells

Amacrine cells are widely spread out over the retina having approximately thirty types. The classification of these cells presents a challenge because of the diverse morphological and physiological properties of amacrine cells (MacNeil and Masland, 1998). However, they can be classified into three groups on the basis of their morphological properties: narrow field, medium field and large field. Narrow-field amacrine cells exhibit dendritic arbors of less than 125 μm diameter, medium-field 125 - 400 μm in diameter and wide-field of larger than 400 μm in diameter (MacNeil and Masland, 1998). Amacrine cells typically generate graded membrane potentials instead of firing action potentials (Zigmond, 1999). However, some studies have indicated that certain types of amacrine cells could fire action potentials (Wollner and Catterall, 1986). Amacrine cells could play a significant role in visual perception by providing inhibitory inputs to ganglion cells (Margalit and Thoreson, 2006).

2.2.6 Ganglion Cells

Ganglion cells form the final stage of processing retinal neuronal circuitry. They play the most significant role in collecting information from bipolar and amacrine cells, transferring this information to the brain via the optic nerve. Regarding primate retinas, some studies have pointed to the diversity of ganglion cells types reaching twenty subtypes in some reports (Kolb et al., 1981; Masland, 2001; Popova, 2015), leading to difficulties in classification of RGCs. To be more specific, based on morphology, retinal ganglion cells (RGCs) can be classified into three types: alpha, beta, and gamma (Boycott and Wässle, 1974). Ganglion cells show two types of responses: (1) a sustained response when their inputs are received from bipolar cells and (2) a transient response when their inputs are received from amacrine cells (Dowling, 2009).

The inner plexiform layer is divided into equal distinct five layers, known as strata. Ganglion cells have distinct stratification patterns in the inner plexiform layer. Therefore, the differentiation between various RGCs types could be based on their stratification. It has been identified that the dendrites of ON ganglion cells project to strata 4 and 5, which lie close to the ganglion cell layer, whereas the dendrites of OFF ganglion cells project to strata 1 and 2, which are closer to the inner nuclear layer. ON-OFF ganglion cells are bi-stratified, projecting into both the ON and OFF RGC layers as shown in Figure 2.3 (Nelson et al., 1978; Wassle and Boycott, 1991).

The response of RGCs in the presence of light has been characterised into three different types. ON RGCs produce a transient burst of impulses at the onset of light stimuli and then generate sustained impulses until the stimulus is terminated. OFF RGCs generate a sustained impulse discharge after the termination of the light stimulus. ON-OFF RGCs generate transient discharge bursts at the onset and offset of light stimuli (Dowling, 2009; Hartline, 1938).

The receptive field refers to the spatial region where a visual stimulus is capable of activating the neuron. The dendritic tree of a single RGC roughly covers the area of its receptive field. Some RGCs show two concentric receptive field regions that antagonise one another and are grouped into ON and OFF types. The receptive field centre of an ON RGC induces impulses responding to the onset of light, whereas its surround evokes impulses at light offset. The OFF RGC centre receptive field responds in the opposite way (Dowling, 2009; Hartline, 1938).

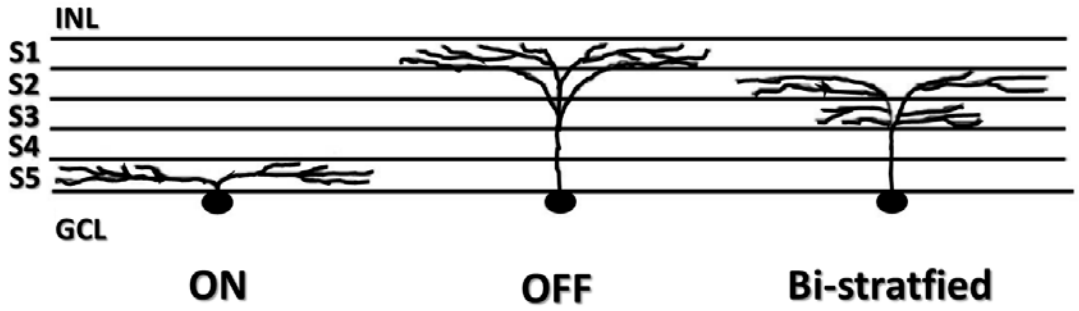

Figure 2.3: Schematic diagram of the stratifications of different RGCs in the inner plexiform layer. The inner plexiform layer is divided into five equal layers called strata (S1 to S5). INL and GCL are the abbreviations for the inner nuclear and ganglion cell layers respectively (O'brien et al., 2012).

2.2.7 Glial Cells

Glial cells are involved in the retinal circuitry, providing both structural and functional properties. Astrocytes, Müller cells and microglia represent the major types of glial cells. Müller cells, which are specific to the retina, constitute the majority of glial cells. These cells span from the outer limiting membrane in the photoreceptor layer to the inner limiting membrane in the nerve fiber layer, providing the structural support to the retina. Their functions involve removal of waste, regulation of glucose metabolism and recycling of neurotransmitters. The malfunction of Müller cells can cause proliferation of the RPE, retinal dysplasia and photoreceptor death (Bringmann et al., 2006; Vecino et al., 2016). Moreover, it has been observed during retinal injury, Müller cells will become gliotic and increase immunolabeling for Glial Fibrillary Acidic Protein (GFAP) (Milam et al., 1998). Astrocytes, which are common in the central nervous system, have been observed surrounding blood vessels in the ganglion cell & nerve fiber layers. However, their role is not well-characterised. Microglia, the third type, are located in the inner retina and they play a significant role in the immune response by repairing the damaged tissue, initiating the inflammatory process and eliminating the degenerate retinal neurons (Bringmann et al., 2006; Vecino et al., 2016).

2.3 Visual pathways

The two major vertical visual pathways in the retina are rod and cone pathways. Cone photoreceptors have a synaptic connection with ON & OFF bipolar cells (Wässle, 2004). Therefore, the two major subdivisions of cone photoreceptors are ON & OFF depending on the types of bipolar cells. The OFF pathway is hyperpolarised in response to light, whereas the ON pathway is depolarised in response to light. Rod photoreceptors only synapse with rod bipolar cells. The most notable connection of rod bipolar cells is with all narrow amacrine cells, which in turn provides either excitatory input to ON cone bipolar cells through gap junctions (electrical synapses), or inhibitory inputs to OFF cone bipolar cells via chemical synapses. The simplified diagram in Fig. 2.4 shows the major visual pathways in the vertebra retina. Additional pathways include the Parvo and magnocellular pathways located in the lateral geniculate nucleus (LGN) of the thalamus. These will be of more importance to cortical prostheses.

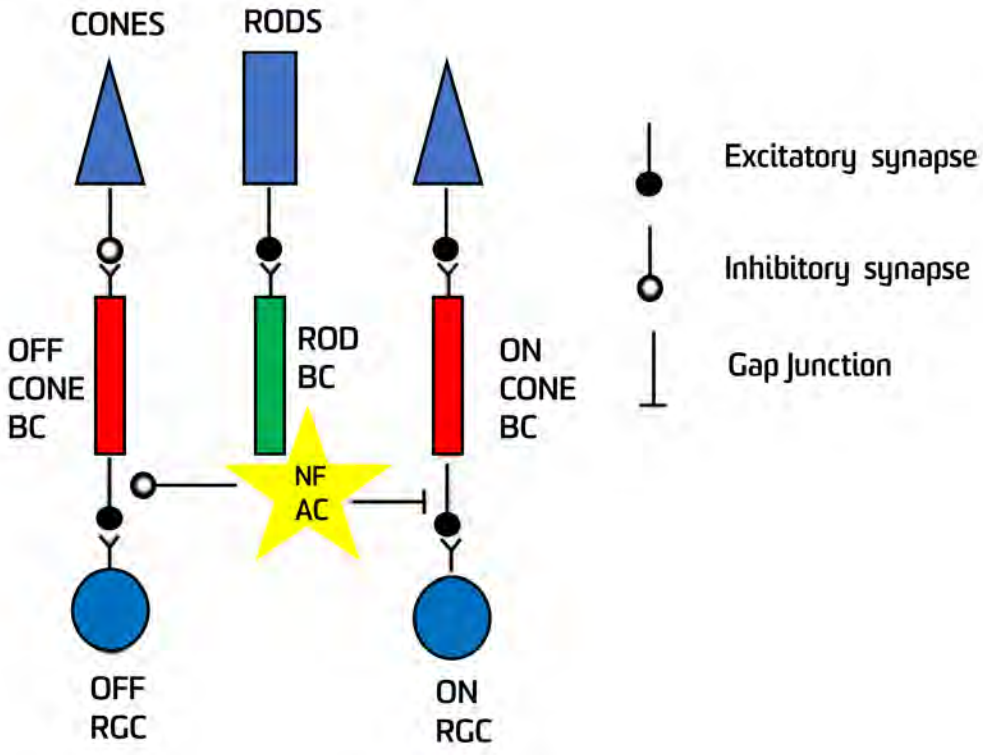

Figure 2.4: Major visual pathways in the vertebra retina (Yin, 2012).

2.4 Retinal synapses

The transmission of signals from one neuron to another is conducted through two mechanisms: gap junctions and synapses (Boinagrov, 2014). The synaptic cleft is the region where the axon of the presynaptic neuron is close to the dendrites of the postsynaptic neuron. The arriving electrical signal at the presynaptic axon stimulates the opening of calcium channels, which in turn release vesicles with neurotransmitters into the synaptic cleft. These substances modulate the ion channels and consequently the electrical potential of the dendrites of the postsynaptic neuron. Different neurotransmitters are utilised in the retina. Photoreceptors, bipolar and ganglion cells use glutamate, whereas amacrine and horizontal cells produce GABA and glycine. The most significant retinal synapses and their neurotransmitters are illustrated in Fig. 2.5.

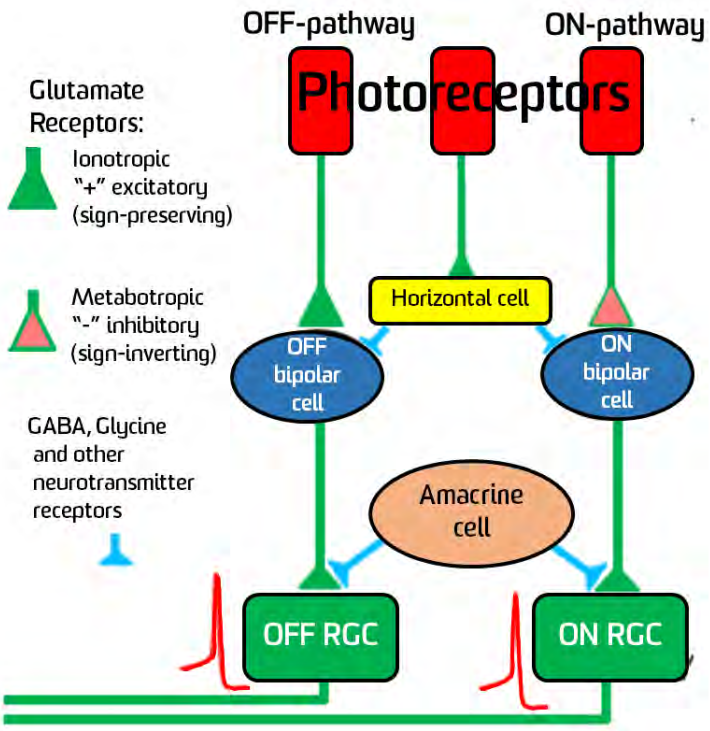

Figure 2.5: Retinal synapses and their neurotransmitters in OFF and ON visual pathways (Boinagrov, 2014).

2.5 Retinal Diseases

The two main diseases that cause degeneration of photoreceptors leading to blindness are RP & AMD. RP is a family of inherited diseases affecting around 2 million people worldwide (Hamel, 2006). This disease results from harmful changes or mutations in genes that are responsible for proteins essential to retinal photoreceptors cell function. Clinical studies have shown that RP begins in the peripheral retina. At early stages, damage occurs in the rods, followed by cones. After the death of rods, affected individuals have difficulty with night vision and the visual field becomes restricted. In the late stages of RP during cone death, visual field loss is increased and those affected cannot perform daily tasks without assistance such as reading, walking or recognizing objects. RP patients experience a difficulty with bright lights. The progression of RP varies greatly from person to person (Milam et al., 1998).

In contrast, AMD targets the central retina (macula), causing blurred vision in the centre of image. AMD initially affects the RPE and Bruch's membrane, which reduces the number of RPE cells and forms drusen, or fatty deposits, between the RPE and Bruch's membrane (Sarks, 1976). There are two types of AMD: wet and dry. Dry AMD, which accounts for 90% of all AMD cases, leads to degeneration of rods first followed by cones, whereas wet AMD starts with choroidal neovascularisation followed by photoreceptor degeneration (Curcio et al., 1996). Currently there is no medical treatment for dry AMD, but there are vitamins that could slow down the progress of degeneration. Clinical examination of human retinas have revealed the survival rate to be 4% for photoreceptors, 30% for ganglion cells and 80% for the other inner retinal cells in the macula of patients with severe RP (Santos et al., 1997). For AMD patients, the viability of inner retinal cells reaches 90%, whereas the percentage of intact RGCs reaches 70% and 53% for patients with dry and wet AMD, respectively (O'Brien, 2012).

Visual acuity represents one of the significant characteristics of vision quality,

quantifying the spatial resolution of the visual system. The visual acuity of normal subjects is 20 / 20. Legal blind subjects have a visual acuity less than 20 / 200 in the USA or 20 / 400 according to the world health organisation (Resnikoff et al., 2004). Fig. 2.6 compares vision between normal subjects and those who have RP or AMD.

Figure 2.6: Typical effects of retinal degeneration on visual field. Top: Visual field of a normal subject; Middle: Subject with macular degeneration. Bottom: Subject with retinitis pigmentosa (Yue et al., 2016).

2.6 Degeneration stages during retinitis pigmentosa

Some studies have classified retinal degeneration into three phases (O'Brien, 2012). Phase 1 can be described as the initial changes in the photoreceptor layer such as a shortening of the outer segments. Moreover, the projection of horizontal cells into the inner nuclear and ganglion cell layers starts to take place. Furthermore, the dendrites of bipolar cells are retracted and Müller cells begin to be gliotic. Phase 2 is characterised by the complete degeneration of photoreceptors, with Müller cells starting to form a seal between the choroid and retina. Phase 3 is defined by significant changes in the inner retina. Moreover, the death of inner retinal cells, migration of neural cells and retinal network rewiring have been observed during phase 3. Formation of large scar layer by Müller cells have been observed in this phase and could be manifest through the whole inner retina, including the ganglion cell layer in the late stages of phase 3.

2.7 Approaches to restoring vision

Three main treatments have been proposed to restore vision in blind patients. These three therapies will be discussed here in some detail.

2.7.1 Stem cell therapy

Stem cell therapy is the transplantation of donor cells into the retina to replace nonfunctional retinal neurons and to connect and integrate with the remaining viable retinal neurons. These cells maybe photoreceptors or RPE, aiming to repopulate the degenerate retina or rescue the surviving neurons from further degeneration. Animal studies have shown the feasibility of this kind of treatment (O'Brien, 2012). A clinical trial of stem cell transplantation for 5 patients with RP

and cone-rod dystrophy showed no adverse events for 10 months (Siqueira et al., 2011). Another clinical study conduced on 6 patients with irreversible vision loss and one patient with RP showed that there was no significant adverse effects for 6 months (Park et al., 2015). However, the efficacy of this treatment is contradictory between clinical studies. One study conducted on two patients with RP who received retinal grafts revealed there is no improvement in visual perception even after 1 year from transplantation (Kaplan et al., 1997). However, a recent study has reported an enhancement in visual acuity for 3 out of 6 patients with RP who received a full retinal transplant (Radtke et al., 2008). The latter finding has encouraged the adoption of this therapy as a solution to restore vision for blind people due to the ease of transplantation and minimal risk to the retina compared to chronic stimulation and complex surgery for a visual prostheses. However, the effectiveness of this therapy to restore vision has not yet been proven (Dias et al., 2017).

2.7.2 Gene therapy

Gene therapy is a strategy which aims to repair genetic malfunction utilising viral or non-viral vectors. This approach is generally divided into two major approaches. The first is replacing the mutant gene in the unhealthy cell with a developed gene. Animal studies have provided promising results on preservation of the retina during degeneration or improvement in light perception. The second approach uses optogenetics to assist specific retinal cells, such as bipolar or ganglion cells, to be intrinsically photosensitive. Animal experiments have reported a recordable visual response with these cells (O'Brien, 2012). A recent review has shown that clinical trials of gene therapy lead to considerable improvement in the visual perception of RP patients (Dias et al., 2017). Luxturna is the first gene therapy for inherited retinal dystrophy approved by the Food and Drug Administration (FDA) (Smith and Agbandje-McKenna, 2018).

2.7.3 Visual prostheses

Multiple approaches to electrical stimulation targeting different parts of the visual pathway for restoring vision have been investigated by different research groups worldwide. The application of electrical stimulation has proved to be successful with other neurological disorders such as deafness, cardiac abnormalities and Parkinson's disease (O'Brien, 2012). This approach is the first approved treatment for blindness resulting from photoreceptor degeneration: so far three retinal implants have been commercialised (Edwards et al., 2018; Yue et al., 2016). Depending on the specific part of visual system targeted, visual implants can be categorised into three kinds: visual cortex, optic nerve and retinal implants.

The main advantages of retinal prostheses over the other two implants is avoiding intracranial implantation and the requirement of individual mapping of stimulation sites in the cortex associated with visual cortex implants, as well as the spatial resolution and topographic mapping associated with optic nerve implants (Dowling, 2005; Weiland et al., 2005). Retinal prostheses are classified into three types based on the location of the stimulus electrodes: epiretinal, subretinal and suprachoroidal prostheses, as shown in Fig. 2.7 .

2.7.3.1 Epiretinal Prostheses

Epiretinal prostheses are inserted just above the inner surface of the retina in the vitreous humour, close to the RGCs and nerve fiber layer, providing direct stimulation of RGCs. The commercial Argus II is the first approved retinal implant device for patients with RP (Yue et al., 2016). More recently, IRIS II, an epiretinal prosthesis with 150 electrodes, has been granted approval to commercialise in Europe (Edwards et al., 2018).

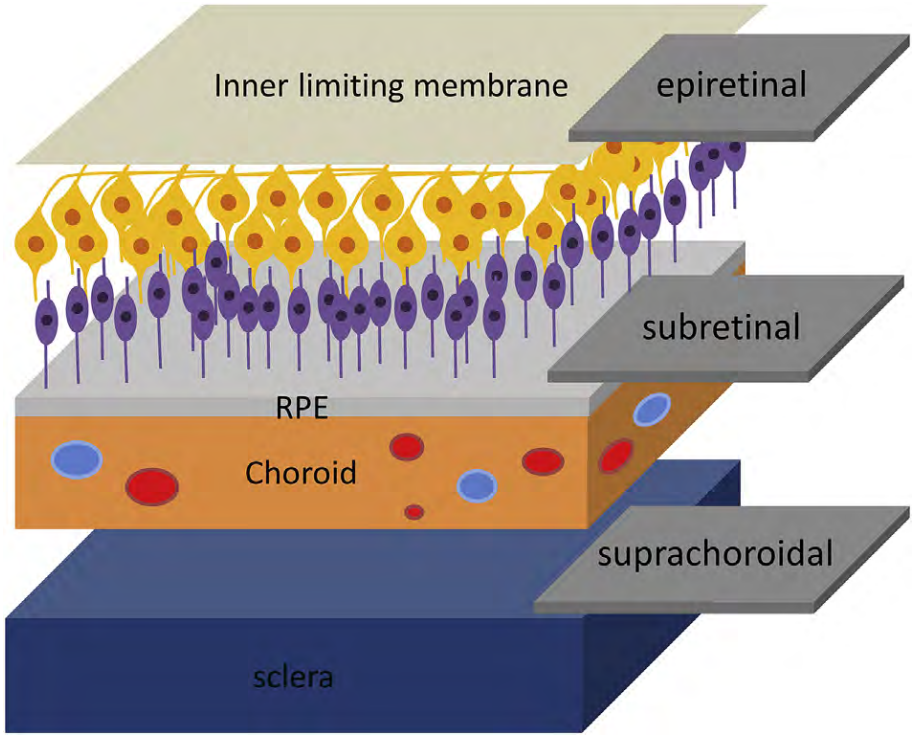

Figure 2.7: The location of electrodes in various retinal prostheses (Yue et al., 2016).

Epiretinal prostheses offer many advantages over other retinal implants. A single action potential can be generated from each stimulation pulse due to the direct activation of RGCs (Sekirnjak et al., 2006). By using this approach, RGCs can accurately follow maximum spike frequencies according to the natural retinal response to light, which reaches up to 250 Hz (Fried et al., 2006). Moreover, these implants can bypass both the high impedance of glial scar layer and remodelled retina associated with network retina stimulation (Marc et al., 2003). The vitreous can be utilised as a heat sink in this approach (Weiland et al., 2005). Furthermore, animal studies have shown this approach has the lowest stimulus thresholds compared to other retinal implants for evoking APs. Recent clinical trials conducted on patients who were implanted with Argus II (Da Cruz et al., 2013), have demonstrated some improvements such as object localisation, motion discrimination and letter identification. The visual acuity was determined to be 20/1260. However, this approach has some drawbacks. Due to the closer

location of the epiretinal implant microelectrodes array (MEA) to the nerve fibre layer, somatic and axonal stimulus thresholds are comparable, especially with the pulse durations used currently with the available epiretinal implants. As such, the possibility of activation of passing axons beneath the electrodes, which have been observed to cause wedged visual precepts, is very high (Nanduri et al., 2012). Moreover, fixation of the MEA represents a challenge compared to other approaches. A recent report has found the MEA of the Argus II system displaced up to 400 μm from its original setting, and as a result the thresholds increased (Ahuja et al., 2013). Furthermore, patients have reported percepts did not match the stimulation pattern. Also, it has been observed the limit of safe charge injection is often exceeded to obtain visual perception in RP patients (Rizzo et al., 2003).

2.7.3.2 Subretinal Prostheses

Subretinal prostheses are located between the RPE and photoreceptors. The AG Alpha IMS implant has recently received the CE mark approval to be the first retinal implant obtaining European regulatory certification (Yue et al., 2016). There are two kinds of subretinal implants. First, multi-photodiode arrays convert the light into electrical signals in order to replicate the function of the degenerate photoreceptors (Chow and Chow, 1997). This device relies on incident light to power it, however, it has been reported that light was insufficient, and external power has been proposed (Zrenner, 2002). The second type uses MEAs receiving input from image processors. They deliver electrical pulses in the outer retina to stimulate retinal network, especially bipolar cells (Zrenner, 2002). The advantages of this approach are its stability due to its location, sandwiched between the retina and choroid. Clinical studies on patients with RP have demonstrated an improvement in the ability of patients to find the location of bright objects in a dark background, discriminating between a knife or fork on a table and discerning letters and some geometric shapes. The best visual acuity obtained with

the Alpha-IMS system was 20/550 (Stingl et al., 2013; Zrenner et al., 2011). A major disadvantage of subretinal and suprachoroidal prostheses is the presence of a glial seal layer. This layer acts like a high impedance barrier impeding the current stimulus from reaching the targeted neurons. Also, the retina undergoes significant retinal remodelling after degeneration, leading to increased difficulty in stimulating the retinal network (Marc et al., 2003). Moreover, the exchange of nutrients and waste between the retina and choroid is an issue due to the presence of the MEA which acts as a barrier. To avoid this problem, a porous MEA has been proposed (Schubert et al., 1999). Furthermore, a thermal source could be generated, due to its location between tissues.

2.7.3.3 Suprachoroidal Prostheses

Suprachoroidal prostheses are placed between the sclera and choroid, or within the sclera as in the case of the suprachoroidal-transcleral (STS) implant. Due to its location, it offers an easy insertion, robust implant fixation, the potential for heat dissipation through choroid blood vessels, easier explantation, minimal invasive surgery and low risk of damage to the retina. However, higher stimulation currents are required because the electrodes are further away from the target cells. Another limitation is the lower spatial resolution due to current spreading (Bareket et al., 2017). The Bionic Vision Australia (BVA) group conducted the first trial of implanting a suprachoroidal retinal prosthesis in a human (Ayton et al., 2014). The follow-up report of this trial in three subjects after one year revealed that the implant is still stable and functional, and visual perception was evoked in all three patients without exceeding the safe charge injection. Moreover, another clinical study conducted on two subjects with RP implanted with a suprachoroidal-transcleral (STS) device have shown the ability of patients to discriminate between two bars, and to grasp an object (Fujikado et al., 2011).

3 Existing Computational Models of Retinal Electrical Stimulation

The human retina has a well-organised architecture, in which the interaction between most retinal neurons is well-characterised and physical identification of functional retinal layers can be easily accomplished (Guo et al., 2014). Accordingly, several computational models of retinal electrical stimulation have been proposed based on the available anatomical and neurophysiological data obtained experimentally. These models range from simple to highly complex, aiming to investigate various aspects of the retinal system's response to light or electrical stimulation. They have enabled researchers to sharpen their understanding of the retina and the role of its intrinsic biophysical and anatomical properties on the perception of light, as well as its behaviour in response to electrical stimulation. The focus of the modelling review in this chapter is on RGC models rather than amacrine, photoreceptor, bipolar or horizontal cell models.

3.1 Intrinsic RGC Electrophysiological Properties

RGCs responses are shaped by their morphology (Fohlmeister and Miller, 1997*b*; O'Brien et al., 2002), their synaptic connections coming from the retinal network (Masland, 2001; Wong et al., 2012), and their intrinsic physiological properties (Kameneva et al., 2011; O'Brien et al., 2002; Wong et al., 2012). It was found that RGCs could reach up to 20 types, having synaptic connections with around 10 types of bipolar cells and more than 20 types of amacrine cells, each connection providing a different response (O'Brien et al., 2002). It has been demonstrated that different types of RGCs exhibit marked differences in their passive (resting membrane potential, time constant, input resistance) and active (spiking behavior, frequency adaptation, rebound excitation, burst firing and

maximum firing rates) properties due to the difference in their morphology (Cho et al., 2016; Fohlmeister and Miller, 1997*b*; Maturana et al., 2014) . Although differences in synaptic network connections and morphology clearly contribute to the functional differentiation among RGC types, intrinsic physiological properties may also play a significant role (Margolis and Detwiler, 2007; Miller et al., 2006; Wong et al., 2012).

The heterogeneity among RGCs in terms of intrinsic membrane properties has been confirmed in many studies (Ishida, 1995; Lipton and Tauck, 1987). For instance, there is a marked variation in the density, number and kinetics of voltage-activated Na^+ currents (I_{Na}) (Kaneda and Kaneko, 1991; Miller et al., 2002), voltage-activated K^+ currents (I_K, I_A, I_B, I_{KCa}, I_{Leak}) (Ishida, 1995; Tabata and Ishida, 1996), the hyperpolarization-activated cation current (I_h) (Margolis and Detwiler, 2007; Tabata and Ishida, 1996) and voltage-activated Ca^{2+} currents (I_{Ca}) (Kaneda and Kaneko, 1991; Miller et al., 2002) among different types of RGCs. It was demonstrated that the input resistance (R_N) varied among rat RGCs up to 10-fold (Wong et al., 2012). This differentiation could be partly accounted for by morphological differences, but also by ion channel distribution. The differential expression of calcium-activated K^+_{KCa} channels has been demonstrated to play a significant role in the variation of frequency adaptation among different RGC types (Wang et al., 1998). The reduction in spike amplitude during repetitive spiking has been attributed to voltage-gated sodium channel (VGSC) deinactivation (Wong et al., 2012). Different studies showed that RGC types vary in their rate of VGSC deinactivation (Kaneda and Kaneko, 1991). Therefore, amplitude and contrast adaptation may be different among RGC types depending upon VGSC subunits that are expressed.

In vitro experiments have indicated that the hyperpolarisation-activated mixed cation current (I_h), the low threshold voltage activated calcium current (I_{CaT}) and the persistent Na^+ current (I_{NaP}) have a significant contribution to neuronal excitability. For example, I_h has an impact on subthreshold membrane and rest-

ing potentials (O'Brien et al., 2002), the mechanism of spontaneous activity (Mccormick and Pape, 1990), reducing input resistance (Surges et al., 2004), supporting dendritic summation (Abbas et al., 2013), as well as handling rebound spike frequency and timing (Engbers et al., 2011). I_{CaT} has contributed to burst firing (Destexhe et al., 1998) and also rebound excitation with the assistance of I_h (Mitra and Miller, 2007). I_{NaP} was found to play a role in subthreshold membrane potential oscillations and the generation of spontaneous activity in RGCs (Margolis and Detwiler, 2007). The presence or expression of these currents among RGCs types was varied. For example, OFF RGCs were found to show subthreshold membrane potential oscillations and spontaneous activity due to the presence of these currents. In contrast, ON RGCs do not display these phenomena due to the absence of these currents.

3.2 Single Cell models

Single cell models are the basis for larger system models such as network or continuum models. They have presented valuable insights by allowing the study of intrinsic properties of specific neurons, facilitating prediction of their behaviour during electrical stimulation.

3.2.1 Single Compartment Models

Voltage clamp studies on retinal ganglion cells of tiger salamander (Lukasiewicz and Werblin, 1988) and rat (Lipton and Tauck, 1987) have indicated the presence of five ionic currents. These studies have led to the first detailed mathematical ionic model of RGCs carried out by Fohlmeister, Coleman and Miller (Fohlmeister et al., 1990), and modified later to incorporate a leakage current (i_L) leading to a landmark single compartment model of the retinal ganglion cell (Fohlmeister and Miller, 1997*a*). This kinetic model of nerve impulse generation in RGCs is a modification of the Hodgkin-Huxley (1952) formulations (Hodgkin and Huxley,

1952), and consists of six ionic currents: four voltage-gated currents, a fifth dependent on intracellular calcium concentration, and a leakage current. This model proposed the following equation to describe the membrane potential:

$$J_m = C_m \frac{dV_m}{dt} + J_{ion} - J_{stim} \tag{1}$$

where J_m is the total membrane current density per unit membrane area, C_m is the specific membrane capacitance, V_m is the membrane potential, J_{ion} is the total ionic current density and J_{stim} is the stimulus current.

The total ionic current density J_{ion} is given by:

$$J_{ion} = i_{Na} + i_k + i_{kA} + i_{kCa} + i_{Ca} + i_L \tag{2}$$

where i_{Na} is the sodium current, i_k is the delayed-rectifier potassium current, i_{kA} is the A-type potassium current, i_{kCa} is the calcium-activated potassium current, i_{Ca} is the calcium current and the leakage current is i_L.

This model was validated by whole cell recordings from tiger salamander ganglion cells using the voltage clamp techniques and pharmacological studies, providing a good agreement with experimental results (Fohlmeister and Miller, 1997*a*). The Fohlmeister and Miller (FM) model has been successfully employed and extended in several modelling studies during the last few decades. This model was largely used in morphologically-realistic simulations to investigate the contribution of cell morphologies and ion channel distribution to neural excitability. This model and its derivatives have helped to clarify different phenomena observed in experimental studies such as spike-frequency adaption (Fohlmeister and Miller, 1997*a*), membrane potential oscillations, burst firing and rebound excitation (Guo et al., 2012; Kameneva et al., 2011). Moreover, it is widely used as a basis for (1) continuum models of retinal electrical stimulation and (2) discrete retinal network models. Models based on the single cell FM model are illustrated in figure 3.1 (Guo et al., 2014).

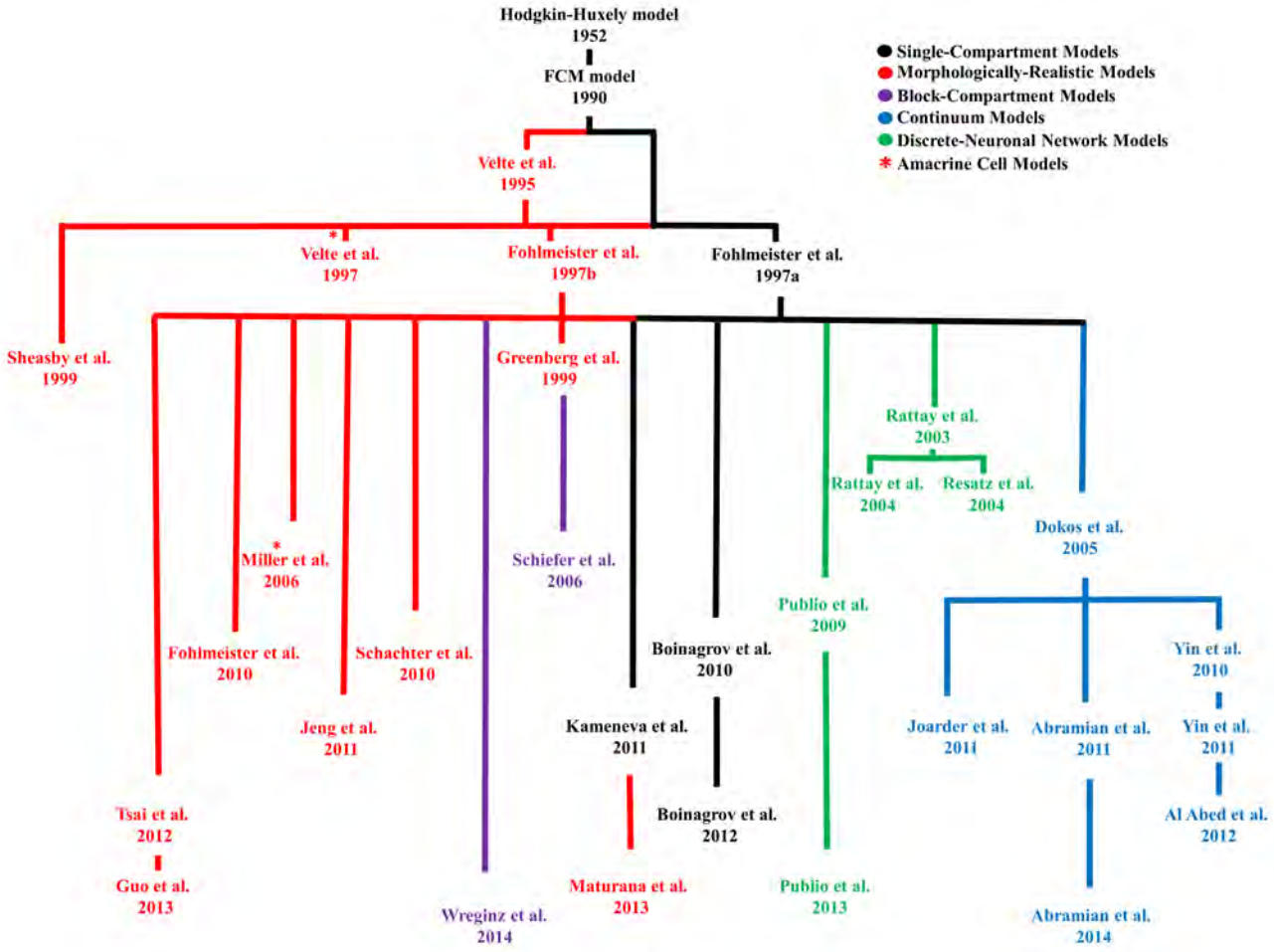

Figure 3.1: Fohlmeister and Miller (FM) 1997b model and its extended models, adapted from Guo et al. (2014).

3.2.2 Cell-Specific Single Compartment Models

Recently, several studies have emphasised the significant role of intrinsic electrophysiological properties of RGCs in shaping and controlling their repetitive firing patterns (Kameneva et al., 2011; Margolis and Detwiler, 2007; Mitra and Miller, 2007). The presence of different types of RGCs exhibiting various patterns of stimulation response in RGCs is due to the variation in their ion channels (Kolb et al., 1981). For example, the spike train frequency of ON RGCs is increased during light stimulation whereas that of OFF RGCs is not (Kameneva et al., 2011). A recent study has shown that OFF RGCs respond to stimulation frequencies different to those of ON RGCs during sinusoidal stimulation (Freeman et al., 2010). To illustrate this variation, a study by Margolis and Detwiler (2007) revealed that the electrophysiological differences between ON and OFF RGCs stem from their

synaptic circuitry and also their intrinsic electrophysiological properties (Margolis and Detwiler, 2007). Moreover, ON RGCs require excitatory inputs to drive their activation whilst OFF RGCs exhibit multiple mechanisms: (1) they generate action potentials in the absence of synaptic input, (2) they exhibit rebound excitation following strong hyperpolarising stimuli, (3) they exhibit subthreshold oscillations, and (4) burst firing. Another significant aspect of the study of Margolis and Detwiler (2007) was the identification of the persistent Na^+ current (I_{NaP}) in rat retinal ganglion cells and its role in the generation of spontaneous spike activity in OFF RGCs at rest. Another experimental study using tiger salamander retina, combined voltage and current clamp studies with pharmacological manipulation to identify the phenomenon of rebound excitation. This was found to be a result of the contribution of two currents: the hyperpolarisation-activated mixed-cation current (I_h) and the low threshold voltage activated calcium current (I_{CaT}) (Mitra and Miller, 2007). A recent modelling study has incorporated these three new currents (i.e. I_h, I_{CaT}, and I_{NaP}) into the FM model, comparing predictions with experimental results, showing the effect of intrinsic properties of OFF and ON RGCs during electrical stimulation (Kameneva et al., 2011). The total ionic current density after adding the new currents is given by:

$$J_{ion} = i_{Na} + i_k + i_{kA} + i_{kCa} + i_{Ca} + i_L + i_h + i_{CaT} + i_{NaP} \tag{3}$$

The mathematical expressions of i_h, i_{CaT}, and i_{NaP} were proposed earlier by (Van Welie et al., 2006) , (Wang et al., 1991), and (Traub et al., 2003) respectively.

The simplicity of this approach and its efficacy in reproducing and elucidating some experimental observations inspired several researchers to adopt it. However, due to the simple representation of the RGC by using a single compartment approach (usually the soma), it is difficult to optimise model parameters or to investigate experimental findings. For example, RGC axon and dendrites have been observed to play an important role during electrical stimulation (Guo et al., 2013). Therefore, the trade-off between simplicity and adding more compart-

ments to reproduce experimental findings should be considered.

In addition to RGCs, the single compartment modelling approach has also been utilised with other retinal neurons such as photoreceptors, bipolar cells, horizontal cells and amacrine cells (Guo et al., 2014).

3.3 Multi-Compartment Models

Multi-compartmental models are constructed, in general, to represent the entire neuron. For example, the RGC is described to consist of a soma, axon hillock, dendritic trees, thin axonal segment and distal axon. These models can be classified into two kinds: multi-compartment with simple geometries and multi-compartment models with morphologically realistic geometries. The latter are more accurate since they utilise anatomical morphologies and ionic channel distributions obtained from experimental data, whereas multi-compartment simple geometries only use the ionic channel distributions. The first detailed multi-compartment RGC model was formulated by Fohlmeister et al. (1997b). In this study, both kinds of multi-compartment models were presented, both providing significant results consistent with experimental findings. One of the key findings of this study was the critical role played by dendrites and the thin axonal segment in shaping the frequency of spike trains and impulse initiation sites (Fohlmeister and Miller, 1997*b*). In contrast, another morphologically realistic modelling study found that spike initiation could be elicited from various sites in the neural cell, with the exception of dendrites which have not been observed to be a site of impulse initiation neither in the model nor in experiments (Sheasby and Fohlmeister, 1999).

Due to the variation of membrane potential in both space and time in multi-compartment models, it can be determined by using the modified version of equation (1), expressed as a partial differential equation (Guo et al., 2014):

$$I_m = \frac{\partial}{\partial s}(\sigma_i \frac{\partial V_m}{\partial s}) = \beta(C_m \frac{\partial V_m}{\partial t} + J_{ion} + J_{stim}) \quad (4)$$

where I_m is the total volumetric current density (i.e. current per unit volume), s is the arc length along the neuron, σ_i is the intracellular conductivity, J_{ion} is the membrane ionic current density and β is the surface to volume ratio.

3.3.1 Cell-Specific Multi-Compartment Models

More recently, a computational study of OFF and ON rabbit RGCs has been published, providing insights into different aspects of the unique response of each RGC subtype to intracellular electrical stimulation (Guo et al., 2016). The authors used three multiple objective cost functions to optimise the model parameters with different spiking properties against multiple experimental data recordings. They compared their OFF and ON RGC models and the Fohlmeister et al. (1997b) model to experimental data, showing the capability of their models to reproduce total spike numbers as well as the rebound excitation for OFF RGCs in response to intracellular current injections, in contrast to the Fohlmeister et al.(1997b) model which could not. They incorporated two currents, namely the hyperpolarisation-activated mixed-cation current (I_h) and the low threshold voltage activated calcium current (I_{CaT}), identified in experiments (Margolis et al., 2010; Mitra and Miller, 2007). Total membrane ionic current was given by:

$$J_{ion} = i_{Na} + i_k + i_{kA} + i_{kCa} + i_{Ca} + i_L + i_h + i_{CaT} \quad (5)$$

The Maturana et al. (2014) multi-compartment formulation represents an extension of the Kameneva et al. (2011) single compartment model (Maturana et al., 2014). Two hundred morphologically-realistic RGCs classified into OFF and ON types were stimulated, showing the influence of both low threshold voltage activated calcium current (I_{CaT}), which is presented only in OFF RGCs, and the in-

fluence of morphology in replicating the differences between OFF and ON RGCs observed experimentally, such as subthreshold oscillations, burst firing, rebound excitation and spontaneous activity. This study showed that only those RGCs exhibiting a smaller ratio of dendrite surface area to the total membrane surface area were able to reproduce the full range of phenomena reported in the literature differentiating between OFF and ON RGCs. A recent modelling study has explored the impact of the hyperpolarisation-activated mixed-cation current (I_h) in generating the rebound excitation following hyperpolarising stimuli (Guo et al., 2012). This study modified a rabbit OFF RGC ionic model, based on the FM model, by adding a hyperpolarisation-activated mixed-cation current (I_h), optimising the parameters from a multi-dataset of experimental recordings. The results showed that by reducing the maximum membrane conductance of (I_h) by 30$\%$, the rebound impulse in OFF RGCs was eliminated. Another modelling study has modelled three types of mice RGCs namely: ON, OFF, and OFF parasol (Guo et al., 2013a). These models shared ionic channel kinetics, but differed in their realistic morphologies and ionic channel distributions. This study optimised the regional ion channel distributions for all three types of RGCs through fitting parameters governing action potential waveshape against experimental data. The results of this study were comparable with other experimental findings and supported the role of morphology and ionic channel distributions in shaping the unique response of each RGC type to electrical stimulation. A morphologically-realistic RGC computational model has scrutinised the influence of dendrites on spiking firing (Guo et al., 2013). Interestingly, the results showed that there is an inverse relationship between the number of dendrite branches and spiking frequency. Also, the first spike latency (FSL) was predicted to reduce with the reduction of dendritic branching.

The aforementioned models described the response of the RGC to intracellular electrical stimulation. However, retinal prostheses use extracellular electrical stimulation to excite the retina, therefore the understanding and control of RGC

responses during extracellular electrical stimulation is the ultimate goal in developing retinal implants. Hence, retinal formulations that use extracellular electrical stimulation will be discussed below.

For extracellular stimulation, the membrane potential can be determined from the difference between the intra and extracellular potentials as follows:

$$V_m = V_i - V_e \tag{6}$$

where V_i is obtained from the following cable equation (Guo et al., 2014)

$$\frac{\partial}{\partial s}(\sigma_i \frac{\partial V_i}{\partial s}) = \beta(C_m \frac{\partial V_i}{\partial t} + J_{ion}) \tag{7}$$

and in finite difference software, such as the NEURON simulation environment, the extracellular voltage distribution usually can be delivered in two ways: using a monopolar point source or a disc electrode to apply external currents.

The following equation is used for a monopolar point source (Greenberg et al., 1999):

$$V_e = \frac{\rho_e I}{4\pi r} \tag{8}$$

where ρ_e denotes the retinal extracellular resistivity, I is the stimulus current, r is the distance between the electrode and the point at which the voltage is being computed.

For the case of disc electrode, the following formula applies (Jeng et al., 2011; Tsai et al., 2012)

$$V_e(r,z) = \frac{2V_o}{\pi} \arcsin(\frac{2a}{\sqrt{((r-a)^2+z^2)} + \sqrt{((r+a)^2+z^2)}}) \tag{9}$$

where r, z are the respective radial and axial distances from the centre of the disk, and holds whenever when $z \neq 0$. V_o is the potential on the surface of the disk, and a is the radius of the disk.

In finite element software such as COMSOL, the extracellular voltage distribution can be generated by using a Neumann boundary condition (Joarder et al., 2011) as follows:

$$\mathbf{n}.(-\sigma_e \nabla V_e) = \frac{I_{stim}}{A} \tag{10}$$

where I_{stim} is the current from stimulating electrode flowing into the domain, A is the electrode surface area, **n** is the unit vector normal to the electrode boundary, and σ_e is the extracellular conductivity.

The first computational model that investigated the response of an entire retinal ganglion cell to extracellular electrical field was proposed by Greenberg et al. (1999). More than 9000 compartments were employed in this model to simulate one ganglion cell. Three membrane models (i.e. a passive model, FM model (active), and a Hodgkin-Huxley model with passive dendrites (HH)) were investigated under extracellular electrical stimulation using point source and disc electrode. Results for the HH and active models showed that RGCs require low thresholds for stimulation when activated near their soma instead of their axon. Moreover, a wedge shaped percept that could perhaps be 'seen' by the patient could be due to the stimulation of overlying axons from distant cell bodies (Greenberg et al., 1999).

Selective activation of OFF or ON RGCs has been observed *in vitro* experiments in rabbit RGCs with the application of high frequency (2 KHz) stimulus pulses (Twyford et al., 2014). A powerful modelling study was undertaken using high frequency stimulation to study the differential activation of OFF and ON RGCs (Kameneva et al., 2016). By using single and multi-compartment approaches, the results showed the impact of the membrane potassium current along with the width of the high sodium channel band (SOCB) on the difference between OFF and ON RGCs responses to high frequency (2 KHz) stimulation.

The impact of the SOCB during electrical stimulation was investigated in detail by Jeng et al. (2011), showing the factors underlying AP initiation in RGCs during electrical stimulation (Jeng et al., 2011). Another valuable model examined how RGCs react to range of frequencies (Guo et al., 2015). This study has indicated the effectiveness of using high frequencies to produce differential activation of RGCs. Simulations have also revealed that with increases in the dendrite sodium channel membrane conductance, the possibility of selective activation between OFF and ON RGCs becomes less pronounced.

The response of mice RGC populations to electrical stimulation has been investigated using an *in vitro* experiment and computational study (Tsai et al., 2012). The monopolar disc electrode used was modelled using equation 9 . Their results demonstrated that the stimulating electrode position determines the site of action potential initiation. Moreover, the AIS always exhibited the minimum threshold, whereas the dendritic region exhibited the higher threshold. Al Abed et al. (2015) presented the first mathematical study investigating the response of a morphologically-realistic OFF RGC population to electrical stimulation using multiple electrodes (Al Abed et al., 2015*b*). The authors compared between three current steering approaches: monopolar, quasi-monopolar (QMP) and hexapolar (hex). The monopolar return electrode configuration used one remote electrode as the return. In the hexapolar arrangement, the stimulating electrode was located at the centre and surrounded by six local return electrodes. The quasi-monopolar electrode configuration was proposed initially by Matteucci et al., (2013) to enhance the efficacy of retinal electrical stimulation by involving the best features of the monopolar and hexapolar approaches (Matteucci et al., 2013). This quasi-monopolar approach involves a pure hex with an additional distant return electrode. The return current is divided between the local hex guards and the distant return electrode according to a quasi-monopolar fraction (QMPF), adjusted by the user. The simulation results indicated that hexapolar stimulation is more localized with suprathreshold currents, even for single or concurrent

pulse injections. Moreover, quasi-monopolar stimulation could combine the lower threshold of monopolar with the localization of hexapolar. These results were consistent with *in vivo* experiments conducted on feline retinas (Matteucci et al., 2013) as well as with a continuum modelling study (Abramian et al., 2014). A powerful morphologically-realistic rat RGC modelling study investigated the inhibition phenomenon (Abramian et al., 2015). It was proposed that there is an upper RGC threshold, beyond which any increase in current stimulus will lead to RGC desensitization (Boinagrov et al., 2012; Weiland et al., 2016). The simulations of (Abramian et al., 2015) confirmed the phenomenon of RGC desensitization, whereby the inhibition current ranged 2-10 times the activation threshold. More interestingly, the activation of passing axons could be reduced by using concentric electrodes with sufficiently high current.

Retinal ganglion cells (RGCs) are the final output of the retinal system, and the only cells generating action potentials, with the exception of very limited types of amacrine cells. Furthermore, morphometric studies on degenerate retinas showed that RGCs exhibit the highest survival rate compared to other cells. These findings inspired most researchers to focus on that type of retinal neuron. However, there are some notable attempts to consider other cells and their effects on visual perception during electrical stimulation.

The response of ON and OFF retinal bipolar cells to extracellular electrical stimulation has been investigated via multi-compartment modelling studies (Werginz et al., 2015; Werginz and Rattay, 2016). Simulation results showed that monophasic cathodic and biphasic pulses lead to different intracellular calcium concentrations in OFF and ON bipolar cells. In OFF bipolar cells, intracellular calcium concentrations were around four-fold higher than the ON bipolar cell. In ON bipolar cells, the application of a biphasic cathodic-first waveform resulted in intracellular calcium concentrations being 2 times higher than when a biphasic anodic-first was applied. However in OFF bipolar cells, no difference in intracellular calcium concentrations was found when biphasic cathodic-first or anodic-first

pulses were applied. Based on these results, the authors proposed that selective activation of either the ON or OFF pathway could be obtained. Moreover, the morphology of the bipolar cell exerts a significant influence on its excitability, similar to what was observed in RGC models (Werginz et al., 2015). Another modelling study found that stronger subretinal stimulation with anodic pulses leads to inhibition of bipolar cells close to the stimulating electrode (Werginz and Rattay, 2016). They ascribed the reason to reversal of the calcium current, which caused a decline in intracellular calcium concentration, leading to the reduction or prevention of vesicle release, leading to the inhibition of nearby bipolar cells. However, they showed that distant bipolar cells were activated during stronger stimulation. These findings could explain the mechanism underlying inhibition of proximal RGCs with higher current amplitudes observed in *in vitro* and *in vivo* experiments (Barriga-Rivera et al., 2017).

Miller et al., (2006) modelled the behaviour of ON-OFF amacrine cells under electrical stimulation, comparing results with *in vitro* experimental data. (Miller et al., 2006). Their model was based on the FM model, adjusting ion channel densities to reflect data from ON-OFF amacrine cell experimental recordings. Their results showed that spikes could be initiated in the dendrites, but failed to propagate to the soma unless the dendritic sodium channel density was 2 or more times the somal sodium channel density.

The multi-compartment modelling approach, particularly the morphologically-realistic approach, represents the most accurate modelling approach to retinal electrical stimulation, since it is based on the reconstruction of realistic neuron morphologies and ion channel densities gained experimentally. However, their large computational cost has posed a challenge when population-based stimulations are desired.

3.4 Network Models

Retinal network computational models display a high level of complexity as they simulate the response and interaction between different retinal neurons. Various retinal cell network interactions have been simulated, leading to a number of significant findings. These models are usually implemented based on non-detailed single or multi-compartment approaches, with limited exceptions. Network models could represent the behaviour of the entire retina or retinal subsystems in response to light or electrical stimulation (Guo et al., 2014).

The effectiveness of retinal stimulation largely depends on the selectivity and exclusivity of target cells. The problem of existing retinal prostheses is the co-stimulation of axons originating from distal ganglion cells with those ganglion cells in the area below the stimulating electrodes. This could reduce the quality of visual perception by effectively smearing the focal perceived image. This issue could be resolved by the activation of ganglion cells through the stimulation of synaptic inputs from bipolar cells (Resatz and Rattay, 2003). A number of studies have been conducted to investigate the contribution of bipolar cells to the activation of retinal ganglion cells during electrical stimulation (Rattay and Resatz, 2004; Rattay et al., 2003; Resatz and Rattay, 2003, 2004). During the stimulation process, the bipolar cells release neurotransmitters that trigger the retinal ganglion cells to generate action potentials (Resatz and Rattay, 2003). The latter study used the multi-compartment model of Greenberg et al.(1999) to model an entire RGC, including the soma, axon, and dendrites. The authors implemented active ion channels in the RGC, and used a passive model for the bipolar cells. 69 compartments with four dendritic sub-branches were used to model the RGC, whilst 14 compartments were employed for the bipolar cell. The simulation results showed that bipolar cells were activated before the RGC axons, even though the stimulating electrode was further away from it (Rattay et al., 2003). These results are in good agreement with *in vitro* experiments conducted in isolated chicken

retina (Rattay and Resatz, 2004). To avoid co-stimulation of bypassing axons, long electrodes parallel to these axons were proposed. The efficacy of these proposed electrodes has been shown by computer simulations (Rattay and Resatz, 2004).

The interaction between cone and horizontal cells simulated by Smith (1995) using a multi-compartment model based on available anatomical and biophysical data (Smith, 1995). The goal of that study was to identify nature of the cone receptive field and its function. Simulations showed model was capable of reproducing some features from published intracellular recordings in cat. The model incorporated an array of cones (60 $\times$ 60) and two arrays of horizontal cells (7$\times$7 for type A, 15$\times$15 for type B). Reciprocal synapses were used to interconnect the cone array with the two arrays of horizontal cells. A small spot of light was applied to the centre of the cone array, and receptive fields were recorded from multiple sites in each array. The results indicated the centre-surround cone receptive field was generated by the cone pedicle circuit. Moreover, optical blur and electrical coupling contributed to shaping the centre receptive field, whereas electrical coupling from the two horizontal cell types influenced the shape of the surround. Furthermore, the centre receptive field prevented aliasing in cone and bipolar cells, functioning as a spatial filter for extracting signal from noise in the cone pedicle. The surround receptive field performed optimisation of signal transfer in the cone pedicle and its neighbours. This model also predicted that the receptive field of type A horizontal cells (HA) was larger than the receptive field of type B horizontal cells (HB). More recently, the interaction between cone photoreceptors and horizontal cell layers and the role of gap junction conductance on the response of horizontal cells during electrical stimulation has been explored via a computational study (Tsai et al., 2017). Their model includes 169 cells for both cones and horizontal cells arranged in a 13 x 13 grid, and gap junctions were utilised to internally connect between these two layers. Horizontal cells responded with damped oscillations and those cells beneath the centre of the electrode showed higher

evoked responses compared to those in the periphery. Moreover, with increasing gap junctional resistance between horizontal cells, the response of horizontal cells decreased.

Other studies have been carried out to examine the effect of integrating synaptic interactions to quantify visual function. An example of this is the cone pathway, which was modelled based on experimental data describing individual retinal cells and synaptic interactions (Teeters et al., 1997). The goal of that study was to investigate communication between networks of similar neurons and/or networks of various neurons to understand how retinal networks encode light stimuli. This study describes the behaviour of six types of retinal neurons, namely: cones, horizontal cells, ON and OFF bipolar cells, narrow- and wide-field amacrine cells, and ON-OFF RGCs. Temporal and spatial properties of the targeted cell were simulated by implementing a low-pass filter and spatial convolution respectively. Sixteen difference equations were used to describe the voltage response for all neuron types. One of the significant results was the ability of the model to isolate each synapse and display its influence on both temporal and spatial responses, and then compare these with the complete network responses. Despite the robustness of this model and its efficacy to simulate experimental data, some limitations were apparent, such as the broad modelling assumptions of the inner retina, and that the model does not contain voltage gated ion channels.

A valuable 3D discrete biophysical model of the retinal network with nine types of retinal cells representing both ON and OFF cone pathways was developed by Cottaris and Elfar (2005) . The spatiotemporal properties of the retinal circuitry were studied under three conditions: (1) light stimulation of normal retina, (2) epiretinal electrical stimulation of normal retina, and (3) epiretinal electrical stimulation of the degenerated retina. The modified leaky integrator model with added membrane and synaptic conductances was employed to simulate the biophysical properties of the retina. For more accurate representation, receptive and dendritic fields were used. During electrical stimulation of both the degenerated

and the normal retina, results showed that ganglion cells are mainly activated by the electrical field from the stimulating electrode, leading to indiscriminate activation of ON and OFF RGCs. After the termination of electrical stimulation, depolarised neurons start discharging. This mechanism creates an excitation wave that passes through the retinal network, resulting in inhibition of OFF RGCs while ON RGCs continue to generate APs. Moreover, at very strong stimulation in both the normal and the degenerated retina, the spatial profile of the cortical input was significantly distorted as ganglion cells start to saturate. Despite these interesting results, some limitations were apparent in this model. For example, the large computational demand of these discrete models, in which a very large number of individual units are required to be solved. Furthermore, the model employed an overly simple representation of epiretinal electrical stimulation by assuming the extracellular medium as an infinite homogeneous domain and the return electrode located in the infinity. Moreover, active membrane properties were not incorporated. Finally, the authors assumed that the electrical stimulation only affected the somas of retinal neurons (Cottaris and Elfar, 2005).

Active membrane properties were not incorporated in these aforementioned network models, with the exception of Tsai et al., (2017). Publio et al. (2009) proposed a mathematical model of ON rod pathways which included all major retinal neurons and incorporated active membrane properties (Publio et al., 2009). This model studied the contribution of electrical synaptic coupling via gap junctions and rod hyperpolarisation activated current (I_h) in the dynamic range of the retina. The modified single compartment models were based on previously published models, and were used to simulate each retinal neuron class. The results indicated that gap junctions with appropriate values of rod (I_h) conductance have a significant impact on the enhancement of vertebrate retina dynamic range. The results were consistent with previous predictions (Copelli et al., 2005; Kinouchi and Copelli, 2006) and experimental data (Deans et al., 2002; Völgyi et al., 2004).

3.5 Continuum Models

Continuum models are ideal for examining the spatial extent of activation of bulk retinal tissue, without explicit representation of individual retinal cells. The concept of a bidomain model was originally proposed by Schmitt (1969), and later the mathematical formulation was given by Tung (1978) (Schmitt, 1969; Tung, 1978). Such continuum models have been adopted for cardiac tissue (Henriquez, 1993) and more recently in neural tissues (Martinek et al., 2008). These continuum bidomain models describe the electrical activity of bulk tissue by coupling the intra- and extracellular domains (Dokos et al., 2005). Dokos et al. (2005) have proposed the first continuum model of the retina for simulating retinal electrical stimulation. This model was used to investigate bulk retinal activation during epiretinal stimulation. The response of retina was investigated by using two or four electrodes, and applying two current waveforms: monophasic & biphasic. The retina was described by two layers: a passive layer (vitreous) and an active layer (RGCs). Simulation results were consistent with experimental studies. For example, a biphasic cathodic-first stimulus was shown to be more effective than anodic-first stimulation for achieving focal activation of retinal tissue. This study suggested that the use of multiple return electrodes could eliminate undesired secondary activation beneath each return electrode (Dokos et al., 2005). Recently, a number of continuum studies have been conducted based on the Dokos et al. (2005) model (Abramian et al., 2014, 2011; Al Abed et al., 2015*a*, 2012; Joarder et al., 2011; Yin et al., 2010, 2011). Simulation of the response of bulk retina to three different electrode placements (epiretinal, subretinal, and suprachorodial) was accomplished by Joarder et al. (2011). This study included seven retinal layers: one active (RGC layer) and six passive layers. It modified formulation of the Dokos et al. (2005) by proposing a remote conductance (g_r) that resistively tied the intracellular potential to a fixed remote resting potential. This modification allowed the stimulation to be more focal beneath the stimulating

electrodes, preventing the spread of activation elsewhere. The model was validated against *in vitro* experimental data and its predictions agreed with published experimental recordings (Joarder et al., 2011). The incorporation of retinal neurons such as bipolar and amacrine cells was introduced in the continuum model of Yin et al. (2010). This study investigated the effects of retinal cell interaction during electrical stimulation. The preliminary findings demonstrated the influence of these cells on the response of ganglion cells to electrical stimulation (Yin et al., 2010). Their simulations showed the occurrence of early and late onset action potentials. The early action potential was generated from the direct stimulation of RGCs, whereas the inner retina (bipolar and amacrine) influenced the RGCs to fire a second action potential. Light stimulation of the retinal ON cone pathway was investigated through a continuum model by applying small and large spots of light (Yin et al., 2011). Computer simulations predicted that the spot size largely correlated with the presence of surround suppression, which was in good agreement with experimental findings. Furthermore, RGC axonal activation was investigated through both the continuum model and an *in vitro* experiment conducted on rabbit retina (Abramian et al., 2011). Computer simulations and experimental findings showed that RGC axons were the neural activation site, and the use of hex electrodes led to localized tissue stimulation. The feasibility of quasi-monopolar (QMP) electrical stimulation compared to hexapolar or monopolar stimulation was studied by using a more recent continuum model. The results of this model have suggested that QMP combines both low threshold of monopolar stimulation with the focal spatial activation of hexapolar configurations, consistent with experimental studies (Abramian et al., 2014). The study of Al Abed et al. (2015a) presented a novel modelling approach, which was the combination between continuum and morphologically-realistic multi-compartment models. In this study, RGCs were described using a morphologically-realistic multi-compartment model whilst bipolar and amacrine cells were represented using the bidomain continuum formulation. Simulations results were comparable with previous ex-

perimental outcomes in terms of the thresholds and latencies of time-locked and network-driven RGCs spikes in a qualitative manner, and that the action potential could be initiated in the dendrites, then propagating to the soma. An improvement to the continuum model was proposed by using a convolution-based method to determine the effective extracellular loading of the dendritic field in retinal ganglion cells (Al Abed et al., 2012). This method will be useful in examining the influence of dendritic tree size on RGC activation.

3.6 Models of Current Steering in Retinal Prostheses

Despite the very promising results indicating that retinal prostheses can assist blind people to perform some limited tasks such as rudimentary letter and word recognition, more advanced levels of visual perception require higher spatial resolution. Hence, enhancement of the spatial resolution of a visual prosthesis is desired, particularly if the micro-electrode array (MEA) is positioned far from the targeted neurons such as in the case of a suprachoroidal placement. One of the proposed strategies is to increase the number of electrodes, leading to an increase in the number of perceived pixels (Dumm et al., 2014). However, this strategy faces considerable engineering and manufacturing challenges. For example, retinal prostheses currently possess up to 1500 electrodes, converging to around 20-50 million retinal ganglion cells in the degenerated human retina (Brooks et al., 1999; Santos et al., 1997). So, if we consider the high amount of surviving RGCs, the ratio of ganglion cells to electrodes is more than 30 thousand to one, indicating a very crude approximation of vision sense. Also, the increased number of MEA electrodes rises the impact of electric crosstalk between concurrently activated electrodes during stimulation, minimising resolution of the perceived image (Moghaddam et al., 2011).

Current steering approaches have been employed successfully in auditory

prosthetics to reduce electrode crosstalk and improve spatial resolution (Bonham and Litvak, 2008). Hence this technique might be useful in retinal implants, however studies that have investigated this are limited. The computational study of Moghaddam et al. (2011) has explored the efficacy of a new 3D MEA design to alleviate the impact of electric crosstalk compared with a planar micro-electrode array. This study investigated three factors: electrode diameter, height of chamber cavity, and distance between MEA and RGCs, to obtain focal stimulation. Instead of directly simulating activation of RGCs, this study used a purely passive approach based on the electric field magnitude $|E|$. To calculate the threshold electric field $|E|_{th}$ to activate RGCs, they converted the strength-duration curve from the experimental data of Sekirnjak et al. (2008) into an $|E|_{th}$-duration curve, finding that the threshold electric field value, $|E|_{th}$, equals 1116 (V/m). Activation of RGCs was determined by comparing $|E|$ with $|E|_{th}$. Their simulations indicated that the effect of electrode cavity chamber height was more significant with larger electrodes. Moreover, the proposed new 3D MEA design exhibited no significant efficacy over a planar MEA when the distance between the MEA and retina is below 100 μm. The mathematical study of Wilke et al.(2011) extensively examined the impact of electric crosstalk on the spatial resolution of retinal prostheses (Wilke et al., 2011). A 3D simplified finite element model was employed to investigate different factors that influence the spatial resolution. This study found the distance between electrodes and targeted cells had a significant effect. Also, the monopolar configuration exhibited the highest spatial resolution when the implantation site was close to the targeted cells. In contrast, the hex configuration provided the highest spatial resolution if it was positioned further away such as in the case of a suprachoroidal implant. Interestingly, electric crosstalk was found to decrease with an increase in the electrode spacing. Moreover, multiplexing of electrodes was proposed to improve the spatial resolution.

Several studies have shown that the monopolar configuration can activate RGCs using lower current, while the hexapolar configuration provides greater fo-

cal activation (Matteucci et al., 2013; Moghadam et al., 2013). The Cicione et al. (2012) study examined five return electrode configurations: remote monopolar, vitreous monopolar, hexapolar, common ground (in which the active electrode is surrounded by many return electrodes) and bipolar (Cicione et al., 2012). The cortical recordings indicated that both monopolar types had the lowest threshold, whereas hexapolar and common ground were the best selective modes. Moreover, by increasing the distance between the active and return electrodes (at least 3 mm) in the bipolar mode, its threshold was similar to the monopolar configuration. More recently, a novel return electrode configuration termed quasi-monopolar (QMP) was proposed by Matteucci et al. (2013) and its efficacy was compared to either monopolar or hexapolar. The Matteucci et al. (2013) *in vivo* study conducted on cats demonstrated that by using the quasi-monopolar configuration, the threshold was reduced by 60% in comparison with hexapolar alone while still producing acceptable focal stimulation. However, the computational study of Moghadam et al. (2013) evaluated the performance of this new configuration in comparison with other available configurations. With the optimal electrode size (10 to 15 μm) suggested by Sekirnjak et al.(2006), QMP was found to have lower activation thresholds regardless of the implantation site. More interestingly, simulation results showed that QMP was beneficial when the distance between the MEA and targeted cells was greater than the electrode dimensions (Moghadam et al., 2013). The continuum modelling study of Abramian et al. (2014) explored the three modes: monopolar, hexapolar and quasi-monopolar using different electrodes sizes and spacing and under single or parallel stimulation (Abramian et al., 2014). Their simulations showed that there was a minimal effect of electrode size on subretinal stimulation thresholds, in contrast to electrode spacing which has a significant influence. More interestingly, the quasi-monopolar configuration combines the low threshold of monopolar and the localisation of hexapolar during parallel stimulation.

The concept of virtual electrodes (VE) has been suggested to increase the

resolution of retinal prosthesis. This technique aims to achieve intermediate activation between active electrodes without adding more physical electrodes. Virtual electrodes and current focusing strategies were examined by Moghaddam et al. (2014) using a mathematical model involving various return electrode configurations. This study used the quasi-monopolar fraction (α) to control the return current, where this fraction ranged from 0 (pure hex) to 1(pure monopolar). In contrast, the creation of virtual electrodes between two active adjacent electrodes could be achieved by using a steering coefficient (β). Simulation results indicated that thresholds are independent of the return electrode configuration when the distance between the MEA and the target layer was smaller than the electrode diameter, consistent with clinical studies in cochlear implants (Mens and Berenstein, 2005; Morris and Pfingst, 2000). Furthermore, simulations indicated that in the case of suprachoroidal quasi-monopolar configuration, it was superior to other paradigms in terms of lowering threshold and spatial selectivity. Moreover, virtual electrodes with quasi-monopolar stimulation were more effective in creating localised activation patterns with lower threshold. Existing retinal implants deliver current pulses via MEA simultaneously with the same current amplitudes. By delivering current pulses simultaneously but with different ratios, the recordings from the visual cortex in *in vivo* experiments conducted on four cats using pairs of electrodes indicated the possibility of creating virtual electrodes, associated with various cortical activation maps, by employing current steering (Dumm et al., 2014). This finding has been extended using two-dimensional current steering to create virtual electrodes using up to six electrodes (Spencer et al., 2018). The results from the cat visual cortex demonstrated the capability of three or six physical electrodes to create virtual electrodes. This result indicates it is possible to increase the number of percepts without increasing the number of electrodes, and more importantly, we can compensate for any faulty electrode by steering the neighbouring electrodes. Furthermore, Cassar et al. (2014) successfully produced virtual electrodes by exploiting the sum of short time offset pulses in two

adjacent electrodes (Cassar et al., 2014).

3.7 Summary

Computational models of retinal stimulation and activation have significantly contributed to the development of retinal implants. These models have investigated a wide range of issues related to the enhancement of efficacy of visual prostheses. Mathematical models have been helpful to find optimal approaches to increase the effectiveness of visual implants. However, existing continuum neural models of retinal electrical stimulation are associated with some limitations. Firstly, these models only simulate the soma or the high sodium channel density segment of the RGC (single compartment) and ignore the influence of other compartments such as the axon and dendrites, whose effects are well-observed experimentally. Also, these models are constructed by connecting to a remote segment of the neuron, for example the axon, by adopting a remote conductance (gr) and determining its value by comparing with experimental data and assuming this remote segment would not be affected by the extracellular potential. Thirdly, these models used only one kind of RGC (undefined) and ignored the other subtypes. However, several experimental studies have confirmed that each RGC subtype has unique responses when exposed to electrical or light stimulation (Margolis and Detwiler, 2007; Mitra and Miller, 2007). Also, these models used FM ionic currents, and did not incorporate any newer discovered ionic currents (Margolis and Detwiler, 2007) that have significant influence on RGC activity. Existing current steering computational models also convey some weaknesses. Most of these are very simplified models, with the exception of the Abramian et al. (2014) continuum modelling study, which used passive homogeneous conductivities for the retinal layers. Also, detailed anatomical and intrinsic electrophysiological properties of the retina were not incorporated. Furthermore, the estimation of E-field threshold ($|E|th$) is a new theoretical approach, which has not been tested experimentally, compared to the conventional way of quan-

tifying the activation threshold by examining transmembrane potential responses of cells. Studies that investigated new selective ways of activating RGCs by exploiting their intrinsic electrophysiological features are beneficial, but very limited. Hence, increasing the efforts of computational modelling to breach this field would certainly improve the efficacy of retinal prostheses.

In the following chapters (chapters 4 & 6), we will construct and validate a new continuum model which avoids the main limitations of existing continuum models. First, the model will include all main RGC compartments (dendrites, soma, AIS and axon), not just one compartment. Second, the model will use an ionic RGC formulation that incorporates newly-discovered ion currents that have a significant contribution in reproducing specific experimental findings, as will be explained. Third, the continuum model will incorporate the most prominent types of RGCs: ON and OFF types, which differs from previous continuum models that only use one type. Moreover, the model will be validated robustly by comparing with discrete and experimental studies.

4 Methods

4.1 Modification of the Cable Equation

4.1.1 Classical Cable Equation

The classical form of the cable equation commonly used in neuroscience modelling assumes that the diameter of the biological fibre is uniform. The biological fibre could be a muscle cell connected to other cells (e.g. cardiomyocytes, purkinje fibres in the heart) or different compartments of neural cells such as the dendrites or axon. In this thesis, the later is the focus of research, but this modification of the cable equation should be applicable to any biological fibre when modelling electrical propagation.

The classical form of the cable equation discretises the biological fibre into cylindrical compartments of length (Δx). The electrical equivalent circuit of three adjacent nodes is shown in Fig. 4.1. The intracellular resistance $R_j = \rho_i \Delta x / \pi r^2$ follows Pouillet's law. The total membrane capacitance (c_m) of a cylindrical fibre compartment of length (Δx) is given by multiplying the specific membrane capacitance (C_m) by the surface area of each compartment. Similarly, the total membrane ionic current of each segment (i_{ion}) is derived from the cell membrane current density (J_{ion}).

By applying Kirchhoff's current law to node j (see Fig. 4.1), the classical discrete form of the cable equation can be written as

$$\frac{V_{j+1} - V_j}{R_j} - \frac{V_j - V_{j-1}}{R_{j-1}} = c_m \frac{dV_j}{dt} + i_{ion} \tag{11}$$

$$\begin{aligned} \frac{V_{j+1} - V_j}{\rho_i \Delta x / \pi r_j^2} - \frac{V_j - V_{j-1}}{\rho_i \Delta x / \pi r_{j-1}^2} \\ = 2\pi \Delta x r_j (C_m \frac{dV_j}{dt} + J_{ion}) \end{aligned} \tag{12}$$

with the assumption $r_j = r_{j-1}$. This equation is traditionally converted to the following continuum equivalent for use in FEM simulations

$$\frac{1}{\rho_i}\frac{\partial^2 V}{\partial x^2} = \frac{2}{r}(C_m\frac{dV}{dt} + J_{ion}) \tag{13}$$

and more generally for branching and/or nonlinear structures in 3D space

$$\nabla.(\frac{1}{\rho_i}\nabla V) = \frac{2}{r}(C_m\frac{dV}{dt} + J_{ion}) \tag{14}$$

where C_m, ρ_i, and r are assumed to be constant along the fibre.

However, biological fibre could be non-uniform in its radius. Therefore, this equation will not be valid if implemented in FEM due to the assumption of fibre uniformity.

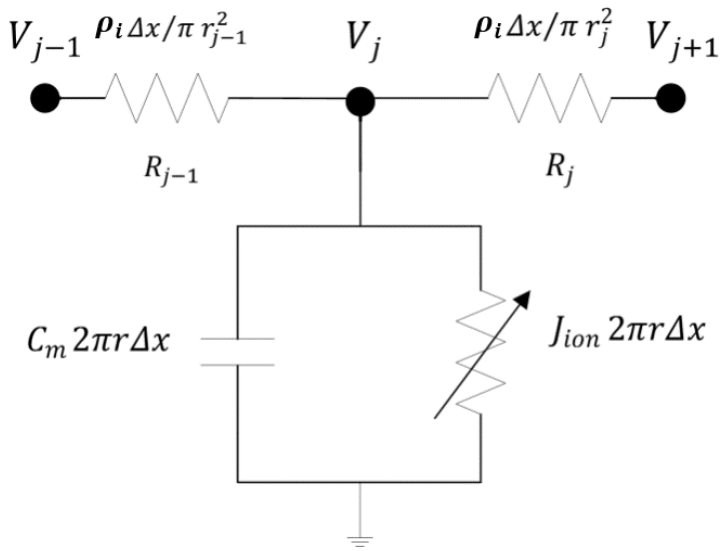

Figure 4.1: Electrical equivalent circuit representation of three adjacent intracellular nodes V_{j-1}, V_j, and V_{j+1} in the discretized biological fibre cable model. The inter-nodal separation is given by Δx, r denotes the fibre radius, and ρ_i is the axoplasmic resistivity. Membrane capacitance C_m and ionic current J_{ion} are given per unit membrane area. For simplicity, the extracellular potential is assumed to be at ground.

4.1.2 Modified Cable Derivation

A modified form of the cable equation suitable for use in continuum models and FEM simulations is derived here to deal with the realistic geometries of excitable

fibres where their radius typically varies along the fibre. The fibre is discretised into small segments of length (Δx). The electrical equivalent circuit for one node is shown in Fig. 4.1.

As before, we apply Kirchhoff's current law to node j, hence the current entering the node is equal to the current leaving it:

$$\frac{V_{j+1}-V_j}{\rho_i \Delta x/\pi r_j^2} - \frac{V_j - V_{j-1}}{\rho_i \Delta x/\pi r_{j-1}^2} = 2\pi \Delta x r_j (C_m \frac{dV_j}{dt} + J_{ion}) \tag{15}$$

$$\frac{\pi}{\rho_i}(r_j^2 \frac{V_{j+1}-V_j}{\Delta x} - r_{j-1}^2 \frac{V_j - V_{j-1}}{\Delta x}) = 2\pi \Delta x r_j (C_m \frac{dV_j}{dt} + J_{ion}) \tag{16}$$

$$\frac{1}{\Delta x}(\frac{r_j^2}{2\rho_i}\frac{V_{j+1}-V_j}{\Delta x} - \frac{r_{j-1}^2}{2\rho_i}\frac{V_j - V_{j-1}}{\Delta x}) = r_j (C_m \frac{dV_j}{dt} + J_{ion}) \tag{17}$$

Taking the limit $(\Delta x \rightarrow 0)$, these finite difference expressions can be approximated to the following partial differential equation:

$$\frac{\partial}{\partial x}[\frac{r^2}{2\rho_i}\frac{\partial V}{\partial x}] = r(C_m \frac{dV}{dt} + J_{ion}) \tag{18}$$

which can be generalised to

$$\nabla.(\frac{r^2}{2\rho_i}\nabla V) = r(C_m \frac{dV}{dt} + J_{ion}) \tag{19}$$

Equation 14 is the classical cable equation which deals with the fixed-radius excitable fibres. In contrast, Equation 19 is the modified cable equation which deals with the varying-radius excitable fibres and is identical to the form of the cable equation with radial taper given by, for example, Eqns (3) and (4) of (Abbott, 1994) (p. 60). Furthermore, to the best of our knowledge, there are no published studies that have pointed to the importance of adopting this modified cable equation, taking into account the variation in nerve radius. Within the retinal modelling context, most computational studies have used the classical cable equation that deals with constant radius.

In chapter 5, we will show the importance of adopting the modified cable equation in modelling neuronal electrical stimulation implemented in FEM. We compared the models' predictions using 1) a finite-difference discrete solver (NEURON), 2) a FEM solver (COMSOL) using the classical continuum formulation (Eq. 14), and 3) a FEM solver using the modified continuum formulation (Eq. 19). We will employ a neuronal ionic model as an example and consider a number of common structural representations (simplified geometry, accurate morphology reconstruction), as well as a range of simulation scenarios (responses to intracellular current injection and extracellular stimulation).

4.2 Development of a Continuum Model of Multi-Compartmental Retinal Ganglion Cells

The scope of this thesis is to develop a novel continuum model of retinal electrical stimulation capable of overcoming many of the limitations associated with existing continuum models (chapters 4 & 6). The main limitations of existing continuum models can be summarised in the following three issues. First, these models only simulate the soma or the high sodium channel density segment of the RGC (single compartment) and ignore the influence of other compartments such as the axon and dendrites, whose effects are well observed experimentally.

Second, these models are constructed by connecting to a remote segment of the neuron, for example the axon, by adopting a remote conductance (gr) and determining its value by comparing with experimental data and assuming this remote segment would not be affected by the extracellular potential. Third, these models used FM ionic currents, and did not incorporate any newer discovered ionic currents that have a significant influence on RGC activity. More details of these limitations will be discussed in section 6.4.4. We construct our new continuum model of retinal electrical stimulation avoiding these main limitations and exploiting the recent findings of experimental work. Moreover, we will first validate the continuum multicompartmental RGC model against a recent discrete computational model and published experimental studies. We will then use this model as a predictive tool to investigate the behaviour of the degenerate retina during electrical stimulation, and to examine the different stimulus strategy approaches that could be beneficial for visual prostheses.

4.2.1 Discrete RGC Model

4.2.1.1 Modelling of RGC Intracellular Current Injection

The Guo et al. (2016) cell-specific computational modelling approach was chosen to be the basis of the RGC ionic formulation model. This model describes the two most dominant RGC types: ON and OFF RGCs. In that model, morphologically-realistic ON and OFF RGCs were implemented in NEURON software and their ion channel densities identified by comparing with *in vitro* experiments. The realistic morphologies of ON and OFF RGCs that were employed in the Guo et al. (2016) study, were imported into the COMSOL Multiphysics 5.3 software (COMSOL AB, Sweden) and the Guo et al. (2016) ionic formulation model was applied with some modifications. These modifications included:

1. The adoption of gating variable dynamics for the low threshold voltage activated calcium current (I_{CaT}), initially proposed by Wang et al. (1991) and

adopted later by others (Kameneva et al., 2011; Maturana et al., 2014).

2. The exclusion of (I_{CaT}) from the intracellular calcium ion concentration $[Ca^2+]i$ Eq. 28, consistent with most RGC electrical stimulation modelling studies (Fohlmeister and Miller, 1997*a*; Kameneva et al., 2011; Maturana et al., 2014).

3. The use of the Ca-activated potassium channel conductance formula 29, with the power exponent equal to 1 (Fohlmeister and Miller, 1997*b*).

This model will be the ionic model for all models presented in this thesis. In cellular morphological models, the membrane potential is both space and time-dependent, with the neuron approximated by multiple discrete cables. Each neural region is associated with its own ionic properties and is connected to neighbouring compartments by axial resistances.

In each particular cellular region, the membrane potential can be described by the modified cable equation, which considers the variation among the radius of RGC compartments, as follows:

$$\frac{\partial}{\partial x}[\frac{r^2}{2\rho_i}\frac{\partial V_m}{\partial x}] = r(C_m\frac{dV_m}{dt} + i_{ion} - i_{stim}) \tag{20}$$

where V_m represents membrane potential, x is the axial cable distance, r the RGC compartment radius (μm), ρ_i the intracellular resistivity ($\Omega \cdot cm$), and C_m the membrane capacitance per unit membrane area ($\mu F \cdot cm^{-2}$). i_{ion} is the total membrane ionic current of each RGC compartment per unit membrane area. i_{stim} is the current injected ($A \cdot cm^{-2}$).The intracellular axial resistivity (ρ_i) was set to 110 ($\Omega \cdot cm$). The simulation temperature was 37 °C.

The ionic currents in the model are composed of seven voltage and time-dependent currents in addition to one leakage current.

$$i_{ion} = I_{Na} + I_K + I_{KA} + I_{Ca} + I_{KCa} + I_h + I_{CaT} + I_L \tag{21}$$

The voltage and time-dependent currents are the voltage-gated sodium current (I_{Na}), the delayed-rectifying potassium current (I_K), the A-type potassium current (I_{KA}), the calcium current (I_{Ca}) , the calcium gated potassium current (I_{KCa}), the hyperpolarisation-activated mixed-cation current (I_h), the low threshold voltage activated calcium current (I_{CaT}), and the leakage current (I_L). All membrane ionic currents are given in terms of membrane current densities.

All ionic current formulations are given as follows:

$$
\begin{aligned}
I_{Na} &= g_{Na}\, m^3\, h\, (V_m - V_{Na}) \\
I_K &= g_K\, n^4\, (V_m - V_K) \\
I_{KA} &= g_{KA}\, A^3\, h_A\, (V_m - V_K) \\
I_{KCa} &= g_{KCa}\, (V_m - V_K) \\
I_{Ca} &= g_{Ca}\, c^3\, (V_m - V_{Ca}) \\
I_h &= g_h\, y\, (V_m - V_h) \\
I_{CaT} &= g_{CaT}\, m_T^3\, h_T\, (V_m - V_{Ca}) \\
I_L &= g_L\, (V_m - V_L)
\end{aligned}
\tag{22}
$$

The gating variables, except those for I_{CaT}, satisfy first order ordinary differential equations (ODEs):

$$
\begin{aligned}
\frac{dx}{dt} &= \alpha_x(1-x) - \beta_x\, x \\
x &\equiv n, m, h, A, h_A, c, y
\end{aligned}
\tag{23}
$$

For I_{CaT}, second order dynamics were used (Kameneva et al., 2011; Wang et al., 1991) :

$$\frac{d}{d_t}[mT] = \alpha_{mT}(1 - mT) - \beta_{mT}\ mT \tag{24}$$

$$\frac{d}{d_t}[hT] = \alpha_{hT}(1 - hT - dT) - \beta_{hT}\ hT \tag{25}$$

$$\frac{d}{d_t}[dT] = \beta_{dT}(1 - hT - dT) - \alpha_{dT}\ dT \tag{26}$$

The Nernst equation was used to compute the equilibrium potential V_{Ca}, dependent on the intracellular $[Ca^{2+}]_i$ and extracellular $[Ca^{2+}]_e$ calcium concentrations according to (Fohlmeister and Miller, 1997*a*; Kameneva et al., 2011).

$$V_{Ca} = \frac{R\ T}{2\ F}\ ln\ (\frac{[Ca^{2+}]_e}{[Ca^{2+}]_i}) \tag{27}$$

Values for the universal gas constant R, temperature T, Faraday's constant F and the extracellular calcium concentration $[Ca^{2+}]_e$ are given in the model parameters Table 4.5 whereas intracellular calcium concentration $[Ca]_i$ is determined by the following equation (Fohlmeister and Miller, 1997*a*; Kameneva et al., 2011).

$$\frac{d[Ca^{2+}]_i}{dt} = -\frac{3\ I_{Ca}}{2\ F\ r} - (\frac{[Ca^{2+}]_i - 0.0001}{\tau}) \tag{28}$$

where (I_{Ca}) is the calcium current, F is Faraday's constant, r is the depth of the shell beneath the membrane for the calcium pump, and 0.0001 is the maximum capacity of the intracellular calcium store in mM. τ is the calcium removal time constant.

The g_{KCa} membrane conductance for I_{KCa} is ligand gated, and is given by the

following equation

$$g_{KCa} = \overline{g}_{KCa}[(\frac{[Ca^{2+}]_i}{(Ca^{2+})_{diss}})/(1 + \frac{[Ca^{2+}]_i}{(Ca^{2+})_{diss}})] \tag{29}$$

where $(Ca^{2+})_{diss}$ is the Ca^{2+} dissociation constant.

Detailed descriptions of all model formulations, rate constants, conductances, and parameter values were obtained from (Guo et al., 2016) and can be found in tables 4.1 to 4.6. Note that the ON RGC rate constants are different to those of the OFF RGC, and are presented in table 4.2.

Table 4.1: ON & OFF RGC Model Rate Constants.

Membrane Current	***Rate Constant (s^{-1})***
I_{Na}	$\alpha_m = -0.6(V_m + 30)/(e^{-0.1(V_m+30)} - 1)$ $\beta_m = 20e^{-(V_m+55)/18}$ $\alpha_h = 0.4e^{-(V_m+50)/20}$ $\beta_h = 6/(1 + e^{-0.1(V_m+20)})$
I_K	$\alpha_n = -0.02(V_m + 40)/(e^{-0.1(V_m+40)} - 1)$ $\beta_n = 0.4e^{-(V_m+50)/80}$
I_{KA}	$\alpha_A = -0.003(V_m + 90)/(e^{-0.1(V_m+90)} - 1)$ $\beta_A = 0.1e^{-(V_m+30)/10}$ $\alpha_{hA} = 0.04e^{-(V_m+70)/20}$ $\beta_{hA} = 0.6/(1 + e^{-0.1(V_m+40)})$
I_{Ca}	$\alpha_c = -0.15(V_m + 13)/(e^{-0.1(V_m+13)} - 1)$ $\beta_c = 10e^{-(V_m+38)/18}$
I_h	$y_\infty = \frac{1}{1+e^{((V_m+75)/5.5)}}$ $\tau_h = 588.2e^{0.01(V_m+10)}/(1 + e^{0.2(V_m+10)})$
I_{CaT}	$\alpha_{mT} = 1/(1.7 + e^{-(V_m+28.8)/13.5})$ $\beta_{mT} = (1 + e^{-(V_m+63)/7.8})/(1.7 + e^{-(V_m+28.8)/13.5})$ $\alpha_{hT} = e^{-(V_m+160.3)/17.8}$ $\beta_{hT} = \alpha_{hT}(\sqrt{0.25 + e^{-(V_m+83.5)/6.3}} - 0.5)$ $\alpha_{dT} = (1 + e^{-(V_m+37.4)/30})/(240(0.5 + \sqrt{0.25 + e^{-(V_m+83.5)/6.3}})$ $\beta_{dT} = \alpha_{dT}\sqrt{0.25 + e^{-(V_m+83.5)/6.3}}$

Table 4.2: ON RGC Model Rate Constants.

Membrane Current	***Rate Constant (s^{-1})***
I_{Na}	$\alpha_m = -0.3041(V_m + 30)/(e^{-0.1(V_m+30)} - 1)$
I_{KA}	$\alpha_{hA} = 0.002e^{-(V_m+70)/20}$ $\beta_{hA} = 0.03/(1 + e^{-0.1(V_m+40)})$
I_h	$\tau_h = 4649e^{0.01(V_m+20)}/(1 + e^{0.2(V_m+20)})$

Table 4.3: Ionic Channel Distributions for the OFF RGC Model

Regional Maximum Membrane Conductance ($mS.cm^{-2}$)					
Membrane Current	***Soma***	***Axon***	***AIS***	***Hillock***	***Dendrites***
I_{Na}	68.4	68.4	249	68.4	21.68
I_K	45.9	45.9	68.85	45.9	42.83
I_{KA}	18.9	—	18.9	18.9	13.86
I_{Ca}	1.6	—	1.6	1.6	2.133
I_{KCa}	0.0474	0.0474	0.0474	0.0474	7.3e-4
I_h	0.1429	0.1429	0.1429	0.1429	0.286
I_{CaT}	0.1983	0.1983	0.1983	0.1983	0.992
I_L	0.0479	0.0479	0.0479	0.0479	0.0513

Table 4.4: Ionic Channel Distributions for the ON RGC Model

Regional Maximum Membrane Conductance ($mS.cm^{-2}$)					
Membrane Current	***Soma***	***Axon***	***AIS***	***Hillock***	***Dendrites***
I_{Na}	147.3	147.3	1072	147.3	105.526
I_K	16.2	16.2	40.5	16.2	7.559
I_{KA}	37.8	—	94.5	37.8	27.7187
I_{Ca}	2.1	—	2.1	2.1	2.7999
I_{KCa}	0.04	0.04	0.04	0.04	6.1e-4
I_h	0.4287	0.4287	0.4287	0.4287	0.5573
I_{CaT}	0.008	0.008	0.008	0.008	0.008
I_L	0.0206	0.0206	0.0206	0.0206	0.0305

Table 4.5: ***Model Parameters***

Symbol	Description	Value	Units
C_m	Specific Membrane capacitance	1	$\mu F.cm^{-2}$
$OFF_{(V_{Na})}$	OFF RGC sodium reversal potential	35	mV
$OFF_{(V_K)}$	OFF RGC potassium reversal potential	-68	mV
$OFF_{(V_h)}$	OFF RGC h reversal potential	-26.8	mV
$OFF_{(V_L)}$	OFF RGC leakage reversal potential	-70.5	mV
$ON_{(V_{Na})}$	ON RGC sodium reversal potential	35	mV
$ON_{(V_K)}$	ON RGC potassium reversal potential	-72	mV
$ON_{(V_h)}$	ON RGC h reversal potential	-45.8	mV
$ON_{(V_L)}$	ON RGC leakage reversal potential	-66.5	mV
$[Ca^{2+}]_{res}$	Residual Ca^{2+} concentration	0.1	$\mu mol.L^{-1}$
Ca_{diss}	Ca^{2+} dissociation constant	10^{-6}	$mol.L^{-1}$
$[Ca^{2+}]_e$	Extracellular Ca^{2+} concentration	1.8	$mmol.L^{-1}$
τ_{Ca}	Ca^{2+} removal time constant	13.75	ms
F	Faraday's constant	96.48	$C.mmol^{-1}$
R	Universal gas constant	8.31	$J.mol^{-1}.K^{-1}$
T	Absolute temperature	310	K
r	The depth of the shell beneath the membrane for the calcium pump	10^{-7}	m

Table 4.6: ***Initial Values.*** *V_{m1}, V_{m2},V_{m3} and V_{m4} are the OFF RGC resting membrane potentials for the dendrites, soma, AIS, and axon compartments, respectively. V_{m5}, V_{m6},V_{m7} and V_{m8} are the ON RGC resting membrane potentials for the dendrites, soma, AIS, and axon compartments, respectively. The remaining initial values were identical for all compartments and for both cell types.*

Variable	***Initial Value***
V_{m1} - V_{m4} (OFF RGC)	-58.66 mV
V_{m5} - V_{m8} (ON RGC)	-57 mV
m	0.0405
n	0.13262
c	0.00228
a	0.0528
h	0.8343
h_A	0.2208
y	0.04905
m_T	0.38824
h_T	0.01795
d_T	0.862

4.2.1.2 Modelling Discrete RGC Activation by Extracellular Stimulation

Poisson's equation was used to govern the extracellular voltage distribution (V_e):

$$\nabla.(-\sigma\nabla V_e) = I \tag{30}$$

where σ is the isotropic electric conductivity of the retinal layers and I is the volumetric current density source $(A \cdot m^{-3})$, defined only on the 1D RGC domain, due to cell membrane current flow into the extracellular space. RGC activation was determined using our modified cable equation 18 .

4.2.2 Multi-Domain Continuum Model of RGC Activation

In the continuum models, the RGC layer was modelled as an active layer, whereas other layers were assumed to be passive volume conductors. Current flow through the retinal layers was modelled using Poisson's equation to govern the extracellular voltage distribution (V_e):

$$\nabla.(-\sigma\nabla V_e) = \begin{cases} 0 & \text{Passive layers} \\ \beta I_m & \text{RGC layer} \end{cases} \tag{31}$$

where (V_e) denotes the isotropic extracellular voltage and σ $(S \cdot m^{-1})$ denotes the electrical conductivity of each layer. β (m^{-1}) is the total surface area of the RGC membrane per unit tissue volume and I_m $(A \cdot m^{-2})$ is the total RGC membrane current.

For OFF RGCs, we estimated β to be 92500 (m^{-1}), 862000 (m^{-1}), 13400 (m^{-1}), and 483000 (m^{-1}) for the soma, dendrites, AIS, and axon compartments respectively, based on a 2000 $(cell/mm^2)$ cell packing density (Oyster et al., 1981), and assuming cylindrical compartments with diameters of 18 μm, 0.67 μm , and 0.94 μm for the soma, dendrites, AIS and axon compartments respectively.

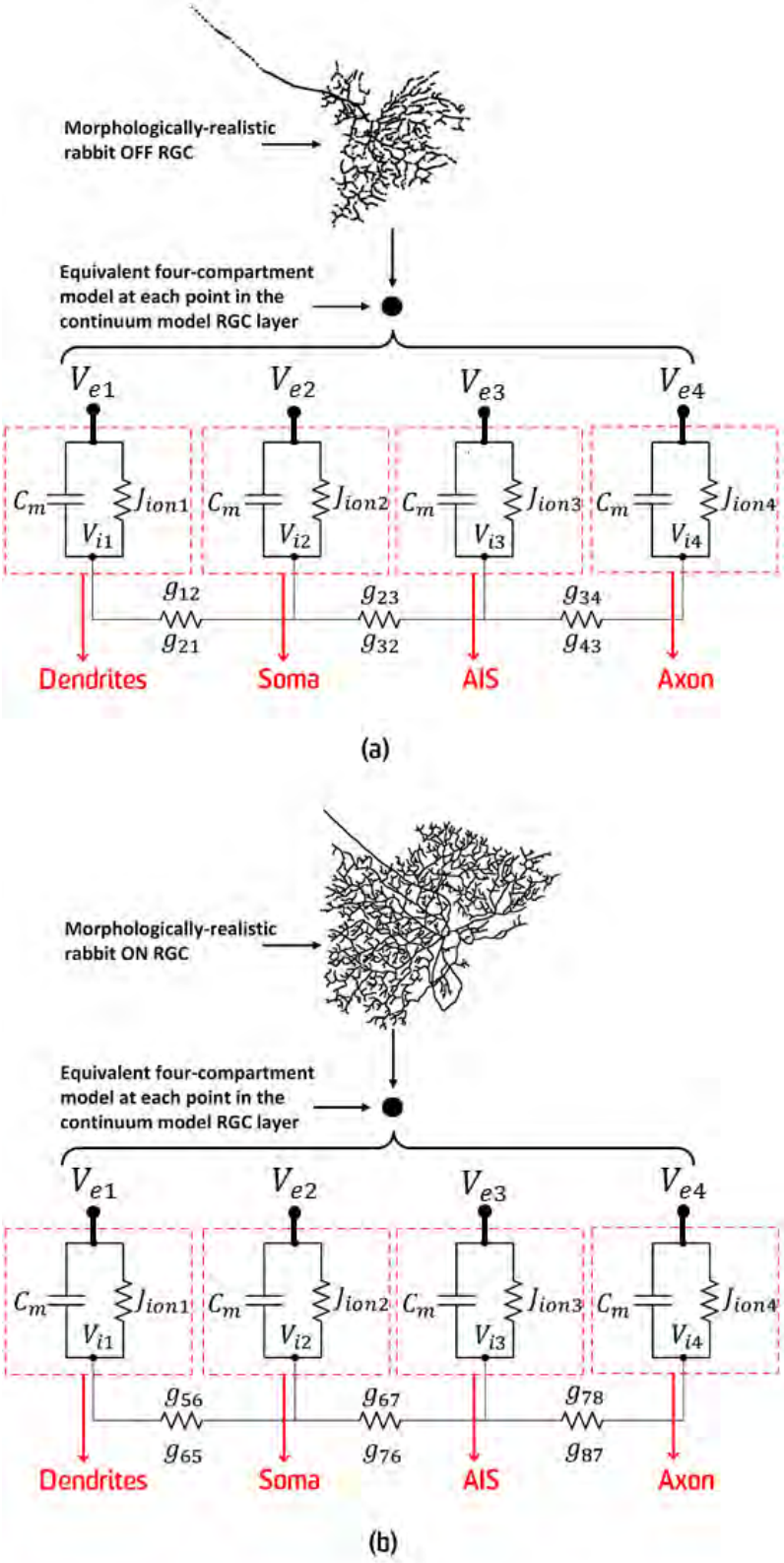

Figure 4.2: Schematic diagram of four-compartment representation of OFF (a) and ON RGC (b) circuitry of each point in the RGC layer of the continuum model after reducing the full morphologically-realistic RGC into a four-compartment point model. V_e *and* V_i *denote the extracellular and intracellular potentials respectively,* C_m *is the membrane capacitance per unit area and* J_{ion} *is the ionic current per unit area.* g *represents the internal conductances between the four compartments.*

For ON RGCs, we estimated β to be 113000 (m^{-1}), 2870000 (m^{-1}), 9930 (m^{-1}), and 617000 (m^{-1}) for the soma, dendrites, AIS, and axon compartments respectively, based on the same diameters and cell density.

In our modified multi-domain continuum formulation, each RGC was composed of four compartments, namely: soma, axon initial segment (AIS), axon, and dendrites, and each compartment is mathematically linked to neighbouring compartment(s) through internal conductances as illustrated in Fig. 4.2. Representation of a discretised biological fibre cable model by pure resistances connecting compartments in series is widely accepted in the literature as seen, for example, in (Rattay et al., 2017, 2018) and (Freeman et al., 2011).

Therefore for each compartment, the total membrane current I_m was determined by

$$\begin{aligned} I_{m(dend)} &= (C_m \frac{\partial V_{m1}}{\partial t} + J_{ion1}) = g_{12}(V_{m2} - V_m) \\ I_{m(soma)} &= (C_m \frac{\partial V_{m2}}{\partial t} + J_{ion2}) = g_{21}(V_m - V_{m2}) \\ &\quad + g_{23}(V_{m3} - V_{m2}) \\ I_{m(AIS)} &= (C_m \frac{\partial V_{m3}}{\partial t} + J_{ion3}) = g_{32}(V_{m2} - V_{m3}) \\ &\quad + g_{34}(V_{m4} - V_{m3}) \\ I_{m(axon)} &= (C_m \frac{\partial V_{m4}}{\partial t} + J_{ion4}) = g_{43}(V_{m3} - V_{m4}) \end{aligned} \tag{32}$$

where V_{m1} and J_{ion1} are the membrane potential and membrane ionic current of the dendrites, respectively. V_{m2} and J_{ion2} are the membrane potential and membrane ionic current of the soma. V_{m3} and J_{ion3} are the membrane potential and membrane ionic current of the axon initial segment and V_{m4} and J_{ion4} are the membrane potential and membrane ionic current of the axon. g is the internal conductance electrically linking two adjacent compartments (Fig. 4.2). The values of these conductances will be presented in the model development chapter.

Each point (X,Y, Z) within the RGC layer represents a retinal ganglion cell composed of four compartments (dendrites, soma, AIS, and axon), as described

above. During electrical stimulation, the effective extracellular potential for these compartments should not be the same, particularly for the axonal and dendritic compartments, but was determined from the corresponding 3D volume conductor potential V_e, which in turn depended on the extracellular conductivity. For the soma and AIS, the V_e value at (X,Y, Z) was used. In the case of the dendrites however, a circular dendritic field was accounted for by averaging V_e at four distal points to calculate the effective dendritic $V_{e(dend)}$.

$$\begin{aligned} V_{e1} &= V_e(X - x_1) \\ V_{e2} &= V_e(X + x_2) \\ V_{e3} &= V_e(Y - y_1) \\ V_{e4} &= V_e(Y + y_2) \\ V_{e(dend)} &= (V_{e1} + V_{e2} + V_{e3} + V_{e4})/4 \end{aligned} \tag{33}$$

where x_1, x_2, y_1 and y_2 are each set to 100 μm for the OFF RGC continuum model. In the case of the ON RGC model, 150 μm was used all these values.

The value of the extracellular potential at the axon was computed from a remote point according to

$$\begin{aligned} V_{e(axon)} &= V_e(X - x) \\ V_{e(axon)} &= V_e(Y - y) \end{aligned} \tag{34}$$

Where x and y are set to 610 μm when the axon was oriented along the x- or y-axis directions for the OFF RGC continuum model respectively. In the case of the ON RGC model, a value of 600 μm was utilised for both x and y.

4.3 Electrical stimulation and boundary conditions

For both the discrete and continuum RGC models, extracellular stimulation was modelled by imposing Neumann boundary conditions at the boundary representing the electrode:

$$\mathbf{n}.(-\sigma_e \nabla V_e) = \frac{i_{stim}}{A} \tag{35}$$

where i_{stim} is the current waveform applied to the stimulating electrode, A is the electrode surface area, **n** is the inward unit vector normal to the boundary, and σ_e is the extracellular conductivity.

In some simulations, we also used a floating potential boundary condition for injecting the current stimulus, as this gave an isopotential boundary, more indicative of real metallic electrodes operation, due to their high conductivity:

$$-\mathbf{n}.\mathbf{J} = I_o \tag{36}$$

where **n** is the outward normal to the boundary and $\mathbf{J}$ is the inward current density vector $(A.m^{-2})$. I_o is the absolute inward current (A).

Zero flux conditions were imposed at all boundaries except for the stimulating and return electrodes:

$$\mathbf{J}.\mathbf{n} = 0 \tag{37}$$

Current was returned via a ground (zero volts) electrode, and a constant current mode of electrical stimulation was utilised for the active electrodes.

At the interface between adjacent retinal layers, a flux continuity boundary condition was imposed, representing continuity in the normal component of current density across internal boundaries:

$$\sigma_{e1}\frac{\partial V_{e1}}{\partial z} = \sigma_{e2}\frac{\partial V_{e2}}{\partial z} \tag{38}$$

where σ_{e1} and σ_{e2} are the extracellular conductivities of the adjacent layers, and z is the vertical coordinate normal to each internal boundary.

4.4 Estimation of Reduced Model Inter-Compartment Conductances

Neuron modelling using fully realistic morphologies and incorporating biophysically accurate ion channel distribution in the various neural compartments are based on several experimental findings. However, high computer processing is needed to run a network of such neurons, such as in the Blue Brain Project (Van Geit et al., 2016), beyond the capabilities of standard computers. Reducing these models while maintaining their capability to reproduce experimental data is desired. Several reduction methods have been proposed: one of these techniques has shown the efficacy is able to reduce the running time of a Purkinje cells model by 200-fold (Marasco et al., 2013).

In the development of the multi-domain continuum model, the fully-realistic morphologies of ON or OFF RGCs were reduced to a point model consisting of only four compartments representing the major parts of the RGC: soma, axon initial segment (AIS), axon, and dendrites. Several experimental and computational studies have shown that the propagation of electrical signals between soma and dendrites is asymmetric (Kim et al., 2014). Furthermore, there are different regions in neuronal axons with varying radii and ion channel distribution, known to influence the propagation of electrophysiological waveforms. Many computational studies have considered this influence by proposing a coupling conductance. However, most of these studies have only considered the relationship between soma and dendrites (Kim et al., 2014). In the multi-domain continuum

model developed in this thesis, a set of finite difference equations was formulated to consider all major RGC compartments, with the influence of each compartment on its neighbouring element characterised through internal (coupling) conductances, with values depending on the direction of coupling..

Estimation of model parameters usually poses a considerable challenge. This challenge will be more difficult if tuning the parameters is accomplished manually. The relationship between model output(s) and parameter values can be described as nonlinear or even complex in most cases. Therefore, and fitting model parameter values is a non-trivial task. Accordingly, the automation of parameter tuning is an interesting topic, inspiring many researchers to propose valuable optimisation algorithms (Friedrich et al., 2014; Van Geit et al., 2008).

The shape of the solution space of a given optimisation problem determines the choice of a search algorithm that should be used. The optimisation process can rely on two choices. The first is the determination of an appropriate error or cost function that is used to indicate how model predictions match or fit experimental or target data. Different cost functions have been proposed for model parameters. The second choice is to allow the optimisation technique to handle the cost function . Therefore, if the problem has many local minima, local optimisation algorithms such as simplex or the local gradient algorithms are not recommended, because they will terminate at the first found local minimum. In this case, global optimisation techniques should be encouraged. Global techniques such as evolutionary and simulated annealing algorithms have been shown to be particularly efficient for neuronal model fitting. The two choices are critical and independent, which means one could choose a good cost function, but you could fail to choose the adequate optimisation algorithm (Van Geit et al., 2008).

In our case, single-objective optimisation was chosen to handle the cost function in each model compartment. One cost function that has been proposed is spike count (Friedrich et al., 2014), where the absolute difference in spike numbers between the model and target data is considered during the entire trace.

We adopted this cost function to estimate the values of internal conductances between compartments of the reduced ON and OFF RGC models, which are able to reproduce results of the full-realistic morphologies of ON and OFF RGC models. The cost function is given by

$$e = \sum_{n=1}^{4} (SN^{original} - SN^{reduced}) \tag{39}$$

where the cost function e is represented by the sum of squares of the difference in total spike number (SN) between the original and reduced model data among each of RGC four compartments.

Various global optimisation algorithms in Matlab (Mathsworks, USA) were used, namely: genetic algorithm, pattern search, and simulated annealing methods. These were used to handle the cost function to obtain the optimal values of internal conductances that minimise the disparity between the original and reduced model. A total of twelve conductance values were estimated: six for the OFF RGC model and six for the ON RGC model.

4.5 Mesh Convergence

Determination of current threshold sufficient to generate responses in experimental preparations, computer models, and in patients is an important system feature, and has been utilized in numerous experimental and modelling studies. Current threshold is also important for determining safe current injection limits that can be delivered to patients. In our mesh convergence analysis, we utilized a single scalar quantity summarizing our model output that could readily be examined as a function of mesh size. To examine the influence of mesh refinement on the accuracy of simulation results, Jensen et al.'s experiment was simulated (Jensen et al., 2005*b*), in which epiretinal electrical stimulation of an OFF RGC was conducted at various electrode distances from the retina. A monopolar stimulating electrode 500 μm in diameter was used to deliver the 1 ms pulse current stimulus. All measurements were taken from the mid-plane of the RGC layer. The influence of maximum element size on the required current thresholds was tested with three different maximum mesh element sizes: 100, 200 and 400 μm. These meshes generated 90636, 30212 and 15148 mesh elements, respectively. There was almost no difference in predictions between models with these meshes as shown in Fig 4.3. We therefore adopted a maximum element size of 400 μm as the default mesh size for the continuum models, avoiding time consuming and memory cost as shown in Table 4.7. We tried to use a more refined mesh with a maximum element size less than 100 μm, for example 75 μm, but our Workstation PC with 2.1 GHz (2 processors) and 128 GB of RAM could not run this model. To use a smaller maximum element size, we reduced the dimensions of the model by 50 % to see if there is any difference with using very fine mesh. In this new dimnesion model, we used three different maximum mesh element sizes: 50, 200 and 400 μm. The results were similar to what we obtained before, which there is no big difference in predictions between these mesh sizes (see the Appendix B).

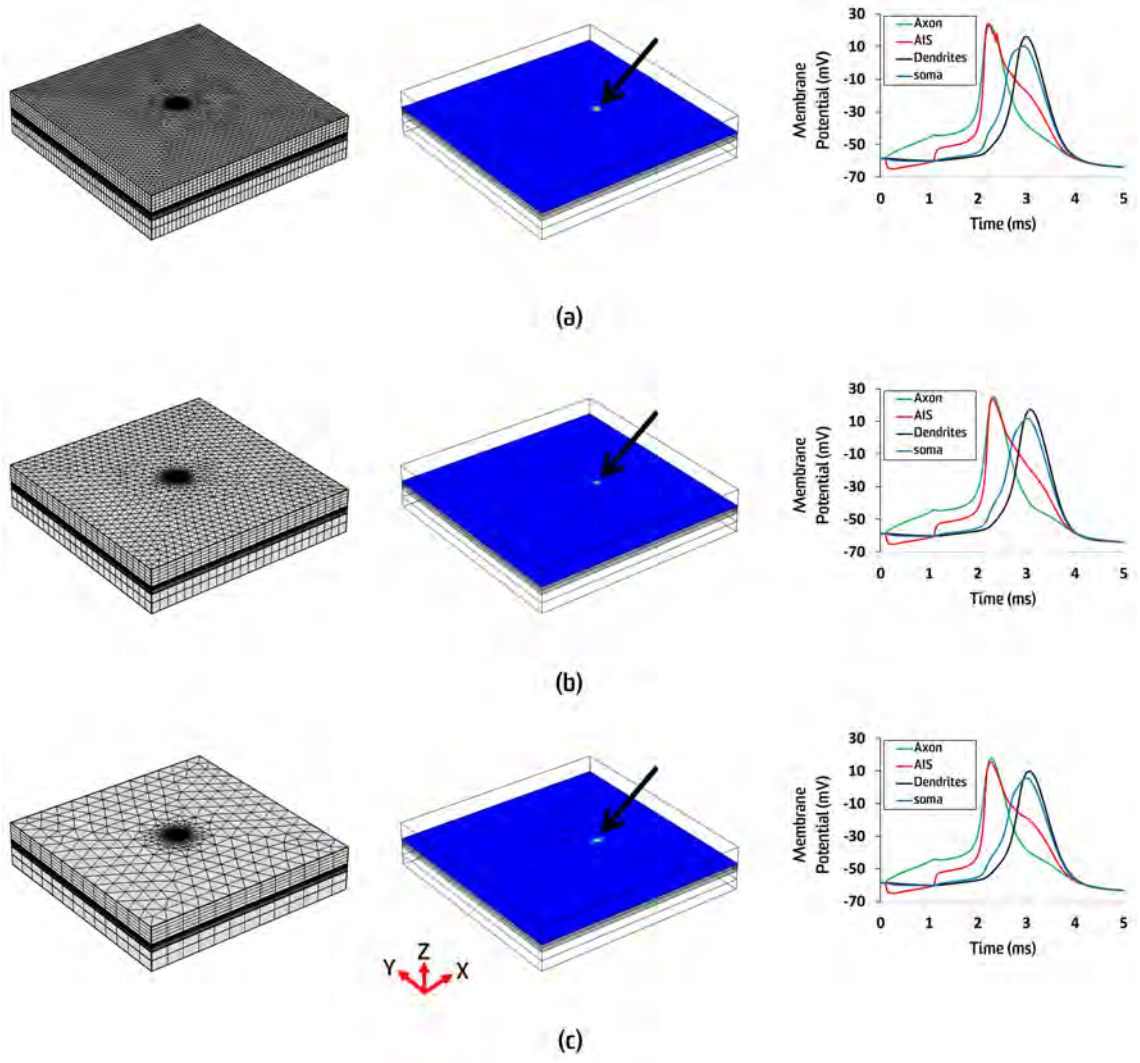

*Figure 4.3: Simulated action potential traces from various compartments of an OFF RGC obtained from a point probe located at the arrow and surface plots of OFF RGC layer activation in response to epiretinal electrical stimulation (replicating the experiment of (Jensen et al., 2005*b*)) corresponding to the three meshing schemes: (a) 100 μm (b) 200 μm (c) 400 μm.*

Table 4.7: Mesh convergence study

	Mesh 1	***Mesh 2***	***Mesh 3***
Maximum element size (μm)	400	200	100
Current threshold (μA)	55	54	54
Solving time ($hours$)	1.5	9	60
Physical memory cost (GB)	13.4	20	70.5
Virtual memory cost (GB)	17.4	25	83.5

Difference compared to finest mesh (Mesh3) ($\%$)

	Mesh 1	***Mesh 2***	***Mesh 3***
Current threshold	1.85	0	0

5 A Cable Equation for Neuronal Modelling

Over the recent decades, electrical stimulation has been extensively utilised in the nervous system for both relieving symptoms of neuronal disorders, restoring wounded functions as well as investigating the organisation and mechanisms underlying neuronal circuits (Grill and Kirsch, 2000; Lovell et al., 2007; Mcintyre and Foutz, 2013; Wilson and Dorman, 2008). The basic principle of all neuroprostheses is based on electrical stimulation of excitable cells to replicate normal neuronal responses. However, despite great progress, the major obstacle remains our limited understanding of the mechanisms by which electrical stimulation modulates target cells. For example, there is ongoing discussion about the mechanisms of deep brain stimulation, a well-known approach to managing the symptoms of central nervous system impairments such as Parkinson's disease. The complicated nature of nervous system organisation limits interpretation and generalisation of the information coming from experimental studies (Cranford et al., 2012; Joucla et al., 2014).

Mathematical modelling is a useful tool that has been employed to enhance our understanding of the complex behaviour of neuronal circuits in ways which cannot be attained by current experimental techniques. It also plays an important role in optimising the design of neuroprosthetics devices. For example, the development of a neural prosthesis requires repeated and exhaustive experimental testing of electrode designs and stimulation algorithms, which can become very costly and prohibitive in terms of the possible number of stimulus parameters and electrode configurations. Alternatively, computational simulation is a powerful tool for exploring and testing new stimulation strategies to improve the efficacy of neural implants. Several computational models have been successfully employed to predict the electrical field thresholds needed to activate targeted neural

cells and to facilitate understanding of the complexity of the nervous system and its behaviour following electrical activation (Joarder et al., 2011; Kang et al., 2015; Moffitt and McIntyre, 2005).

Compartmental modelling is the most detailed computational approach in computational neuroscience (Lee et al., 2002; Meffin et al., 2012). It offers accurate descriptions of biological neuronal behaviour through implementing detailed anatomical representations and biophysical properties of neural elements (Guo et al., 2014). These models are mostly based on cable equation theory (Meffin et al., 2012), whose originis the telegrapher's equation, discovered by Lord Kelvin to describe signal decay in an underwater cable across the Atlantic Ocean (Lee et al., 2002). Significant contributions by Hodgkin & Rushton (1946) and Davis & Lorente de NO (1947) presented derivations of cable theory for the neural axon and included transient solutions, thereby developing neuronal cable theory. This theory was extended by the landmark work of Wilfrid Rall, who analysed the effects of dendrites on action potential (AP) propagation. Rall's modifications to the cable equation corrected several errors and misinterpretations related to then perceived role of dendrites (Koch and Segev, 1998). He proposed a general formula for any arbitrary dendritic branching pattern under steady state (Rall, 1959) and transient (Rall, 1962) conditions. The use of compartmental models employing intracellular electrical stimulation has greatly contributed to our quantitative understanding of the mechanisms underlying neuronal excitation and propagation.

In 1976, McNeal proposed the first widely-used model for simulating nerve responses to extracellular stimulation. Although he used point source stimulation, he argued that his approach was capable of dealing with any arbitrary electrode configuration. This model was an extension of Rall's intracellular stimulation model to account for extracellular stimulation. McNeal's model divided the myelinated neuron into infinite isopotential compartments linked by intracellular conductances (Joucla and Yvert, 2012; McNeal, 1976). This model has been further developed by Rattay (1986) to describe the activation of myelinated and non-

myelinated axons (Rattay, 1986). For modelling responses to intracellular current injection, these formulation assumes that the extracellular potential at each compartment is fixed to zero (Gold et al., 2006).

The two common approaches to model extracellular neural stimulation are the volume conductor and bidomain methods (Meffin et al., 2012, 2014). Bidomain models calculate the membrane, and intra- and extra-cellular potentials at each point on the excitable tissue. Despite its capability in terms of efficient computation, for example in computational cardiac electrophysiology, this formulation has not been used extensively to model neurons (Meffin et al., 2014). On the other hand, the volume conductor approach constitutes a one way coupling of two physics, Laplace's and Maxwell's equations, to describe current injection and subsequent electric field generation in the extracellular space, and the mono-domain formulation of the cable equation to describe excitation and AP propagation in neurons (Joucla and Yvert, 2012; Meffin et al., 2014). Volume conductor models are usually implemented in two stages. The first stage utilises the finite element method (FEM) to compute the extracellular potential while neglecting the presence of neurons. The second stage involves segmenting the target neuron into compartments, using the extracellular potential calculated from stage 1 in each compartment to compute the membrane potential. Stage 2 is usually achieved using finite difference method software such as NEURON (Hines and Carnevale, 1997) or GENESIS (Bower and Beeman, 1998), which rely on the 1D cable formulation derived from the aforementioned models (Cranford et al., 2012; Joucla et al., 2014)).

Classical cable models have generally relied on two assumptions: a uniform membrane and extracellular potential over each compartment, and that the presence of a neuron does not influence the extracellular potential field (Joucla and Yvert, 2012; Meffin et al., 2012, 2014). However, these two assumptions have been claimed to be invalid (Meffin et al., 2013; Schnabel and Struijk, 2001), especially when the stimulation electrodes are close to the neurons (Schnabel and

Struijk, 2001).

There are many studies in neuroscience modelling that have adopted the cable equation describing the spatiotemporal dynamic changes of the membrane potential along a given length of a dendrite or axon with fixed diameter (Joucla and Yvert, 2012; López-Sánchez and Romero, 2017; Rall, 1977). However, several experimental studies have shown that the diameter of the axon and dendrites could be non-uniform, potentially modifying the conduction velocity and changing the AP amplitude, or even blocking AP initiation or propagation (Lee et al., 2012; Schierwagen and Ohme, 2008). The morphological inhomogeneities of the axon such as discrete swellings along its length, could be indicative of neurodegenerative disease, including Alzheimers, Parkinsons, and multiple sclerosis (López-Sánchez and Romero, 2017). Therefore, modifications to the standard fixed-radius cable equation are essential to estimate the accurate response of non-uniform neural segments during electrical stimulation.

In this chapter, we have developed a full three-dimensional FEM approach based on a modified cable equation, suitable for all neuron morphologies and non-uniform geometries. The approach enables modellers to simulate more accurately the response of neurons during intracellular or extracellular stimulation, addressing some of the limitations associated with previous neural stimulation models by implementing an explicit representation of neuron morphology and solving for the membrane potential during the delivery of extracellular stimulation. Therefore, this method provides researchers with a highly simplified simulation framework by allowing all physics to be solved in a fully coupled manner.

5.1 Illustrative Model

In this simple circuit, two purely resistive compartments are connected end-to-end, to represent a non-uniform axon as shown in Fig. 5.1 (a). The compartments are of equal lengths and equal intracellular resistivity, but with different radii, with one compartment double the radius of the other (2 μm and 1 μm respectively). We

imposed a Dirichlet boundary condition V_1 = 1 V on the first node, setting the third node to ground, namely V_3 = 0 V. In this illustrative model, the cell membrane was assumed to be insulating, so current travelled only intacellularly along the fibre. All formulations examined were 1D representations of voltage against the length along the fibre.

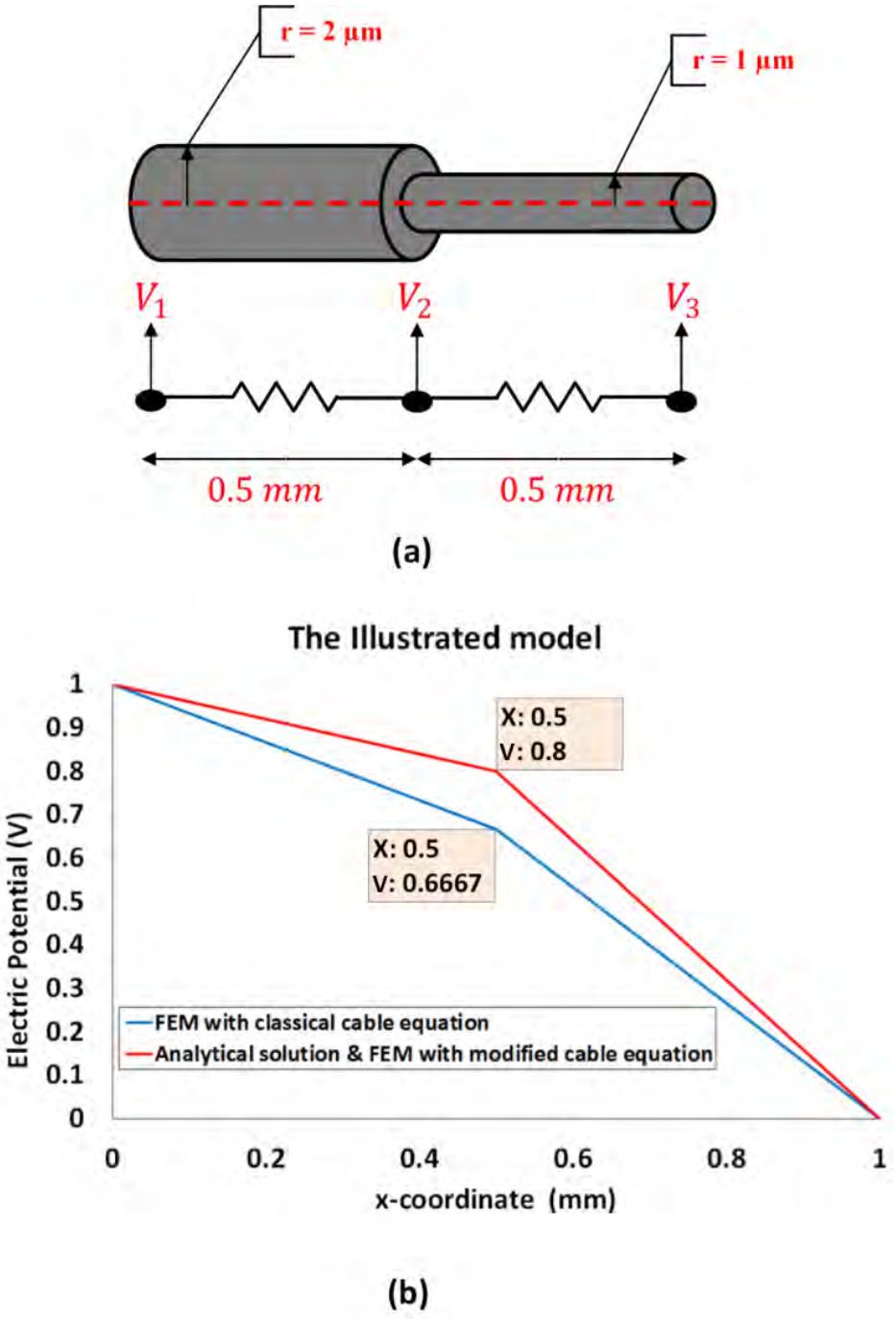

Figure 5.1: Illustrative model settings. (a) Schematic diagram of model geometry (b) Variation in electric potential along the length of the model using analytical calculations, as well as finite element method (FEM) simulations of the classical (i.e. constant radius) and modified forms of the cable equation.

The electrical potential at the second node V_2, where the radius change occurs, was calculated to be 0.666 V using FEM. However, the analytical solution was determined as V_2 = 0.8 V, as shown in Fig. 5.1 (b). Hence the difference between the analytical and numerical solution was significant, at almost 17%. This error is expected to increase with more complex geometries and after the addition of active membrane electrical properties and capacitance, which we have ignored in this illustrative example. Therefore, a modified formulation of the cable equation is essential to take into account the change in the radius along the fibre.

A modified form of the cable equation suitable for use in continuum models and FEM simulations is derived here, to deal with realistic geometries of excitable fibres, namely the variation in radius along the fibre. The FEM solution of the modified cable equation is illustrated in Fig. 5.1 (b), and is identical to the analytical solution $(V_2 = 0.8V)$.

Next, we demonstrate the improvement in solution accuracy attained by the modified continuum formulation of the cable equation. We compare model predictions using 1) a finite-difference discrete solver (NEURON), 2) a FEM solver (COMSOL) using the classical continuum formulation, 3) and a FEM solver using the modified continuum formulation. We employed a neuron ionic model as an example, and considered a number of common structural representations (simplified geometry, accurate morphological reconstruction) and simulation scenarios (responses to intracellular current injection and extracellular stimulation).

5.2 Conventions

In this chapter, we used the term *segment* to refer to a part of the neuron with identical biophysical properties (e.g. soma or hillock, axon initial segment, etc). On the other hand, we used the term *compartment* to indicate one unit of discretisation in the geometry or mesh.

5.3 Modelling Intracellular Electrical Stimulation

To validate the modified cable equation, we utilised the equivalent cylinder representation of the Fohlmeister & Miller (FM) ionic model of retinal ganglion cells (RGCs) (Fohlmeister and Miller, 1997*b*). This model represents the RGC as five cylindrical segments: the soma, initial segment (IS), narrow segment (NS), axon, and dendrites. We chose the equivalent cylinder dendritic 2.5 diameter model (Fohlmeister and Miller, 1997*b*), whose predictions are closest to the RGC realistic morphology model presented in that paper. In the finite-difference setup, this model is composed of a total of 800 compartments each 15 μm in length. The number of compartments for each RGC segment is: soma 2, IS 3, NS 6, axon 754, and dendrites 35. Compartments in each segment had different diameters: dendrites (2.5 μm), soma (20 μm), IS (1 μm), NS (0.4 μm), and axon (1 μm). We will refer to this model as FM-EC2.5. The illustrative geometry of this model is shown in Fig. 5.2.

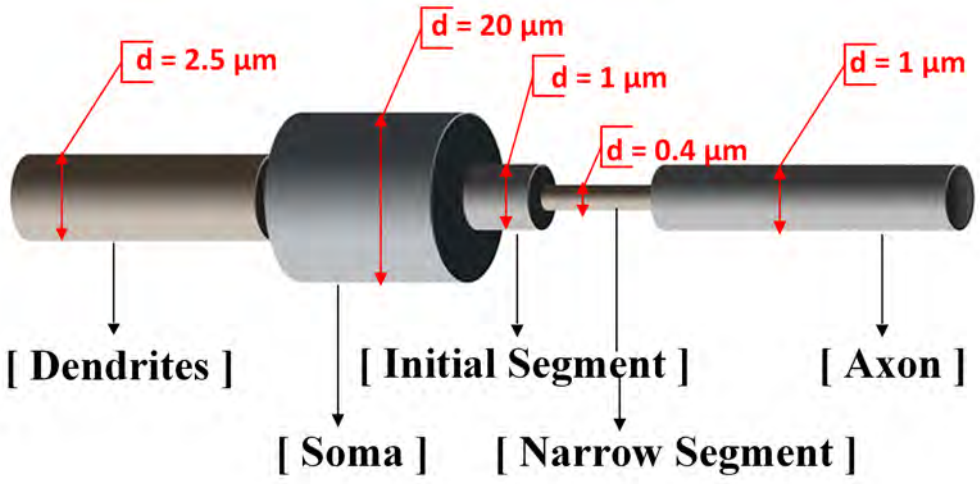

Figure 5.2: Illustrative geometry of FM-EC2.5. The diameters are as follows: dendrites (2.5 μm), soma (20 μm), narrow segment NS (0.4 μm), initial segment (IS) and axon (1 μm).

To reproduce the current injection settings of Fohlmeister and Miller (1997b), the cell was excited by injecting a depolarising constant current stimulus ($10pA$) into the second 15 μm compartment of the soma, adjacent to the initial segment (IS), and models were run for the entire 400 ms of stimulation duration. Models were solved using a finite-difference algorithm in NEURON as well as through the finite element solver COMSOL, using both the classical and modified forms of the cable equation (Fig. 5.3). The COMSOL model, based on the modified form of the cable equation, generates four action potentials, which were in an agreement with Figure 3c of Fohlmeister and Miller (1997b), in which they used the finite-difference NEURON software.

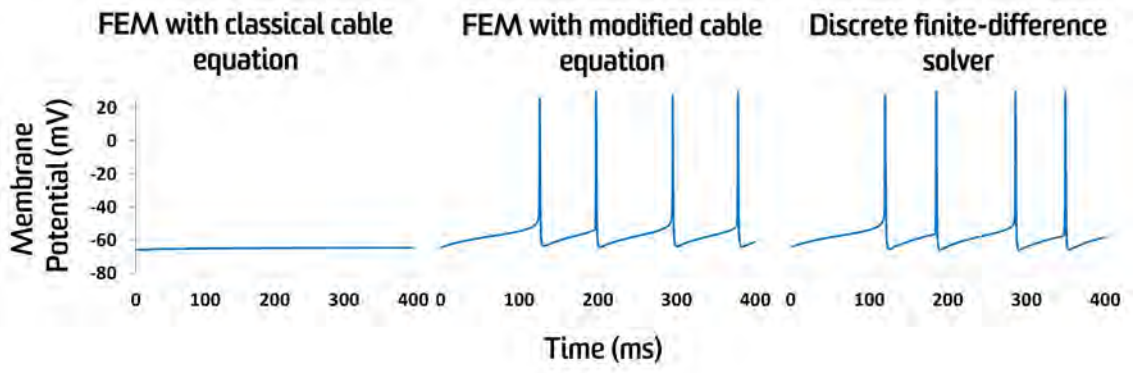

Figure 5.3: The simulations of FM-EC2.5 model (Fohlmeister and Miller, 1997b) using different solvers and cable formulations. The model was solved using the FEM by implementing the classical (left) and modified (middle) forms of the cable equation, as well as the discrete finite difference method (right). A 10 pA depolarising constant current injection was applied in all cases.

From these results, it can be seen that the modified cable equation is capable of reproducing results of (Fohlmeister and Miller, 1997*b*) study whilst the classical cable equation form is not. To examine the efficiency of the modified cable formulation, we calculated how much current is required with the classical form to reproduce the (Fohlmeister and Miller, 1997*b*) study results. Using the classical cable form, more than nine-fold depolarising current (95 pA) was needed to

regenerate the same number of spikes, as shown in Fig. 5.4.

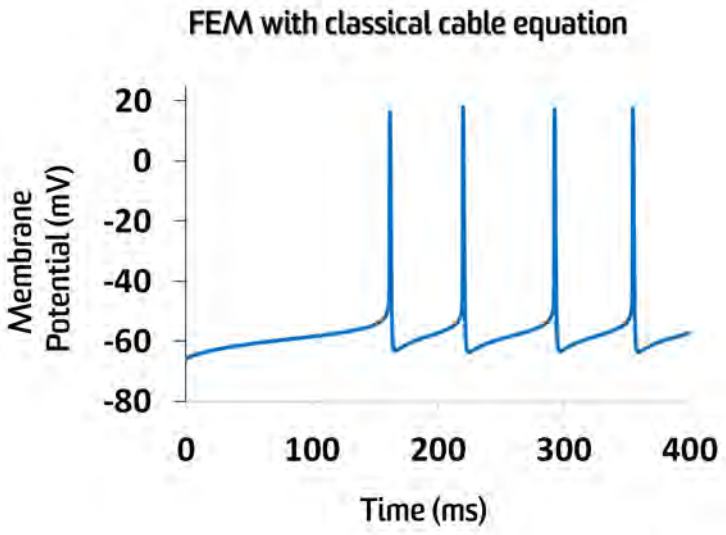

Figure 5.4: Simulation of FM-EC 2.5 model when solved using the classical continuum form of the cable equation with 95 pA depolarising intracellular constant current injection into the soma.

5.4 Modelling Morphologically-Realistic Neurons

Next, this modified derivation of the cable equation was investigated with a more complex neuron morphology to explore its ability to cope with more realistic dendritic branching pattern and variation in radius along the neuron's segments. We selected the model published by Sheasby and Fohlmeister (1999) . One RGC from the medium complex group, namely lws9287m, was chosen arbitrarily and its geometry was reconstructed in both COMSOL and NEURON (Fig. 5.5), and all published model settings of Sheasby and Fohlmeister (1999) were implemented. The cell was composed of soma and dendrite segments, with a soma radius of 7.2 μm and an average dendritic radius of 0.335 μm. We added an axon, IS, and NS with corresponding lengths and radii of (5340 μm, 0.5 μm), (40 μm, 0.5 μm), and (90 μm, 0.2 μm) for the axon, IS, and NS, respectively. We will refer to this model hereafter as the SF model.

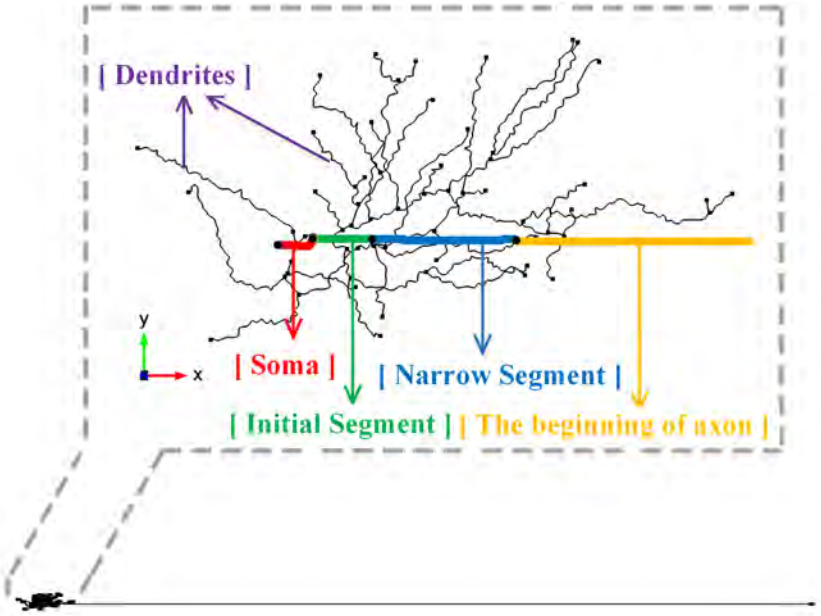

Figure 5.5: Realistic morphology of the Sheasby and Fohlmeister lws9287m retinal ganglion cell. (Sheasby and Fohlmeister, 1999).

A depolarising constant current of 15 pA was injected into the whole soma, lasting for the entire duration of the simulation (450 ms). Results from the finite difference and FEM simulations using the classical and modified cable formulation are displayed in Fig. 5.6. The FEM model based on the modified cable formulation generates five action potentials, which were consistent with Sheasby and Fohlmeister (1999), in which they used the finite-difference NEURON software (https://senselab.med.yale.edu/ModelDB/ShowModel.cshtml?model=18501#tabs-1).

The classical formulation of the cable equation implemented using FEM required a depolarising constant current (250 pA) into the soma, which was more than sixteen-fold that required with the finite difference or modified cable equation FEM implementation, to reproduce the same number of spikes, as shown in Fig. 5.7.

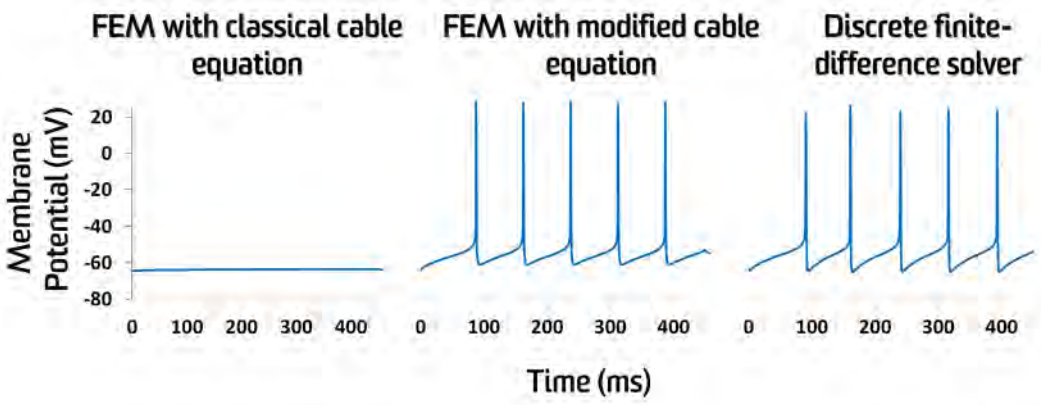

Figure 5.6: Results of intracellular stimulation for the SF model (Sheasby and Fohlmeister, 1999). The model was solved using FEM by implementing the classical (left) and modified (middle) forms of the cable equation, as well as the discrete finite difference method (right). A 15 pA depolarising constant current injection was applied into the soma in all cases.

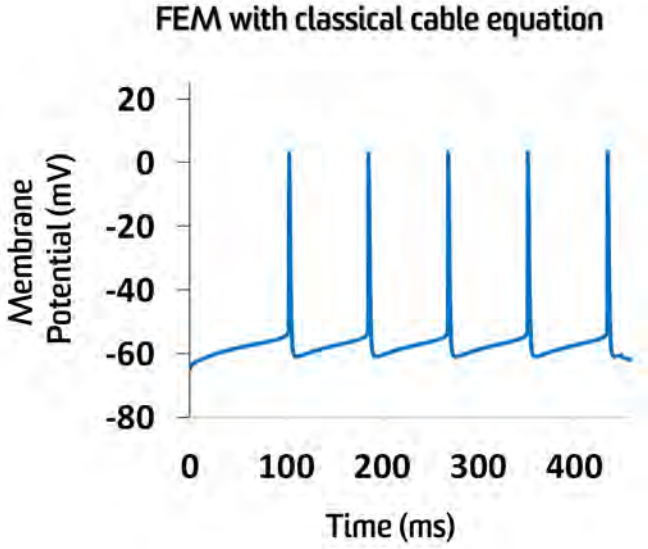

Figure 5.7: Result of the SF model (Sheasby and Fohlmeister, 1999) when solved using the classical form of cable equation implemented using FEM with a depolarising constant current stimulus of 250 pA into the soma.

5.5 Modelling Extracellular Electrical Stimulation

A 3D computational model of extracellular electrical stimulation of the FMEC2.5 RGC was implemented, with the axon set to 510 μm in length (Fohlmeister and Miller, 1997*b*). For the FEM simulations, the RGC was immersed inside a semi-elliptic domain representing the retina with axes 1800 μm X 900 μm X 180 μm. The RGC geometry was implemented as one-dimensional edge segments, with the entire model geometry shown in Fig. 5.8.

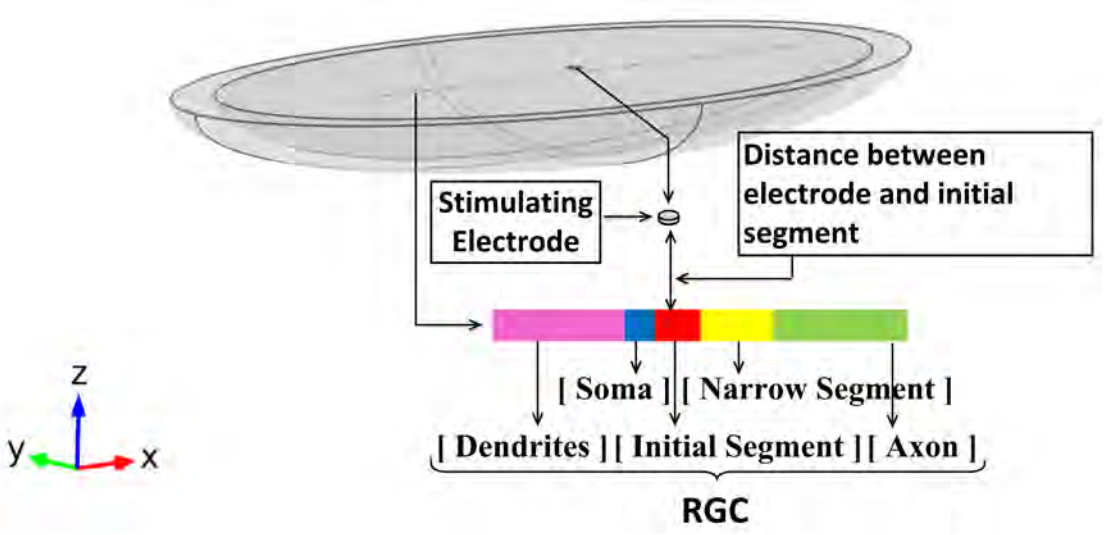

Figure 5.8: FM-EC2.5 RGC model geometry constructed in COMSOL. Schematic diagram of model geometry and placement of electrode with respect to the RGC.

In order to provide electrical grounding in the model an infinite element domain was applied on the outer external boundary of the semi-ellipsoid, in order to imitate the extracellular stimulation environment in NEURON software as discussed below.

In the finite difference NEURON solver, the RGC morphology was represented with five segments. The length and diameter of each segment was specified, and each segment was divided into a number of equal length compartments (15 μm). The external medium was assumed to be homogeneous, of infinite extent and isotropic. The extracellular voltage distribution was determined by utilising a modified version of the isopotential disk electrode formula (Wiley and Webster, 1982): the derivation of this equation is detailed in the Appendix A.

$$V(r,z) = \frac{\rho I_o}{2\pi a} \arcsin \left(\frac{2a}{\sqrt{((r-a)^2+z^2)} + \sqrt{((r+a)^2+z^2)}} \right) \tag{40}$$

where $V(r,z)$ is the extracellular potential and r, z represent the radial and axial distance from the centre of the stimulating electrode. I_o is the applied current, ρ is the extracellular resistivity, and a is the radius of the disk electrode.

For each compartment, the extracellular potential was calculated at its centre and delivered uniformly to the extracellular surface of the whole compartment. Subsequently, these potentials were incorporated into each compartment and the membrane potential of each was computed.

For both NEURON and COMSOL simulations, the radius of the stimulating electrode was identical (15 μm), and positioned 10 μm above the centre of the IS. A monophasic cathodic current (20 μA) pulse was delivered 0.1 ms in duration. The value of the extracellular resistivity was 78.125 $\Omega.cm$, and the value used for intracellular resistivity was 110 $\Omega.cm$.

This model was solved in both COMSOL and NEURON, for a simulation time of 5 ms. Both formulations of the cable equation were employed in the COMSOL simulations, with all results of this model shown in Fig. 5.9.

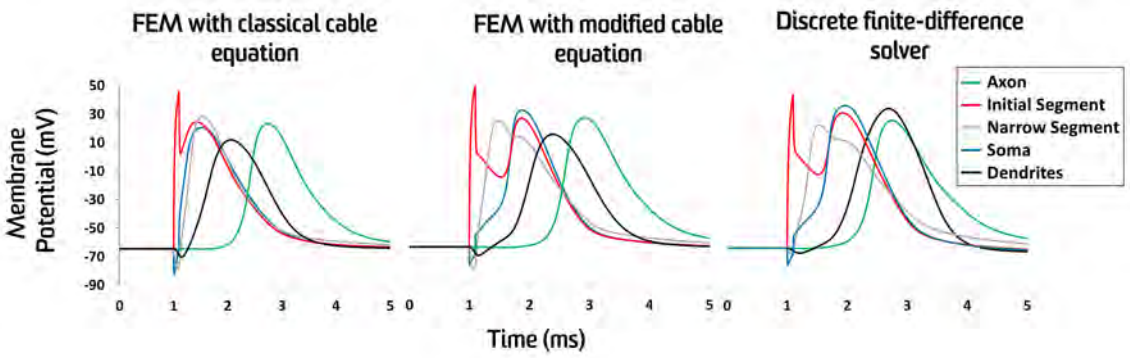

Figure 5.9: Results of the extracellular electrical stimulation model. The membrane potential was calculating by using a general form of the cable equation (left), the modified cable equation (middle), and the result from NEURON software (right).

5.6 Numerical and Computational Settings

5.6.1 Intracellular Electrical Stimulation Settings

Discrete finite-difference models were solved using NEURON (Hines and Carnevale, 1997). The geometry was discretized to compartments using the parameter (nseg) to specify the number of compartments for each segment. In the FM-EC2.5 model, 800 sequential compartments, each 15 μm long were used. In the SF model, in addition to the traced soma and dendritic tree, other segments were discretized using 15 μm compartments. A backward Euler time-stepping routine was employed for all models with a maximum time step of 25 μs. The continuum finite element models were solved using COMSOL Multiphysics 5.2 (COMSOL AB, Sweden). The illustrative, FM-EC2.5, and Sheasby models were meshed using linear elements with a maximum element size of 1 μm. Quadratic Lagrange base functions were used for computing the membrane potential, the channel gating variables, and calcium concentration. An adaptive backward differential formula time-stepping routine was employed with a maximum time step of 25 μs. Results from all intracellular current injection simulations were digitized at 40 kHz (25 μs intervals).

5.6.2 Extracellular Electrical Stimulation Settings

As for the intracellular stimulation case, the discrete finite-difference model was solved using NEURON (Hines and Carnevale, 1997). The FM-EC2.5 geometry was discretized into compartments using the parameter (nseg) to specify the number of segments for each segment, and the backward Euler time-stepping routine was employed with a maximum time step of 10 μs. The continuum finite-element model was solved using COMSOL Multiphysics 5.2, with the mesh locally refined around the RGC and disc electrode to improve the simulation accuracy.

The RGC was meshed using linear elements with maximum element size 5 μm. The disk electrode was meshed using triangular elements with maximum element size 2 μm. The remaining volume was meshed with free tetrahedral elements with minimum element size of 10 μm and maximum element size 50 μm. The total mesh was comprised of 47106 elements with 72016 degrees of freedom. Quadratic Lagrange base functions were used for computing the membrane voltage, the channel gating variables, and calcium concentration. An adaptive backward differential formula (BDF) time-stepping routine was employed with a maximum time step 10 μs. Results from all simulations were obtained at 100 kHz output sampling rate..

5.7 Discussion

Recently, the finite element method (FEM) has been increasingly employed in neural engineering. For instance, to predict neuron membrane potential during extracellular stimulation with realistic morphologies and complex stimulation environments (Joucla et al., 2014), or to estimate the required thresholds to activate neurons, and propose novel electrode designs (Moghaddam et al., 2014).

In the present chapter, various computational models of neural electrical stimulation were simulating using finite element method software to assess the performance of the classical and modified versions of the cable equation, providing valuable insights into the most efficient neural modelling framework. Results demonstrate that finite element models using the modified cable equation to take into account changing diameter along the neuron, are highly effective in reproducing experimental findings of previous neural electrical stimulation studies in terms of the evoked action potentials number with the same current stimulus (Fohlmeister and Miller, 1997*b*; Sheasby and Fohlmeister, 1999) and in accurately predicting the response of excitable fibres to a variety of electrical stimulation scenarios. We also demonstrated the shortcomings of implementing the classical cable equation.

The finite method approach based on modified cable equation formalism was verified and validated by comparing with published compartmental neural models implemented in a discrete finite difference solver software, NEURON, showing excellent consistency.

The results of FEM modelling of intracellular electrical stimulation ranged from a simple geometry (Fig. 5.2) to a more realistic morphology (Fig. 5.5) showed the efficacy of the modified cable equation compared to the classical cable form in terms of handling the variations of radius along the neuron and its dendritic branches. This approach was able to reproduce the same number of action potential spikes similar to the published modelling studies (Fohlmeister and Miller,

1997*b*; Sheasby and Fohlmeister, 1999) , as seen in Fig. 5.3 and Fig. 5.6. On the other hand, finite element models based on the classical cable equation failed to generate these results (Fig. 5.3 and Fig. 5.6). Importantly, FEM models using the classical cable equation required more than nine- and sixteen-fold intracellular current stimulus respectively to reproduce the simulation results of the simple and realistic morphological models, as clearly seen in Fig. 5.4 and Fig. 5.7.

In all intracellular stimulation results, the responses at the soma only were shown. When we injected current into the soma, the number of spikes observed in the soma was similar to what was obtained in every other segment (see the Appendix C), therefore, we only displayed the somal spikes. Traces of action potentials for each segment however were shown in Fig. 5.9. Furthermore, simulating current injected into the dendrites did not represent a physiological mode of external electrical stimulation, where stimulus thresholds are lowered markedly when electrodes are placed around the axonal initial segment adjacent to the soma, rather than over the dendrites (Tsai et al., 2012).

Extracellular electrical stimulation simulations have shown the utility of the finite element models based on the modified cable equation, yielding a better agreement with NEURON benchmark models than the finite element model based on the classical cable equation in terms of the action potential shape and threshold current for electric excitation. In the extracellular model settings (Fig. 5.8), the electrode was located above the initial segment (IS), which means this segment and adjacent segments (soma & narrow segment (NS)) will be affected by extracellular stimulation more than the axon and dendrites, which were far away. If we look to the action potentials (APs) of IS, soma and NS in Fig. 5.9 for the modified cable and NEURON software, we will find these traces are almost identical and the traces of axon and dendrites were only slightly different in amplitude. This difference could be due to choosing different locations for recording the response of these segments in the two software. In contrast, the finite element model based on the classical cable equation showed a slight difference in the shape of action

potential in various segments of the neuron, as indicated in Fig. 5.9.

The intracellular current injection simulation results demonstrated that the modified cable equation yielded similar results in terms of the evoked action potentials number to (Fohlmeister and Miller, 1997*b*; Sheasby and Fohlmeister, 1999) studies, which they used the finite-difference NEURON scheme. In contrast for extracellular stimulation with a single pulse, the classical and modified cable equations generated almost similar results. This finding may explain how previous published finite element models based on the classical cable equation were able to successfully replicate experimental outcomes, including extracellular stimulation of rat RGCs (Abramian et al., 2015). Even though the modified cable equation exhibited only a slight influence on predictions in the simple extracellular stimulation modelling scenario considered in this chapter, we expect this disparity will become more significant with complex simulation scenarios involving, for example, high frequency stimulation, random pacing with and without synaptic inputs, or multiple electrode configurations required for neuroprostheses.

The illustrative model (Fig. 5.1) clarified the difference between the classical and modified forms of the cable equation in finite element modelling software. This model focused only on the heterogeneity in the radius of excitable fibres. The model based on the classical equation was unable to accurately reproduce the analytical solution. Since the classical cable equation was based on the assumption of a uniform radius, it was unable to tackle the change in radius along the fibre. It should be noted that several compartmental models have been implemented successfully in spite of the variation in radius by using the finite difference solver software based on the classical cable equation (Fohlmeister and Miller, 1997*b*; Goldstein and Rall, 1974; Guo et al., 2016). Such software discretised the fibre into compartments connected via resistors, with each segment consisting of a number of compartments. The average of diameter, axial resistance, and surface area are computed at the centre of each compartment, and compartment membrane potential calculated based on these parameters (Hines

and Carnevale, 1997). In contrast, finite element software computes the electrical potential around the fibre in a continuum way. A continuity equation is applied at internal boundaries between different segments of the fibre, and Maxwell's equations are used as governing equations for calculating the distribution of the electric field (Joucla and Yvert, 2012). Therefore, finite element software utilising the classical cable equation will not able to predict the response of neurons at regions with abrupt changes in diameter.

Extensive research has been conducted on the applications of the cable equation in neural modelling. Wilfrid Rall has pioneered this work by proposing several models, based mainly on dendrites, to treat various issues associated with the cable equation (Rall, 1959, 1962, 1977). His studies have played a crucial role in understanding the significant function of dendrites in electrical stimulation, estimating the dendritic parameters, and planning and interpreting experimental findings (Rall, 1995). He has presented analytical solutions for dendritic branching patterns under steady state (Rall, 1959) and transient (Rall, 1962) conditions, and has inspired many researchers to use his compartmental approaches as starting models for investigating many issues related to neuron modelling (Joyner et al., 1978). A common approach for studying the classical cable equation is the longitudinal mode of stumulation, which assumes the depolarisation of the membrane is caused by current flowing along the neuron from one part to another. In contrast, membrane depolarisation in the transverse mode of stimulation is a consequence of current passing perpendicularly to the neuron axis. Whilst most computational studies using the cable equation have studied the longitudinal mode of stimulation, there were a few studies that considered the transverse mode. This was achieved by a set of differential equations and appropriate boundary conditions taking into account the confined extracellular space. These equations have described the spatiotemporal behaviour of the subthreshold membrane potential under extracellular stimulation (Meffin et al., 2012, 2014; Tahayori et al., 2012, 2014).

Non-uniformity in neuron geometry has been investigated in many mathematical studies. Several axonal or dendritic geometries were explored and analytical solutions were proposed for steady or transient state, and with passive or active properties (Goldstein and Rall, 1974; Herrera-Valdez et al., 2014; Joyner et al., 1978; Khodorov and Timin, 1976; Manor et al., 1991; Ohme and Schierwagen, 1998; Rattay et al., 2001; Schierwagen, 1989; Zhou and Bell, 1994). Most of these studies aimed to reduce the dendrites with their branches into one dendritic cylinder, with Rall's "equivalent cylinder" models being utilised as a basis for many of these studies. A more recent computational study has examined the influence of abrupt changes in cable geometry, such as the swelling in axons encountered in some neurodegenerative diseases, by proposing a general cable equation formula based on the Frenet-Serret frame approach. Despite using passive properties, their numerical findings using the finite-difference method have shown that the amount of change in voltage amplitude is correlated with the level of morphological inhomogeneities (López-Sánchez and Romero, 2017). Another study by Altenberger et al. (2001) based on the finite element method, pointed out that the influence of geometric inhomogeneity is related to membrane kinetics. They used the Morris-Lecar and Hodgkin-Huxley membrane models with matching variables, finding that the Morris–Lecar model is more sensitive to non-uniform axon segment morphology (Altenberger et al., 2001). Other studies have presented a valuable review of extracellular stimulation modelling approaches in neural tissues (Joucla and Yvert, 2012), proposing a new estimator for membrane potential (Joucla and Yvert, 2009). In (Joucla and Yvert, 2012), the derivation of the cable equation for uniform, non-uniform, myelinated or unmyelinated, and realistic neurons was presented. The following finite-difference formula represented the non-uniform case:

$$\begin{aligned} &\tau_n \frac{dV_{m,n}}{dt} - \lambda_n^2 \frac{(V_{m,n-1} - 2V_{m,n} + V_{m,n+1})}{\Delta s^2} + V_{m,n} \\ &+ \frac{I_{i,n}}{G_{m,n}} = \lambda_n^2 \frac{(V_{n-1} - 2V_n + V_{n+1})}{\Delta s^2} \end{aligned} \tag{41}$$

However, this derivation is inaccurate, since the squared lambda is not inside the second derivative of membrane potential, leading to errors in computing the membrane potential.

Although analytical solutions can be computed with simple geometries, handling realistic morphologies requires numerical solvers. Compartmental models have been typically employed to compute the electrical potential of complex realistic neurons during electrical stimulation. However, these models are associated with discretisation errors. These errors can be avoided by utilising the finite element method because directly utilises ordinary differential equations (Altenberger et al., 2001). These models compute the extracellular potential by two ways. Firstly by assuming the neuron exists in an infinite homogeneous extracellular medium, as is done in the NEURON simulation environment (Lindén et al., 2014; Moulin et al., 2008). However with this assumption, the analytical simplification can produce significant errors in the prediction of extracellular voltages as demonstrated by Mueller and Grill (25% relative and 67 mV mean absolute difference compared to FEM) (Mueller and Grill, 2013). Secondly, the hybrid Finite Element-Finite Difference (FE-FD) approach computes the electric field distribution during the stimulus without the presence of a neuron and then imports the solution into the finite difference solver software, which maps onto the compartmental model of the neuron (Joucla et al., 2014; Meffin et al., 2012). However it has been demonstrated that the presence of the neuron has an influence on the extracellular potential field, hence, errors could be generated by the latter approach (Joucla et al., 2014). Obviously, the modified cable equation is suitable for using with any numerical solver to handle realistic neuron morphologies during intracellular or extracellular stimulations and using only one simulation environment. To the best of our knowledge, no available study investigated the impact of using the classical cable equation with varying neuronal diameter in the finite element method modelling approach.Therefore, the modified cable equation could be a platform for future intra- or extracellular electrical simulation research based on the finite

element approach.

The explicit representation of inclusion of a neuron during stimulation can alter the extracellular potential field (Joucla et al., 2014; Moulin et al., 2008; Tahayori et al., 2014). A study by Moulin et al. (2008) has examined the impact of the presence of the neuron during the extracellular electrical stimulation. They proposed a new finite element (FE) model based on the thin-film approximation of the neuron membrane. This approximation is only valid under two conditions: (1) the membrane is very thin (2) the current flows perpendicularly through the membrane. This FE model splits the whole geometry into two domains separated virtually and coupled using Neumann boundary conditions in order to avoid the meshing requirements around the vicinity of the neuron. In contrast to hybrid FE-FD models, this approach is capable of computing extra and intracellular potential fields as well as membrane potential simultaneously in the one software environment (Moulin et al., 2008). More recently, a valuable computational study compared these two approaches, the hybrid FE-FD and the "whole finite element model", identifying that the latter approach, which represent the neuron explicitly, provides more precise description of membrane potential responses (Joucla et al., 2014). These studies have emphasised the impact of the presence of realistic morphology during stimulation, especially when the MEA is located near the neuron, as is the case in retinal prostheses. Although that study (Moulin et al., 2008) has presented a powerful approach for extracellular electrical stimulation modelling, representation of the neuron is based on the thin-film approximation of the neuron membrane, which is vulnerable to inaccuracies in some cases. Our approach provides the more accurate response of neuron membrane potential, based on a modification of the cable equation which has been used widely and accepted as an accurate predictor of membrane potential. Hence, the finite element approach based on the modified cable equation will be helpful for handling complex neuron geometries under various modes of electrical stimulation.

5.8 Verification of models

Our findings stress the importance of model verification in computational neuroscience. In contrast to model validation, which checks model predictions against experimental benchmarks, model verification involves determining whether the implemented maths and numerical solver accurately represents and solves the modeled biophysics. With the modification of published model parameters to reproduce cell-specific biophysics, and the use of a variety of simulation software based on different underlying numerical solvers becoming more popular, care should be taken so that these modifications do not hide any underlying errors in physics or code implementation. Our attempt to implement a published model in a software package different to that in which it was originally implemented in, has revealed the need to modify the classical cable equation. To assist this process, a set of standard models with simulations under various electrical and pharmacological conditions could be curated to serve as benchmarks for the neuroscience community, and a standard notation adopted to ease reproducibility (e.g. CellML (Cuellar et al., 2003)), such as in the computational cardiac electrophysiology field (Niederer et al., 2011).

6 Development of Continuum Multi-Compartment Retinal Model

Retinal implants aim to target viable retinal ganglion cells (RGCs) in the degenerate retina of age related macular degeneration (AMD) or retinitis pigmentosa (RP) patients in order to produce visual perception. However, several factors need to be considered to optimise these devices. Significant cellular changes like cell death, synaptic remodelling, and glial scar layer occur in the degenerate retina at times when patients are implanted with a retinal prosthesis (O'brien et al., 2012). These anatomical changes may contribute to unsatisfactory visual perception during electrical stimulation, however, these issues can be investigated by the use of computational models of retinal activation (Joarder et al., 2011).

Several computational models have been reported in the literature for electrical stimulation of the retina (Abramian et al., 2015; Greenberg et al., 1999; Joarder et al., 2011; Joucla and Yvert, 2012). A common approach is via discrete neuronal (multi-compartmental) models, where neuronal morphologies are reconstructed from trace images and distributions of membrane ion channels are incorporated from experimental data (Fohlmeister and Miller, 1997*b*; Guo et al., 2016). Despite their accuracy, the main limitation of these models is their requirement for high performance computing when applied to investigate spatial activation patterns of large volumes of retinal tissue. An alternate approach is continuum bidomain models, in which the electrical activation of neural tissue is determined by coupling the intra- and extra-cellular domains without explicit representation of individual cells. Such models are beneficial for investigating the spatial activation of larger areas of neural tissue. They have been employed in cardiac and more recently neural modelling. The first continuum bidomain model of retinal electrical stimulation was proposed by Dokos et al. (2005). More recently, this model has been extended to study the response of RGCs to different

electrode placements (Joarder et al., 2011) and the response of retinal network to either electrical stimulation with different electrode configurations (Yin et al., 2010) or to light stimulation (Yin et al., 2011), as well as to explore factors that might affect the quality of visual implants (Abramian et al., 2014).

These models have highlighted valuable insights on retinal responses to electrical stimulation. However, all of these previous continuum retinal models represent each neuron as a single compartment consisting of either a soma (Joarder et al., 2011; Yin et al., 2010, 2011) or axonal sodium channel band (Abramian et al., 2014), and ignoring the influence of other compartments such as the axon or dendrites. Therefore, the scope of this thesis is to develop a novel continuum model of retinal electrical stimulation capable of overcoming some limitations associated with current continuum models and exploiting the recent findings of experimental work.

In this chapter, the first continuum multi-domain model of electrical stimulation of the retina involving all main RGC segments is developed. We validate the multicompartmental continuum RGC model against either a developed discrete computational model or published *in vitro* experimental data.

6.1 Validation against discrete RGC model

Validation of the continuum model of electrical stimulation of rabbit OFF & ON RGCs was undertaken over three stages. The first stage was the implementation of a modified version of a recently published discrete morphologically-realistic rabbit OFF & ON RGC model (Guo et al., 2016). The second was to reduce this RGC model to a four-compartment version by implementing a set of finite difference equations and computing the internal conductances that connected RGC compartments to each other. The final stage was the implementation of a continuum model of rabbit ON & OFF RGCs based on compartmental equations and the calculated conductivities. The model was deemed valid if RGC activation sites of the first stage (discrete model) and the third stage (continuum model) were sim-

ilar. All three stages were implemented for each OFF & ON RGC separately. We began with the OFF RGC, followed by the ON RGC, and eventually combined both formulations in one model.

6.1.1 The Discrete Model (Stage 1)

6.1.1.1 Intracellular Modelling of RGC

The morphologies of OFF & ON RGCs, which were taken from the NeuroMorpho database ((Guo et al., 2013b)), were imported into COMSOL Multiphysics finite element simulation software (COMSOL AB, Sweden) as equivalent-cylinder cable models, consisting of one-dimensional edge segments representing the soma, axon hillock, axonal initial segment (AIS), the distal axon, and dendrites, with radii 9 μm, 0.47 μm, 0.47 μm, 0.47 μm and 0.335 μm respectively. Their morphologies are shown in Fig. 6.1.

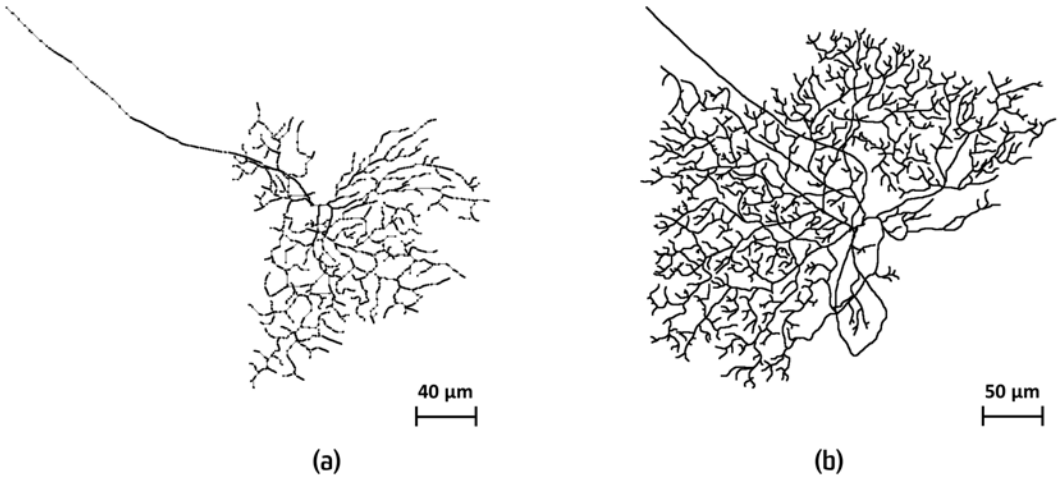

Figure 6.1: The fully realistic OFF (a) and ON (b) RGC geometries imported into COMSOL Multiphysics.

The ionic models of rabbit OFF & ON RGCs of Guo et al. (2016) study were modified with some modifications as mentioned below.

1. The adoption of gating variable dynamics for the low threshold voltage activated calcium current (I_{CaT}), initially proposed by Wang et al. (1991) and adopted later by others (Kameneva et al., 2011; Maturana et al., 2014).

2. The exclusion of (I_{CaT}) from the intracellular calcium ion concentration $[Ca^2+]i$ Eq. 28, consistent with most RGC electrical stimulation modelling studies (Fohlmeister and Miller, 1997*a*; Kameneva et al., 2011; Maturana et al., 2014).

3. The use of the Ca-activated potassium channel conductance formula 29, with the power exponent equal to 1 (Fohlmeister and Miller, 1997*b*).

Model implementation was validated by comparing with the experimental data of Guo et al. (2016) study (Figures 2 & 3), by applying intracellular current injections to the soma of the COMSOL OFF & ON RGC models. The modified cable equation derived in chapter 4 was used to describe electric excitation and propagation within the RGCs.

Figs. 6.2 and 6.3 show the results of intracellular current injection in the OFF and ON RGCs in COMSOL Multiphysics. Various depolarising and hyperpolarising intracellular electrical stimulation amplitudes were injected in the soma of both OFF and ON RGCs over a 500 ms stimulus duration interval. Results of depolarising current injection for OFF and ON RGCs is displayed in Figs. 6.2 a & 6.3 a respectively. Moreover, the reconstructed OFF RGC model was able to reproduce the rebound excitation when a hyperpolarising current (for example, -38 μA) was applied, as seen in Fig. 6.2 b whereas the ON RGC could not generate the rebound excitation, consistent with the experimental data presented in figures 2 &3 of (Guo et al., 2016) study, as shown in Fig. 6.3 b. The reconstructed models in COMSOL Multiphysics were able to regenerate almost a similar number of spikes in response to hyper- and depolarising current compared to the experimental data presented in figures 2 &3 of (Guo et al., 2016) study (Fig. 6.2 c & Fig. 6.3 c). There was a slight difference in the number of spikes particularly for

the ON RGC, which has large dendrites.

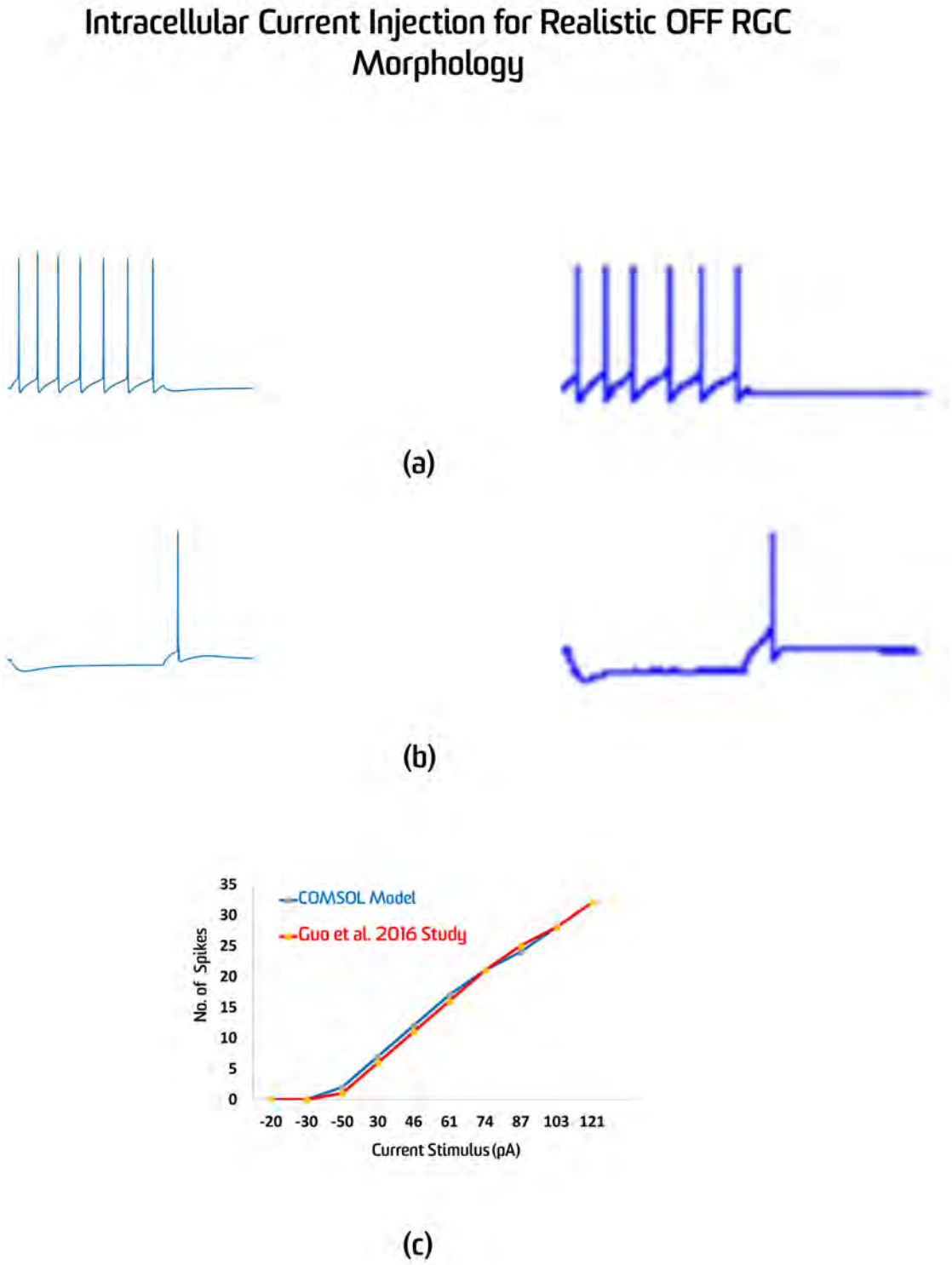

Figure 6.2: OFF RGC intracellular stimulation results. (a) The example of depolarising current injection at the soma (30 μA) in the COMSOL model (left) and the experimental data presented in figure 3 of Guo et al., (2016) study (right). (b) The example of hyperpolarising current injection at the soma (-38 μA) in the COMSOL model (left) and the experimental data presented in figure 3 of Guo et al., (2016) study (right). (c) Comparison of the total number of spikes obtained with every current injection in the experimental data presented in figure 3 of Guo et al., (2016) study and COMSOL model.

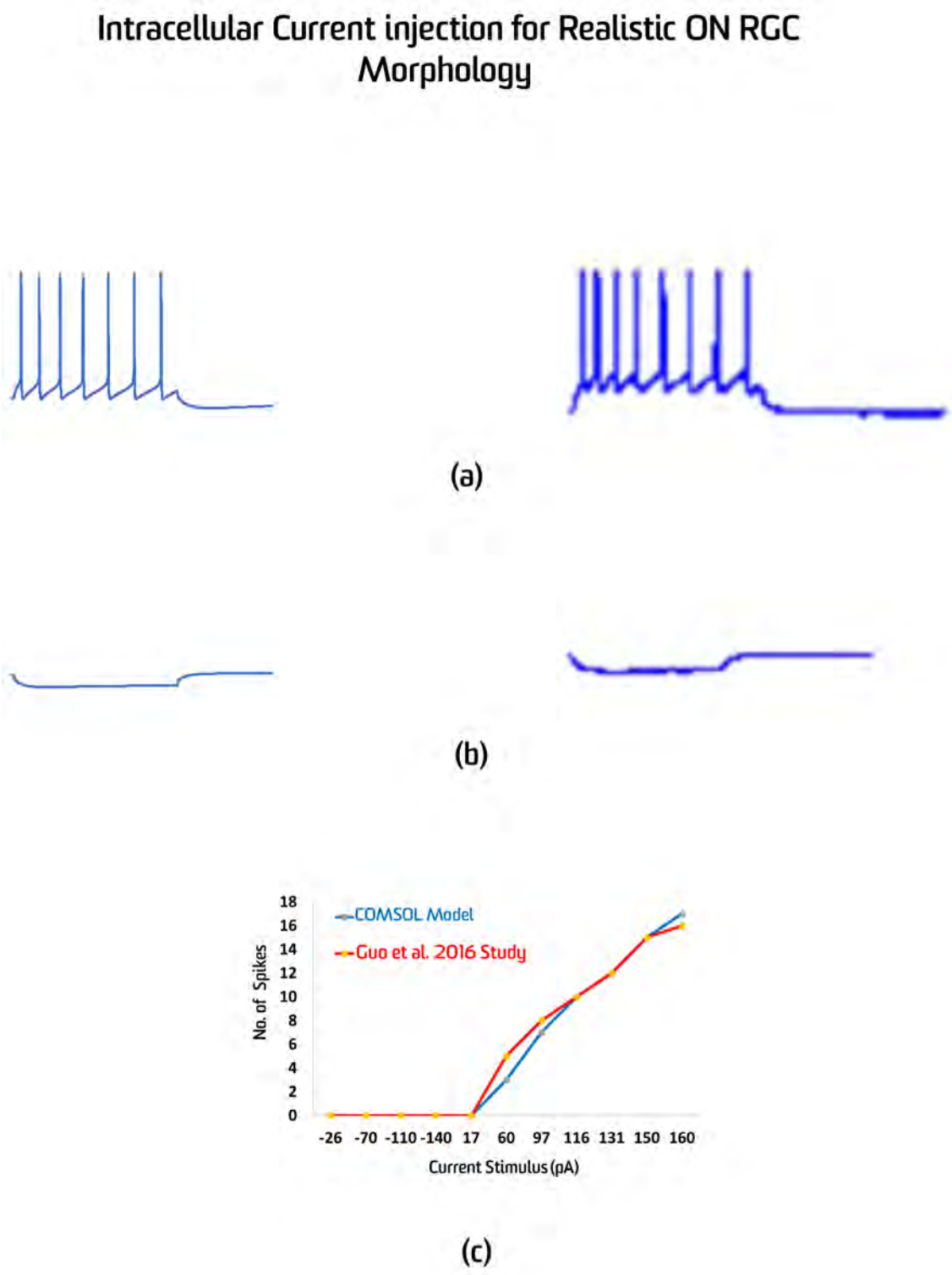

Figure 6.3: ON RGC intracellular stimulation results. (a) The example of depolarising current injection at the soma (97 μA) in the COMSOL model (left) and the experimental data presented in figure 2 of Guo et al., (2016) study (right). (b) The example of hyperpolarising current injection at the soma (-70 μA) in the COMSOL model (left) and the experimental data presented in figure 2 of Guo et al., (2016) study (right). (c) Comparison of the total number of spikes obtained with every current injection in the experimental data presented in figure 2 of Guo et al., (2016) study and COMSOL model.

6.1.1.2 Extracellular Electrical Stimulation Model of Rabbit ON & OFF RGCs

We extended the previous ON/OFF RGC models to simulate extracellular electrical stimulation of the morphologically-realistic RGCs in COMSOL. The RGCs, consisting of soma, dendrites, axon hillock, axon initial segment (AIS) and axon, were placed inside a semi-ellipsoid domain representing the extracellular medium for both models.

A hexagonal arrangement of circular disc electrodes was implemented, each being 190 μm in radius with 730 μm centre-centre spacing (Fig. 6.4), were taken from the *in vivo* study done by (Matteucci et al., 2013). These electrodes dimensions were chosen to be closer to the realistic electrodes' dimensions used in existing retinal prostheses. The central electrode was the active electrode, with the surrounding six electrodes being the return electrodes, set to ground. A cathodic monophasic current stimulus 0.5 ms in duration was used to provide an easier comparison of our results with several published retinal electrical stimulation studies. Current thresholds were applied to both models, which were 160 μA and 350 μA for the OFF and ON RGC models respectively.

To map spatial activation, the RGC was positioned arbitrarily to about 120 μm from the plane of the electrodes at each of the 25 sites of a 5 x 5 grid of points, spaced 500 μm X 500 μm apart (Figs. 6.5a & 6.6a). For each position, one set of simulations was obtained when the axon was oriented along the x-axis while another set was taken with axon oriented along the y-axis. The results when the axon was oriented along the y-axis were identical with those obtained when the axon was oriented along the x-axis. So, for simplicity, only the results of the axon oriented along x-axis are presented.

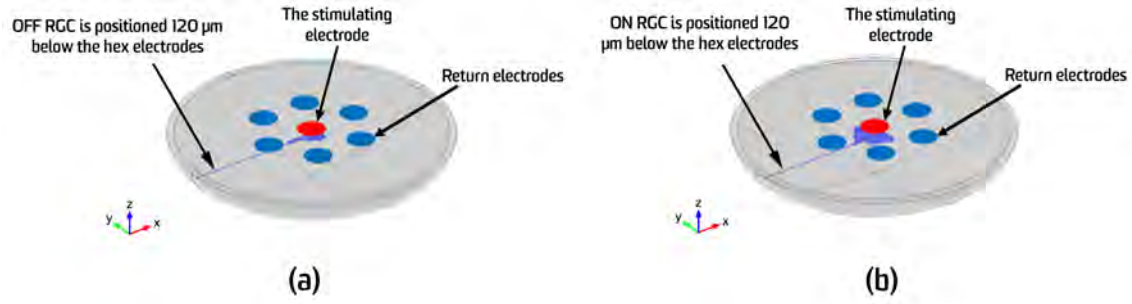

Figure 6.4: Extracellular electrical stimulation model settings for the morphologically-realistic OFF (a) and ON (b) RGCs.

Figs. 6.5a & 6.6a display the 25 placement sites for the OFF & ON RGCs when the axon was oriented parallel to the x-axis. Both OFF & ON RGCs were activated at only 3 out of 25 sites, as seen in Figs. 6.5b & 6.6b respectively. For each of these three sites, action potential traces from various compartments of the discrete OFF & ON RGCs are presented in Figs. 6.5c & 6.6c. Initiation of the action potential was in the AIS and propagated into the other compartments when the OFF or ON RGC was directly beneath the centre of the active electrode. The other two sites of activation were when the active electrode was above the axon: the action potential began at the axon and then propagated to the other compartments. Snapshots of the spatial activation of the OFF RGC discrete model has been shown in (Fig. 6.8), which the action potential was initiated in the AIS at 1.1 ms (0.5 ms after termination the stimulus) when the electrode was located above the RGC whereas the action potential was initiated in the axon at 1.1 ms when the electrode was far away from the RGC. Similarly, (Fig. 6.9) shows snapshots of the spatial activation of the ON RGC discrete model, which the action potential was initiated in the AIS at 0.6 ms (at the termination the stimulus) when the electrode was located above the RGC whereas the action potential was initiated in the axon at 0.6 ms when the electrode was far away from the RGC. One representative example of the 22 non-activated sites for the OFF & ON RGC are presented in Fig. 6.7 for discrete and continuum modelling approaches.

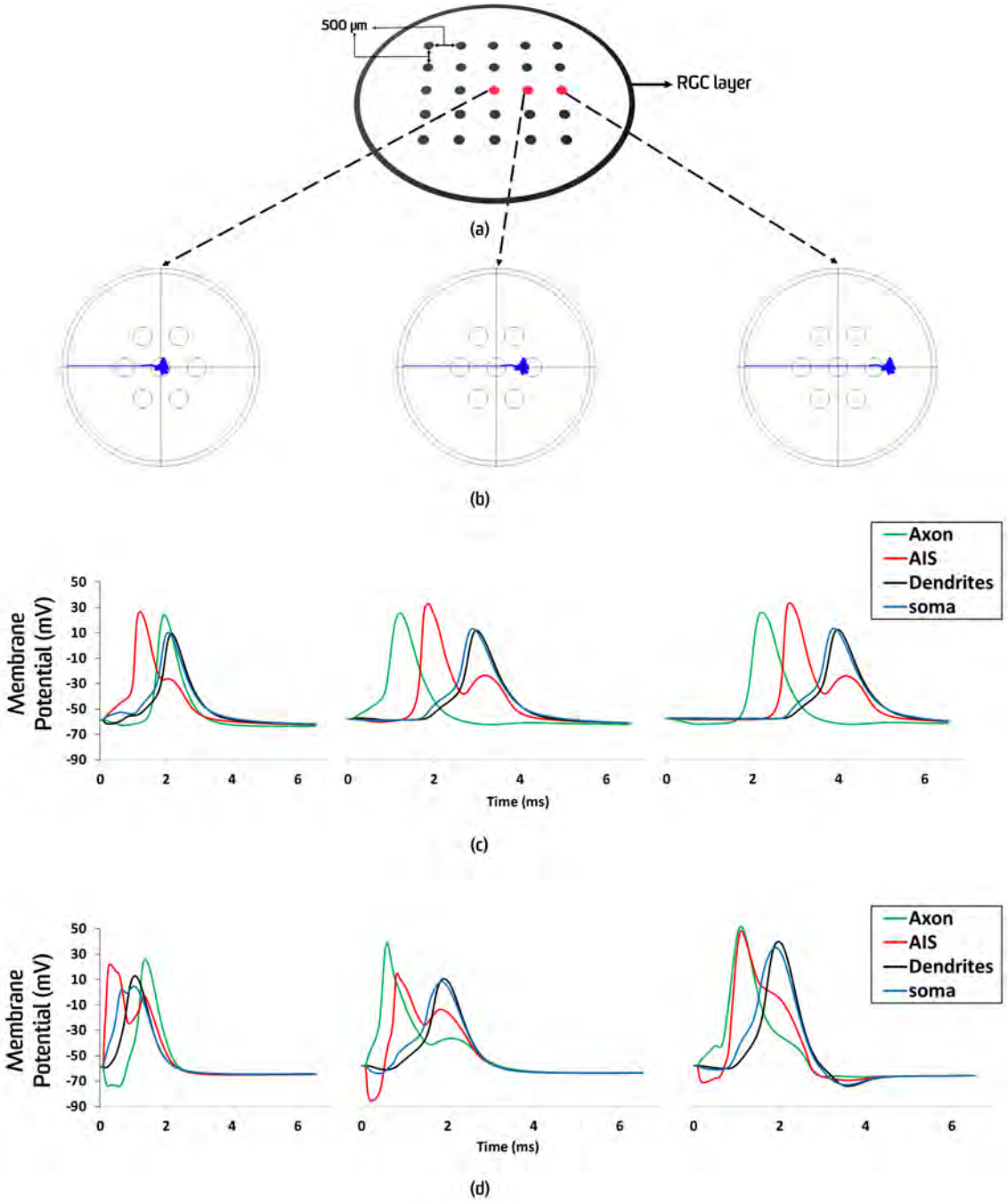

Figure 6.5: Comparison of spatial activation in OFF RGC simulated using discrete and continuum computation approaches in response to extracellular electrical stimulation. In both cases, the axon was oriented along the x-axis. (a) The 25 point grid representing the locations where RGC spatial activation was measured. (b) The sites of RGC activation. For each of these three sites, action potential traces from various neuronal compartments utilising the (c) discrete and (d) continuum modelling approaches are presented. A 160 μA was injected via the stimulating electrode for both modelling approaches.

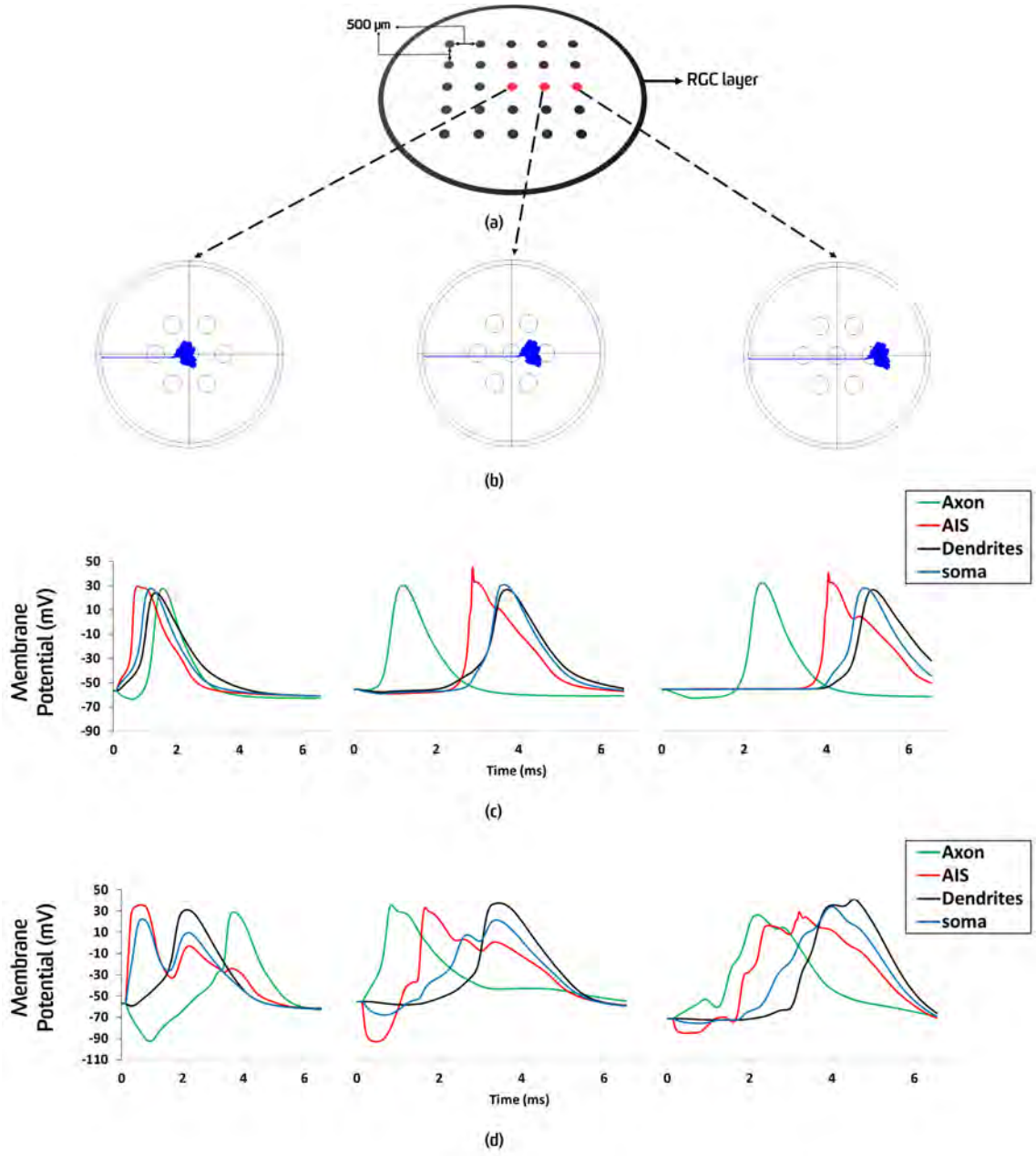

Figure 6.6: Comparison of spatial activation in ON RGC simulated using discrete and continuum computation approaches in response to extracellular electrical stimulation. In both cases, the axon was oriented along the x-axis. (a) The 25 point grid representing the locations where RGC spatial activation was measured. (b) The sites of RGC activation. For each of these three sites, action potential traces from various neuronal compartments utilising the (c) discrete and (d) continuum modelling approaches are presented. A 350 μA was injected via the stimulating electrode for both modelling approaches.

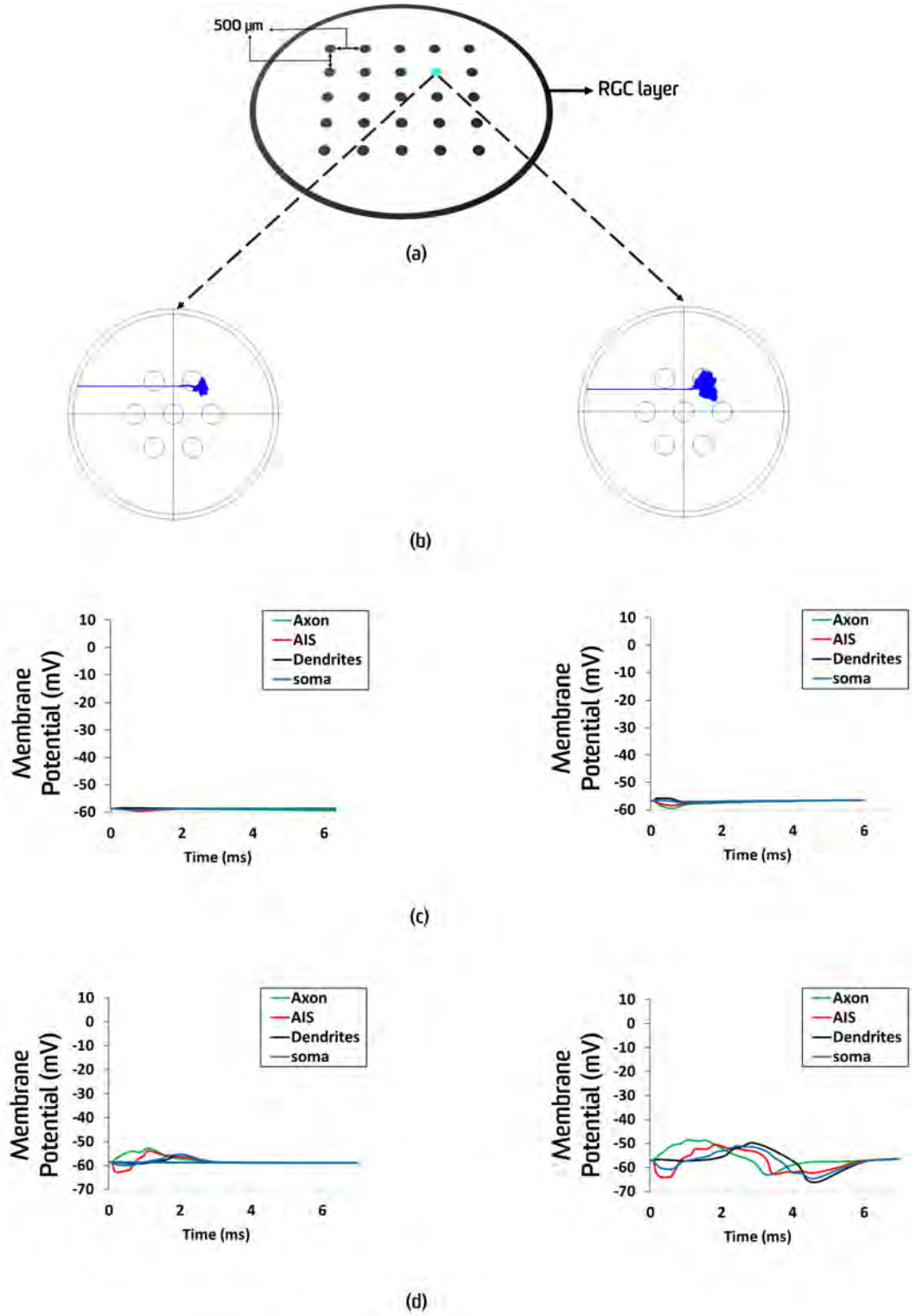

Figure 6.7: A representative example of one of the 22 non-activated sites of OFF & ON RGC discrete and continuum computation approaches in response to extracellular electrical stimulation. (a) The total of 25 locations that the response of RGC was measured over (b) Location example of a non-activated OFF (left) and ON (right) RGC. (c) Action potential traces from various neuronal compartments of OFF (left) and ON (right) RGC discrete models. (d) Action potential traces from various neuronal compartments of OFF (left) and ON (right) RGC continuum models. A 160 μA was used for OFF RGC models whereas 350 μA for ON RGC models.

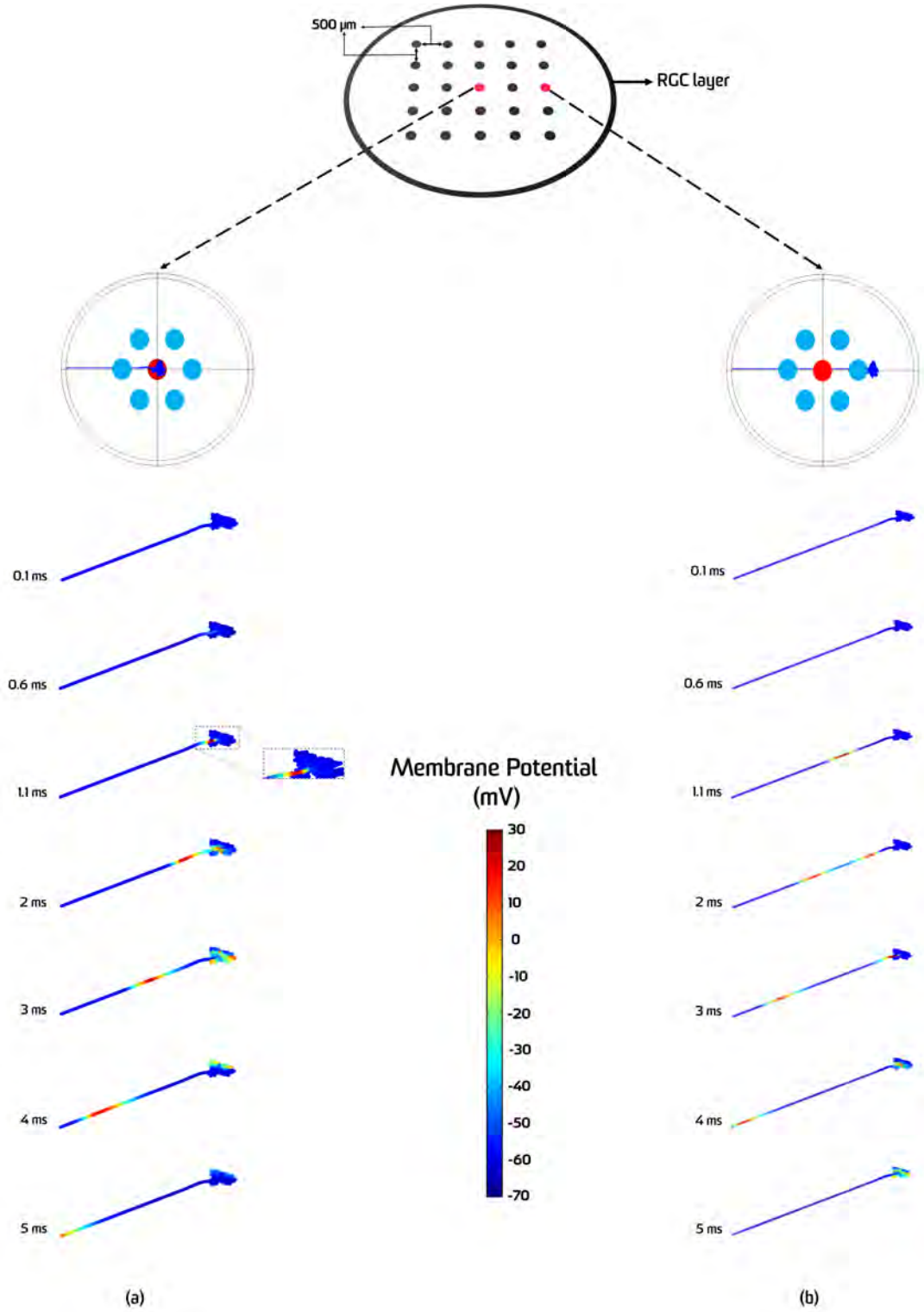

Figure 6.8: Spatiotemporal activation of the discrete OFF RGC model. (a) Initiation of the action potential was at 1.1 ms at the AIS when the electrode was located above the RGC. (b) Initiation of the action potential was at 1.1 ms at the axon when the electrode was located far away from the RGC. A 160 μA was injected via the stimulating electrode for both cases. Red electrode is the stimulating electrode whereas the blue six surrounding electrodes connected to ground.

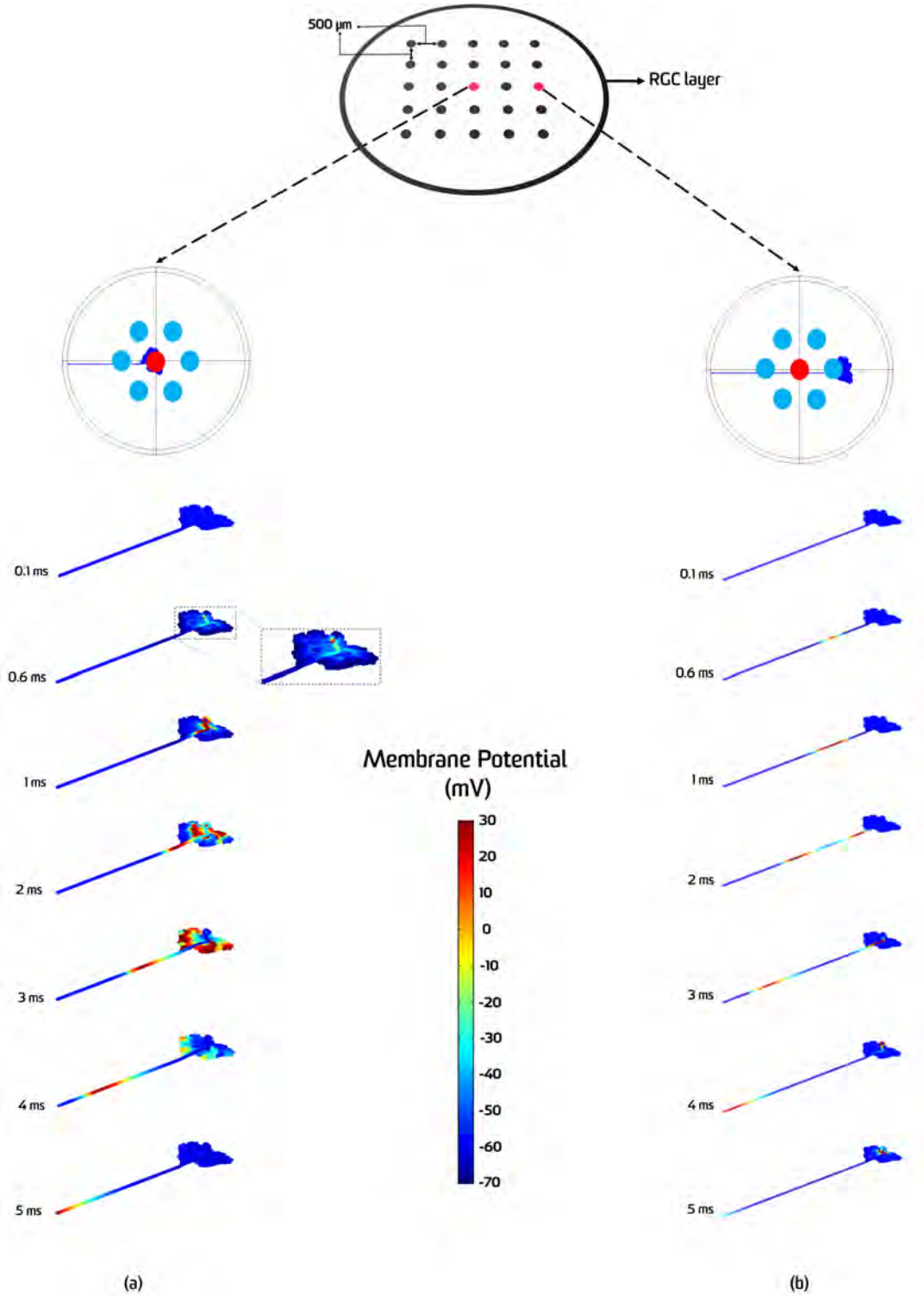

Figure 6.9: Spatiotemporal activation of the discrete ON RGC model. (a) Initiation of the action potential was at 0.6 ms at the AIS when the electrode was located above the RGC. (b) Initiation of the action potential was at 0.6 ms at the axon when the electrode was located far away from the RGC. A 350 μA was injected via the stimulating electrode for both cases. Red electrode is the stimulating electrode whereas the blue six surrounding electrodes connected to ground.

6.1.2 Reducing the Morphologically-Realistic Rabbit OFF & ON RGC Models to Four-Compartment Models (Stage 2)

The morphologically-realistic rabbit OFF & ON RGC models were composed of thousands of compartments, each classified as one of: dendrites, soma, axon hillock, axonal initial segment (AIS), and axon, based on ion channel expression. For further simplicity, we combined the soma and axon hillock into one compartment (called hereafter the soma) due to their identical maximum ion channel conductance values and channel kinetics. We implemented a Matlab (Mathworks, USA) script to reduce the morphologically-realistic RGC to a four-compartment point model. Between each two adjacent compartments, there are two internal conductances to describe the influence of each compartment on its neighbour, as shown in Fig. 6.10. The biophysical properties of each compartment will play a crucial role in determining the magnitude of its electrotonic influence on its neighbouring compartments. For each RGC model, a total of six optimised conductances were used to connect between all RGC compartments as listed in Table 6.1.

Table 6.1: OFF and ON RGC inter-compartment conductances.

OFF RGC		ON RGC	
Conductance	Value (mS/cm^2)	Conductance	Value (mS/cm^2)
g_{12}	3	g_{56}	1
g_{21}	15	g_{65}	9.5
g_{23}	3	g_{67}	3
g_{32}	15	g_{76}	29.5
g_{34}	15	g_{78}	7.5
g_{43}	3	g_{87}	0.75

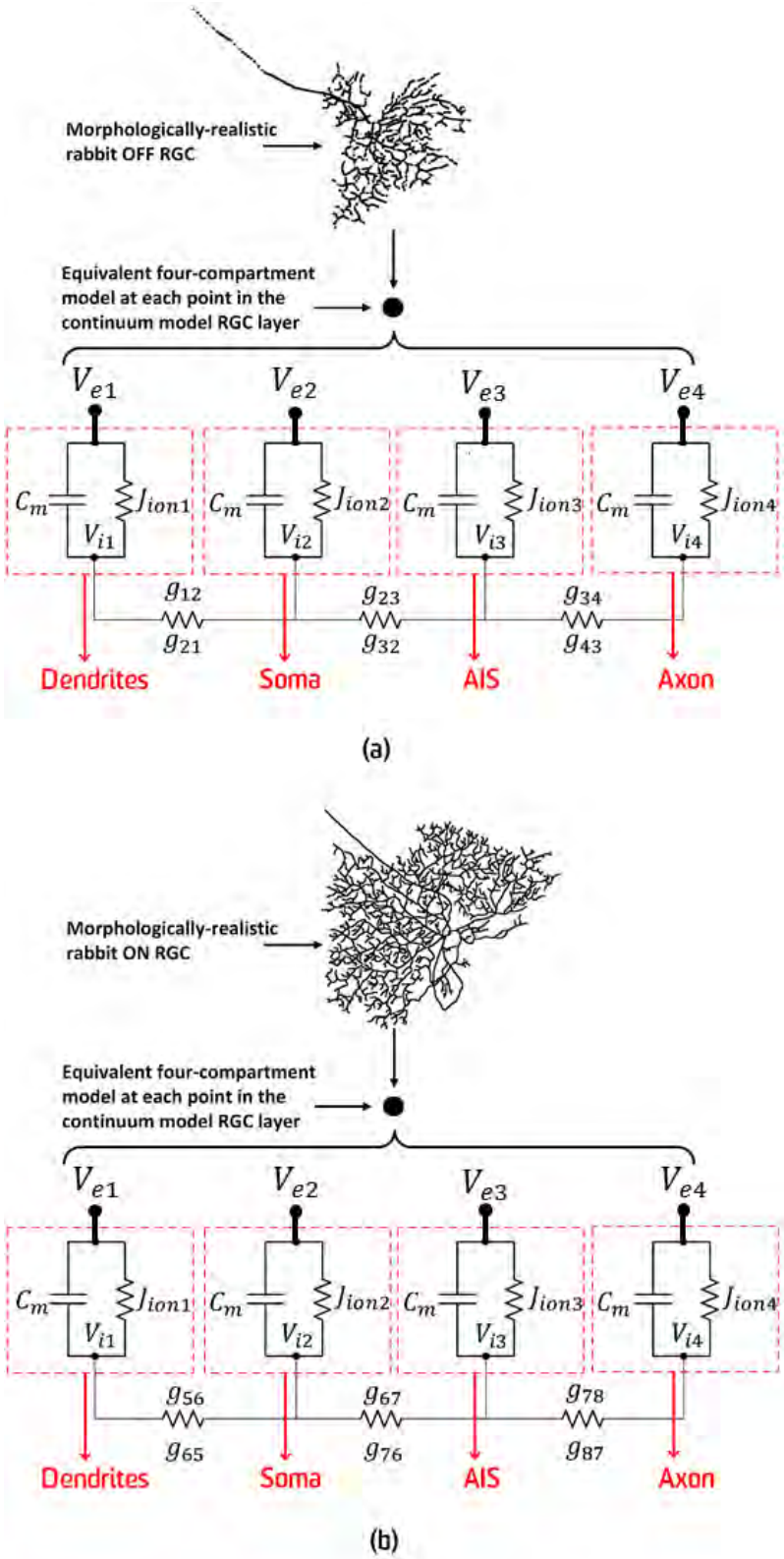

Figure 6.10: Schematic diagram of four-compartment representation of OFF (a) and ON RGC (b) circuitry at each point in the RGC layer of the continuum model after reducing the full morphologically-realistic RGC into a four-compartment point model. V_e and V_i denote the extracellular and intracellular potentials respectively, C_m is the membrane capacitance per unit area and J_{ion} is the ionic current per unit area. g represents the internal conductances between the four compartments.

A combination of global optimisation algorithms (genetic algorithm, pattern search and simulated annealing) was used to minimise the cost function, which was the total spike number difference between the four compartment and realistic-morphologically models. Using the total number of spikes in the cost function for model reduction is well-known, as seen in (Friedrich et al., 2014) and (Van Geit et al., 2016). The use of intracellular current injections at different locations of the RGC in the cost function is more appropriate than spike count in response to extracellular stimulation since intracellular stimulation more directly depends on the intrinsic properties of the cell we wish to reduce. Therefore, in order to accomplish this reduction approach, a multi-dataset optimisation approach was used: (1) the current was injected intracellularly in the soma, and the spike number was counted in each compartment for both the full realistic-morphologically and reduced models. (2) similarly, current was injected in the AIS, and the number of spikes in each compartment was determined, to ensure we obtained the same spike numbers with different current injections in different locations.

Fig. 6.11a & b (left) are examples of the number of spikes that were obtained when the same current stimulus was injected in the soma for both the morphologically-realistic RGC in COMSOL and the optimised reduced models in Matlab for the OFF & ON RGCs respectively. Fig. 6.11a & b (right) demonstrates the capability of the compartmental equations (reduced model), implemented in Matlab, to reduce the membrane potential responses of morphologically-realistic models with thousands of compartments for both OFF & ON RGCs. Also, we compared the reduced model with the morphologically-realistic RGC model by injecting different current amplitudes in another location, namely the AIS, and counted the number of spikes generated in each compartment. The results of AIS simulations were similar to those obtained with soma simulations. (In the Appendix D, we show the comparison between morphologically-realistic and reduced models during injecting the current at the AIS for an OFF RGC.) ”

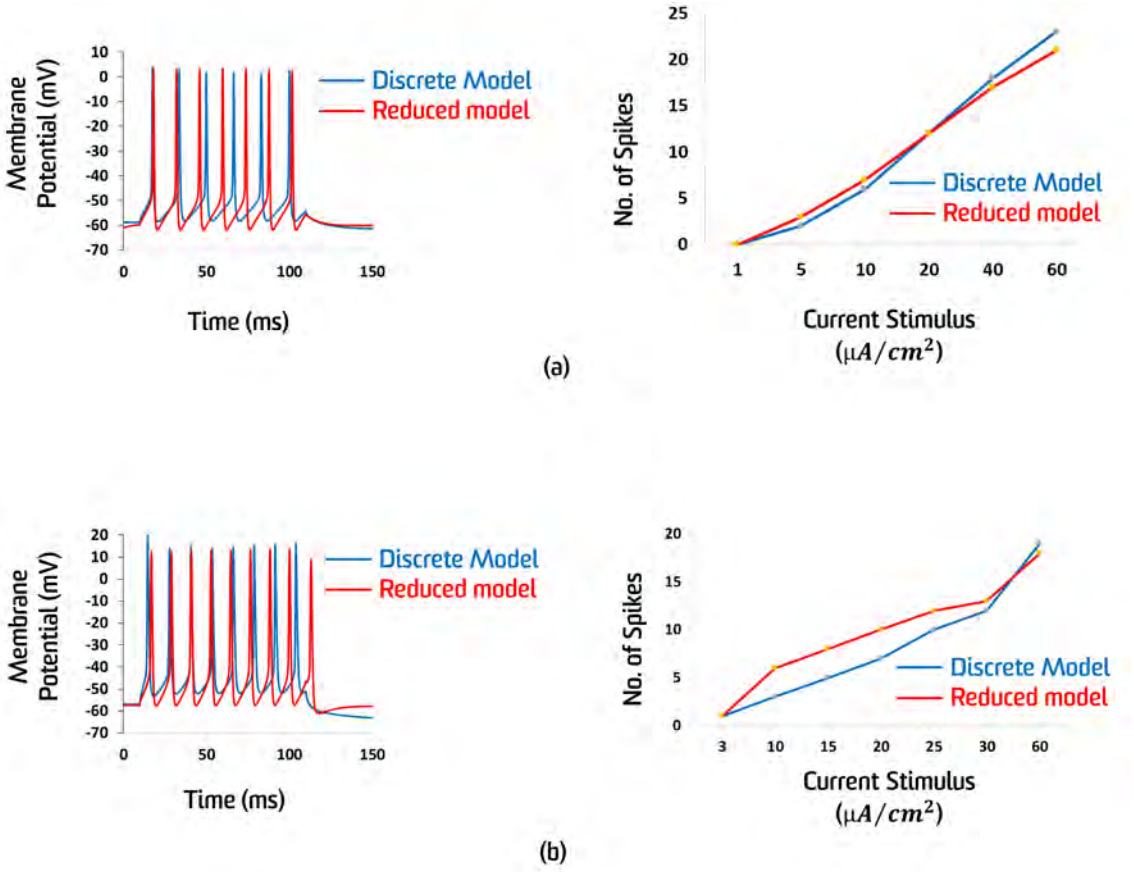

Figure 6.11: Comparison of the responses of the morphologically-realistic (discrete) OFF & ON RGCs and the reduced four-compartment models to intracellular stimulation. (a) Comparison between morphologically-realistic OFF RGC and reduced models in terms of the number of spikes for different depolarising current injections in the soma (right) and one example of 10 $\mu A/cm^2$ somatic injections in both models (left). (b) Comparison between morphologically-realistic ON RGC and reduced models in terms of the number of spikes for different depolarising current injections in the soma (right) and one example of 20 $\mu A/cm^2$ somatic injections in both models (left). In all cases, depolarising current injections were delivered into the soma for 100 ms.

6.1.3 Continuum Model of Extracellular Electrical Stimulation of Rabbit OFF and ON RGC (Stage 3)

A 3D finite element model of retinal electrical stimulation consisting of vitreous fluid and ganglion cell layer was implemented in COMSOL Multiphysics (Fig.6.12). The settings of this model were identical those of the first stage (discrete model), with the exception of the following: instead of the presence of a discrete morphologically-realistic RGC, a continuum RGC layer was incorporated. The four compartmental equations and the six values of internal conductances, determined from stage 2, were used to represent a cell at each point of the layer to simulate the extent of spatial activation, instead of using a discrete representation of each cell. To allow comparison of the two approaches, the responses of rabbit OFF & ON RGCs in the continuum model were sampled at the same 25 sites utilised in the first stage (discrete model).

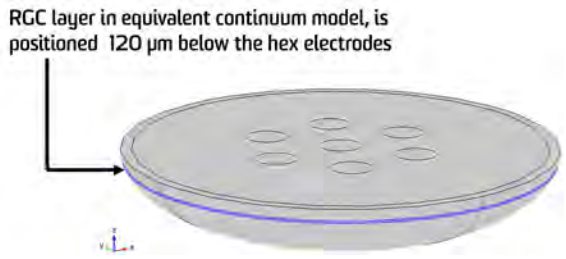

Figure 6.12: Extracellular electrical stimulation of OFF & ON RGCs using the continuum modelling approach.

Fig. 6.5d shows that the OFF RGC continuum model reproduced the same results as the OFF RGC discrete model (Fig. 6.5c), in which RGC activation occurred at only the same 3 out 25 locations for the same stimulus current (160 μA). Moreover, activation of the RGC directly below the active electrode occurred by AIS activation first, whereas at the other two sites axonal activation occurred first. Similarly, in Fig. 6.6d, the ON RGC continuum model reproduced the same

results as the ON RGC discrete model (Fig. 6.6c) in terms of the same sites of activation (3 out 25 locations) and the site of action potential initiation, both using the same current stimulus (350 μA).

Significantly, in terms of computational requirements, continuum models are more efficient than discrete models. For example, the OFF RGC continuum model which represents thousands of RGCs required 1.52 GB of random access memory (RAM) and less than 30 minutes to solve for a 7 ms simulation period, compared to a discrete model with only five RGCs, which needed about 70 minutes and 7.53 GB of RAM to be solved with identical simulation and solver settings.

6.2 Continuum Model of the Combined Rabbit OFF & ON RGC

After validating each RGC model separately, we combined the OFF and ON RGC multi-domain continuum models into one model. This approach will be beneficial for optimising electrode settings in retinal prostheses with various scenarios of electrical stimulation in the presence of two prominent kinds of retinal neurons: OFF and ON RGCs. The response of each RGC type to the two current stimulus amplitudes (160 μA and 350 μA monophasic cathodic constant current), used to validate the OFF and ON RGC multi-domain continuum models, is shown in Figs. 6.13 & 6.14.

As mentioned earlier, both OFF and ON RGC multi-domain continuum models were activated only in 3 out of 25 locations: the first position was directly under the stimulating electrode, whilst the other two locations were immediately on the right of the first position along the x-axis. In Fig. 6.13, the ON RGC was activated over the first two sites, whereas the third site did not activate, since the injected current stimulus was not enough to excite it. Furthermore, the action potential shape at the first site was slightly different to that obtained when 350 μA was injected (Fig. 6.6d). The response of the OFF RGC over the three sites of activation

was explored by using 350 μA as the current amplitude in Fig. 6.14 . The axon was inhibited at the first site, in which the RGC was located under the centre of the active electrode. The second site for the RGC was close to the edge of the electrode, and shows inhibition for all compartments except the axon. The third site was not affected by this higher current injection.

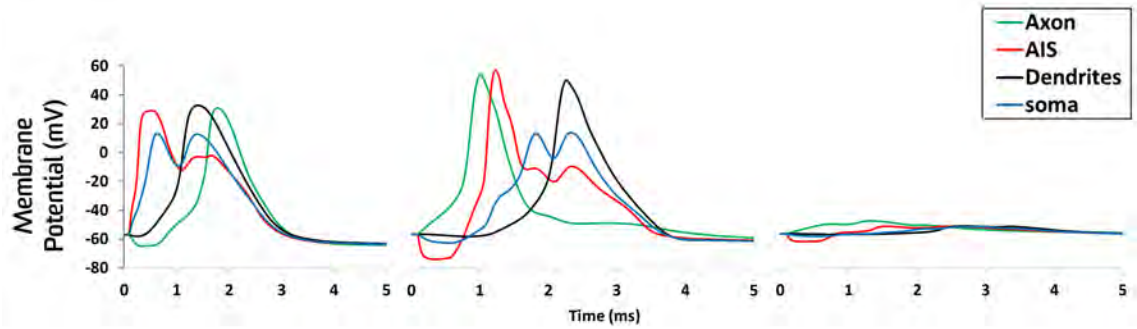

Figure 6.13: Spatial activation of ON RGC in the combined model comprised of both OFF and ON RGCs, following injection of 160 μA monophasic cathodic current stimulus delivered via the hex electrodes for the three sites of activation.

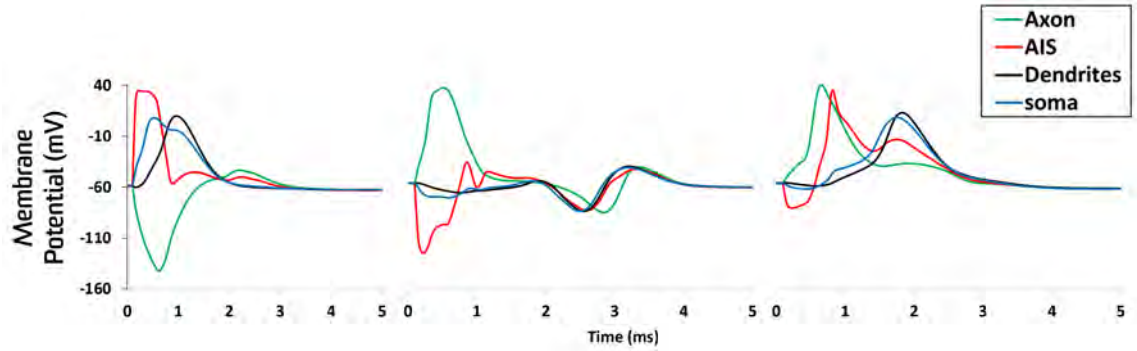

Figure 6.14: Spatial activation of OFF RGC in the combined model comprised of both OFF and ON RGCs, following injection of 350 μA monophasic cathodic current stimulus delivered via the hex electrodes for the three sites of activation.

6.3 Validation against *in vitro* experimental data

The incorporation of retinal layer anatomical and electrical properties is essential for developing computational models of retinal electrical stimulation. This kind of information will be beneficial for enhancing the design of visual prostheses through optimising various temporal and spatial features such as current threshold, activation area, and best location of stimulus electrodes. Unfortunately, experimental studies that have measured the resistivity of various retinal layers are limited. Layer thicknesses and electrical properties have been characterised in frogs by Karwoski et al. (1985) and in rabbits by Karwoski and Xu (1999) . More recently, retinal layer resistivity profiles for both rats and embryonic chicks have been determined by adopting a new technique Peak Resistance Frequency (PRF) (Kasi et al., 2011).

The retinal layer models presented in this thesis typically consist of ten layers; in some cases not all of these are used. These layers include the vitreous, ganglion cell layer (GCL), inner plexiform layer (IPL), inner nuclear layer (INL), outer plexiform layer (OPL), outer nuclear layer (ONL), subretinal space layer (SRS), retinal pigment epithelium (RPE), choroid, and sclera.

The representation of electrical properties of retinal layers by pure conductivities was adopted in many other experimental studies (Karwoski et al., 1985; Karwoski and Xu, 1999; Kasi et al., 2011) as well as modelling studies (Abramian et al., 2015; Cao et al., 2015; Joarder et al., 2011; Loizos et al., 2016). The ON & OFF RGC ionic models used in this thesis were formulated from rabbit *in vitro* experiments. As a result, we used electrical properties and thickness of retinal layers from available rabbit information as much as possible. Retinal conductivities and layer thicknesses were largely derived from the work of Karwoski and Xu (1999). Choroid and sclera thicknesses were taken from Brown et al. (2009) and Olsen et al. (2002) respectively. The thickness and conductivity of vitreous and retinal pigment epithelium (RPE) were obtained from Dokos et al. (2005)

and Karwoski et al. (1985), respectively. The conductivities of choroid and sclera were estimated from Brindley (1956) and Ogden and Ito (1971) respectively. A list of retinal layer conductivities and thickness parameters is given in Table 6.2 .

Table 6.2: Retinal layer thickness and electrical conductivity values.

Layer	***Conductivity*** $(S.m^{-1})$	***Thickness*** (μm)
Vitreous	1.28	50- 400
Ganglion Cell	0.02262	22
Inner Plexiform	0.03717	23
Inner Nuclear	0.01277	27
Outer Plexiform	0.019	16
Outer Nuclear	0.01244	31
Subretinal Space	0.04831	40
Retinal Pigment Epithelium	0.0147	20
Choroid	0.030874	200
Sclera	0.019	240

6.3.1 Validation against *in vitro* epiretinal stimulation experimental data

We developed a model of the retina and calibrated against epiretinal current stimulation threshold data of rabbit OFF RGCs (Jensen et al., 2005*b*). The model consisted of a three-dimensional finite element formualtion composed of bulk vitreous fluid, multiple retinal layers, choroid and sclera (Fig. 6.15). A monopolar circular disc electrode configuration was employed as a stimulating electrode, 500 μm in diameter, positioned in the vitreous at various distances above the middle of the RGC layer (50 to 400 μm). The return electrode (surface area 1.2 cm^2) was set to ground (zero volts) and placed beneath the sclera. A monophasic cathodic current pulse 1 ms in duration was delivered through the stimulating electrode. All retinal layer conductivities and thicknesses are listed in Table 6.2 .

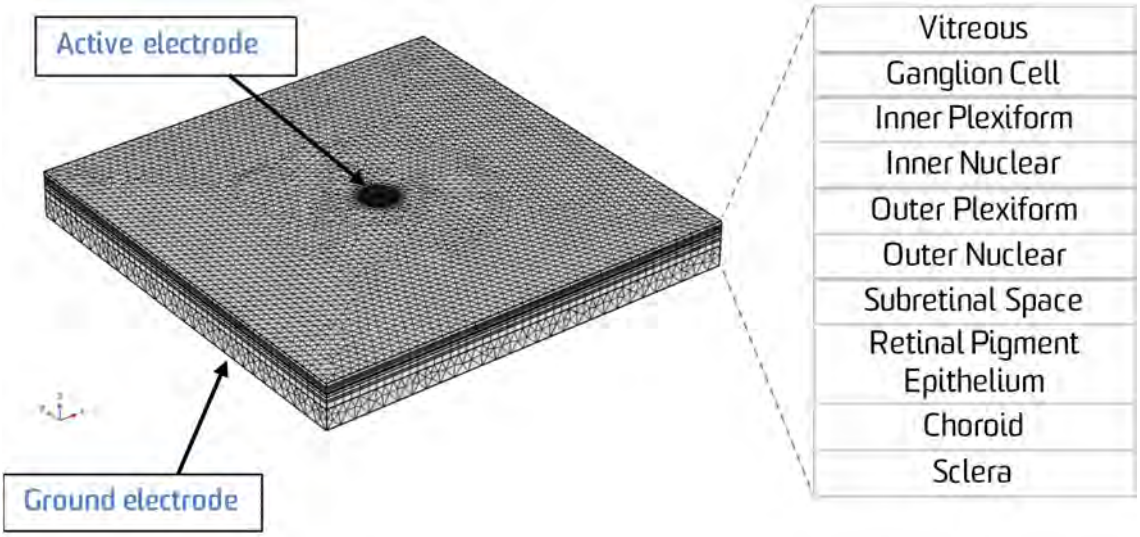

Figure 6.15: Epiretinal extracellular electrical stimulation model.

The experimental configurations of Jensen et al. (2005b) were simulated. We reproduced the relationship between threshold current required to elicit action potentials and stimulating electrode distance above the retinal surface. Simulated current thresholds were within the range of experimental values obtained by Jensen et al. (2005b) and often close to the median thresholds (Fig. 6.16). A bisection search method was used to determine threshold stimulus current amplitude with an error tolerance of 1 μA.

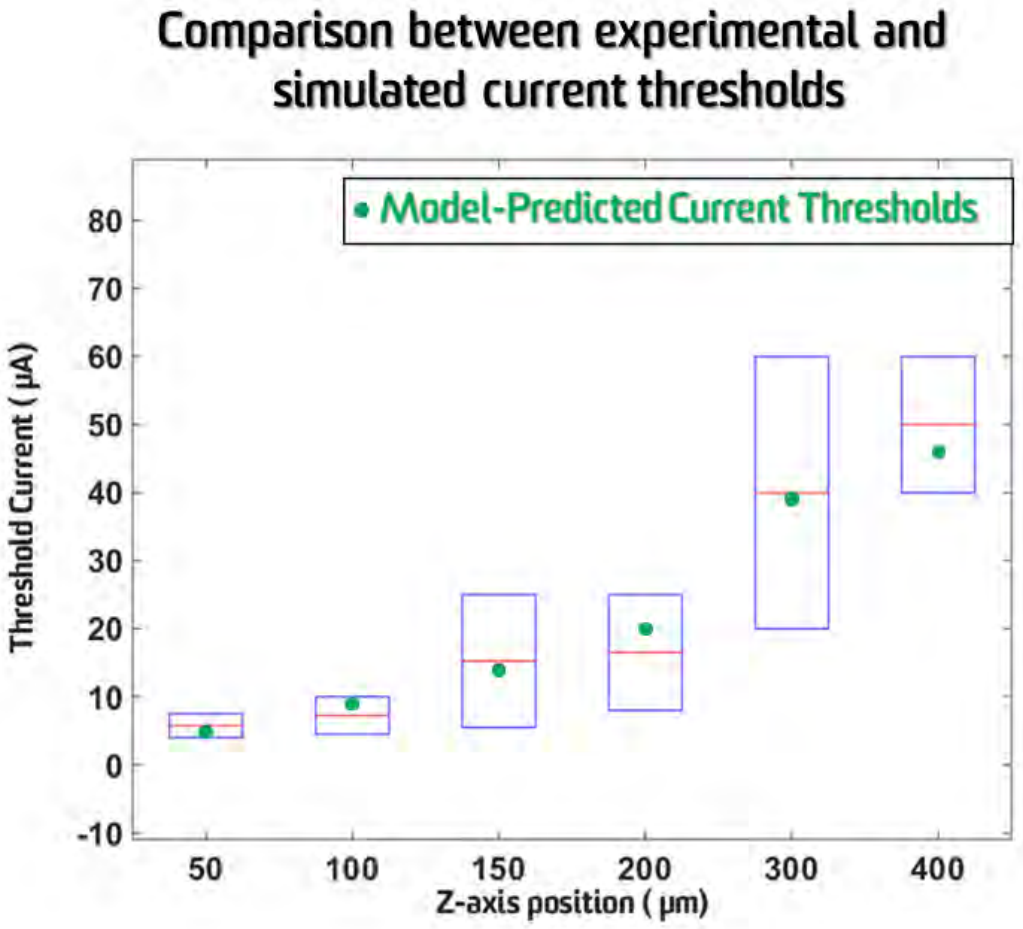

Figure 6.16: Simulated current thresholds of OFF RGCs compared with the experimental data of Jensen et al. (2005b). Horizontal midlines within each box represent the experimental median, whilst the top and bottom edge of each box denote the highest and lowest threshold current respectively. Z-axis position represents the distance between stimulating electrode and RGC layer.

6.3.2 Validation against *in vitro* subretinal stimulation experimental data

To further demonstrate the predictive power of our continuum models of OFF & ON RGCs, we validated against a recent published experimental study conducted on rabbit RGCs stimulated subretinally (Tsai et al., 2009). In these simulations, all layers used for the epiretinal approach were used except: retinal pigment epithelium, choroid and sclera (Fig. 6.17). All experimental work procedures of the Tsai et al. (2009) study were followed to obtain an accurate comparison between our finite element model simulations and experimental thresholds. A monopolar electrode configuration was used for delivering the extracellular potentials consisting of a 25 μm diameter stimulating electrode placed beneath the subretinal space layer. Replicating experimental conditions, the returning electrode was positioned far away from the stimulating electrode at distance of 2 cm. A charge-balanced cathodic-first biphasic pulse was applied without interphase delay. Figure 3 of the Tsai et al. (2009) study summarised and compared current injections thresholds for various rabbit RGCs subtypes with a range of pulse durations to evoke short-latency spikes. The 3D continuum OFF & ON RGCs model simulations were compared with current thresholds of OFF & ON RGCs from that figure.

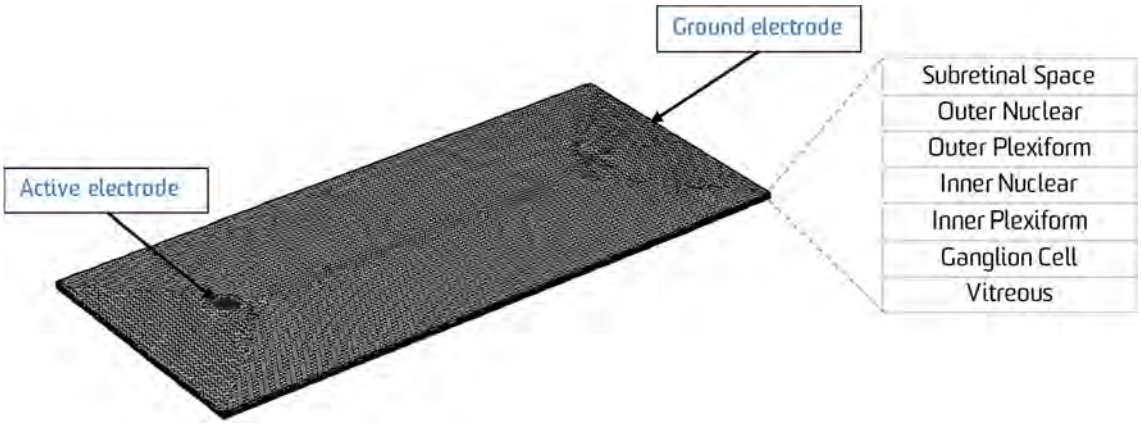

Figure 6.17: Subretinal extracellular electrical stimulation model.

The effect of pulse duration on threshold current during subretinal electrical stimulation was reproduced. Simulated current thresholds were within the range of experimental values obtained by Tsai et al. (2009) for OFF & ON RGCs as shown in Fig. 6.18a & b respectively.

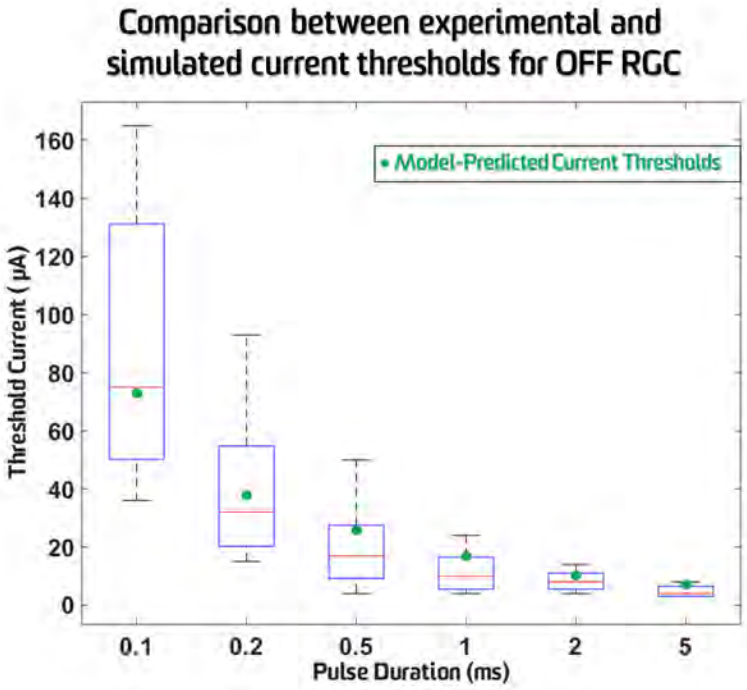

(a)

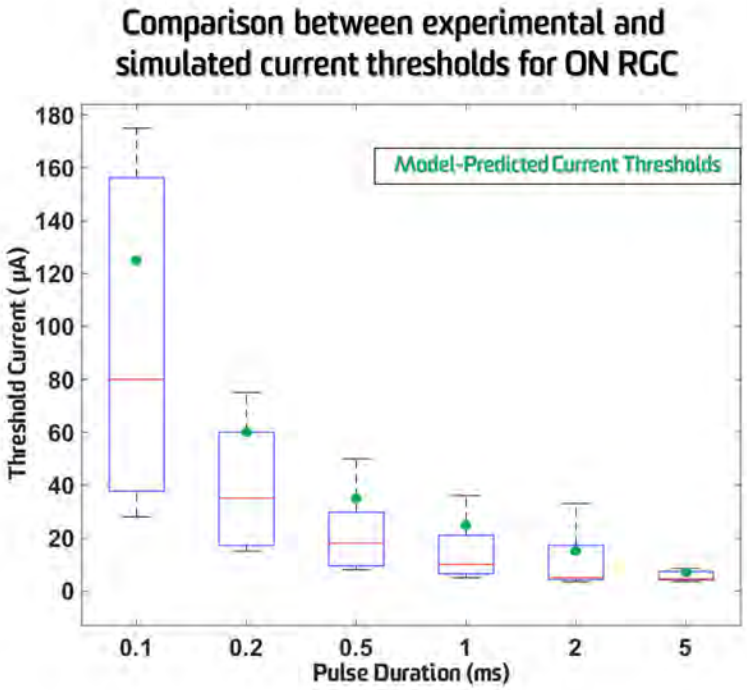

(b)

Figure 6.18: Simulated current thresholds of (a) OFF and (b) ON RGCs compared with the experimental data of Tsai et al. (2009). The box-and-whisker plot indicates (from top to bottom) the maximum, third quartile, median, first quartile, and minimum experimentally-determined values.

6.4 Discussion

Continuum models of retinal electrical stimulation have increased our knowledge of the response of bulk retina to electrical stimulation. In a recent paper, current thresholds required to stimulate RGCs were investigated in the presence of retinal layers and with three different electrode locations (epiretinal, subretinal, and suprachoroidal) (Joarder et al., 2011). Another study simulated and compared various current stimulation strategies, and investigated the retinal network effects on RGC activation (Yin et al., 2010). A novel continuum model of retinal electrical stimulation was developed and validated against both a developed version of the discrete RGC model of the Guo et al., (2016) study and experimental studies (Jensen et al., 2005*b*; Tsai et al., 2009).

6.4.1 Validation against discrete computational model

In this chapter, we validated the continuum model against a developed version of the discrete RGC model of the Guo et al., (2016) study, incorporating detailed ionic currents and realistic morphological architecture. The reconstructed OFF and ON RGC intracellular electrical stimulation results were almost similar to the experimental data of Guo et al., (2016) study as seen in Figs. 6.2 and 6.3. Point models are a class of simplified models that reduce the full morphologically-realistic RGC with thousands of compartments into a point with limited number of compartments (four compartments in our model) connected to each other by a set of inter-compartmental conductances. Hence, more detailed features, such as the variation between discrete and point models in terms of AP peak and onset in each compartment, as well as the number of spikes as seen in Figs. 6.5 and 6.6, are expected. This variation in timing also occurs between different compartments of discrete models, for example between proximal and distal dendrites. However, the continuum model was able to reproduce the general aspects of the discrete model results, especially in terms of activation threshold and spatial acti-

vation patterns. For example, following monophasic extracellular stimulation with a single electrode, OFF & ON RGCs were activated only at 3 out of 25 sites (Figs. 6.5d & 6.6d) when the axon was oriented along the x-axis in the continuum model, similar to the discrete model (Figs. 6.5c & 6.6c).

Activation of the RGC directly below the active electrode was caused by AIS activation first (Figs. 6.5 & 6.6), with the AP then propagating to other compartments. While at the other two sites axonal activation occurred first, followed by activation of other compartments retrogradely. This finding was in agreement with many experiments and mathematical studies which have shown that when the stimulating electrode is above or close to the RGC soma, AP initiation will begin at the region with high sodium channel density; i.e. the AIS in our model (Abramian et al., 2015; Fried et al., 2009; Jeng et al., 2011). Clearly, this is obvious in Fig. 6.8 and Fig. 6.9 where snapshots show that the AP started in the AIS and then propagated bidirectionally to the soma and to the distal axon. In contrast, AP initiation occurred in the axon when the active electrode was far away from the cell body and above the axon, consistent with *in vitro* experiments (Jensen et al., 2005*b*) . Spatial activation of the OFF RGC discrete model was shown in Fig. 6.8 and for the ON RGC discrete model in Fig. 6.9. However, for the continuum model, it is difficult to show the action propagation through a point because every point in bulk retinal layers represents a single RGC, therefore, the best way to compare between discrete and continuum models at specific locations is the way indicated in Figs. 6.5 & 6.6, i.e. by displaying the traces of action potentials at specific locations.

The optimisation algorithm adopted in reducing the full morphologically-realistic RGC into the four compartment point model demonstrated good efficacy, particularly for the OFF RGC model. The slight difference in ON RGC between the full morphologically-realistic and reduced models is expected, because the large dendritic field poses a hurdle in reduce this large dendritic field with thousands of compartments to only one compartment.

In the membrane voltage waveforms simulated in the continuum model, peak action potential amplitudes and rebound hyperpolarizations may exceed the maximum or minimum reversal potentials of of Na^+ and K^+ respectively (Figs. 6.5 and 6.6). We believe coupling currents from adjacent compartments provide a significant contribution to this action potential overshoot as well as to the maximum hyperpolarization attained. Furthermore, the calcium reversal potential in our model is variable, reaching values up to $+130$ mV at rest, and lowering to around $+60$ mV during the action potential itself: this may also contribute to the peak overshoot, in which the study of Fohlmeister and Miller (1997a) demonstrated that I_{Ca} could add up to 10 mV to the action potential peak. However, similar overshoot phenomena (i.e. the response exceeds the max or min Na^+/K^+ reversal potentials) is also observed in physiological experiments when higher currents are applied (Cho et al. (2011), Guo et al. (2019) and O'Brien et al. (2002)). During the application of a higher current, the extracellular voltage (Ve) becomes the main contributor to the transmembrane potential (Vm) more than the intracellular membrane (Vi) and starts exceeding the sodium reversal potential (depolarization period) or potassium reversal potential (hyperpolarization period), resulting in the Vm range increasing in proportion to the increasing stimulus amplitude. Also, this phenomenon was shown in other modelling studies such as (Rattay et al. (2017), Meng et al. (2018), Werginz and Rattay, (2016) and Rattay and Wenger, (2010)).

6.4.2 Validation against *in vitro* experimental data

In addition to validation against a developed version of the discrete RGC model of the Guo et al., (2016) study, we validated the multi-domain continuum models of OFF and ON RGCs against published *in vitro* experiments, to emphasise the predictive power of the model. Originally, parameters for the OFF & ON RGC ionic formulation were estimated to reproduce results of experimental intracellular electrical stimulation recordings of rabbit RGCs (Guo et al., 2016). To

validate the present model, we chose the Jensen et al. (2005b) and Tsai et al. (2009) studies, because their experiments were also conducted on rabbit RGCs, recording the responses following extracellular electrical stimulation. Interestingly, the thresholds predicted by the epiretinal simulations of OFF RGCs are within the range reported by Jensen et al. (2005b), often close to the median thresholds. These results confirm the capability of the model to reproduce experimental findings characterising the impact of electrode distance on current thresholds. Moreover, our OFF and ON RGC multi-domain continuum model thresholds results are within the range reported by Tsai et al. (2009), revealing the model's efficacy in reproducing the relationship between pulse duration and current threshold for OFF & ON RGCs found in the Tsai et al. (2009) experiments.

6.4.3 The effect of higher current stimuli on neural activation

Excessive current injection can inhibit neurons. An experimental study conducted on motor nerves has shown that cathodic currents 2-3 times higher than the current threshold inhibited the action potential (Miledi, 1965). Moreover, another study revealed that action potential inhibition occurred when a current 8-10 fold larger than the activation threshold was used in spinal cord neurons (Jankowska and Roberts, 1972). Neurons located close to the active electrode required lower current thresholds compared to distant neurons (Rattay, 1987). Therefore, the inhibition phenomena could occur in proximal RGCs rather than distant ones, depending on the amount of stimulus current, pulse waveform and RGC subtypes (Abramian et al., 2015; Jensen and Rizzo III, 2006; Jensen et al., 2003).

This mechanism could account for the result in the combined multi-domain model (OFF & ON RGCs together). OFF RGCs located near the active electrode were inhibited when we injected 350 μA, which is approximately 2.2 times higher than the current stimulus used to validate the OFF RGC continuum model

(section 6.1.1.2). As we will see in the next chapter 7, the lowest current threshold for OFF RGCs with monophasic cathodic stimuli of 0.5 ms duration occurred just on the right of the stimulating electrode. Therefore, the OFF RGC whose soma was located 500 μm to the right of the stimulating electrode centre had all of its compartments inhibited, except the axon (Fig. 6.14). In contrast, OFF RGCs located far away were not affected by the excessive current injection (Fig. 6.14). These findings were consistent with the aforementioned studies and with a recent *in vitro* experimental study conducted in RGCs, APs were not generated with current stimuli ranging from 1.7 to 7.6 times the current threshold (Boinagrov et al., 2012). Moreover, simulation results presented here agree with a very recent study conducted on RGCs using *in vivo*, *in vitro* and *in silico* measurements, showing RGCs near the stimulating electrode were inhibited by high current amplitudes, while far away RGCs were not affected (Barriga-Rivera et al., 2017). Recently, a computational study by Abramian et al. (2015) investigated activation and inhibition RGC thresholds. They found inhibition thresholds ranging from 2-10 times the activation threshold, and more interestingly axonal activation could be reduced using an appropriately high current stimulus applied using a concentric stimulating electrode. Hex electrodes used in this thesis are close to the concentric electrode in terms of its principle of operation; six guards of hex electrodes resemble the outer return circle electrode of a concentric electrode.

Limited studies have tried to explain this inhibition phenomenon. A computational modelling study conducted on RGCs by Boinagrov et al. (2012) and confirmed experimentally, have shown there is an upper current threshold for somatic stimulation, which means no spike will be generated beyond that threshold due to sodium current reversal at strong depolarisations (Boinagrov et al., 2012). Another modelling study revealed strong stimulus current amplitudes and monophasic anodic pulses contributed to reducing or preventing vesicle release in retinal bipolar cells, due to the reversal of calcium flow into the extracellular space in cells close to the electrode (Werginz and Rattay, 2016).

6.4.4 Advantages and limitations of published continuum models

Every point in the modified bidomain formulation used in existing continuum models may be considered to be analogous to the soma/AIS of the neuron, as it is widely accepted that the AIS is the site of RGC spike initiation (Fried et al., 2009; Kole et al., 2008), due to elevated expression of voltage-gated sodium channels relative to other cellular compartments. These models (Abramian et al., 2014; Joarder et al., 2011; Yin et al., 2010) were constructed by assuming the soma or the AIS of each neuron is mathematically and resistively linked to a remote compartment always at rest. The remote compartment could, for example, represent distal portions of the axon that are not appreciably affected by the extracellular electrical stimulus. From a numerical perspective, the fixed potential of the remote compartment allows a solution to the bidomain model. An appropriate value of conductance that links the soma or AIS to the remote compartment was adjusted manually to match RGC extracellular activation thresholds of published epiretinal *in vitro* experimental data (Joarder et al., 2011).

However, published continuum models of retinal electrical stimulation are associated with some limitations. First, the assumption that the remote compartment potential is fixed: this could be accurate only to the extent that the site of impulse initiation has not yet propagated to the remote compartment, as would be the case typically during the short time interval underlying direct stimulation of the soma or AIS (high sodium channel density in some references). It is likely that the RGC soma or AIS is preferentially activated with near threshold stimuli. However for larger stimuli, the site of impulse initiation may occur in the axon, leading to retrograde activation of the soma. Under such scenarios, the remote compartment potential would not be fixed during direct stimulation of the soma or AIS, but would be a time-varying waveform dependent on the applied field and the orientation of the axon. In addition, the dendrites themselves do possess active

channels, helping propagate the nerve impulse into the soma. Such complex activation dynamics cannot be captured by the simplified continuum model requiring a more detailed multi-domain representation of the cell and therefore the tissue.

Second, these studies had each only considered one type of RGC and ignored other subtypes. Interestingly, several experimental studies have confirmed that each RGC subtype has unique responses when exposed to electrical or light stimulation, attributing this to their intrinsic electrophysiological properties (Margolis and Detwiler, 2007; Mitra and Miller, 2007). For example, ON RGCs are more excitable in the presence of light, producing more spikes, whereas OFF RGCs are not. Also, OFF RGCs have a complex mechanism for generating action potentials which exhibits burst firing, rebound excitation and spontaneous activity. In contrast, ON RGCs do not show these phenomena and require an excitatory input to be excitable. Various experimental and computational modelling studies have shown there is a difference between OFF and ON RGCs in response to depolarising and hyperpolarising current injections (Guo et al., 2016; Kameneva et al., 2011). This difference has been proposed to be exploited as a selective electrical stimulation approach between these two RGC types. A set of experimental and mathematical studies have demonstrated that differentiation between OFF and ON RGC activation could be obtained using high frequency electrical stimulation (Kameneva et al., 2016; Twyford et al., 2014). Therefore, the presence of more than one cell type in a continuum model will be effective and valuable for investigating complex mechanisms of electrical stimulation.

Third, the ionic formulation used in the current continuum models are based on the Fohlmeister and Miller (FM) formulation (Fohlmeister and Miller, 1997*b*). Although this formulation was able to reproduce many experimental findings, it does not include some ionic currents observed recently in experimental studies which have a significant role in explaining key phenomena. For example, the presence of a persistent Na^+ current (I_{NaP}) has a significant role in the generation of spontaneous spike activity of OFF RGCs at rest in rats (Margolis and

Detwiler, 2007). Another experimental study, which includes voltage and current clamp studies with pharmacological manipulations on tiger salamander retinas, has identified the phenomenon of rebound excitation as a result of the contribution of two currents: the hyperpolarisation-activated mixed-cation current (I_h) and the low threshold voltage activated calcium current (I_{CaT}) (Mitra and Miller, 2007). Moreover, computional modelling studies have emphasised the role of these currents in reproducing particular experimental data (Kameneva et al., 2016, 2011). Therefore, the use of ionic current formulations incorporating up to date ionic currents will be beneficial in modelling studies in order to optimise retinal implants.

6.5 Model Limitations

The continuum model developed in this chapter was accounted for all main RGC segments: the soma, AIS, axon and dendrites. Each segment was represented by one compartment. This representation is very simplified because each segment has many compartments in morphologically-realistic RGCs, particularly those of the axon and dendrites. It would be beneficial to add more compartments to the axon and dendrites to imitate the realistic physical shape and reproduce the fine features of these segments. However, this addition will cause the model to become more complex. Therefore, the trade-off between simplicity and reproducing the fine properties of these segments will be a challenge. In addition, synaptic inputs from the retinal network were not incorporated in the continuum description. Therefore, the models are likely to exhibit direct activation of RGCs. However, incorporation of synaptic inputs would provide more accurate simulation of retinal responses to electrical stimulation, particularly for suprachoroidal electrode placements. Accordingly, the influence of the retinal network on the response of RGCs to electrical stimulation should be included in future models. Another limitation is the assumption of isotropic conductivities within retinal layers, which is may not be the case in the real retina, despite the lack of available experimental data.

7 Stimulation Strategies for electrical stimulation of healthy and degenerate retina

Retinal implants are being developed to restore vision for those with outer retinal degenerative disease such as RP or AMD, due to death of photoreceptors. As the disease progresses, the photoreceptors are gradually damaged, and retina undergoes severe remodelling and rewiring especially in the later stages of degeneration. Animal studies in degenerate retinas have shown that the dendrites of rod bipolar cells are retracted. The size of horizontal cell dendrites has been reported to be smaller, and these cells sprout towards the inner plexiform layer. Moreover, the morphology of AII amacrine cells has been observed to alter. Furthermore, neurochemical changes have been reported in addition to morphological changes in the degenerate retina. For example, the levels of GABA are higher, and the sensitivity of rod bipolar cells to GABA increased in the rd1 mouse retina (Jensen and Rizzo III, 2011). Despite the severe changes in retinal architecture following photoreceptor degeneration, morphometric studies conducted on affected animals and humans have shown that a considerable amount of inner retinal neurons still remain viable, providing hope of restoring vision to blind people by artificially exciting the remaining retinal cells.

Despite the very promising results of current retinal implants, which have indicated that blind people could perform limited tasks such as orientation, mobility to a certain extent, letter and word reading and even to perform spatiomotor tasks (Dumm et al., 2014; Wilke et al., 2011), the advanced level of visual perception, such as face recognition and sentence reading, requires higher spatial resolution. Hence, the enhancement of spatial resolution of visual prosthesis is a demand, especially if the micro-electrode array (MEA) is located far away from targeted

neurons such as in the case of suprachoroidal implants. One of the proposed strategies is to increase the number of electrodes leading to an increase in the number of evoked phosphenes (Dumm et al., 2014). However, this strategy faces some engineering and manufacturing challenges. For example, retinal prosthesis currently possess up to 1500 electrodes, which should converge to around 20-50 million retinal ganglion cells in the degenerated human retina (Brooks et al., 1999; Santos et al., 1997). Hence, the ratio of ganglion cells to electrodes, if we consider the high amount of surviving RGCs, is more than 30 thousand to one, indicating a very crude approximation of the sense of vision. Moreover, it was demonstrated that small electrodes generate high charge density which may affect retinal tissues. Also, increasing the number of MEA electrodes raises the impact of electric crosstalk between electrodes during concurrent stimulation, leading to reduced resolution of the perceived image (Moghaddam et al., 2011). Therefore, researchers have proposed and tested some useful techniques to enhance the spatial resolution. Current focusing or steering and virtual electrodes techniques could provide an acceptable solution. Current steering approaches have been applied to modern neuroprostheses, providing localisation of induced visual perception and minimising the impact of crosstalk. Virtual electrode techniques aim to increase the number of discriminable phosphenes without increasing the number of physical electrodes by exciting the intermediate areas between adjacent electrodes.

In this chapter, we develop a multi-domain continuum model of electrical stimulation of degenerate retina and compare it to the healthy retina. Different strategies to improve the spatial resolution are investigated. Various parameters that be important to the mechanisms underlying retinal electrical stimulation have been examined. The models of this chapter incorporate OFF and ON RGCs in the case of both healthy and degenerate retinas.

7.1 Development of a degenerate model of retinal electrical stimulation

Retinal degeneration has been investigated in various experimental studies. Several animal models have been proposed to represent photoreceptor degeneration, highlighting the response of the degenerate retina to electrical stimulation and its status after degeneration. More importantly, stimulus thresholds have been quantified and factors affecting thresholds have been studied to some extent. A valuable study conducted by Sekirnjak et al. (2009) on P23H rats over a two year timeframe showed that the total thickness of the retina was reduced by 50% and the photoreceptor layer had completely disappeared (Sekirnjak et al., 2009). This finding was consistent with other studies (Jensen and Rizzo III, 2011; O'Hearn et al., 2006). Moreover, the thickness of the inner nuclear and inner plexiform layers was observed to be reduced in rd1 mice (Ward, 1982) and could be reduced up to 25% (O'Brien, 2012). Furthermore, the formation of a high-impedance layer from glial cells during the mid stage of degeneration has been identified, and in later stages this layer could form over the whole inner retina, as shown in Fig. 7.1 (Marc et al., 2003; O'Brien, 2012). Morphometric studies have shown the survival rate of ganglion cells in RP and AMD patients to reach 30% and 53-97%, respectively (O'Hearn et al., 2006). Although a few animal studies found no difference in RGC counts between normal and degenerate retina (Mazzoni et al., 2008; Strettoi et al., 2002), a recent study has demonstrated the decline in RGCs; their numbers in the degenerate retina were half compared to the normal retina, consistent with previous studies (Chan et al., 2011). The receptive field of P23H rat RGCs was reported to decrease by 50% (Sekirnjak et al., 2011).

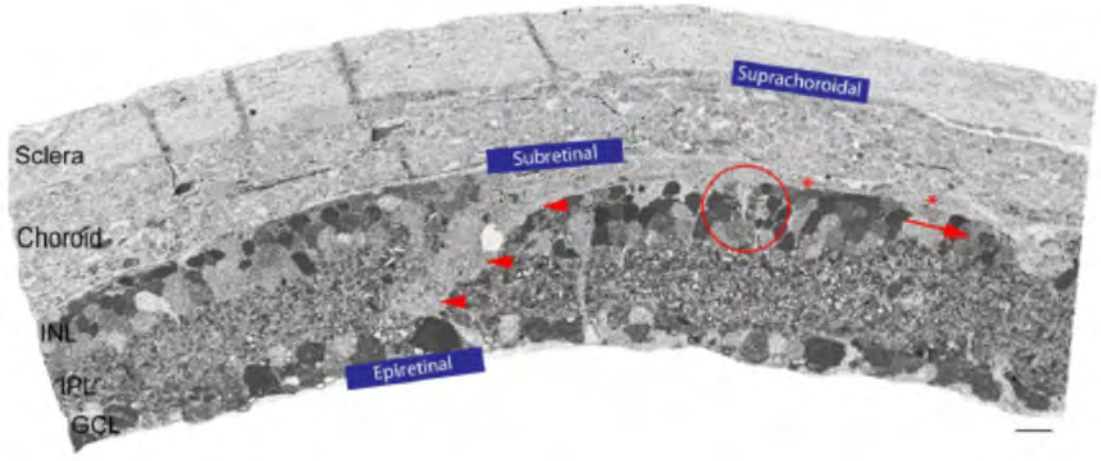

Figure 7.1: The formation of a glial scar layer in the degenerate retina. This vertical section was taken from rd1 mice at 16 months after degeneration. Müller scarring is denoted by the arrow heads, and glial seal by asteriks (O'Brien, 2012).

The healthy retinal model consisted of a three-dimensional finite element formulation composed of ten layers: vitreous, multi-layered retina, choroid and sclera, calibrated against threshold data of epiretinal and subretinal current stimulation of rabbit OFF & ON RGCs, as discussed in chapter 6.

We developed a computational model of the degenerate retina based on information from the literature. The model was based on the mid-to-late stage of retinal degeneration with the following features:

1. The retinal pigment epithelium, photoreceptors, outer plexiform, and outer nuclear layers were removed.

2. The thickness of the inner nuclear and inner plexiform layers was reduced by 25$\%$.

3. The decline in the total RGC number was introduced by adjusting the RGC surface-volume ratio parameter (β) to half of its standard value.

4. A 20 μm thick fibrotic glial scar layer was introduced parallel to the retinal layers with a very low conductivity, as opposed to a pure insulator assumed in previous modelling studies (Connolly and Bishop, 2016). To the best

of our efforts, we could not find any published studies that measured the resistivity of glial scar layer in the degenerate retina. Therefore we estimated glial scar resistivity to be a multiple (x2, x4, x6, x8, and x10) of the retinal pigment epithelium, as it has the highest resistivity in the model.

5. The reduction in dendritic field was implemented by reducing the inter-compartment conductivities between dendrites and soma (g_{12}, g_{21}) by 50%.

A hexagonal (hex) arrangement of circular disc electrodes, each 380 μm in diameter with 730 μm centre-centre spacing, was utilised for the healthy and degenerate models. The central electrode was the stimulating electrode, with the surrounding electrodes being the returns. Each return electrode of six guards received 1/6th of the amplitude of the current injected via the stimulating electrode and reversed in direction (Push-Pull). A biphasic charge-balanced, cathodic-first waveform with no interphase delay and 0.5 ms phase width was applied. Hex electrodes were placed on the top boundary of the vitreous or the bottom boundary of the choroid for both epiretinal and suprachoroidal stimulation, respectively. All threshold measurements were taken at the middle of the RGC layer.

Current thresholds required to activate OFF and ON RGCs in the multi-compartment continuum model were determined for both healthy and degenerate cases. In the case of epiretinal stimulation of healthy retina, thresholds were 33 μA and 72 μA for OFF and ON RGCs, respectively. In contrast, current thresholds were increased in the case of suprachoroidal simulation of the healthy retina to 84 μA and 180 μA for OFF and ON RGCs, respectively. Figs. 7.2 & 7.3 compares the healthy and degenerate models in terms of the activated area of each RGC compartment during suprachoroidal simulation.

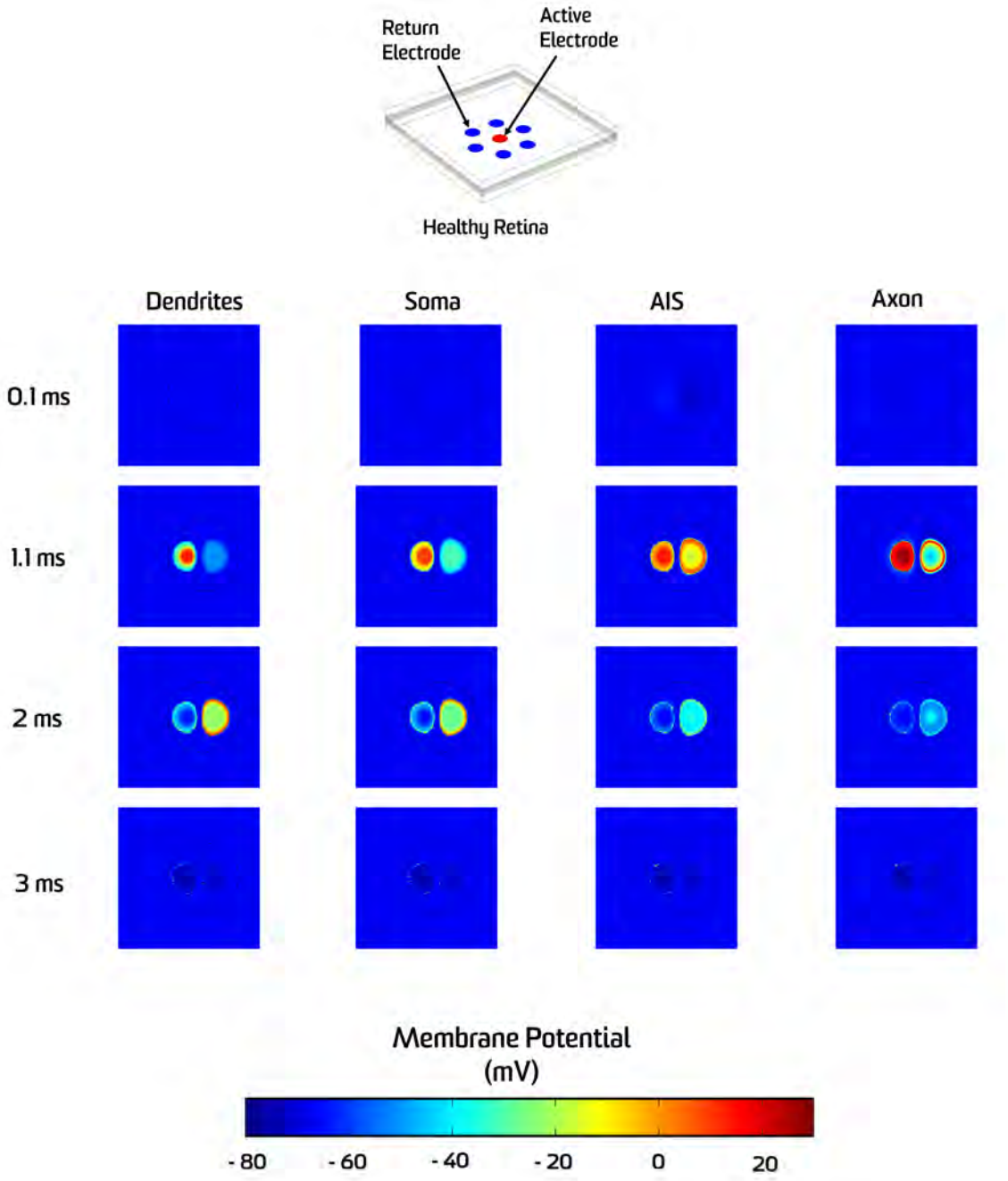

Figure 7.2: Simulated spatial activation maps for different RGC compartments in the case of suprachoroidal stimulation in the healthy OFF RGC retinal continuum model. The onset of stimulation was at 0.1 ms and stimulation lasted for 1 ms. The stimulus current was 315 μA. The large circle in the middle represents a region with fine mesh implementation.

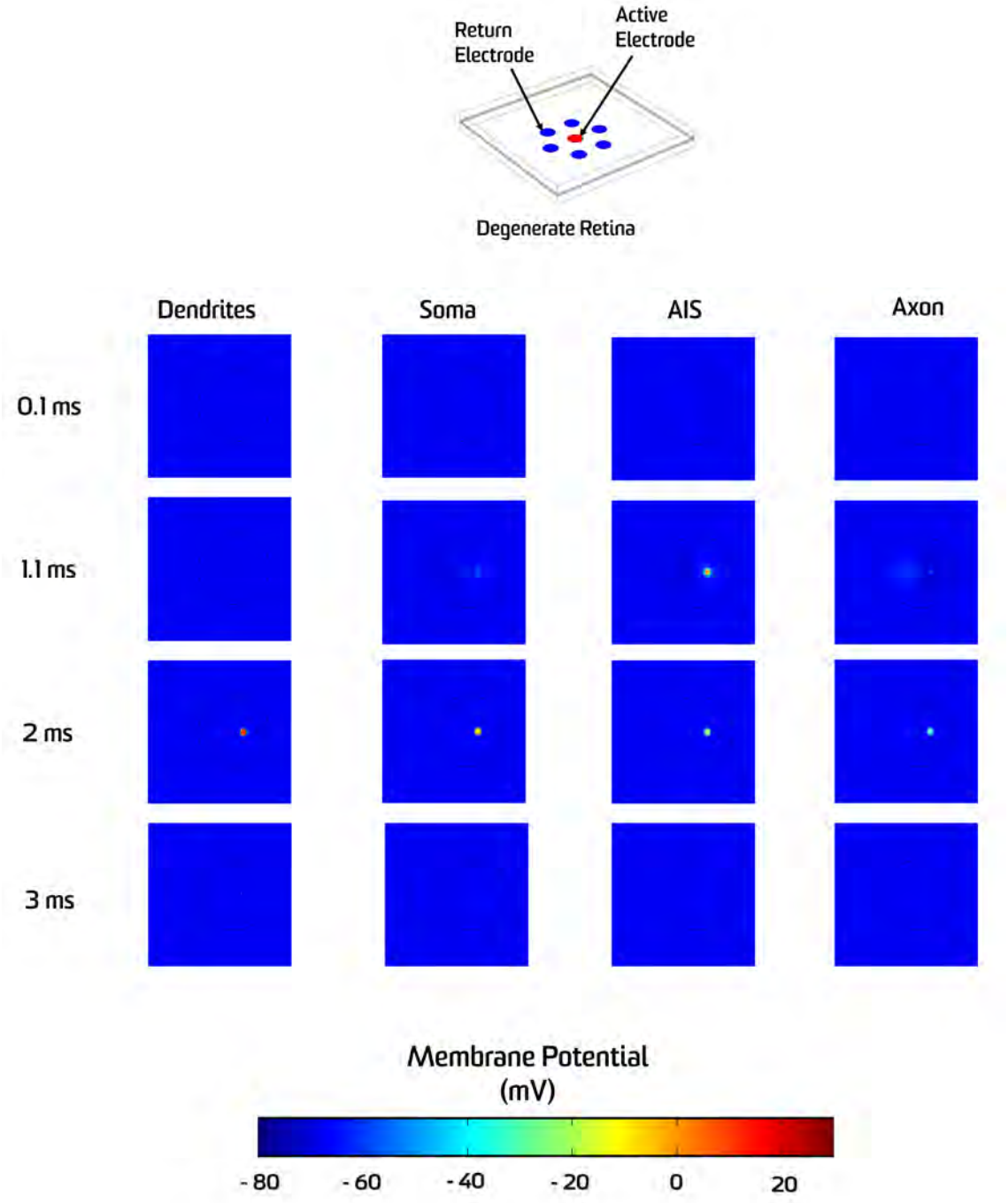

Figure 7.3: Simulated spatial activation maps for different RGC compartments in the case of suprachoroidal stimulation for the degenerate OFF RGC retinal continuum model. The onset of stimulation was at 0.1 ms and stimulation lasted for 1 ms. The stimulus current was 315 μA. The large circle in the middle represents a region with fine mesh implementation.

In Fig. 7.4, we show the impact of the glial scar layer on current thresholds of the degenerate retina for both epiretinal and suprachoroidal electrode simulations. In the suprachoroidal case, the current threshold of OFF RGCs ranged between 73 μA and 294 μA, corresponding to 32.2 $\mu C/cm^2$ and 129.7 $\mu C/cm^2$ for different values of glial layer resistivity. For ON RGCs, the current threshold ranged between 165 μA and 670 μA, corresponding to 72.8 $\mu C/cm^2$ and 295.5 $\mu C/cm^2$. All these values are below the safe charge injection limit of platinum electrodes, reported to be 300-350 $\mu C/cm^2$ (Merrill et al., 2005). However, another study found the safe charge injection limit of platinum electrodes varied based on the surface patterning of the electrode, ranging between 80 $\mu C/cm^2$ and 325 $\mu C/cm^2$ for *in vitro* studies, and between 30 $\mu C/cm^2$ and 125 $\mu C/cm^2$ for *in vivo* studies with 0.5 ms duration (Green et al., 2014). These results demonstrate a significant influence of the glial scar layer on current thresholds in the case of the suprachoroidal electrode configuration, with thresholds rising with higher values of glial layer resistivity. In contrast, there was no correlation between the presence of a glial scar and current threshold in the epiretinal simulations (Fig. 7.4).

For the remainder of this chapter, we will use 10 times the value of retinal pigment epithelium resistivity as the resistivity value for the glial scar layer. Also, we will focus on suprachoroidal electrical stimulation.

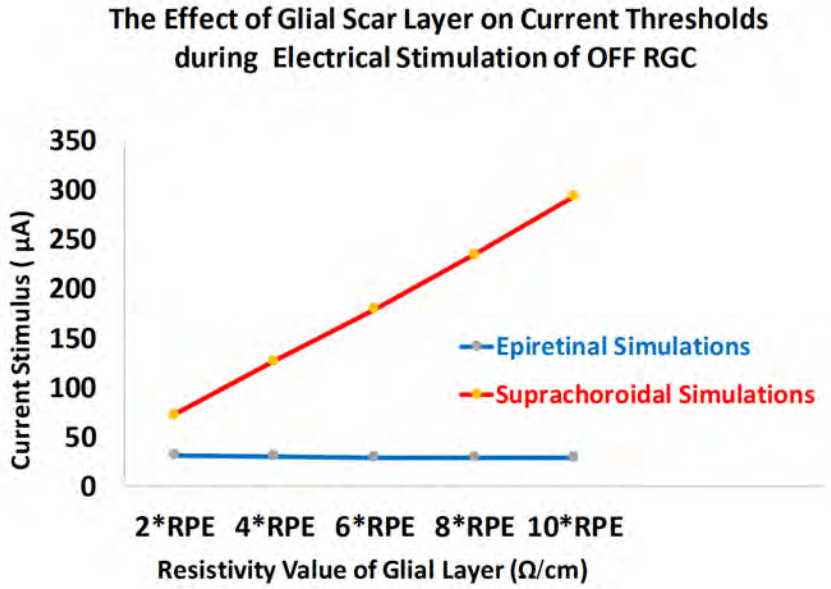

(a)

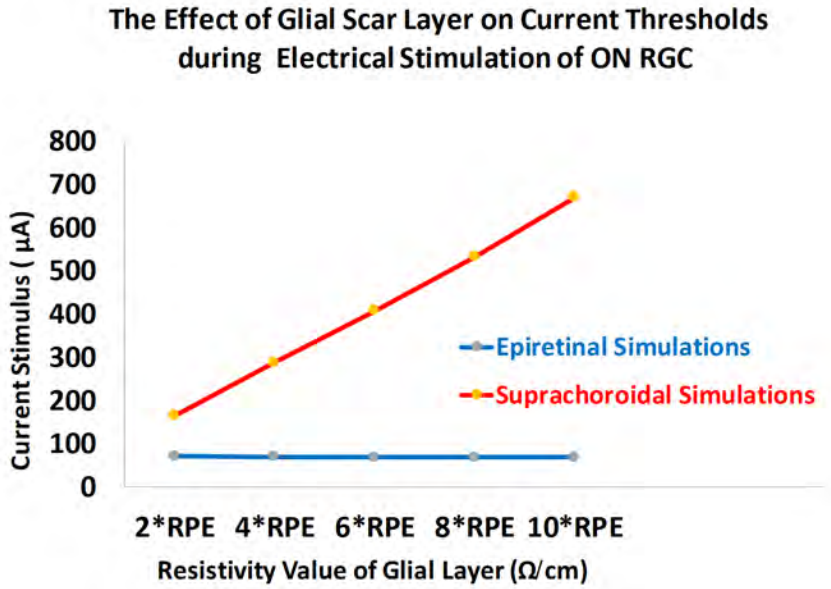

(b)

Figure 7.4: The influence of glial scar layer on excitation current thresholds for epiretinal and suprachoroidal stimulation configurations for (a) OFF and (b) ON RGCs. A biphasic charge-balanced, cathodic-first waveform with no interphase delay and 0.5 ms phase width was applied.

7.2 The effect of return electrode configuration

7.2.1 Overview of return electrode configurations

The electrical field distribution and the efficacy of electrical stimulation can be affected by the return electrode configuration and their location. Different types of return (ground) electrodes have been proposed in the field of retinal electrical stimulation such as monopolar, bipolar, bipolar concentric, hexapolar (hex), quasi-monopolar (QMP) and common ground, as illustrated in Figure 7.5. In the monopolar configuration, the return electrode is usually located remotely at the vitreous or sclera. In the bipolar return configuration, a single return electrode is adjacent to the stimulating electrode. The hexapolar and common ground return configuration are almost similar in principle, but the difference is that in the hexapolar case, the stimulating electrode is surrounded by six return electrodes, whereas in the common ground the stimulating electrode is surrounded by many electrodes. The quasi-monopolar return electrode configuration is a combination of monopolar and hexapolar configurations in which the percentage of returning current received by either monopolar return or hexapolar return electrodes can be adjusted by the user. In the bipolar concentric configuration, the stimulating electrode is surrounded by a large ring representing the return electrode.

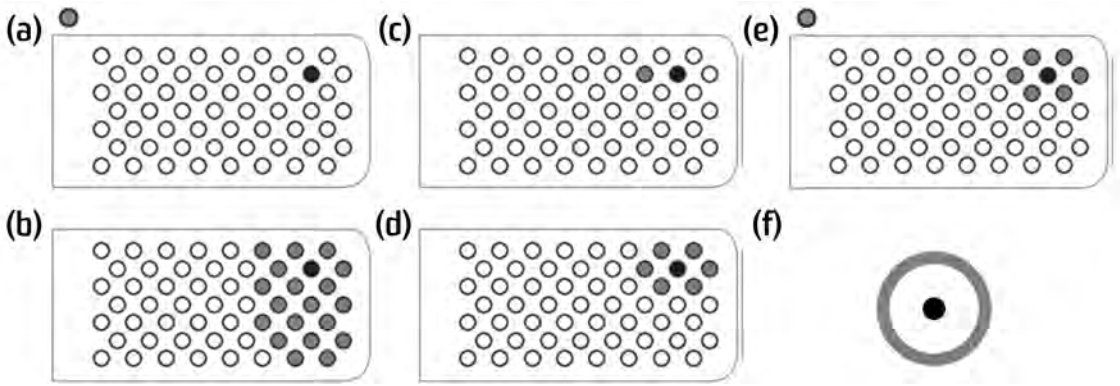

Figure 7.5: Examples of return electrode configurations used in retinal implants. Black represents the stimulating electrodes, whereas gray represents the return electrodes (a) monopolar (b) common ground (c) bipolar (d) hexapolar (e) quasi-monopolar (f) bipolar concentric. Adapted from Cicione et al. (2012).

7.2.2 The effect of return electrode configurations

The influence of the return electrode configuration on both the threshold and spatial distribution of auditory cortex induced activity during electrical stimulation has been clearly observed in animal studies of the cochlear implant (Cicione et al., 2012). These studies showed that by varying the return electrode configuration, spatial selectivity can be improved. It is expected that suprachoroidal implants require higher thresholds to excite RGCs, and their resolution is very low compared to other retinal implants due to the larger distance between electrodes and target neurons. Therefore, the resolution of suprachoroidal stimulation could be enhanced with an appropriate choice of return electrode configuration.

In this section, the effect of monopolar, QMP and hex return electrodes on the current thresholds for healthy and degenerate OFF and ON RGC models is investigated for suprachoroidal electrical stimulation. A biphasic charge-balanced, cathodic-first waveform with no interphase delay and 0.5 ms pulse duration is delivered via the central electrode of the hexagon for all configurations. A hexagonal (hex) arrangement of circular disc electrodes, each being 380 μm in diameter and 730 μm centre-centre spacing, was employed for the healthy and degenerate models. In the case of monopolar configuration stimulation, the six guard electrodes were removed and the remote ground was utilised for the current return. In the hexapolar configuration, each return electrode of six guards received 1/6th of the amplitude of the current injected via the stimulating electrode, but reversed in polarity (Push-Pull). In quasi-monopolar stimulation, the current return was divided between the remote ground and the guard electrodes. For example at 80% QMP stimulation, 80% of the injected current was returned through the six guard electrodes and the remaining current was returned via the remote ground.

Figures 7.6a and 7.7a illustrate the spatial activation on the mid-plane of the RGC layer for all OFF RGC compartments utilising hex, monopolar and QMP return electrode configurations with double current threshold magnitudes for the healthy and degenerate models. To be more accurate, measurements were taken from the mid-plane boundary of the RGC layer because the lower RGC layer boundary exhibits most of the spatial activation due to its proximity to the supra-choroidal electrodes, whilst the upper boundary is further away and may be affected by the vitreous. Figures 7.6b and 7.7b summarise threshold currents obtained from the OFF and ON RGC models using monopolar, QMP and hex return electrode configurations for the healthy and degenerate models. In all configurations, current thresholds were almost similar for both healthy and degenerate cases and for both types OFF and ON RGCs. However, even their thresholds were similar, it was found that in all cases, the hex and QMP configurations resulted in more focal spatial activation, even when the current stimulus value was twice the threshold: this being more obvious in the degenerate model.

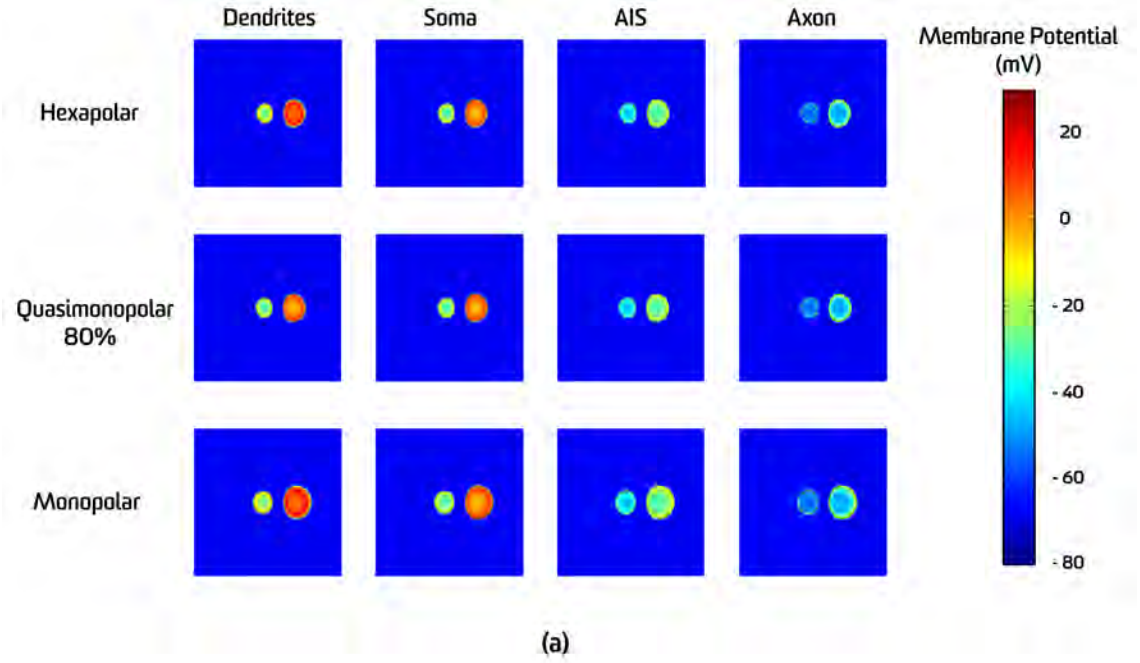

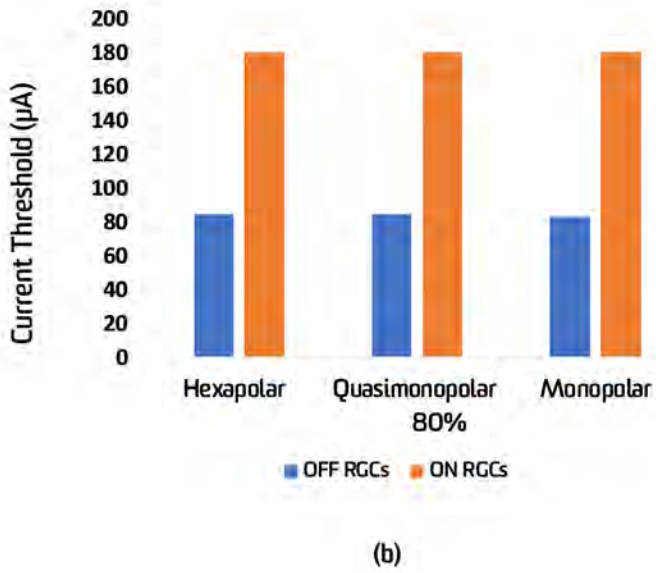

Figure 7.6: The effect of utilising hex, monopolar and QMP return electrode configurations for suprachoroidal stimulation of healthy OFF and ON RGC models. (a) The spatial activation on the middle plane of the RGC layer for all OFF RGC compartments utilising hex, monopolar and QMP return electrode configurations at twice threshold at 0.7 ms after termination of the stimulus pulse. (b) Current thresholds for evoking APs using monopolar, QMP and hex return electrode configurations for OFF and ON RGCs.

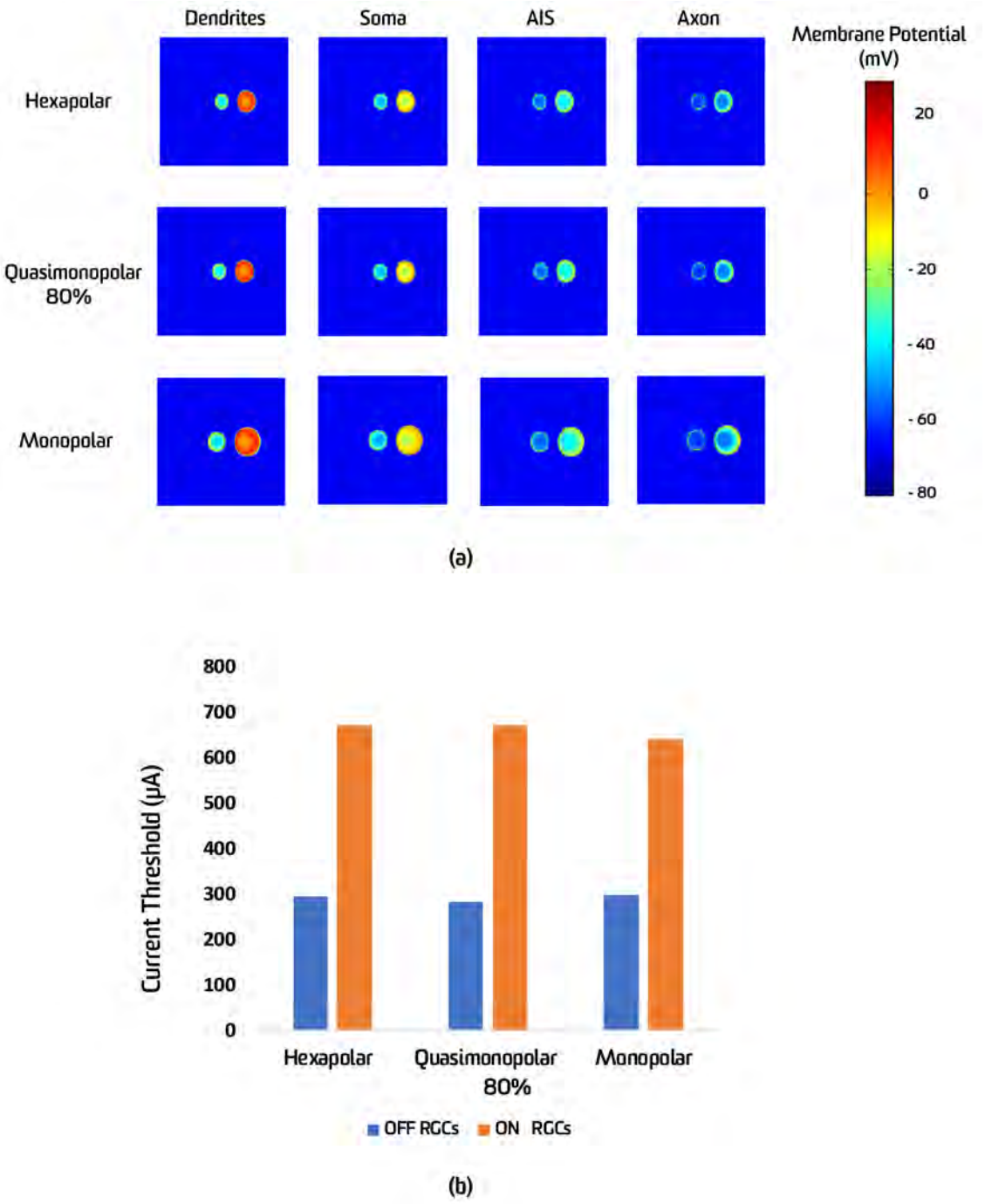

Figure 7.7: The effect of utilising hex, monopolar and QMP return electrode configurations for suprachoroidal stimulation of degenerate OFF and ON RGC models. (a) The spatial activation on the middle plane of the RGC layer for all OFF RGC compartments utilising hex, monopolar and QMP return electrode configurations at twice threshold at 0.7 ms after termination of the stimulus pulse. (b) Current thresholds for evoking APs using monopolar, QMP and hex return electrode configurations for OFF and ON RGCs.

7.2.3 The effect of increasing choroid thickness

Next, we investigated the effect of choroid thickness on the response of the healthy RGC model during electrical stimulation. Figs 7.8a and b demonstrate the spatial activation on the mid-plane boundary of the RGC layer, and summarise threshold currents obtained for all main OFF RGC compartments using the three return electrode configurations when the thickness of the choroid was increased to 426 μm for the healthy OFF RGCs. Increasing the thickness of choroid from 200 μm to 426 μm resulted in elevation of thresholds for all configurations. However, the monopolar case exhibited the lowest thresholds, whereas hexapolar showed the higher thresholds of 1.2 times the monopolar threshold. The spatial activation maps demonstrate that hexapolar stimulation results in more focused activation even though it requires higher thresholds. Furthermore, hexapolar and QMP showed the same patterns of localised activation.

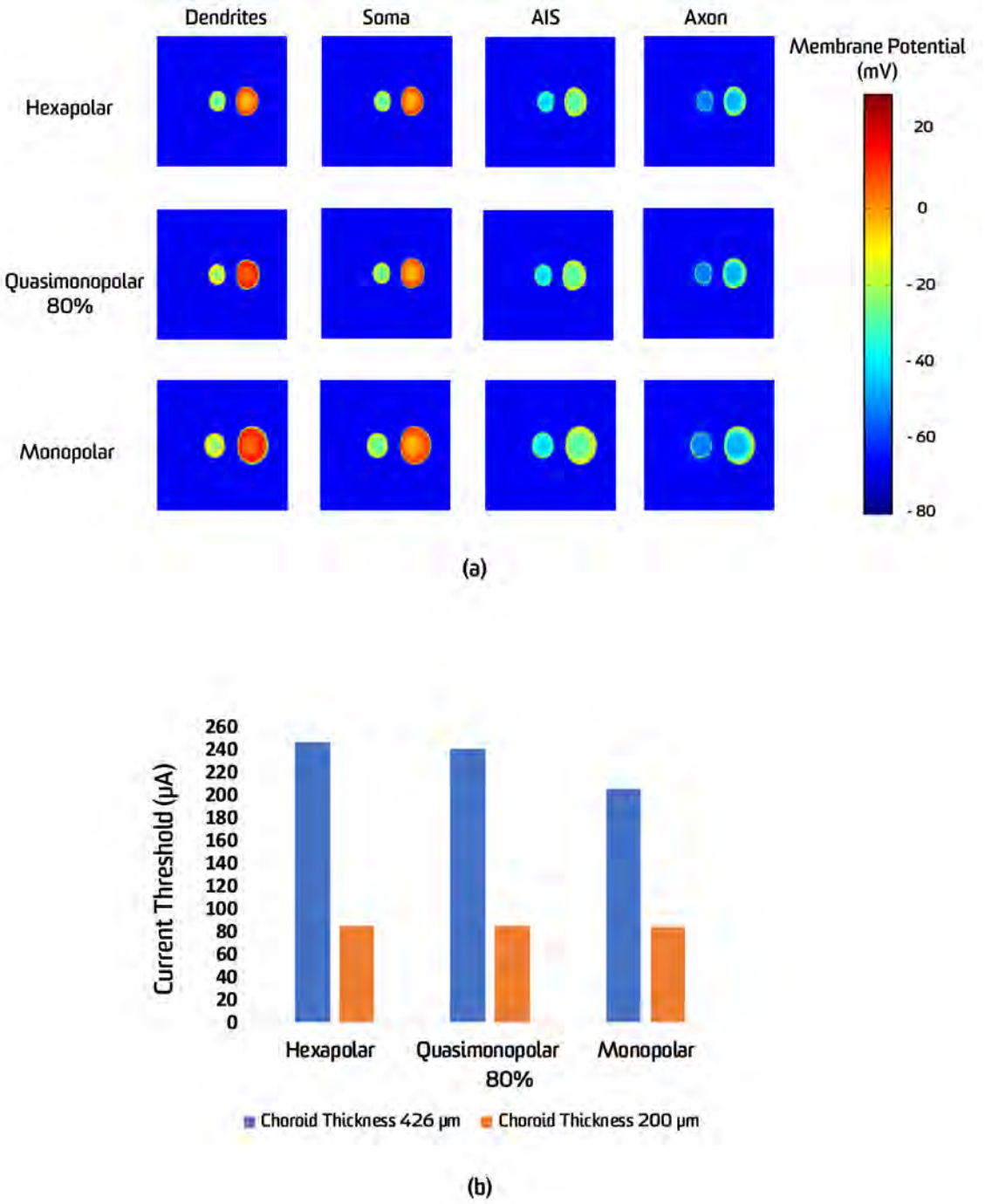

Figure 7.8: The effect of using a larger choroid thickness on current thresholds for the healthy OFF RGC model. (a) Spatial activation on the middle plane of the RGC layer for all OFF RGC compartments utilising hex, monopolar and QMP return electrode configurations stimulating at twice stimulus threshold. (b) Current thresholds using monopolar, QMP and hex return electrode configurations.

7.2.4 The effect of electrode size and centre-centre spacing

Next, we examined the impact of electrode size and centre-centre spacing in addition to the above three return electrode configurations on the response of the healthy RGC model during electrical stimulation.

The electrode diameters investigated were 50 and 380 μm, and centre-to-centre spacings ranged from 100 to 730 μm. Using a different set of electrode sizes and spacing, electrical stimulations were conducted and thresholds were identified for the case of hexapolar, monopolar and 80% QMP configurations.

Figure 7.9 summarises the effect of electrode size on the threshold currents in the healthy OFF RGC model utilising hex, monopolar and QMP return electrode configurations in the case of suprachoroidal stimulation. The influence of return electrode size on current thresholds was marginal. Figure 7.9 reveals no significant difference among the three return electrode configurations with the two sizes of electrodes: 50μm and 380 μm. Moreover, there was a slight decline in current threshold with decreasing electrode size.

The impact of closely spaced electrodes on the elevation of current thresholds was more pronounced, as shown in Figure 7.10. Monopolar and hexapolar return configurations showed the lowest and highest thresholds respectively, with QMP thresholds were in between. For example with electrodes size of 50 μm and 100 μm centre-centre spacing, hex and 80% QMP return electrode configurations thresholds were approximately 15 and 4 times higher than the monopolar threshold. With the same electrode size and using an electrode spacing of 400 μm, this ratio was reduced to nearly 1.5 and 1.3 for hex and 80% QMP respectively. Similarly, with electrode size 380 μm and 450 μm centre-centre spacing, hex and 80% QMP return electrode configurations thresholds were approximately 2 and 1.85 times higher than the monopolar configuration threshold. However with increasing electrode spacing to 730 μm, the thresholds were similar for all configurations.

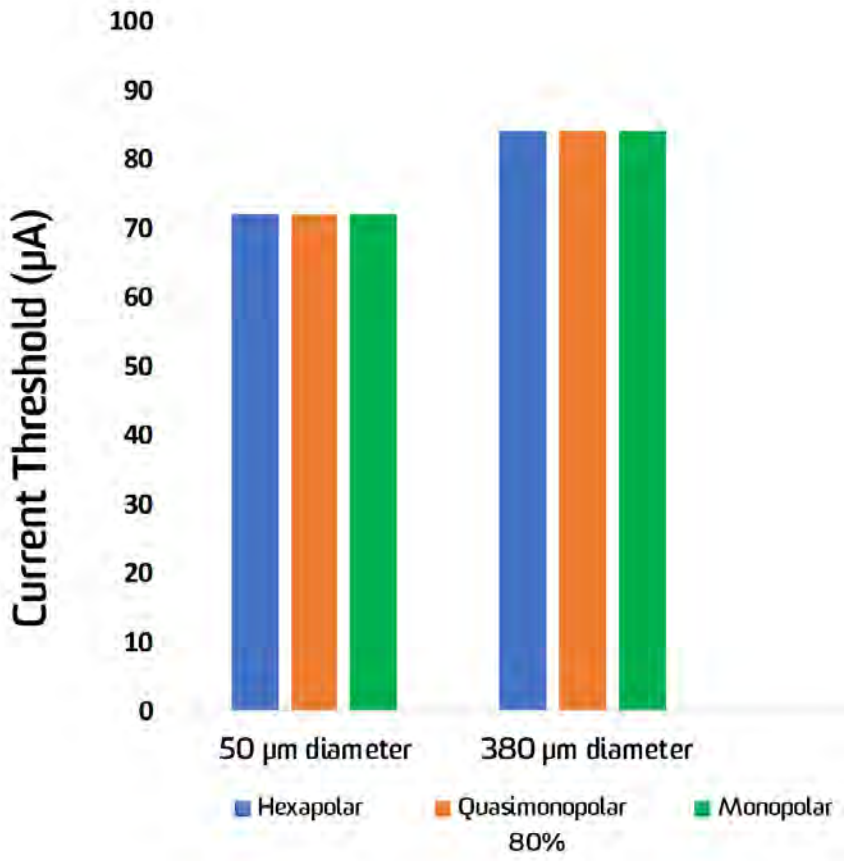

Figure 7.9: The influence of electrode size on excitation current thresholds for supra-choroidal stimulation configurations of the healthy OFF RGC model. Electrode centre-centre spacing was fixed at 730 μm and two different electrode sizes were used: 50 and 380 μm diameters.

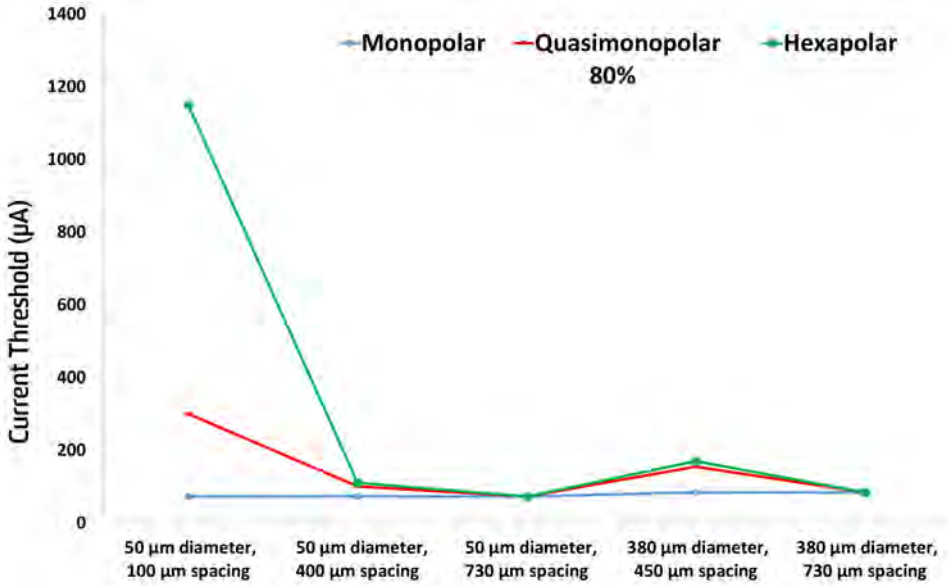

Figure 7.10: Current thresholds for simulated suprachoroidal stimulation utilising hex, monopolar and QMP return electrode configurations with different electrode sizes and spacing. Electrode sizes were 50 μm and 380 μm in diameter, and centre-to-centre spacing was 100 μm, 400 μm, 450 μm and 730 μm.

7.2.5 The effect of using one, two and six return electrodes

Next, we studied the influence of using various numbers of surrounded local return electrodes on the response of the healthy RGC model during electrical stimulation. Figs 7.11a and b illustrate the spatial extent of activation of the healthy OFF RGC model with one, two and six guards, and summarise threshold currents in the case of suprachoroidal stimulation at twice the current threshold for each configuration. A single return electrode (bipolar) required a lower current to activate RGCs than that of twin return electrodes and that of six return electrodes. Moreover, the shape of the evoked phosphenes was affected by the return electrode configuration.

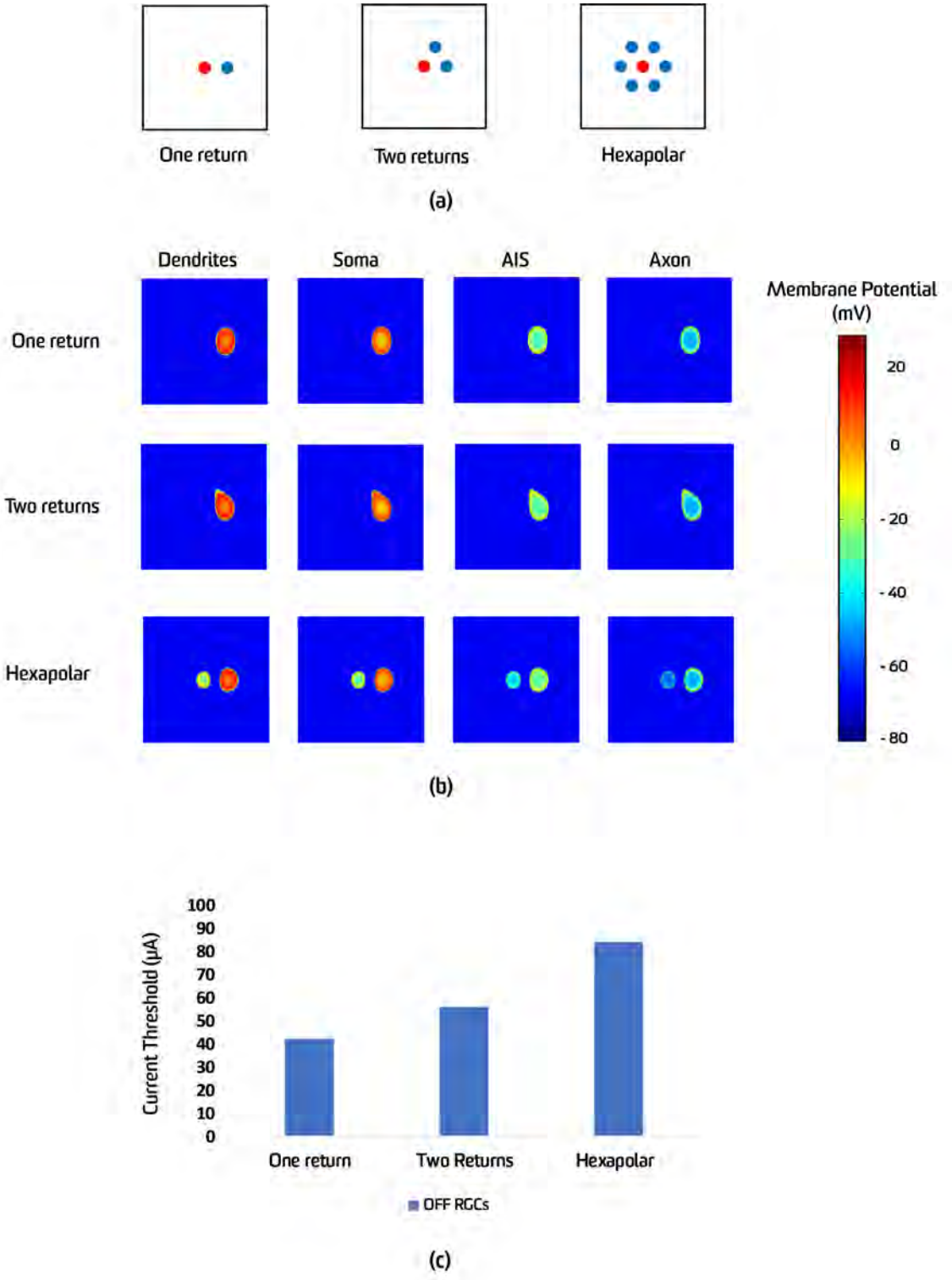

Figure 7.11: The effect of using one, two and six return guards on the simulated shape of phosphenes and current thresholds in the healthy OFF RGC model. (a) The configuration of one, two and six return electrodes. (b) The spatial extent of activated membrane potential with one, two and six return guards active in the case of suprachoroidal placement of electrodes 0.7 ms after the termination of stimulus at twice threshold for each configuration. (c) Stimulus thresholds for one, two and six return guards.

7.3 The effect of pulse polarity and duration

Various stimulation parameters have been explored in many studies to optimise retinal implants (Shivdasani et al., 2010; Weiland et al., 2016). The impact of these factors on spatiotemporal properties of elicited spikes, selective activation of RGC subtypes and avoiding activation of passing axons has been investigated in some detail (Weiland et al., 2016). Pulse duration, stimulation waveforms, electrode size, electrode placement and return electrode configurations represent examples of factors that may pose a significant influence on the mechanisms of electrical stimulation. Some of these parameters have already been discussed in section 7.2 .

In this section, the effects of pulse polarity and duration on the effectiveness of retinal stimulation have been examined. Most studies have examined the effect of pulse duration on the required current to activate RGCs, finding that with longer pulse durations, lower current amplitudes are needed and vice versa (Jensen and Rizzo III, 2009; Jensen et al., 2005*b*; Sekirnjak et al., 2006; Tsai et al., 2009). Here we studied the influence of pulse polarity and duration on the localisation of activated regions. We tested two pulses: 0.1 ms and 0.5 ms with four different electrical pulse waveforms, namely: monophasic cathodic, monophasic anodic, symmetric biphasic charge-balanced cathodic first, and symmetric biphasic charge-balanced anodic first, as illustrated in Fig. 7.12. A duration of 0.1 ms is considered a short pulse, whereas 0.5 ms is a long pulse (Jensen et al., 2003). This investigation was done for both RGC subtypes: OFF and ON RGCs, and for both healthy and degenerate models.

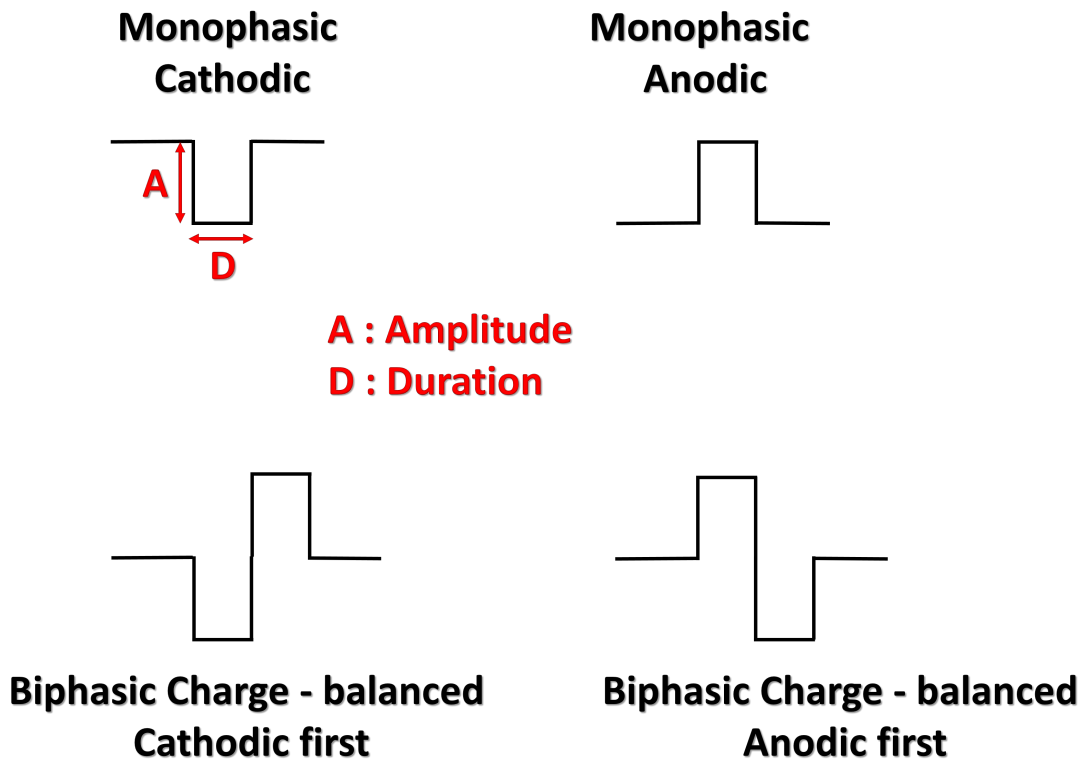

Figure 7.12: Various current stimulus waveforms used in our simulations and in most retinal electrical stimulation experiments.

Figure 7.13 demonstrates the effect of pulse duration on the location of spatial activation of RGCs in the healthy continuum OFF and ON RGC models. It can be clearly seen that activation occurred beneath the stimulating electrode for both RGC subtypes when using a symmetric biphasic anodic waveform with short or long pulse durations. When using a symmetric biphasic cathodic waveform, OFF RGCs are always activated far away from the stimulating electrode, regardless of the pulse duration, whereas ON RGCs are activated below the stimulating electrode. When using a short pulse duration, the monophasic anodic waveform will lead to activation of OFF and ON RGCs far away from the stimulating electrode, whereas OFF and ON RGCs located under the stimulating electrode are activated with a monophasic cathodic stimulus. On the other hand, pulses using a long pulse duration activate ON RGCs beneath the stimulating electrode regardless of the pulse waveform. Either using monophasic cathodic or biphasic cathodic

waveforms with long pulse duration will result in activation of OFF RGCs further away from the stimulating electrode, whereas monophasic anodic and biphasic anodic waveforms with long pulse duration will activate OFF RGCs directly below the stimulating electrode.

Figure 7.14 illustrates the effect of pulse polarity and duration on the location of spatial activation of RGCs in the degenerate continuum OFF and ON RGC models. Similar to the healthy continuum OFF and ON RGC models, it is evident that activation always occurred below the stimulating electrode for both RGC subtypes when applying symmetric biphasic anodic waveforms, regardless of the pulse duration. With the symmetric biphasic cathodic waveform, OFF and ON RGCs are activated far away from the stimulating electrode with either a short or long duration pulse, with the exception of ON RGCs at short pulse, where the activation occurred below the stimulating electrode. Applying monophasic cathodic waveforms with short duration pulses activated OFF and ON RGCs positioned under the stimulating electrode. In contrast, monophasic anodic waveforms with short duration pulses activated OFF and ON RGCs located far away from the stimulating electrode. The impact of using monophasic cathodic waveforms with long duration pulses for both RGC subtypes is similar to employing monophasic anodic with short duration pulses. Similarly, the impact of using monophasic anodic waveforms with long duration pulses for both RGC subtypes is similar to employing monophasic cathodic short duration pulses.

The symmetric biphasic current waveform is the most common pulse shape utilised in existing retinal prostheses (Weitz et al., 2014). This kind of pulse is more safe because it prevents buildup of toxic products that result from electrochemical reactions between electrodes and surrounding solution in the retina that may affect the retinal tissues. Asymmetric biphasic waveforms are also used in some clinical studies (Weitz et al., 2015). Here, we highlight and compare symmetric and asymmetric biphasic waveforms and their influence on the spatial activation of OFF and ON RGCs in both healthy and degenerate retinas. Figure

7.15 shows the influence of the asymmetric pulse waveform on the localisation of spatial activation of RGCs in the healthy continuum OFF and ON RGC models. This figure compares symmetric and asymmetric pulse waveforms on the position of OFF and ON RGC activation in the healthy retina. Symmetric biphasic charge-balanced cathodic first with short pulses (0.1 ms) resulted in activation of OFF RGCs far away from the stimulating electrode and activation of ON RGCs below the stimulating electrode in both healthy and degenerate retinas. In contrast, both OFF and ON RGCs in both healthy and degenerate (results not shown) retinas were activated under the stimulating electrode when asymmetric biphasic charge-balanced cathodic first waveforms with short pulses (0.1 ms) were employed Fig. 7.15.

For all figures presented in this section, we showed only the axonal compartment of OFF or ON RGCs because all compartments show almost the same responses, and the APs propagate along the RGC axons to the optic nerve. Therefore, the response of the RGC axon will be closer to what will be received by visual processing centres in the brain.

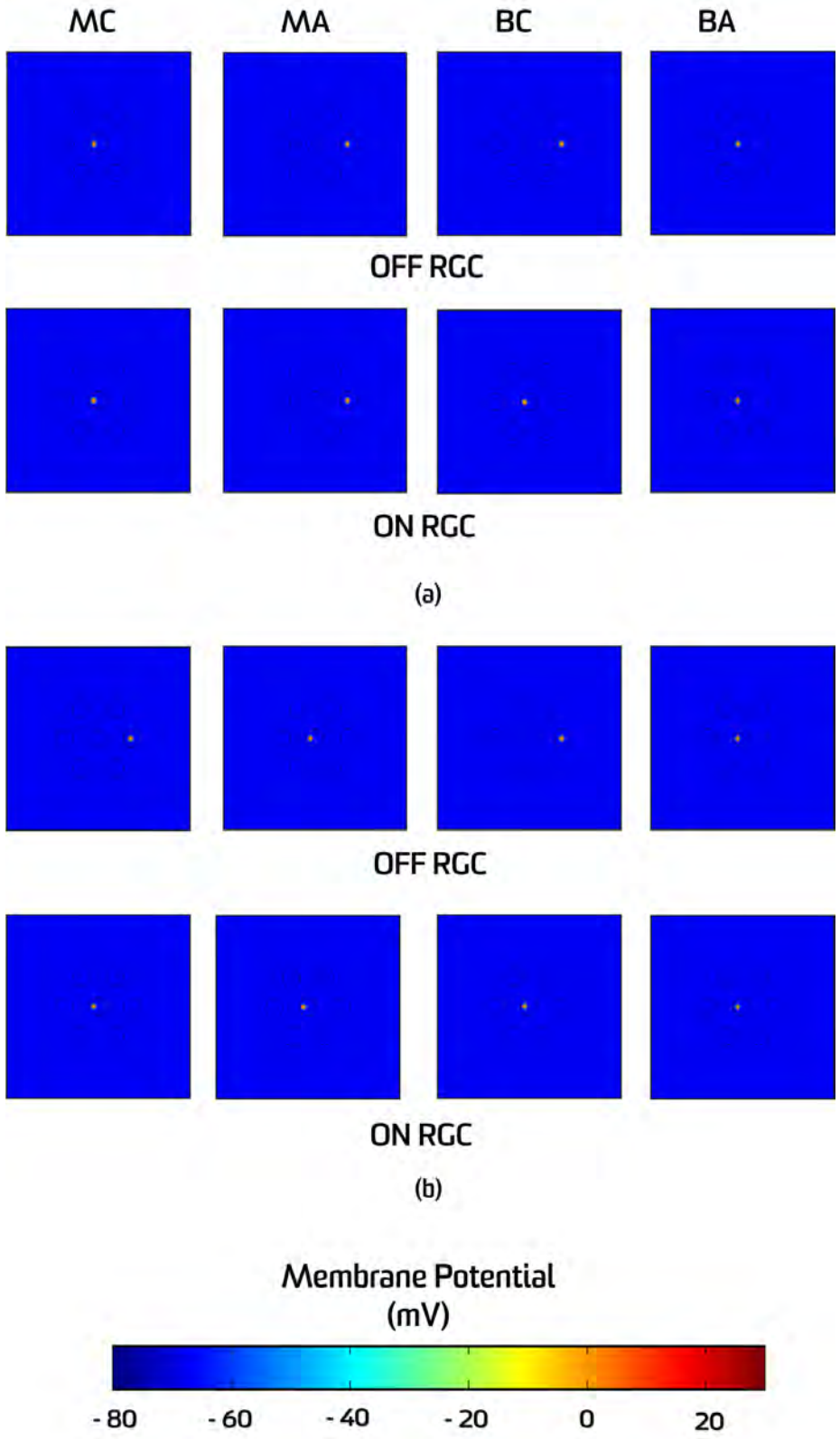

Figure 7.13: The influence of various pulse polarities and durations on the localisation of evoked phosphenes during suprachoroidal electrical stimulation of the healthy OFF and ON RGC models. Red dots represent the activated region of the axonal compartment of OFF and ON RGCs at threshold with (a) 0.1 ms and (b) 0.5 ms durations for different pulse polarity waveforms. MC (monophasic cathodic), MA (monophasic anodic), BC (biphasic cathodic), BA (biphasic anodic).

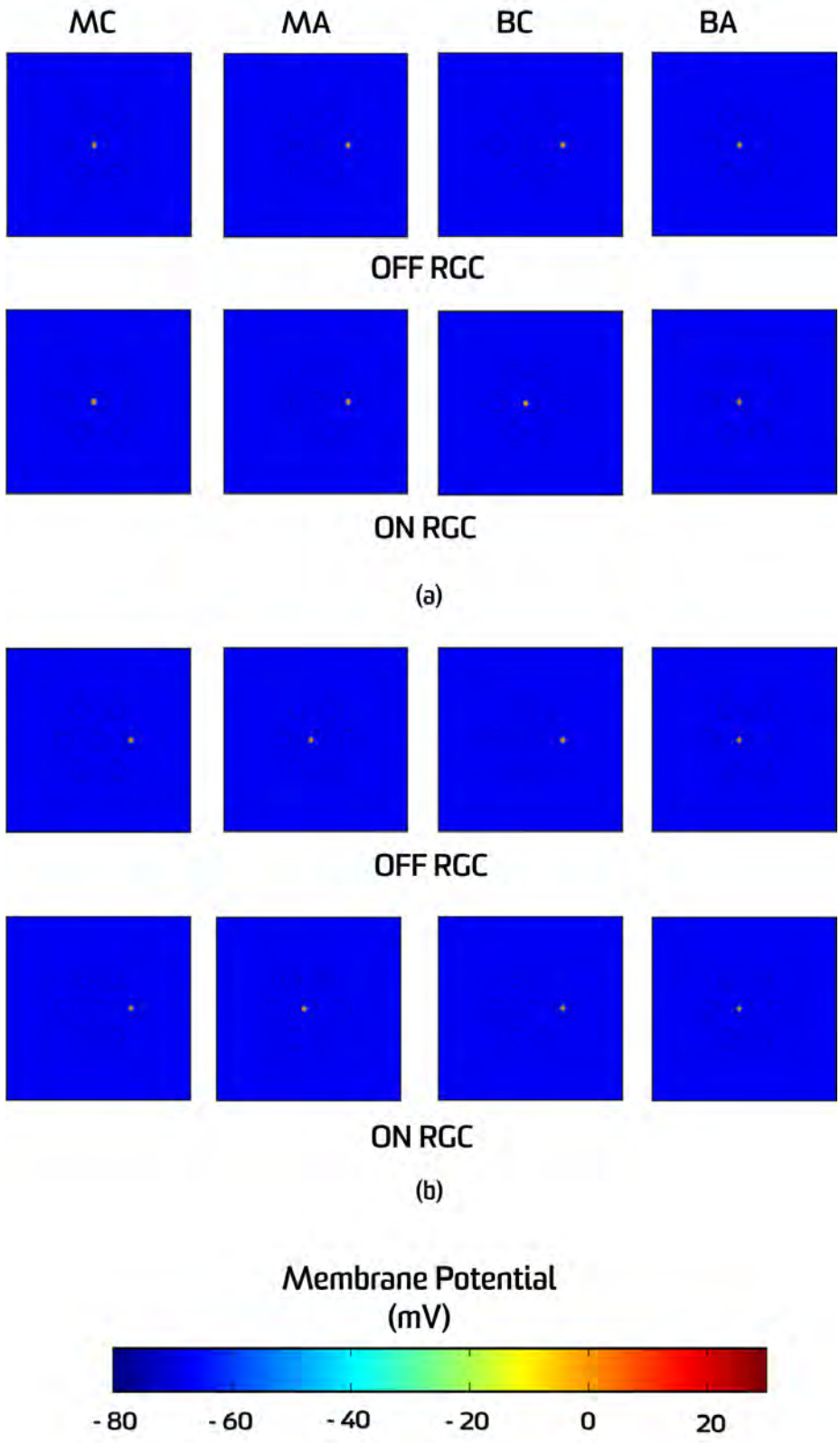

Figure 7.14: The influence of various pulse polarities and durations on the localisation of evoked phosphenes during suprachoroidal electrical stimulation of the degenerate OFF and ON RGC models. Red dots represent the activated region of the axonal compartment of OFF and ON RGCs at threshold with (a) 0.1 ms and (b) 0.5 ms durations for different pulse polarity waveforms. MC (monophasic cathodic), MA (monophasic anodic), BC (biphasic cathodic), BA (biphasic anodic).

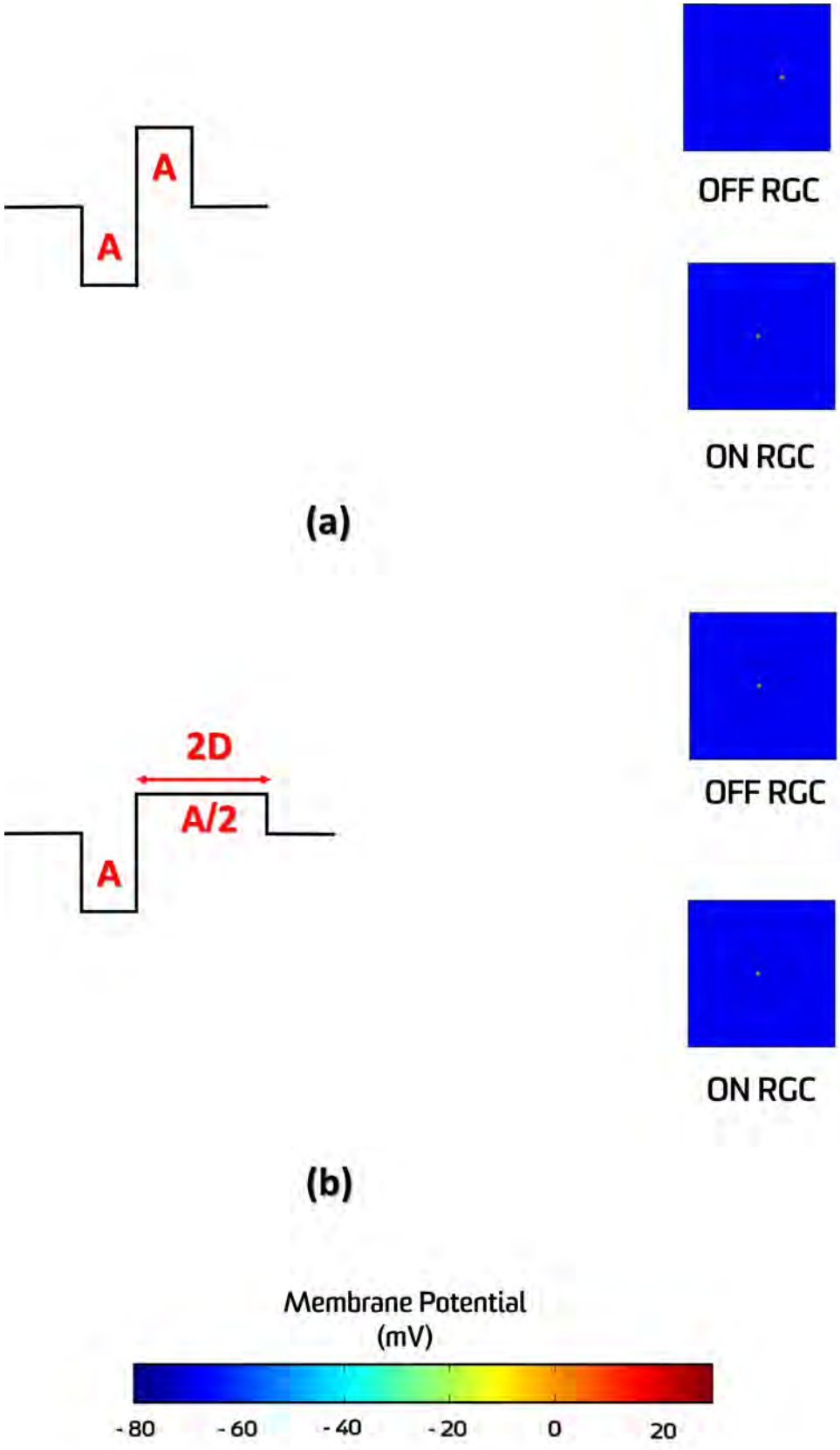

Figure 7.15: The influence of using (a) symmetric and (b) asymmetric biphasic charge-balanced cathodic first current waveforms on the localisation of evoked phosphenes in the healthy OFF and ON RGC retinal models. Red dots represent the activated region of the axonal compartment of OFF and ON RGCs at threshold with 0.1 ms duration. A (amplitude), D (duration).

7.4 Virtual Electrodes

The development of high-acuity visual prostheses requires an increase in the number of discernible excitation sites. The increase in the number of electrodes is hypothesised to be a solution for this aim. However, electric crosstalk between electrodes during simultaneous stimulation is one of the serious limitations of increasing the number of physical electrodes. Crosstalk can be defined as the spatial superposition of electrical fields, causing the degradation in the discriminable stimulation sites, hence, undesirable activation of RGCs can occur. This issue can affect the spatial selectivity, defined as the ability to discriminate between evoked phosphenes. Apart from increasing physical electrodes, virtual electrodes (VEs) can be used to improve the spatial selectivity (resolution) by activating intermediate areas between adjacent electrodes through controlling the percentage of current amplitude or pulse duration delivered by each electrode (Cassar et al., 2014; Dumm et al., 2014; Moghaddam et al., 2014).

In this section, two identical short pulses were injected into two adjacent electrodes to activate a neuron, but different scenarios of time offset were used. A virtual electrode of twice the pulse duration appears in the centre, activating neurons in the intermediate areas between these two adjacent electrodes. In the healthy OFF RGC model, we applied 120 μA biphasic, symmetric charge-balanced cathodic first pulses of 0.1 ms duration and no interphase interval on two suprachoroidal monopolar stimulating electrodes (with the return electrode being the top boundary of the vitreous) under three different scenarios: 1) simultaneously, 2) the second waveform starts immediately after the termination of the first, and 3) the second waveform starts when the first phase of the first waveform has finished.

Figure 7.16 illustrates the effect of time shift on creating virtual electrodes. When the stimulus waveforms were delivered simultaneously to the two stimulating electrodes, the electrodes only activated the local area adjacent to each

one. The trend to activate the region between two stimulating electrodes was obvious when the second waveform started after the first one. In addition, a virtual electrode which activates the intermediate region between the two stimulating electrodes was also clearly seen when the second waveform started just after the first phase of the first waveform.

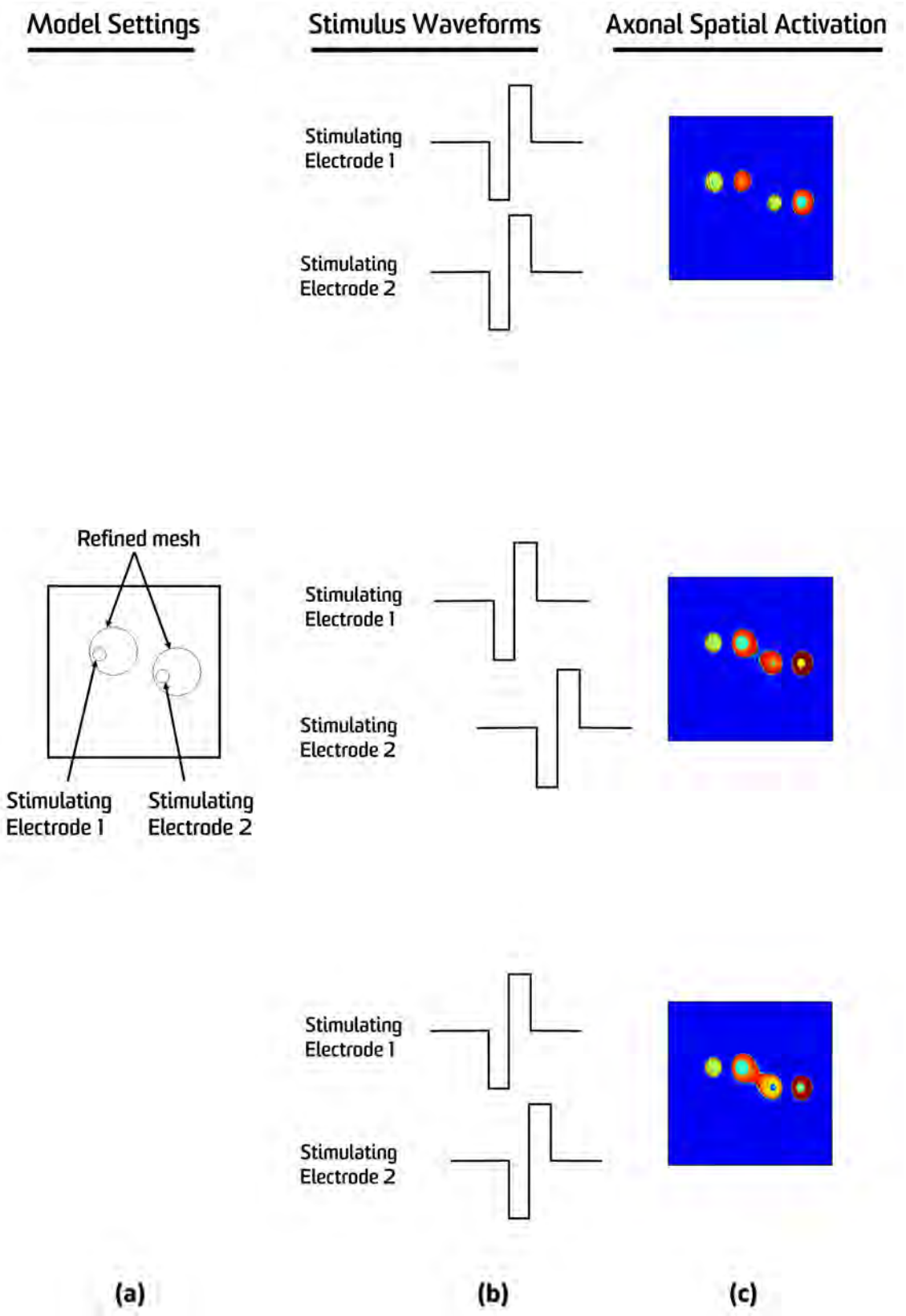

Figure 7.16: The effect of time shift on creating virtual electrodes. (a) Suprachoroidal stimulation settings for healthy OFF RGC model. Two stimulating electrodes (small circles) were used and localised refined mesh regions (large circles) were used to obtain good images. The return electrode was located remotely (above the vitreous) (b) The three different stimulus waveforms (c) Activation of axonal compartment of healthy OFF RGCs corresponding to these waveforms.

7.5 Discussion

7.5.1 Electrical stimulation of healthy and degenerate retina

In the previous chapter, the multi-domain continuum model of RGC electrical stimulation was validated against either a developed version of the discrete RGC model of the Guo et al., (2016) study or published *in vitro* experiments (Jensen et al., 2005*b*); (Tsai et al., 2009). Originally, parameters of the OFF & ON RGC ionic formulation were estimated to reproduce results of experimental intracellular electrical stimulation recordings from rabbit RGCs (Guo et al., 2016). To accurately validate the healthy retinal model, we chose the Jensen et al. (2005b) and Tsai et al. (2009) studies because their experiments were also conducted on rabbit RGCs, recording responses from extracellular electrical stimulation. Interestingly, the thresholds for evoking APs predicted by our simulations are within the range reported by Jensen et al. (2005b) for OFF RGCs, often close to the median thresholds. Similarly, our simulation results have replicated the thresholds reported by Tsai et al. (2009) for OFF & ON RGCs. These results confirm the capability of the model to reproduce experimental findings such as characterising the impact of electrode distance or pulse duration on current thresholds.

In this chapter, the first degenerate model of retinal electrical stimulation incorporating active membrane properties has been developed based on information obtained from the literature. This degenerate model differs from the Cottaris and Elfar (2005) model as follows:

1. They modelled the degenerate retina by only excluding photoreceptors from the retinal network. In contrast, the degenerate model presented in this thesis is more complex and developed based on changes occurring in the retina following degeneration such as cell death, the decrease in retinal layer thickness, and the formation of a glial seal.

2. Cottaris and Elfar (2005) only included the soma and dendrites to represent a neuron, whereas all RGC compartments are incorporated in our model.

3. They used non-gated ion channels (leaky conductances) whereas gated ion channels are employed in our model (active conductances).

4. Extracellular electrical stimulation only affects the soma in their model. However, all RGC compartments (soma, dendrites, AIS, and axon) are influenced by extracellular electrical stimulation.

5. They assumed the extracellular medium to be an infinite homogeneous domain, with the return electrode located at infinity. Our model resembles the realistic electrical stimulation environment by enclosing the retina inside a finite domain, with stimulating and return electrodes located locally.

The degenerate retinal model has been implemented and compared with the healthy retinal model. Two electrode placements (epiretinal and suprachoroidal) were simulated with the healthy and degenerate retinal models. The influence of glial scar layer on current thresholds was investigated for both electrode placements.

7.5.1.1 Electrical stimulation thresholds in healthy RGC

The threshold charge needed to activate the healthy epiretinal model was 16.5 nC and 36 nC for OFF and ON RGCs respectively, by applying biphasic symmetric charge-balanced cathodic first pulse waveforms of 0.5 ms duration and no interphase gap. These findings are in a good agreement with epiretinal monopolar stimulation thresholds reported for rabbit RGCs by Jensen et al. (2005a) with 125 μm electrode size (0.8-40 nC and 0.5-60 nC for OFF and ON RGCs respectively with monophasic cathodic pulses of 1 ms pulse duration) (Jensen et al., 2005*a*). Sekirnjak et al. (2006) have provided a valuable review of most studies that reported thresholds for epiretinal electrical stimulation for human and animal *in vitro* and *in vivo* experimental data. The required charge threshold to activate

RGCs *in vitro* studies on retina was quantified to be between 8-30 nC (Sekirnjak et al., 2006).

Our healthy suprachoroidal model required a higher threshold for RCG activation than the healthy epiretinal case. The required charge to excite OFF and ON RGCs in the case of suprachoroidal electrical stimulation was 42 nC and 90 nC, respectively. Our simulated threshold was in the range reported in the literature. The study conducted by Nakauchi et al. (2005) found the required charge was 27.5 $\pm$ 5 nC using biphasic pulses with 0.5 ms pulse duration (Nakauchi et al., 2005). The Sakaguchi et al. (2004) study determined the required charge to be 33 $\pm$ 16.1 nC with biphasic pulses of 0.5 ms pulse duration (Sakaguchi et al., 2004). The Wong et al. (2009) study indicated the charge threshold was 76.47 $\pm$ 8.76 nC when utilising biphasic pulses of 0.4 ms duration (Wong et al., 2009). John et al. (2013) found the required charge to evoke cortical responses during suprachoroidal electrical stimulation on normally sighted cats was between 40-130 nC for pulses ranging from 0.1 ms to 3 ms (John et al., 2013). The required charge determined by Yamauchi et al. (2005) to stimulate RGCs was 150 $\pm$ 122 nC using biphasic pulses of 1 ms pulse duration (Yamauchi et al., 2005). The higher thresholds in suprachoroidal electrical stimulation were expected due to the presence of the retinal pigment epithelium, which is known to have a high resistance, as well as the larger distance between the stimulating electrode(s) and the RGC layer (Wong et al., 2009).

7.5.1.2 Electrical stimulation thresholds in degenerate RGC

For the suprachoroidal electrode configuration simulations, the healthy model exhibited lower thresholds compared to the degenerate model. Interestingly, there was significant variation in current thresholds between healthy and degenerate suprachoroidal stimulation, especially with higher resistance values for the glial scar layer. In some cases, there was more than a three-fold difference, which is consistent with the elevated thresholds reported in published experimental stud-

ies. The median current threshold was found to be higher in rd1 mice, and ranged from 1.2 to 7.4 times the thresholds of wild-type mice (Jensen and Rizzo III, 2008, 2009; Suzuki et al., 2004). Moreover, current thresholds in P23H rats were determined to be 1.8 to 3 fold higher compared to SD rats (Jensen, 2012; Jensen and Rizzo III, 2011). Furthermore, in another study the threshold of S334ter-line-3 rats reached up to four times that of control rats (Chan et al., 2011). The thresholds were 2-6 times higher in Royal College of Surgeons rats compared to wild type (Mathieson et al., 2012). Reported thresholds for inducing phosphenes in RP patients were between 2.2-12 fold higher compared to healthy subjects (Jensen and Rizzo III, 2008). In a more recent *in vivo* study conducted on feline retinas, higher cortical thresholds were reported in the degenerate retina with mid-to-late stage remodelling during suprachoroidal electrical stimulation, attributed to the impact of glial scar (Aplin et al., 2016).

In contrast, for the case of epiretinal stimulation, the degenerate model activation threshold values were almost similar to those in the healthy model, regardless of the resistivity of the glial scar layer. Sekirnjak et al. (2009) found no difference in current thresholds between healthy and late stage degenerate rat retina in response to epiretinal electrical stimulation, which is in agreement with our results (Sekirnjak et al., 2009). Similarly a more recent study by Weitz et al. (2015) found the thresholds of epiretinal electrical stimulation of S334ter-line-3 rats and wild-type rats were similar (Weitz et al., 2015).

7.5.1.3 Possible causes of discrepancy in reported thresholds for electrical stimulation of degenerate RGC

The aforementioned experimental data of degenerate retinal electrical stimulation have indicated contradictory reports in current thresholds relative to healthy retina.. Most studies investigating the required current threshold to activate the degenerate retina noted the elevation in threshold regardless of the electrode placement. In contrast, some studies showed no difference in current thresholds

between healthy and degenerate retinas. However, differences in electrical stimulation settings and the stage of degeneration could be one source of variation between these studies. A possible explanation for the elevation in threshold for most studies could be attributed to the excitation of both RGC and bipolar cell types. Long-latency spikes have been observed, which are indicative of stimulation of inner retina (Weitz et al., 2015). Direct stimulation of RGCs by applying short pulse widths (0.05 ms to 0.1 ms) and synaptic blockers, revealed no differences in thresholds between normal and degenerate retina (Sekirnjak et al., 2009). Similarly, Weitz et al. (2015) corroborated this finding: when they applied short pulses (0.06 ms) to the late stage of rat degenerate retina the thresholds were similar, but when they applied long pulse (25 ms) the thresholds were elevated in the degenerate retina, which was attributed to bipolar cell stimulation (Weitz et al., 2015). A recent epirtinal stimulation study applied pulses with four different pulse durations (0.1 ms, 0.2 ms, 0.5 ms and 1 ms) on normal and degenerate mice retinas, classifying the observed response into two groups for each retina: slow (below 2 Hz) and high (10-14 Hz) spontaneous firing rate (Cho et al., 2016). They found the thresholds of the rd10 RGC slow spontaneous rate group were two-fold higher than the wild-type (WT) high spontaneous rate group. In contrast, the rd10 RGC high spontaneous rate and WT low spontaneous rate groups were almost similar. However, they did not identify the relationship between pulse duration and threshold and they also used retinal tissue in an intermediate stage of degeneration in which the retina had not undergone substantial remodelling such as the formation of a glial seal and retinal rewiring. Collectively, epiretinal stimulation with short pulses may bypass the degenerative architecture, such as the high impedance glial scar and retinal rewiring, associated with network retinal stimulation (Marc et al., 2003; Weitz et al., 2015). The continuum models could be considered as models of direct RGC stimulation, since we modelled the inner retina as a passive layers. As we have not included inner nuclear cells, the model cannot be applied to investigate differences in responses to short or long

pulses, nevertheless the most effective factor will be the placement of electrodes. In the suprachoroidal electrode configuration, the current will pass through the high impedance glial scar layer, whereas it will not in the epiretinal configuration.

7.5.2 The effect of return electrode configuration on spatiotemporal activation of RGCs

7.5.2.1 The suprachoroidal electrical stimulation case

Our simulation results (using electrodes of size 380 μm and centre to centre spacing of 730 μm) suggested that thresholds for RGC stimulation were similar for all return electrode configurations in the case of healthy and degenerate OFF and ON RGC models during suprachoroidal electrical stimulation. However, hexapolar and 80% QMP electrode configurations exhibited more focal spatial activation. Our current threshold results seem to be in disagreement with experimental studies (Cicione et al., 2012; Habib et al., 2013; Matteucci et al., 2013; Wong et al., 2009). An *in vitro* experimental study conducted on rabbit retina showed that using the hexapolar configuration produced more focal activation and higher thresholds compared to monopolar configuration (Habib et al., 2013). Moreover, the *in vivo* studies using suprachoroidal electrical stimulation indicated that hexapolar configuration required 2-3 times higher than monopolar thresholds for evoking cortical responses in cats (Cicione et al., 2012; Matteucci et al., 2013; Wong et al., 2009). However, the simulation results of the Abramian et al. (2014) computational study have indicated no difference between the various return electrode configurations when using electrodes of size 100 μm and spacing 400 μm. Furthermore, another mathematical study by Moghaddam et al. (2014) revealed that there is negligible difference among the three return electrode configurations (monopolar, quasi-monopolar and hexapolar) in activation threshold or activated retinal area where the distance between electrodes and targeted cells is less than the electrode diameter, as is the case in our simulations where electrode diame-

ters were greater than the distance between electrodes and RGCs. Furthermore, a more recent study by Eiber et al. (2017) using electrode configurations almost identical to the hexapolar configuration employed in our simulations (360 μm and 720 μm for diameter and centre to centre spacing respectively) using *in vitro* recordings and simulations of morphologically and physiologically accurate human RGC cable models, found that monopolar thresholds were not significantly different from multipolar thresholds .

7.5.2.2 The effect of using larger choroid thickness, electrode size and electrode centre-centre spacing

Our simulation results of suprachoroidal electrical stimulation are in agreement with the Abramian et al. (2014) study on the marginal impact of electrode size, with the most significant influence being the electrode centre-centre spacing (Abramian et al., 2014). The marginal effect of electrodes size is clearly observed in Figures 7.9 and 7.10 when using electrode spacing 730 μm with two electrode diameters, 50 μm and 380 μm, which in both cases the thresholds of monopolar, QMP and hexapolar electrode configurations were similar. In contrast, electrode centre-centre spacing was the most important factor influencing thresholds among the three return configurations. With the closely spaced electrode arrangement, the current threshold for hexapolar ranged 1.3-15 times higher than for the monopolar (Figure 7.10). Moreover, our suprachoroidal simulations with an average human choroid thickness of 426 μm (Brown et al., 2009) revealed an increase in hexapolar threshold by 20% compared to the monopolar configuration (Figure 7.8), comparable to an *in vivo* study which showed that hexapolar thresholds were only higher by 32% compared to monopolar (Spencer et al., 2016). There was no difference in thresholds among all three return electrode configurations when we used the original choroid thickness of 200 μm (Figures 7.6 and 7.7), however increasing the choroid thickness to 426 μm increased the difference in threshold among these configurations. Before increasing the choroid thickness,

the distance between the MEA and the target RGC layer was less than our electrode diameters (380 μm), but after increasing the choroid thickness the distance was larger than the electrode size. The latter finding confirms the results of the Moghaddam et al. (2014) study, which revealed there was no difference between return electrode configurations when the distance between the MEA and targeted cells is less than the electrode diameters.

7.5.3 The effect of pulse polarity and duration

7.5.3.1 Direct vs indirect retinal electrical stimulation

The recorded response observed from the retina is largely dependent on stimulus configuration and parameters such as the electrode placement, pulse polarity and pulse duration (John et al., 2013; Shivdasani et al., 2010; Weiland et al., 2016). It is recognised that the electric field will be strongest closest to the electrode, decreasing with the square of the distance away. Therefore, retinal ganglion cells will be exposed to the strongest electrical field with epiretinal prostheses, whereas the inner retina will experience the strongest electrical field with subretinal and suprachoroidal prostheses. Hence, the response elicited from the retina may be different depending on the position of the stimulating electrode (Weiland et al., 2016). Electrical stimulation of the retina usually targets bipolar or ganglion cells. As a result, the mechanism that activates RGCs is divided between direct and indirect stimulation. Direct stimulation targets ganglion cells by directly depolarising their membrane, generating action potentials without presynaptic input from the inner retina network. This mechanism can be accomplished by using epiretinal implants and short duration pulses ($\leq$ 0.1 ms), which preferentially stimulate RGCs and are ineffective in activating inner retinal neurons. Indirect stimulation aims to activate the inner retinal network, particularly bipolar cells, which in turn activate RGCs through synaptic inputs. This kind of stimulation can be achieved using epiretinal implants with using long duration pulses

($\geq$ 0.5 ms) or using subretinal and suprachoroidal implants which preferentially activate the inner retinal neurons (Jensen et al., 2003; Weiland et al., 2016).

7.5.3.2 The effect of pulse polarity

Many experimental studies have been conducted to determine RGC current (Jensen and Rizzo III, 2009; Jensen et al., 2003, 2005*a*; Sekirnjak et al., 2006; Tsai et al., 2009). It was found that electrode placement, pulse polarity and pulse duration have a significant influence on the responses to current stimuli. Monophasic cathodic current stimulation of ganglion cells exhibited lower thresholds than monophasic anodic stimulation in epiretinal stimulation (Jensen et al., 2003, 2005*b*). In contrast, monophasic anodic stimulation exhibited lower thresholds than monophasic cathodic current waveforms with subretinal stimulation (Boinagrov et al., 2014; Stett et al., 2007). Jensen and Rizzo III (2009) compared monophasic cathodic, monophasic anodic and biphasic charge balanced anodic first current pulses in normal and degenerate mouse retinas stimulated subretinally, finding that monophasic cathodic pulses were less effective than other waveforms in both retina types. Monophasic anodic waveforms were slightly better in normal retina, whereas monophasic anodic and biphasic waveforms showed similar thresholds in the degenerate retina . Current thresholds for short, intermediate, and long latency responses for different pulse durations were found to be similar for cathodic epiretinal stimulation and anodic subretinal stimulation (Eickenscheidt et al., 2012). When using 2 ms biphasic charge balanced cathodic first stimuli, epiretinal and subretinal implants exhibited similar thresholds (Sim et al., 2014). The difference in current thresholds for different current pulse polarity waveforms exhibits also a strong relationship with the size of electrode and RGC subtype (Jensen and Rizzo III, 2006; Jensen et al., 2003, 2005*b*). During epiretinal stimulation with small electrode size (5 μm), it was found that monophasic cathodic stimuli were 7-10 times lower than monophasic anodic stimuli (Jensen et al., 2003), compared to only 2 times lower when

using larger electrodes (500 μm) (Jensen et al., 2005*b*). The impact of RGC subtype on current thresholds has been examined by using subretinal stimulation, with results indicating that monophasic cathodic stimulation of OFF RGCs exhibits higher thresholds 2-7.5 times that of monophasic anodic pulses, whereas ON RGCs exhibited similar thresholds for both waveforms (Jensen and Rizzo III, 2006). The same investigators found that using monophasic anodic pulses, current thresholds for OFF and ON RGCs were similar. These findings indicate that using subretinal implants with monophasic cathodic pulses, selective stimulation of OFF and ON RGCs may be possible.

7.5.3.3 The effect of pulse polarity and duration on evoked phosphenes

Pulse waveform and duration have been recognised to play a significant role in retinal electrical stimulation (Weiland et al., 2016; Weitz et al., 2014, 2015). Reducing the pulse duration was found to be a viable solution to avoid the activation of passing axons which has been observed to affect the shape of visual percepts seen by patients (Weiland et al., 2016; Weitz et al., 2015). Epiretinal stimulation using short duration pulses ($\leq$ 0.1 ms) activate RGCs near the stimulating electrode, and the activation threshold of passing axons was two-fold higher than that of somatic activation (direct stimulation). Additionally, long duration pulses (25 ms) delivered via epiretinal stimulation provided focal activation, with the range of activation threshold between somatic and passing axons larger than that attained using short duration pulses, attributed to the activation of bipolar cells which in turn activate RGCs (indirect stimulation) (Weitz et al., 2015). Nanduri (2011) and Nanduri et al. (2012) found by using the same stimulating electrode, patients reported two types of percept shapes: focal (when 25 ms pulses were used) (Nanduri, 2011) and elongated (when 0.45 ms pulses were used) (Nanduri et al., 2012). Clinical data have shown that the increase in stimulus amplitude leads to phosphenes being larger and brighter (Weitz et al., 2014). Therefore, reducing

current thresholds will have a significant impact on retinal prostheses through increasing the dynamic range, defined as the difference between the charge safety limit and threshold. By increasing the dynamic range, we can control the size and brightness of phosphenes while not exceeding the safety limit. Pulse duration was also found to be a solution to decrease current thresholds. The Weitz et al. (2014) study results indicated that the threshold for electrical activation of RGCs can be reduced up to 20-25% in salamander RGCs (*in vitro* experimental & computational simulations), 50% in cat (simulations) and 10-15% in perceptual thresholds of five retinal prosthesis patients by increasing the length of the Interphase Gap (IPG) (Weitz et al., 2014).

7.5.3.4 Spatial activation properties of RGCs

Many experimental studies have investigated the temporal properties of electrically evoked RGC spikes. The development of retinal implants however requires depth understanding of the spatial RGC activation properties and how it impacts vision acuity. Calcium imaging experimental data of electrical stimulation of RGCs has provided valuable insights on the spatial activation of large populations of RGCs (Behrend et al., 2011; Weitz et al., 2014, 2015). Behrend et al. (2011) found the minimum attained spatial resolution was 150 μm, and this resolution could result in a visual acuity of 20/660. Such acuity will assist patients to read text with font size larger than 70-point at a distance of 35 cm. Additionally, these studies have demonstrated the importance of pulse duration on the focal activation and localisation of visual percepts. By applying charge-balanced, asymmetric biphasic cathodic first current waveforms with different pulse durations, their results have indicated that RGCs nearest the stimulating electrodes were activated at lower thresholds compared to distal RGCs when short pulses ($\leq$ 0.1 ms) or long pulses ($\geq$ 25 ms) were used, even for normal or degenerate retinas (Weitz et al., 2015). A very recent experimental study found approximately a 20% difference between somatic and axonal activation when biphasic symmet-

ric charge-balanced waveforms with short pulses ($\leq$ 0.15 ms) were used (Chang and Weiland, 2017). Interestingly, that study revealed that biphasic anodic first waveforms with short duration pulses (0.04 ms) were more effective in avoiding the activation of passing axons than biphasic cathodic first waveforms with the same pulse duration. It was proposed that cathodal stimulation of any excitable cell depolarises the cells nearest to the stimulating electrode, whilst anodal stimulation hyperpolarises those cells under the electrode, depolarising more distant cells. Consequently, the location of the lowest RGC threshold could be different depending on whether cathodal or anodal stimulation is used (Jensen et al., 2003).

7.5.3.5 Comparison simulation results to previous studies

Our suprachoroidal simulation results have demonstrated the influence of pulse polarity and duration on the spatial activation profile of healthy and degenerate retina. Symmetric charge-balanced anodic first stimulus waveforms always activated both RGC subtypes under the stimulating electrode for both healthy and degenerate retina, regardless of the pulse duration. This finding could be considered as a solution to avoid the activation of passing axons, since this waveform produces more focal activation directly under the stimulating electrode. This result is in high agreement with the *in vitro* calcium imaging study conducted on mice, demonstrating that biphasic symmetric charge-balanced anodic first waveforms are more effective in activating RGCs located near the stimulating electrode (Chang and Weiland, 2017). Moreover, the selective activation of OFF and ON RGCs in healthy retina could be attained by using symmetric charge-balanced cathodic first waveforms, which activate OFF RGCs far away and ON RGCs close to the stimulating electrode, using the fact that activation thresholds of OFF RGCs are lower than ON RGCs. In contrast, both OFF and ON RGCs were activated close to the stimulating electrode in degenerate retina for both pulse durations. These findings in healthy and degenerate retina have some agreement with ex-

perimental calcium imaging studies, which reveal that with short pulses ($\leq$ 0.1 ms) activation was more focal in the healthy and degenerate retina, whereas with longer (0.4 ms) pulses, the focal activation was less pronounced in the healthy retina (Behrend et al., 2011; Weitz et al., 2015). However, these experiments used asymmetric biphasic waveforms and did not distinguish between RGC subtypes. The location of lowest thresholds for both OFF and ON RGCs in healthy and degenerate retinas for monophasic cathodic with short duration pulses (0.1 ms) was different when monophasic anodic waveforms with short pulses were used: cathodic waveforms activated cells nearest the stimulating electrode and anodic waveforms activated more distal cells. The opposite mechanism occurred when long pulses (0.5 ms) were used. Monophasic waveforms with short pulse results are consistent with the notion that cathodal stimulation excites those cells close to the stimulating electrode whereas anodal stimulation activates distal cells. It was observed in our simulations that monophasic cathodic waveforms always operate opposite to monophasic anodic waveforms for both short and long pulse durations and for healthy and degenerate retina. For example, monophasic cathodic waveforms with short pulse duration (0.1 ms) activated RGCs close to the stimulating electrode whereas monophasic anodic waveforms activated distal RGCs.

The difference between asymmetric and symmetric pulse durations has been investigated in both healthy and degenerate retinal models. When applying asymmetric biphasic charge-balanced cathodic first stimuli with short pulse duration (0.1 ms), the activation was always under the stimulating electrode for both OFF and ON RGCs in both healthy and degenerate retina models. These results are in excellent agreement with the study of Weitz et al. (2015), which found that when using the same asymmetric waveforms with the same pulse duration, activation was more focal under the stimulating electrode for both healthy and degenerate retina. Moreover, these results have indicated the impact of pulse duration shape: asymmetric biphasic charge-balanced cathodic first waveforms changed the location of activated OFF RGCs in both healthy and degenerate retina models to

be under the stimulating electrode, which was different to what was obtained with symmetric biphasic waveform.

7.5.4 Virtual Electrodes

Simulation results have demonstrated that the virtual electrode stimulation technique allows for activation of the intermediate regions between the stimulating electrodes, leading to improvement in the acquired visual perception. The principle of virtual electrode was implemented successfully by stimulating two neighbouring electrodes using a slight time offset between two pulse duration waveforms. Previous studies on virtual electrodes in retinal electrical stimulation are limited (Dumm et al., 2014; Moghaddam et al., 2014; Spencer et al., 2018), with one preliminary study investigating the effect of time shift on creating virtual electrodes (Cassar et al., 2014). However, this technique (virtual electrodes) is implemented clinically in cochlear implants to improve the resolution of auditory spectral provided to patients (Spencer et al., 2018). In the retina, limited pre-clinical studies examined the influence of field shaping approaches. Virtual electrodes can be elicited between two physical electrodes and its location can be shifted to one of them by increasing the amount of current stimulus to that electrode (Dumm et al., 2014). Virtual electrodes can resolve one of the significant problems associated with prosthetic devices which is electrode failure. By manipulating the current stimulus delivered to neighbouring electrodes, the faulty electrode can be compensated. Hence, deficits in phosphene counts and possible damage associated with reimplantation can be avoided (Spencer et al., 2018).

Our simulations have revealed that the creation of virtual electrodes occurred clearly when overlapping the second phase of the first waveform and the first phase of the second waveform. This finding is consistent with the Cassar et al.(2014) study, which used two biphasic cathodic first waveforms with 1 ms pulse width and a 1.75 ms interphase delay. However, this study only examined this technique in saline solution, showing only the effective doubling in pulse duration

as a result of overlapping stimulus phases (Cassar et al., 2014). Interestingly, we also demonstrated this result using the active multi-compartmental continuum model of RGCs: our results indicating that the spatial activation of membrane potential was spread between the two stimulating electrodes when there was a time shift between the pulses delivered to each stimulating electrode (Figure 7.16). In contrast, the area surrounding the stimulating electrodes was only activated when the pulses were delivered simultaneously, which is the case in current retinal prostheses. This finding could be useful in enhancing our understanding of the mechanisms underlying virtual electrodes, hence improving the efficacy of retinal implants by inducing more phosphenes with less numbers of physical electrodes.

8 Conclusion

This thesis developed a novel multi-compartment continuum model to assist in the understanding of mechanisms underlying RGC activation in response to electrical stimulation, both intracellular and extracellular. The results outlined in chapters 5, 6, and 7 have three major contributions to existing RGC studies and current retinal prosthesis development.

8.1 Modification of the Standard Neural Cable Equation

We have proposed a finite element method PDE approach for modelling intra- or extracellular electrical stimulation of discrete neuronal structures. This approach is based on a modification of the classical cable equation to account for the variation in geometry along the neuron, in particular the neuron radius. It presents significant benefits for the neuroscience modelling community. Firstly, the entire extracellular domain as well as neuronal stimulation can be implemented using the one numerical solver. Secondly, this modelling approach offers accurate solutions through implementing explicit realistic neuronal morphology during extracellular electrical stimulation. More significantly, this approach is also able to overcome inaccurate simulations associated with the classical cable equation during intracellular stimulation of excitable neurons utilising finite element solvers. Furthermore, this method is valid for any 1D excitable fibre morphology, electrode configuration, or non-uniformity in ion channel expression.

8.2 Development of novel multi-compartment continuum model of the retina

We have developed a novel multi-compartment continuum model of the retina, validated against developed version of the recent discrete RGC model incorporating detailed ionic currents and realistic morphological architecture. Its predictions matched published *in vitro* experiments under various electrode placements to ensure we obtained a robust model. Moreover, all RGC compartments have been accounted for in this model. The effect of axon orientation on RGC activation is well-reproduced by the multi-compartment continuum model. This will be useful in future studies of axonal activation, which has been shown to cause distortions in the shape of evoked phosphenes (Abramian et al., 2015). This new continuum model has included the two prominent types of ganglion cells: OFF and ON RGCs. Furthermore, the multi-compartmental continuum model incorporates the most up to date ionic currents, which have been observed to have a significant impact on RGC firing patterns.

The modelling framework presented here is modular, and developed in mind of applicability to any neural tissue. This continuum modelling approach, incorporating dendritic field and axonal representation, captures current flow in the extracellular domain. Relative differences in extracellular potentials between the soma and distal dendrites or the distal axon act as a driver for eliciting somatic responses to external electrical stimulation. The effective extracellular potential experienced by the dendrites in each neuron in the bulk tissue was determined by taking the average of four equidistant points at the perimeter of its dendritic field. The effective extracellular potential of the distal axon was characterized by taking the extracellular potential at a remote offset point in the direction of the axon.

8.3 Comparison between our Multi-Compartment Continuum Model and Previous Continuum Models

The developed continuum model in this thesis differs from those previous continuum models in terms of its implementation and its validation. In contrast to previous continuum models that were composed of only one compartment (soma or AIS), our continuum model incorporates multiple RGC compartments. This makes it possible to simulate the spatial extent of activation of individual compartments, including RGC axons, which is useful in simulating the response of the retina to electrical stimulation. Moreover, our continuum model includes up to date ionic currents discovered recently, that have been found to play a significant role during electrical stimulation of the retina (Margolis and Detwiler, 2007; Mitra and Miller, 2007). Furthermore, the two prominent types of RGCs: ON and OFF RGCs were involved in our model rather than one type as in previous continuum models (Abramian et al., 2014; Al Abed et al., 2015*a*; Joarder et al., 2011; Yin et al., 2010). The validation of our continuum model was undertaken using a more robust process compared to existing continuum models. In the validation of previous continuum models, the remote conductance (g_r) parameter (i.e. one value) was tuned manually to match experimental threshold in only one experiment (Abramian et al., 2014; Joarder et al., 2011). In contrast, we validated our continuum model against both a modified version of a recent discrete RGC model (Guo et al., 2016) and the data of different *in vitro* experiments (Jensen et al., 2005*b*; Tsai et al., 2009). During validation against the discrete model, our continuum model passed over three stages of validation, and the values of intercompartmental conductances (i.e. twelve values: six values for each model) were estimated and optimized automatically using an optimization algorithm (see section 6.1.2). Without tuning any parameters of the model which was validated

successfully against the discrete model, we proceeded to compare against experimental epi- and subretinal electrical stimulation studies for both OFF and ON RGCs, replicating RGC thresholds as a function of electrode distance and frequency of current stimulation observed in these studies (Jensen et al., 2005*b*; Tsai et al., 2009). Results presented in chapter 6 & 7 agree with many published experimental (Aplin et al., 2016; Barriga-Rivera et al., 2017; Chang and Weiland, 2017; Eiber et al., 2017; Fried et al., 2009; Jensen et al., 2005*a*,*b*; Sekirnjak et al., 2009; Tsai et al., 2009) and modelling studies (Abramian et al., 2014, 2015; Eiber et al., 2017; Guo et al., 2016; Jeng et al., 2011), proving the efficacy of our continuum model as a tool for investigating or predicting the response of the retina under various electrical stimulation scenarios. For example, we showed action potential (AP) traces in different cellular compartments (see chapter 6). Furthermore, AP initiation occurred in the AIS when the electrode was located above the RGC, whereas the AP was initiated in the axon compartment when the electrode was positioned far away, consistent with many experimental studies (Fried et al., 2009; Jensen et al., 2005*b*) (see chapter 6). Compared to previous continuum models, the initiation of the AP was always from one location, because these models were formulated from one compartment (soma or AIS). Also, using our continuum model, we showed the inhibition phenomenon that could occur for some RGC compartments when high current was injected (Barriga-Rivera et al., 2017) (see chapter 6). Moreover, symmetric charge-balanced anodic first stimulus waveforms always activated both RGC subtypes under the stimulating electrode for both healthy and degenerate retina, regardless of the pulse duration, providing a high agreement with a very recent *in vitro* calcium imaging study conducted on mice (Chang and Weiland, 2017) (see chapter 7). More details on the difference between our continuum model and other continuum models, along with the results predicted by our continuum model, were presented in chapters 6 and 7.

8.4 Development of a degenerate retinal model including OFF and ON RGCs

We developed a degenerate retinal model of electrical stimulation of OFF and ON RGCs based on information from existing literature, including cellular and tissue remodelling. To the best of our knowledge, this is the first degenerate model of retinal electrical stimulation accounting for the changes occurring in the whole retina using very detailed models of OFF and ON RGCs. Current thresholds required to activate RGCs in the degenerate model were quantified and compared with the healthy models. In the suprachoroidal case, current thresholds of degenerate OFF RGCs ranged between 73 μA and 294 μA, depending on the resistivity of the glial scar layer, whereas the threshold of ON RGCs ranged between 165 μA and 670 μA. In contrast, thresholds of healthy OFF and ON RGCs were 84 μA and 180 μA respectively. Depending on the resistivity of the glial scar layer, it is evident there was an elevation in current thresholds in the degenerate model, up to four-fold higher than the healthy model for both RGC subtypes. This is consistent with previous experimental data that found the difference ranged 1.2-7.4 higher than the thresholds of healthy animals (Jensen and Rizzo III, 2008, 2009; O'Hearn et al., 2006; Weitz et al., 2015). However, in the case of epiretinal stimulation, the current thresholds of healthy and degenerate models were almost similar for both OFF and ON RGCs, in agreement with recent epiretinal animal experiments (Cho et al., 2016; Sekirnjak et al., 2009; Weitz et al., 2015). In the case of epiretinal stimulation of healthy and degenerate retina, thresholds were 33 μA and 72 μA for OFF and ON RGCs respectively.

8.5 Stimulus strategies for electrical stimulation of healthy and degenerate retinas

Various electrode configurations and stimulus parameters were investigated using the healthy and degenerate models of OFF and ON RGCs to optimise retinal prostheses. In the case of suprachoroidal stimulation, the effect of return electrode configurations the current thresholds, spatial activation and the shape of evoked phosphenes was examined using three different configurations (monopolar, quasi-monoploar and hexapolar). Our simulations suggest there was no significant difference among all three return electrode configurations if the distance between electrodes and the target layer is less than the electrode diameter. This is clearly evident when we increased the thickness of the choroid to 426 μm (in this case, the electrode diameters were less than their distance to the target layer). With this increase in choroid thickness, current thresholds were elevated with hexapolar to be 20% higher than monopolar. Moreover, our results have shown the marginal effect of electrode size on reducing current thresholds, and no difference among all configurations either using small or large electrode sizes. The most influential factor on differentiation between the three configurations was electrode-electrode spacing. With closely spaced electrodes, the current threshold for hexapolar ranged 1.3-15 times higher than that of monopolar.

The influence of pulse polarity and duration on the spatial activation of OFF and ON RGCs in both healthy and degenerate retinas was also examined. By using four pulse waveforms and two pulse durations, our simulations presented interesting findings indicating the effect of these stimulus parameters on the spatial activation of OFF and ON RGCs. Based on our results, the symmetric charge-balanced anodic first waveform is the most effective stimulus for obtaining focal activation for both RGC subtypes in the healthy and degenerate retina, regardless of the pulse duration. Similarly, the asymmetric charge-balanced cathodic

first waveform with short pulse localised OFF and ON RGCs under the stimulating electrode in both healthy and degenerate models (long pulses not examined). The latter finding demonstrated the difference between symmetric and asymmetric biphasic pulses, and the impact of the asymmetric pulse on the localisation of evoked phosphenes. Moreover, selective activation between OFF and ON RGCs could be obtained using a symmetric charge-balanced cathodic first waveform with short pulse.

We implemented the first computational study that investigated the impact of time shift on the creation of virtual electrodes in retinal electrical stimulation. The principle of virtual electrodes was adopted and applied using our model, indicating it was possible to increase the number of evoked phosphenes without increasing the number of physical electrodes. As discussed, cross talk between electrodes increases with the increase in physical electrode number, causing degradation in the spatial resolution.

8.6 Future work

In future work, the model presented could be expanded in its retinal architecture by incorporating a synaptic connection from the retinal network, such as inputs from amacrine and bipolar cells. After incorporating these synaptic inputs, further work on virtual electrodes and current steering approaches may yield additional improvements to retinal prostheses. More interestingly, the model can serve as a basis for investigating selective activation between the two types of RGCs. Moreover, it will be possible to further explore how axonal activation can be avoided, which often results in elongated phosphenes during electrical stimulation of the retina in blind patients.

Appendices

Appendix A

Derivation of Extracellular Voltage Distribution Equation

The extracelluar potential of a circular disk electrode with radius a in a semi-infinite medium can be computed using the following isopotential disk formula (Wiley and Webster, 1982) for $z \neq 0$, where z is the height above the electrode perpendicular to the plane of the disk:

$$V(r,z) = \frac{2V_o}{\pi} \arcsin \left(\frac{2a}{\sqrt{((r-a)^2+z^2)} + \sqrt{((r+a)^2+z^2)}} \right) \tag{A.1}$$

At the surface of the electrode (z = 0), we have a normal current density of

$$J_z(r,0) = \frac{2\sigma V_o}{\pi} \frac{1}{\sqrt{(a^2-r^2)}} \tag{A.2}$$

or

$$J_z(r,0) = \frac{J_o}{2\sqrt{(1-\frac{r^2}{a^2})}} \tag{A.3}$$

By equating (A.2) and (A.3), we obtain:

$$\frac{2\sigma V_o}{\pi} \frac{1}{\sqrt{(a^2-r^2)}} = \frac{J_o}{2\sqrt{(1-\frac{r^2}{a^2})}} \tag{A.4}$$

$$V_o = \frac{a\pi J_o}{4\sigma} \tag{A.5}$$

Substituting (A.5) into (A.1), we obtain:

$$V(r,z) = \frac{aJ_o}{2\sigma} \arcsin \left(\frac{2a}{\sqrt{((r-a)^2+z^2)} + \sqrt{((r+a)^2+z^2)}}\right) \tag{A.6}$$

and the final formula after substituting $J_o = \frac{I_o}{\pi a^2}$ will be

$$V(r,z) = \frac{\rho I_o}{2\pi a} \arcsin \left(\frac{2a}{\sqrt{((r-a)^2+z^2)} + \sqrt{((r+a)^2+z^2)}}\right) \tag{A.7}$$

where I_o is the total applied to the electrode and ρ is the resistivity of the infinite medium current.

Appendix B

Mesh Convergence of Model After Reducing its Dimensions

We aimed to use a smaller maximum mesh element size (50 μm) to see if there is any difference in the required current threshold to activate RGCs in the model, which reproduces the (Jensen et al., 2005*b*) study. In following figure B.1, the comparison between different maximum mesh element sizes (50, 200 and 400 μm) was conducted when the dimensions of the origional model were reduced by 50 % . We found there is no effect on the current threshold between using a fine mesh of 50 μm and the normal mesh size of 400 μm (the difference was only 1 μA).

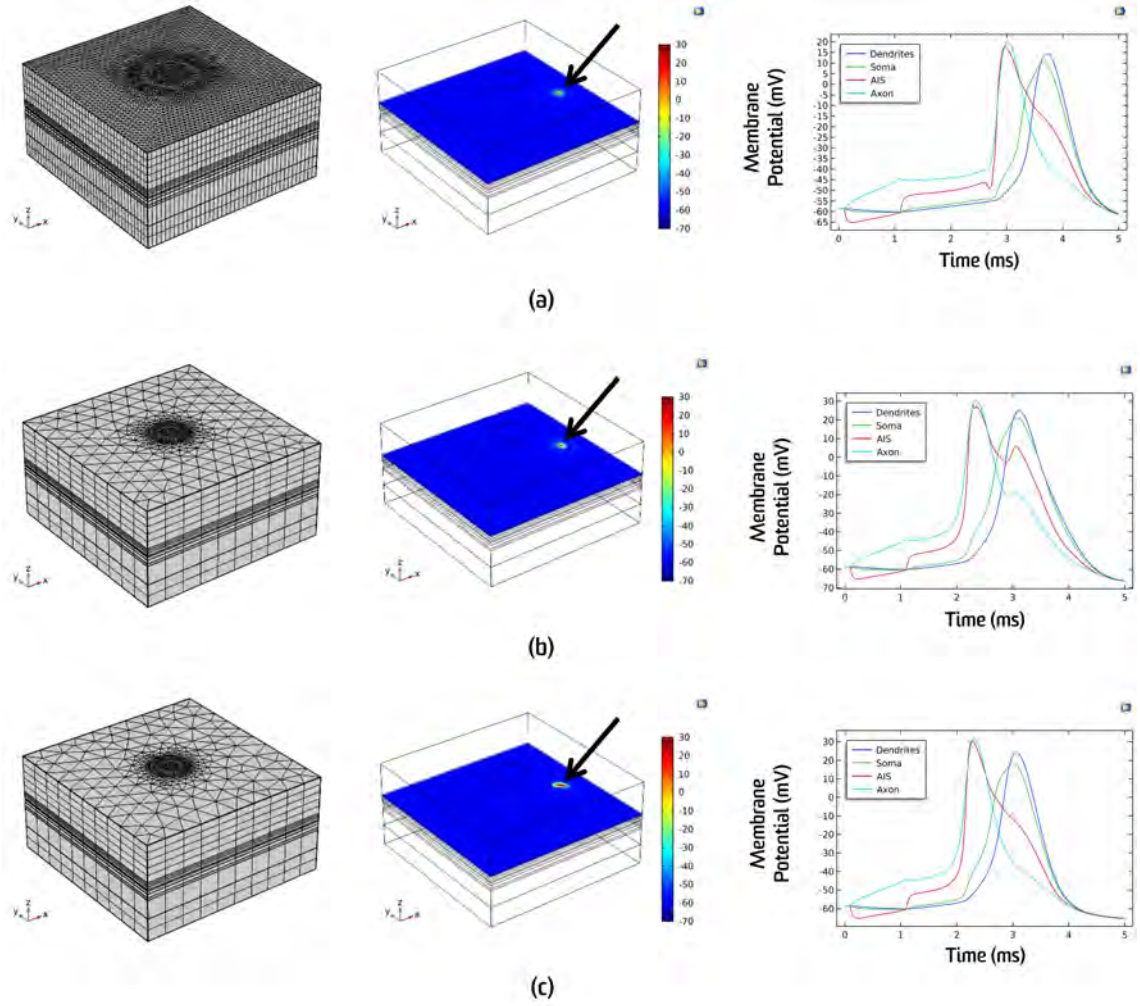

Figure B.1: Simulated action potential traces from various compartments of an OFF RGC obtained from a point probe located at the arrow and surface plots of OFF RGC layer activation in response to epiretinal electrical stimulation (replicating the experiment of (Jensen et al., 2005b)) corresponding to the three meshing schemes: (a) 50 μm (b) 200 μm (c) 400 μm.

Appendix C

The Presentation of Activation of Different RGC Segments During Intracellular Stimulation

During the intracellular stimulation, spatial as well as temporal patterns of the membrane voltage responses of different RGC compartments were slightly different, however, the number of spikes observed in each compartment was similar for all. In the following figure C.1, the activation of different RGC compartments during intracellular stimulation is shown.

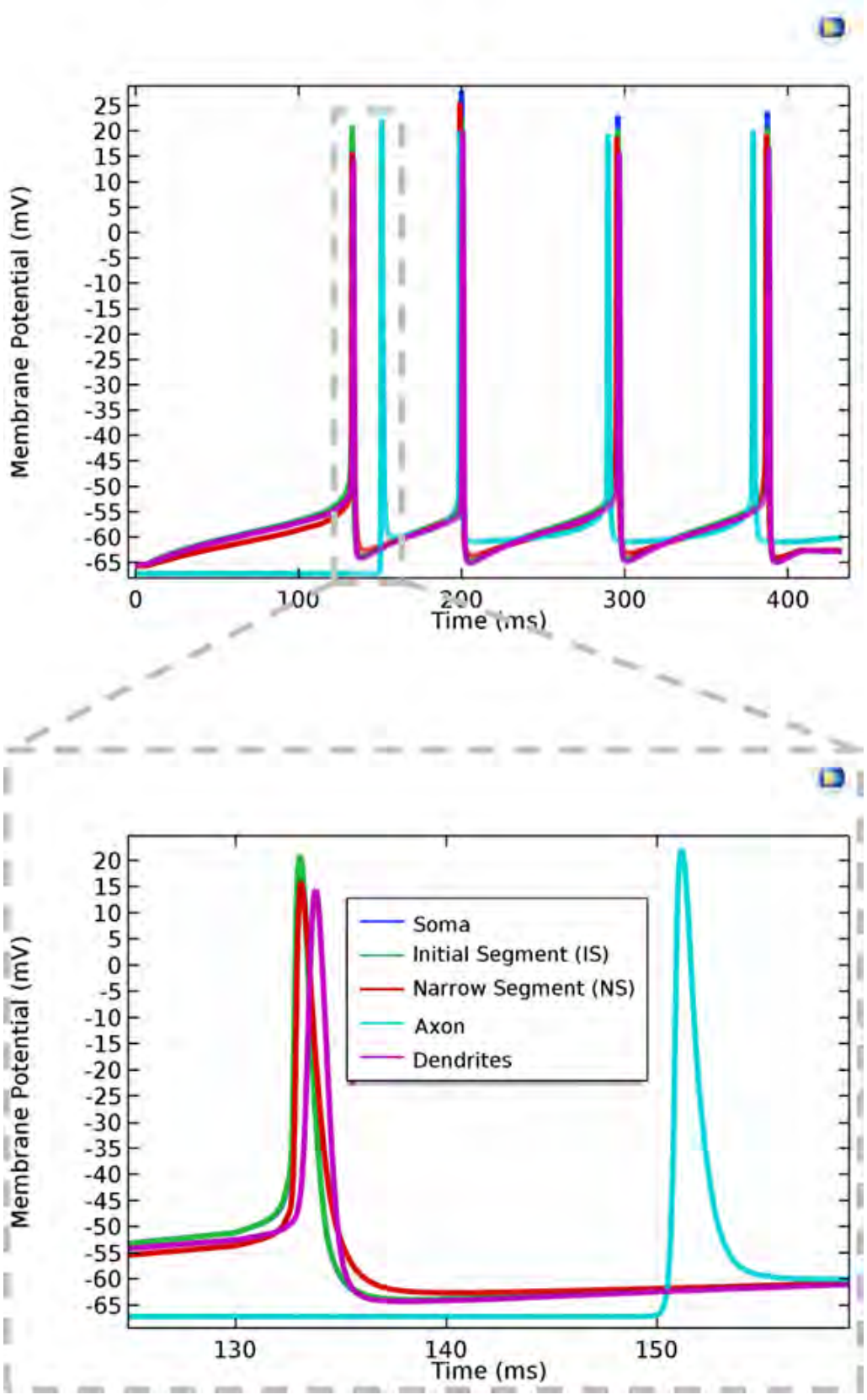

Figure C.1: The activation of different RGC segments during intracellular stimulation of FM-EC2.5 model (Fohlmeister and Miller, 1997b) using FEM based on the modified cable equation. A 10 pA depolarising constant current injection was applied in the soma and lasted for 400 ms.

Appendix D

Comparison of the Responses of the Morphologically-Realistic (discrete) OFF RGC and the Reduced Four-Compartment Models to Intracellular Stimulation

The comparison between the morphologically-realistic and reduced models of the OFF RGC through two different injection locations: (a) at the AIS, and (b) at the soma was presented in the following figure D.1.

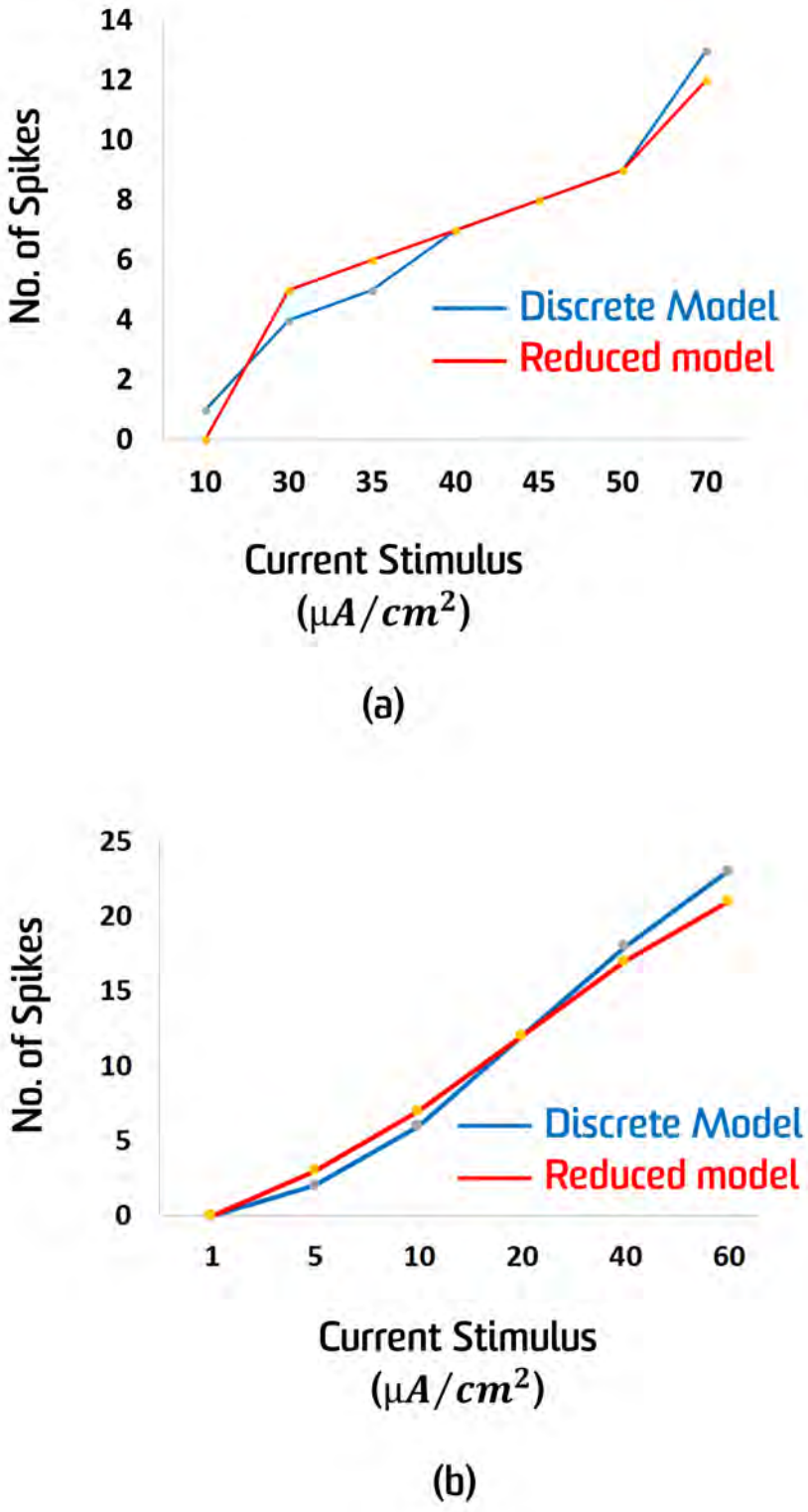

Figure D.1: Comparison between morphologically-realistic (discrete) and reduced models of OFF RGC in terms of the number of spikes for all RGC segments with different depolarising current injections. (a) in the AIS and (b) in the soma. In all cases, depolarising current injections were delivered into either the soma or AIS and lasted for 100 ms.

Bibliography

Abbas, S. Y., Hamade, K. C., Yang, E. J., Nawy, S., Smith, R. G. and Pettit, D. L. (2013), 'Directional summation in non-direction selective retinal ganglion cells', *PLoS computational biology* **9**(3), e1002969.

Abbott, L. F. (1994), Single neuron dynamics: an introduction, *in* 'Neural modeling and neural networks', Elsevier, pp. 57–78.

Abramian, M., Lovell, N. H., Habib, A., Morley, J. W., Suaning, G. J. and Dokos, S. (2014), 'Quasi-monopolar electrical stimulation of the retina: a computational modelling study', *Journal of Neural Engineering* **11**(2), 025002.

Abramian, M., Lovell, N. H., Morley, J. W., Suaning, G. J. and Dokos, S. (2011), 'Activation of retinal ganglion cells following epiretinal electrical stimulation with hexagonally arranged bipolar electrodes', *Journal of Neural Engineering* **8**(3), 035004.

Abramian, M., Lovell, N. H., Morley, J. W., Suaning, G. J. and Dokos, S. (2015), 'Activation and inhibition of retinal ganglion cells in response to epiretinal electrical stimulation: a computational modelling study', *Journal of Neural Engineering* **12**(1), 016002.

Ahuja, A., Yeoh, J., Dorn, J., Caspi, A., Wuyyuru, V., McMahon, M., Humayun, M., Greenberg, R., Group, A. I. S. et al. (2013), 'Factors affecting perceptual threshold in argus ii retinal prosthesis subjects', *Translational Vision Science & Technology* **2**(4), 1–1.

Al Abed, A., Lovell, N. H., Suaning, G. and Dokos, S. (2015*a*), A hybrid continuum-discrete computational model of electrical stimulation of the retinal network, *in* 'Neural Engineering (NER), 2015 7th International IEEE/EMBS Conference on', IEEE, pp. 352–355.

Al Abed, A., Lovell, N. H., Suaning, G. and Dokos, S. (2015*b*), A model of electrical stimulation of a retinal cell population using a multi-electrode array, *in* 'Engineering in Medicine and Biology Society (EMBC), 2015 37th Annual International Conference of the IEEE', IEEE, pp. 2287–2290.

Al Abed, A., Yin, S., Suaning, G. J., Lovell, N. H. and Dokos, S. (2012), Convolution based method for calculating inputs from dendritic fields in a continuum model of the retina, *in* 'Engineering in Medicine and Biology Society (EMBC), 2012 Annual International Conference of the IEEE', IEEE, pp. 215–218.

Altenberger, R., Lindsay, K., Ogden, J. and Rosenberg, J. (2001), 'The interaction between membrane kinetics and membrane geometry in the transmission of action potentials in non-uniform excitable fibres: a finite element approach', *Journal of Neuroscience Methods* **112**(2), 101–117.

Aplin, F. P., Fletcher, E. L., Luu, C. D., Vessey, K. A., Allen, P. J., Guymer, R. H., Shepherd, R. K. and Shivdasani, M. N. (2016), 'Stimulation of a suprachoroidal retinal prosthesis drives cortical responses in a feline model of retinal degeneration', *Investigative Ophthalmology & Visual Science* **57**(13), 5216–5229.

Ayton, L. N., Blamey, P. J., Guymer, R. H., Luu, C. D., Nayagam, D. A., Sinclair, N. C., Shivdasani, M. N., Yeoh, J., McCombe, M. F., Briggs, R. J. et al. (2014), 'First-in-human trial of a novel suprachoroidal retinal prosthesis', *PloS One* **9**(12), e115239.

Bareket, L., Barriga-Rivera, A., Zapf, M. P., Lovell, N. H. and Suaning, G. J. (2017), 'Progress in artificial vision through suprachoroidal retinal implants', *Journal of Neural Engineering* **14**(4), 045002.

Barriga-Rivera, A., Guo, T., Yang, C.-Y., Al Abed, A., Dokos, S., Lovell, N. H., Morley, J. W. and Suaning, G. J. (2017), 'High-amplitude electrical stimulation can reduce elicited neuronal activity in visual prosthesis', *Scientific Reports* **7**, 42682.

Baylor, D. A. (1987), 'Photoreceptor signals and vision. proctor lecture.', *Investigative Ophthalmology & Visual Science* **28**(1), 34–49.

Behrend, M. R., Ahuja, A. K., Humayun, M. S., Chow, R. H. and Weiland, J. D. (2011), 'Resolution of the epiretinal prosthesis is not limited by electrode size', *IEEE Transactions on Neural Systems and Rehabilitation Engineering* **19**(4), 436–442.

Boinagrov, D. (2014), Electrical Neural Stimulation and Its Application to High-resolution Retinal Prosthesis, PhD thesis, Stanford University.

Boinagrov, D., Loudin, J. and Palanker, D. (2010), 'Strength–duration relationship for extracellular neural stimulation: numerical and analytical models', *Journal of Neurophysiology* **104**(4), 2236–2248.

Boinagrov, D., Pangratz-Fuehrer, S., Goetz, G. and Palanker, D. (2014), 'Selectivity of direct and network-mediated stimulation of the retinal ganglion cells with epi-, sub-and intraretinal electrodes', *Journal of Neural Engineering* **11**(2), 026008.

Boinagrov, D., Pangratz-Fuehrer, S., Suh, B., Mathieson, K., Naik, N. and Palanker, D. (2012), 'Upper threshold of extracellular neural stimulation', *Journal of Neurophysiology* **108**(12), 3233–3238.

Bonham, B. H. and Litvak, L. M. (2008), 'Current focusing and steering: modeling, physiology, and psychophysics', *Hearing Research* **242**(1-2), 141–153.

Boycott, B. and Wässle, H. (1974), 'The morphological types of ganglion cells of the domestic cat's retina', *The Journal of Physiology* **240**(2), 397–419.

Boycott, B. and Wässle, H. (1991), 'Morphological classification of bipolar cells of the primate retina', *European Journal of Neuroscience* **3**(11), 1069–1088.

Brindley, G. S. (1956), 'The passive electrical properties of the frog's retina, choroid and sclera for radial fields and currents', *The Journal of Physiology* **134**(2), 339–352.

Bringmann, A., Pannicke, T., Grosche, J., Francke, M., Wiedemann, P., Skatchkov, S. N., Osborne, N. N. and Reichenbach, A. (2006), 'Müller cells in the healthy and diseased retina', *Progress in Retinal and Eye Research* **25**(4), 397–424.

Brooks, D. E., Komaromy, A. and Kallberg, M. (1999), 'Comparative retinal ganglion cell and optic nerve morphology', *Vet Ophthalmol* **2**(1), 3–11.

Brown, J. S., Flitcroft, D. I., Ying, G.-s., Francis, E. L., Schmid, G. F., Quinn, G. E. and Stone, R. A. (2009), 'In vivo human choroidal thickness measurements: evidence for diurnal fluctuations', *Investigative Ophthalmology & Visual Science* **50**(1), 5–12.

Bunce, C. and Wormald, R. (2006), 'Leading causes of certification for blindness and partial sight in england & wales', *BMC Public Health* **6**(1), 58.

Cao, X., Sui, X., Lyu, Q., Li, L. and Chai, X. (2015), 'Effects of different three-dimensional electrodes on epiretinal electrical stimulation by modeling analysis', *Journal of neuroengineering and rehabilitation* **12**(1), 73.

Cassar, I., Davis, T., Lo, Y.-K. and Liu, W. (2014), 'A virtual electrode through summation of time offset pulses', *Int. J. Med. Health Biomed. Pharm. Eng* **8**(9), 586–581.

Chan, L. L., Lee, E.-J., Humayun, M. S. and Weiland, J. D. (2011), 'Both electrical stimulation thresholds and smi-32-immunoreactive retinal ganglion cell density correlate with age in s334ter line 3 rat retina', *Journal of Neurophysiology* **105**(6), 2687–2697.

Chang, Y.-C. and Weiland, J. D. (2017), Stimulation strategies for selective activation of retinal ganglion cells, *in* 'Neural Engineering (NER), 2017 8th International IEEE/EMBS Conference on', IEEE, pp. 345–348.

Cho, A., Ratliff, C., Sampath, A. and Weiland, J. (2016), 'Changes in ganglion cell physiology during retinal degeneration influence excitability by prosthetic electrodes', *Journal of Neural Engineering* **13**(2), 025001.

Chow, A. Y. and Chow, V. Y. (1997), 'Subretinal electrical stimulation of the rabbit retina', *Neuroscience Letters* **225**(1), 13–16.

Cicione, R., Shivdasani, M. N., Fallon, J. B., Luu, C. D., Allen, P. J., Rathbone, G. D., Shepherd, R. K. and Williams, C. E. (2012), 'Visual cortex responses to suprachoroidal electrical stimulation of the retina: effects of electrode return configuration', *Journal of Neural Engineering* **9**(3), 036009.

Cohen, A. I. (1965), 'A possible cytological basis for the 'r'membrane in the vertebrate eye', *Nature* **205**(4977), 1222.

Cohen, E. D. (2007), 'Prosthetic interfaces with the visual system: biological issues', *Journal of Neural Engineering* **4**(2), R14.

Connolly, A. J. and Bishop, M. J. (2016), 'Computational representations of myocardial infarct scars and implications for arrhythmogenesis', *Clinical Medicine Insights: Cardiology* **10**, CMC–S39708.

Copelli, M., Oliveira, R. F., Roque, A. C. and Kinouchi, O. (2005), 'Signal compression in the sensory periphery', *Neurocomputing* **65**, 691–696.

Cottaris, N. P. and Elfar, S. D. (2005), 'How the retinal network reacts to epiretinal stimulation to form the prosthetic visual input to the cortex', *Journal of Neural Engineering* **2**(1), S74.

Cranford, J. P., Kim, B. J. and Neu, W. K. (2012), 'Asymptotic model of electrical stimulation of nerve fibers', *Medical & Biological Engineering & Computing* **50**(3), 243–251.

Cuellar, A. A., Lloyd, C. M., Nielsen, P. F., Bullivant, D. P., Nickerson, D. P. and Hunter, P. J. (2003), 'An overview of cellml 1.1, a biological model description language', *Simulation* **79**(12), 740–747.

Curcio, C. A., Medeiros, N. E. and Millican, C. L. (1996), 'Photoreceptor loss in age-related macular degeneration.', *Investigative Ophthalmology & Visual Science* **37**(7), 1236–1249.

Da Cruz, L., Coley, B. F., Dorn, J., Merlini, F., Filley, E., Christopher, P., Chen, F. K., Wuyyuru, V., Sahel, J., Stanga, P. et al. (2013), 'The argus ii epiretinal prosthesis system allows letter and word reading and long-term function in patients with profound vision loss', *British Journal of Ophthalmology* pp. bjophthalmol–2012.

DAVIS, J. L. and de NO LORENTE, R. (1947), 'Contribution to the mathematical theory of the electrotonus.', *Studies from the Rockefeller Institute for Medical Research. Reprints. Rockefeller Institute for Medical Research* **131**, 442–496.

Deans, M. R., Volgyi, B., Goodenough, D. A., Bloomfield, S. A. and Paul, D. L. (2002), 'Connexin36 is essential for transmission of rod-mediated visual signals in the mammalian retina', *Neuron* **36**(4), 703–712.

Destexhe, A., Neubig, M., Ulrich, D. and Huguenard, J. (1998), 'Dendritic low-threshold calcium currents in thalamic relay cells', *Journal of Neuroscience* **18**(10), 3574–3588.

Dias, M. F., Joo, K., Kemp, J. A., Fialho, S. L., da Silva Cunha, A., Woo, S. J. and Kwon, Y. J. (2017), 'Molecular genetics and emerging therapies for retinitis pigmentosa: basic research and clinical perspectives', *Progress in Retinal and Eye Research* .

Dokos, S., Suaning, G. J. and Lovell, N. H. (2005), 'A bidomain model of epiretinal stimulation', *IEEE Transactions on Neural Systems and Rehabilitation Engineering* **13**(2), 137–46.

Dowling, J. (2005), 'Artificial human vision', *Expert Review of Medical Devices* **2**(1), 73–85.

Dowling, J. E. (2009), *Retina: An Overview*, Elsevier Science, pp. 159–168.

Dumm, G., Fallon, J. B., Williams, C. E. and Shivdasani, M. N. (2014), 'Virtual electrodes by current steering in retinal prostheses', *Investigative Ophthalmology & Visual Science* **55**(12), 8077–8085.

Edwards, T. L., Cottriall, C. L., Xue, K., Simunovic, M. P., Ramsden, J. D., Zrenner, E. and MacLaren, R. E. (2018), 'Assessment of the electronic retinal implant alpha ams in restoring vision to blind patients with end-stage retinitis pigmentosa', *Ophthalmology* **125**(3), 432–443.

Eiber, C. D., Dokos, S., Lovell, N. H. and Suaning, G. J. (2017), 'Multipolar field shaping in a suprachoroidal visual prosthesis', *IEEE Transactions on Neural Systems and Rehabilitation Engineering* **25**(12), 2480–2487.

Eickenscheidt, M., Jenkner, M., Thewes, R., Fromherz, P. and Zeck, G. (2012), 'Electrical stimulation of retinal neurons in epiretinal and subretinal configuration using a multicapacitor array', *Journal of Neurophysiology* **107**(10), 2742–2755.

Engbers, J. D., Anderson, D., Tadayonnejad, R., Mehaffey, W. H., Molineux, M. L. and Turner, R. W. (2011), 'Distinct roles for it and ih in controlling the frequency and timing of rebound spike responses', *The Journal of physiology* **589**(22), 5391–5413.

Fitzpatrick, D. (2014), *Retinal Implants*, Elsevier.

Fohlmeister, J., Coleman, P. and Miller, R. (1990), 'Modeling the repetitive firing of retinal ganglion cells', *Brain Research* **510**(2), 343–345.

Fohlmeister, J. F., Cohen, E. D. and Newman, E. A. (2010), 'Mechanisms and distribution of ion channels in retinal ganglion cells: using temperature as an independent variable', *Journal of Neurophysiology* **103**(3), 1357–1374.

Fohlmeister, J. and Miller, R. (1997*a*), 'Impulse encoding mechanisms of ganglion cells in the tiger salamander retina', *Journal of Neurophysiology* **78**(4), 1935–1947.

Fohlmeister, J. and Miller, R. (1997*b*), 'Mechanisms by which cell geometry controls repetitive impulse firing in retinal ganglion cells', *Journal of Neurophysiology* **78**(4), 1948–1964.

Freeman, D. K., Jeng, J. S., Kelly, S. K., Hartveit, E. and Fried, S. I. (2011), 'Calcium channel dynamics limit synaptic release in response to prosthetic stimulation with sinusoidal waveforms', *Journal of neural engineering* **8**(4), 046005.

Freeman, D. K., Rizzo III, J. F. and Fried, S. (2010), 'Electric stimulation with sinusoids and white noise for neural prostheses', *Frontiers in Neuroscience* **4**, 1.

Fried, S. I., Hsueh, H.-A. and Werblin, F. S. (2006), 'A method for generating precise temporal patterns of retinal spiking using prosthetic stimulation', *Journal of Neurophysiology* **95**(2), 970–978.

Fried, S. I., Lasker, A. C. W., Desai, N. J., Eddington, D. K. and Rizzo, J. F. (2009), 'Axonal sodium-channel bands shape the response to electric stimulation in retinal ganglion cells', *Journal of Neurophysiology* **101**(4), 1972–1987.

Friedrich, P., Vella, M., Gulyás, A. I., Freund, T. F. and Káli, S. (2014), 'A flexible, interactive software tool for fitting the parameters of neuronal models', *Frontiers in Neuroinformatics* **8**, 63.

Fujikado, T., Kamei, M., Sakaguchi, H., Kanda, H., Morimoto, T., Ikuno, Y., Nishida, K., Kishima, H., Maruo, T., Konoma, K. et al. (2011), 'Testing of semichronically implanted retinal prosthesis by suprachoroidal-transretinal stimulation in patients with retinitis pigmentosa', *Investigative Ophthalmology & Visual Science* **52**(7), 4726–4733.

Gold, C., Henze, D. A., Koch, C. and Buzsaki, G. (2006), 'On the origin of the extracellular action potential waveform: a modeling study', *Journal of Neurophysiology* **95**(5), 3113–3128.

Goldstein, S. S. and Rall, W. (1974), 'Changes of action potential shape and velocity for changing core conductor geometry', *Biophysical Journal* **14**(10), 731–757.

Green, R., Matteucci, P., Dodds, C., Palmer, J., Dueck, W., Hassarati, R., Byrnes-Preston, P., Lovell, N. and Suaning, G. (2014), 'Laser patterning of platinum electrodes for safe neurostimulation', *Journal of Neural Engineering* **11**(5), 056017.

Greenberg, R. J., Velte, T. J., Humayun, M. S., Scarlatis, G. N. and De Juan, E. (1999), 'A computational model of electrical stimulation of the retinal ganglion cell', *IEEE Transactions on Biomedical Engineering* **46**(5), 505–514.

Grill, W. M. and Kirsch, R. F. (2000), 'Neuroprosthetic applications of electrical stimulation', *Assistive Technology* **12**(1), 6–20.

Guo, T., Lovell, N. H., Tsai, D., Twyford, P., Fried, S., Morley, J. W., Suaning, G. J. and Dokos, S. (2015), Optimizing retinal ganglion cell responses to high-frequency electrical stimulation strategies for preferential neuronal excitation, *in* 'Neural Engineering (NER), 2015 7th International IEEE/EMBS Conference on', IEEE, pp. 252–255.

Guo, T., Tsai, D., Bai, S., Morley, J. W., Suaning, G. J., Lovell, N. H. and Dokos, S. (2014), 'Understanding the retina: A review of computational models of the

retina from the single cell to the network level', *Critical Reviews™ in Biomedical Engineering* **42**(5).

Guo, T., Tsai, D., Morley, J. W., Suaning, G. J., Kameneva, T., Lovell, N. H. and Dokos, S. (2016), 'Electrical activity of on and off retinal ganglion cells: a modelling study', *Journal of Neural Engineering* **13**(2), 025005.

Guo, T., Tsai, D., Morley, J. W., Suaning, G. J., Lovell, N. H. and Dokos, S. (2013a), Cell-specific modeling of retinal ganglion cell electrical activity, *in* 'Engineering in Medicine and Biology Society (EMBC), 2013 35th Annual International Conference of the IEEE', IEEE, pp. 6539–6542.

Guo, T., Tsai, D., Morley, J. W., Suaning, G. J., Lovell, N. H. and Dokos, S. (2013b), Influence of cell morphology in a computational model of on and off retinal ganglion cells, *in* 'Engineering in Medicine and Biology Society (EMBC), 2013 35th Annual International Conference of the IEEE', IEEE, pp. 4553–4556.

Guo, T., Tsai, D., Sovilj, S., Morley, J. W., Suaning, G. J., Lovell, N. H. and Dokos, S. (2013), Influence of active dendrites on firing patterns in a retinal ganglion cell model, *in* 'Engineering in Medicine and Biology Society (EMBC), 2013 35th Annual International Conference of the IEEE', IEEE, pp. 4557–4560.

Guo, T., Tsai, D., Suaning, G. J., Lovell, N. H. and Dokos, S. (2012), Modeling normal and rebound excitation in mammalian retinal ganglion cells, *in* 'Engineering in Medicine and Biology Society (EMBC), 2012 Annual International Conference of the IEEE', IEEE, pp. 5506–5509.

Habib, A. G., Cameron, M. A., Suaning, G. J., Lovell, N. H. and Morley, J. W. (2013), 'Spatially restricted electrical activation of retinal ganglion cells in the rabbit retina by hexapolar electrode return configuration', *Journal of Neural Engineering* **10**(3), 036013.

Hamel, C. (2006), 'Retinitis pigmentosa', *Orphanet Journal of Rare Diseases* **1**(1), 40.

Hartline, H. K. (1938), 'The response of single optic nerve fibers of the vertebrate eye to illumination of the retina', *American Journal of Physiology-Legacy Content* **121**(2), 400–415.

Henriquez, C. S. (1993), 'Simulating the electrical behavior of cardiac tissue using the bidomain model.', *Critical Reviews in Biomedical Engineering* **21**(1), 1–77.

Herrera-Valdez, M. A., Suslov, S. K. and Vega-Guzmán, J. M. (2014), 'A graphical approach to a model of a neuronal tree with a variable diameter', *Mathematics* **2**(3), 119–135.

Hines, M. L. and Carnevale, N. T. (1997), 'The neuron simulation environment', *Neural Computation* **9**(6), 1179–1209.

Hodgkin, A. L. and Huxley, A. F. (1952), 'A quantitative description of membrane current and its application to conduction and excitation in nerve', *The Journal of Physiology* **117**(4), 500–544.

Hodgkin, A. and Rushton, W. (1946), The electrical constants of a crustacean nerve fibre, *in* 'Proc. R. Soc. Lond. B', Vol. 133, The Royal Society, pp. 444–479.

Ishida, A. T. (1995), 'Ion channel components of retinal ganglion cells', *Progress in Retinal and Eye Research* **15**(1), 261–280.

Jankowska, E. and Roberts, W. (1972), 'An electrophysiological demonstration of the axonal projections of single spinal interneurones in the cat', *The Journal of Physiology* **222**(3), 597–622.

Jeng, J., Tang, S., Molnar, A., Desai, N. and Fried, S. (2011), 'The sodium channel band shapes the response to electric stimulation in retinal ganglion cells', *Journal of Neural Engineering* **8**(3), 036022.

Jensen, R. J. (2012), 'Activation of ganglion cells in wild-type and p23h rat retinas with a small subretinal electrode', *Experimental Eye Research* **99**, 71–77.

Jensen, R. J. and Rizzo III, J. F. (2006), 'Thresholds for activation of rabbit retinal ganglion cells with a subretinal electrode', *Experimental Eye Research* **83**(2), 367–373.

Jensen, R. J. and Rizzo III, J. F. (2008), 'Activation of retinal ganglion cells in wild-type and rd1 mice through electrical stimulation of the retinal neural network', *Vision Research* **48**(14), 1562–1568.

Jensen, R. J. and Rizzo III, J. F. (2009), 'Activation of ganglion cells in wild-type and rd1 mouse retinas with monophasic and biphasic current pulses', *Journal of Neural Engineering* **6**(3), 035004.

Jensen, R. J. and Rizzo III, J. F. (2011), 'Effects of gaba receptor antagonists on thresholds of p23h rat retinal ganglion cells to electrical stimulation of the retina', *Journal of Neural Engineering* **8**(3), 035002.

Jensen, R. J., Rizzo, J. F., Ziv, O. R., Grumet, A. and Wyatt, J. (2003), 'Thresholds for activation of rabbit retinal ganglion cells with an ultrafine, extracellular microelectrode', *Investigative Ophthalmology & Visual Science* **44**(8), 3533–3543.

Jensen, R. J., Ziv, O. R. and Rizzo, J. F. (2005*a*), 'Responses of rabbit retinal ganglion cells to electrical stimulation with an epiretinal electrode', *Journal of Neural Engineering* **2**(1), S16.

Jensen, R. J., Ziv, O. R. and Rizzo, J. F. (2005*b*), 'Thresholds for activation of rabbit retinal ganglion cells with relatively large, extracellular microelectrodes', *Investigative Ophthalmology & Visual Science* **46**(4), 1486–1496.

Joarder, S. A., Abramian, M., Suaning, G. J., Lovell, N. H. and Dokos, S. (2011), 'A continuum model of retinal electrical stimulation', *Journal of Neural Engineering* **8**(6), 066006.

John, S. E., Shivdasani, M. N., Williams, C. E., Morley, J. W., Shepherd, R. K., Rathbone, G. D. and Fallon, J. B. (2013), 'Suprachoroidal electrical stimulation:

effects of stimulus pulse parameters on visual cortical responses', *Journal of Neural Engineering* **10**(5), 056011.

Joucla, S., Glière, A. and Yvert, B. (2014), 'Current approaches to model extracellular electrical neural microstimulation', *Frontiers in Computational Neuroscience* **8**, 13.

Joucla, S. and Yvert, B. (2009), 'The "mirror" estimate: an intuitive predictor of membrane polarization during extracellular stimulation', *Biophysical Journal* **96**(9), 3495–3508.

Joucla, S. and Yvert, B. (2012), 'Modeling extracellular electrical neural stimulation: from basic understanding to mea-based applications', *Journal of Physiology-Paris* **106**(3-4), 146–158.

Joyner, R., Westerfield, M., Moore, J. and Stockbridge, N. (1978), 'A numerical method to model excitable cells', *Biophysical Journal* **22**(2), 155–170.

Kameneva, T., Maturana, M., Hadjinicolaou, A., Cloherty, S., Ibbotson, M., Grayden, D., Burkitt, A. and Meffin, H. (2016), 'Retinal ganglion cells: mechanisms underlying depolarization block and differential responses to high frequency electrical stimulation of on and off cells', *Journal of Neural Engineering* **13**(1), 016017.

Kameneva, T., Meffin, H. and Burkitt, A. N. (2011), 'Modelling intrinsic electrophysiological properties of on and off retinal ganglion cells', *Journal of Computational Neuroscience* **31**(3), 547–561.

Kaneda, M. and Kaneko, A. (1991), 'Voltage-gated sodium currents in isolated retinal ganglion cells of the cat: relation between the inactivation kinetics and the cell type', *Neuroscience research* **11**(4), 261–275.

Kang, S., Chwodhury, T., Moon, I. J., Hong, S. H., Yang, H., Won, J. H. and Woo, J. (2015), 'Effects of electrode position on spatiotemporal auditory nerve fiber

responses: a 3d computational model study', *Computational and Mathematical Methods in Medicine* **2015**.

Kaplan, H. J., Tezel, T. H., Berger, A. S., Wolf, M. L. and Del Priore, L. V. (1997), 'Human photoreceptor transplantation in retinitis pigmentosa: a safety study', *Archives of Ophthalmology* **115**(9), 1168–1172.

Karwoski, C. J., Frambach, D. and Proenza, L. M. (1985), 'Laminar profile of resistivity in frog retina', *Journal of Neurophysiology* **54**(6), 1607–1619.

Karwoski, C. J. and Xu, X. (1999), 'Current source-density analysis of light-evoked field potentials in rabbit retina', *Visual Neuroscience* **16**(2), 369–377.

Kasi, H., Meissner, R., Babalian, A., Van Lintel, H., Bertsch, A. and Renaud, P. (2011), 'Direct localised measurement of electrical resistivity profile in rat and embryonic chick retinas using a microprobe', *Journal of Electrical Bioimpedance* **1**(1), 84–92.

Khodorov, B. and Timin, E. (1976), 'Nerve impulse propagation along nonuniform fibres:(investigations using mathematical models)', *Progress in Biophysics and Molecular Biology* **30**, 145–184.

Kim, H., Jones, K. E. and Heckman, C. (2014), 'Asymmetry in signal propagation between the soma and dendrites plays a key role in determining dendritic excitability in motoneurons', *PLoS One* **9**(8), e95454.

Kinouchi, O. and Copelli, M. (2006), 'Optimal dynamical range of excitable networks at criticality', *Nature Physics* **2**(5), 348.

Koch, C. and Segev, I. (1998), *Methods in neuronal modeling: from ions to networks*, MIT press.

Kolb, H. (1979), 'The inner plexiform layer in the retina of the cat: electron microscopic observations', *Journal of Neurocytology* **8**(3), 295–329.

Kolb, H. (2003), 'How the retina works: Much of the construction of an image takes place in the retina itself through the use of specialized neural circuits', *American Scientist* **91**(1), 28–35.

Kolb, H., Nelson, R. and Mariani, A. (1981), 'Amacrine cells, bipolar cells and ganglion cells of the cat retina: a golgi study', *Vision Research* **21**(7), 1081–1114.

Kole, M. H., Ilschner, S. U., Kampa, B. M., Williams, S. R., Ruben, P. C. and Stuart, G. J. (2008), 'Action potential generation requires a high sodium channel density in the axon initial segment', *Nature Neuroscience* **11**(2), 178.

Lee, D. C., McIntyre, C. C. and Grill, W. M. (2002), Extracellular electrical stimulation of central neurons: quantitative studies, *in* 'Handbook of Neuroprosthetic Methods', CRC Press, pp. 98–128.

Lee, D., Lee, S.-G. and Kim, S. (2012), 'A compartment model with variable ion channel density on the propagation of action potentials along a nonuniform axon', *The European Physical Journal B* **85**(12), 400.

Lindén, H., Hagen, E., Leski, S., Norheim, E. S., Pettersen, K. H. and Einevoll, G. T. (2014), 'Lfpy: a tool for biophysical simulation of extracellular potentials generated by detailed model neurons', *Frontiers in Neuroinformatics* **7**, 41.

Lipton, S. A. and Tauck, D. L. (1987), 'Voltage-dependent conductances of solitary ganglion cells dissociated from the rat retina.', *The Journal of Physiology* **385**(1), 361–391.

Loizos, K., RamRakhyani, A. K., Anderson, J., Marc, R. and Lazzi, G. (2016), 'On the computation of a retina resistivity profile for applications in multi-scale modeling of electrical stimulation and absorption', *Physics in Medicine & Biology* **61**(12), 4491.

López-Sánchez, E. J. and Romero, J. M. (2017), 'Cable equation for general geometry', *Physical Review E* **95**(2), 022403.

Lovell, N. H., Hallum, L. E., Chen, S., Dokos, S., Byrnes-Preston, P., Green, R., Poole-Warren, L., Lehmann, T. and Suaning, G. J. (2007), 'Advances in retinal neuroprosthetics', *Handbook of Neural Engineering* pp. 337–356.

Lukasiewicz, P. and Werblin, F. (1988), 'A slowly inactivating potassium current truncates spike activity in ganglion cells of the tiger salamander retina', *Journal of Neuroscience* **8**(12), 4470–4481.

MacNeil, M. A. and Masland, R. H. (1998), 'Extreme diversity among amacrine cells: implications for function', *Neuron* **20**(5), 971–982.

Manor, Y., Koch, C. and Segev, I. (1991), 'Effect of geometrical irregularities on propagation delay in axonal trees', *Biophysical Journal* **60**(6), 1424–1437.

Marasco, A., Limongiello, A. and Migliore, M. (2013), 'Using strahler's analysis to reduce up to 200-fold the run time of realistic neuron models', *Scientific Reports* **3**, 2934.

Marc, R. E., Jones, B. W., Watt, C. B. and Strettoi, E. (2003), 'Neural remodeling in retinal degeneration', *Progress in Retinal and Eye Research* **22**(5), 607–655.

Margalit, E. and Thoreson, W. B. (2006), 'Inner retinal mechanisms engaged by retinal electrical stimulation', *Investigative Ophthalmology & Visual Science* **47**(6), 2606–2612.

Margolis, D. J. and Detwiler, P. B. (2007), 'Different mechanisms generate maintained activity in on and off retinal ganglion cells', *Journal of Neuroscience* **27**(22), 5994–6005.

Margolis, D. J., Gartland, A. J., Euler, T. and Detwiler, P. B. (2010), 'Dendritic calcium signaling in on and off mouse retinal ganglion cells', *Journal of Neuroscience* **30**(21), 7127–7138.

Martinek, J., Stickler, Y., Reichel, M., Mayr, W. and Rattay, F. (2008), 'A novel

approach to simulate hodgkin–huxley-like excitation with comsol multiphysics', *Artificial Organs* **32**(8), 614–619.

Masland, R. H. (2001), 'The fundamental plan of the retina', *Nature Neuroscience* **4**(9), 877.

Masland, R. H. (2012), 'The neuronal organization of the retina', *Neuron* **76**(2), 266–280.

Mathieson, K., Loudin, J., Goetz, G., Huie, P., Wang, L., Kamins, T. I., Galambos, L., Smith, R., Harris, J. S., Sher, A. et al. (2012), 'Photovoltaic retinal prosthesis with high pixel density', *Nature Photonics* **6**(6), 391.

Matteucci, P. B., Chen, S. C., Tsai, D., Dodds, C. W., Dokos, S., Morley, J. W., Lovell, N. H. and Suaning, G. J. (2013), 'Current steering in retinal stimulation via a quasimonopolar stimulation paradigm', *Investigative Ophthalmology & Visual Science* **54**(6), 4307–4320.

Maturana, M. I., Kameneva, T., Burkitt, A. N., Meffin, H. and Grayden, D. B. (2014), 'The effect of morphology upon electrophysiological responses of retinal ganglion cells: simulation results', *Journal of Computational Neuroscience* **36**(2), 157–175.

Mazzoni, F., Novelli, E. and Strettoi, E. (2008), 'Retinal ganglion cells survive and maintain normal dendritic morphology in a mouse model of inherited photoreceptor degeneration', *Journal of Neuroscience* **28**(52), 14282–14292.

Mccormick, D. A. and Pape, H.-C. (1990), 'Properties of a hyperpolarization-activated cation current and its role in rhythmic oscillation in thalamic relay neurones.', *The Journal of physiology* **431**(1), 291–318.

Mcintyre, C. C. and Foutz, T. J. (2013), Computational modeling of deep brain stimulation, *in* 'Handbook of Clinical Neurology', Vol. 116, Elsevier, pp. 55–61.

McNeal, D. R. (1976), 'Analysis of a model for excitation of myelinated nerve', *IEEE Transactions on Biomedical Engineering* (4), 329–337.

Meffin, H., Tahayori, B., Grayden, D. B. and Burkitt, A. N. (2012), 'Modeling extracellular electrical stimulation: I. derivation and interpretation of neurite equations', *Journal of Neural Engineering* **9**(6), 065005.

Meffin, H., Tahayori, B., Grayden, D. B. and Burkitt, A. N. (2013), Internal inconsistencies in models of electrical stimulation in neural tissue, *in* 'Engineering in Medicine and Biology Society (EMBC), 2013 35th Annual International Conference of the IEEE', IEEE, pp. 5946–5949.

Meffin, H., Tahayori, B., Sergeev, E. N., Mareels, I. M., Grayden, D. B. and Burkitt, A. N. (2014), 'Modelling extracellular electrical stimulation: Iii. derivation and interpretation of neural tissue equations', *Journal of Neural Engineering* **11**(6), 065004.

Meng, K., Fellner, A., Rattay, F., Ghezzi, D., Meffin, H., Ibbotson, M. R. and Kameneva, T. (2018), 'Upper stimulation threshold for retinal ganglion cell activation', *Journal of neural engineering* **15**(4), 046012.

Mens, L. H. and Berenstein, C. K. (2005), 'Speech perception with mono-and quadrupolar electrode configurations: a crossover study', *Otology & Neurotology* **26**(5), 957–964.

Merrill, D. R., Bikson, M. and Jefferys, J. G. (2005), 'Electrical stimulation of excitable tissue: design of efficacious and safe protocols', *Journal of Neuroscience Methods* **141**(2), 171–198.

Milam, A. H., Li, Z.-Y. and Fariss, R. N. (1998), 'Histopathology of the human retina in retinitis pigmentosa.', *Progress in Retinal and Eye Research* **17**(2), 175–205.

Miledi, R. (1965), Propagation of electric activity in motor nerve terminals, *in* 'Proc. R. Soc. Lond. B', Vol. 161, The Royal Society, pp. 453–482.

Miller, R. F., Staff, N. P. and Velte, T. J. (2006), 'Form and function of on-off amacrine cells in the amphibian retina', *Journal of Neurophysiology* **95**(5), 3171–3190.

Miller, R., Stenback, K., Henderson, D. and Sikora, M. (2002), 'How voltage-gated ion channels alter the functional properties of ganglion and amacrine cell dendrites.', *Archives italiennes de biologie* **140**(4), 347–359.

Mitra, P. and Miller, R. F. (2007), 'Mechanism underlying rebound excitation in retinal ganglion cells', *Visual Neuroscience* **24**(5), 709–731.

Moffitt, M. A. and McIntyre, C. C. (2005), 'Model-based analysis of cortical recording with silicon microelectrodes', *Clinical Neurophysiology* **116**(9), 2240–2250.

Moghadam, G. K., Wilke, R., Suaning, G. J., Lovell, N. H. and Dokos, S. (2013), 'Quasi-monopolar stimulation: a novel electrode design configuration for performance optimization of a retinal neuroprosthesis', *PloS One* **8**(8), e73130.

Moghaddam, G. K., Lovell, N. H., Wilke, R. G., Suaning, G. J. and Dokos, S. (2014), 'Performance optimization of current focusing and virtual electrode strategies in retinal implants', *Computer Methods and Programs in Biomedicine* **117**(2), 334–342.

Moghaddam, G. K., Wilke, R. G., Dokos, S., Suaning, G. J. and Lovell, N. H. (2011), Electrode design to optimize ganglion cell activation in a retinal neuroprosthesis: A modeling study, *in* 'Neural Engineering (NER), 2011 5th International IEEE/EMBS Conference on', IEEE, pp. 542–545.

Morris, D. J. and Pfingst, B. E. (2000), 'Effects of electrode configuration and stimulus level on rate and level discrimination with cochlear implants', *Journal of the Association for Research in Otolaryngology* **1**(3), 211–223.

Moulin, C., Glière, A., Barbier, D., Joucla, S., Yvert, B., Mailley, P. and Guillemaud, R. (2008), 'A new 3-d finite-element model based on thin-film approximation for

microelectrode array recording of extracellular action potential', *IEEE Transactions on Biomedical Engineering* **55**(2), 683–692.

Mueller, J. K. and Grill, W. M. (2013), 'Model-based analysis of multiple electrode array stimulation for epiretinal visual prostheses', *Journal of Neural Engineering* **10**(3), 036002.

Mustafi, D., Engel, A. H. and Palczewski, K. (2009), 'Structure of cone photoreceptors', *Progress in Retinal and Eye Research* **28**(4), 289–302.

Nakauchi, K., Fujikado, T., Kanda, H., Morimoto, T., Choi, J. S., Ikuno, Y., Sakaguchi, H., Kamei, M., Ohji, M., Yagi, T. et al. (2005), 'Transretinal electrical stimulation by an intrascleral multichannel electrode array in rabbit eyes', *Graefe's Archive for Clinical and Experimental Ophthalmology* **243**(2), 169–174.

Nanduri, D. (2011), *Prosthetic vision in blind human patients: Predicting the percepts of epiretinal stimulation*, University of Southern California.

Nanduri, D., Fine, I., Horsager, A., Boynton, G. M., Humayun, M. S., Greenberg, R. J. and Weiland, J. D. (2012), 'Frequency and amplitude modulation have different effects on the percepts elicited by retinal stimulation', *Investigative Ophthalmology & Visual Science* **53**(1), 205–214.

Nelson, R., Famiglietti Jr, E. and Kolb, H. (1978), 'Intracellular staining reveals different levels of stratification for on-and off-center ganglion cells in cat retina', *Journal of Neurophysiology* **41**(2), 472–483.

Niederer, S. A., Kerfoot, E., Benson, A. P., Bernabeu, M. O., Bernus, O., Bradley, C., Cherry, E. M., Clayton, R., Fenton, F. H., Garny, A. et al. (2011), 'Verification of cardiac tissue electrophysiology simulators using an n-version benchmark', *Phil. Trans. R. Soc. A* **369**(1954), 4331–4351.

O'Brien, B. J., Isayama, T., Richardson, R. and Berson, D. M. (2002), 'Intrinsic

physiological properties of cat retinal ganglion cells', *The Journal of physiology* **538**(3), 787–802.

O'Brien, E. (2012), The condition of the retina in retinitis pigmentosa during late stages of degeneration, PhD thesis.

O'brien, E. E., Greferath, U., Vessey, K. A., Jobling, A. I. and Fletcher, E. L. (2012), 'Electronic restoration of vision in those with photoreceptor degenerations', *Clinical and Experimental Optometry* **95**(5), 473–483.

Ogden, T. E. and Ito, H. (1971), 'Avian retina. ii. an evaluation of retinal electrical anisotropy.', *Journal of Neurophysiology* **34**(3), 367–373.

O'Hearn, T. M., Sadda, S. R., Weiland, J. D., Maia, M., Margalit, E. and Humayun, M. S. (2006), 'Electrical stimulation in normal and retinal degeneration (rd1) isolated mouse retina', *Vision Research* **46**(19), 3198–3204.

Ohme, M. and Schierwagen, A. (1998), 'An equivalent cable model for neuronal trees with active membrane', *Biological Cybernetics* **78**(3), 227–243.

Olsen, T. W., Sanderson, S., Feng, X. and Hubbard, W. C. (2002), 'Porcine sclera: thickness and surface area', *Investigative Ophthalmology & Visual Science* **43**(8), 2529–2532.

Oyster, C. W., Takahashi, E. S. and Hurst, D. C. (1981), 'Density, soma size, and regional distribution of rabbit retinal ganglion cells', *Journal of Neuroscience* **1**(12), 1331–1346.

Park, S. S., Bauer, G., Abedi, M., Pontow, S., Panorgias, A., Jonnal, R., Zawadzki, R. J., Werner, J. S. and Nolta, J. (2015), 'Intravitreal autologous bone marrow cd34+ cell therapy for ischemic and degenerative retinal disorders: preliminary phase 1 clinical trial findings', *Investigative Ophthalmology & Visual Science* **56**(1), 81–89.

Popova, E. (2015), 'Gabaergic neurotransmission and retinal ganglion cell function', *Journal of Comparative Physiology A* **201**(3), 261–283.

Publio, R., Ceballos, C. C. and Roque, A. C. (2012), 'Dynamic range of vertebrate retina ganglion cells: Importance of active dendrites and coupling by electrical synapses', *PloS One* **7**(10), e48517.

Publio, R., Oliveira, R. F. and Roque, A. C. (2009), 'A computational study on the role of gap junctions and rod ih conductance in the enhancement of the dynamic range of the retina', *PLoS One* **4**(9), e6970.

Radtke, N. D., Aramant, R. B., Petry, H. M., Green, P. T., Pidwell, D. J. and Seiler, M. J. (2008), 'Vision improvement in retinal degeneration patients by implantation of retina together with retinal pigment epithelium', *American Journal of Ophthalmology* **146**(2), 172–182.

Rall, W. (1959), 'Branching dendritic trees and motoneuron membrane resistivity', *Experimental Neurology* **1**(5), 491–527.

Rall, W. (1962), 'Electrophysiology of a dendritic neuron model', *Biophysical Journal* **2**(2 Pt 2), 145.

Rall, W. (1977), *Core conductor theory and cable properties of neurons*, Am. Physiol. Soc.

Rall, W. (1995), *The theoretical foundation of dendritic function: selected papers of Wilfrid Rall with commentaries*, MIT press.

Rattay, F. (1986), 'Analysis of models for external stimulation of axons', *IEEE Transactions on Biomedical Engineering* (10), 974–977.

Rattay, F. (1987), 'Ways to approximate current-distance relations for electrically stimulated fibers.', *Journal of Theoretical Biology* **125**(3), 339–349.

Rattay, F., Bassereh, H. and Fellner, A. (2017), 'Impact of electrode position on the elicitation of sodium spikes in retinal bipolar cells', *Scientific reports* **7**(1), 17590.

Rattay, F., Bassereh, H. and Stiennon, I. (2018), 'Compartment models for the electrical stimulation of retinal bipolar cells', *PloS one* **13**(12), e0209123.

Rattay, F., Lutter, P. and Felix, H. (2001), 'A model of the electrically excited human cochlear neuron: I. contribution of neural substructures to the generation and propagation of spikes', *Hearing Research* **153**(1-2), 43–63.

Rattay, F. and Resatz, S. (2004), 'Effective electrode configuration for selective stimulation with inner eye prostheses', *IEEE Transactions on Biomedical Engineering* **51**(9), 1659–1664.

Rattay, F., Resatz, S., Lutter, P., Minassian, K., Jilge, B. and Dimitrijevic, M. (2003), 'Mechanisms of electrical stimulation with neural prostheses', *Neuromodulation: Technology at the Neural Interface* **6**(1), 42–56.

Rattay, F. and Wenger, C. (2010), 'Which elements of the mammalian central nervous system are excited by low current stimulation with microelectrodes?', *Neuroscience* **170**(2), 399–407.

Resatz, S. and Rattay, F. (2003), Excitability of bipolar and ganglion cells with retinal prosthesis: a modeling study, *in* 'Engineering in Medicine and Biology Society, 2003. Proceedings of the 25th Annual International Conference of the IEEE', Vol. 3, IEEE, pp. 2039–2042.

Resatz, S. and Rattay, F. (2004), 'A model for the electrically stimulated retina', *Mathematical and Computer Modelling* **10**(2), 93–106.

Resnikoff, S., Pascolini, D., Etya'Ale, D., Kocur, I., Pararajasegaram, R., Pokharel, G. P. and Mariotti, S. P. (2004), 'Global data on visual impairment in the year 2002', *Bulletin of the World Health Organization* **82**(11), 844–851.

Rizzo, J. F., Wyatt, J., Loewenstein, J., Kelly, S. and Shire, D. (2003), 'Methods and perceptual thresholds for short-term electrical stimulation of human retina with microelectrode arrays', *Investigative Ophthalmology & Visual Science* **44**(12), 5355–5361.

Sakaguchi, H., Fujikado, T., Fang, X., Kanda, H., Osanai, M., Nakauchi, K., Ikuno, Y., Kamei, M., Yagi, T., Nishimura, S. et al. (2004), 'Transretinal electrical stimulation with a suprachoroidal multichannel electrode in rabbit eyes', *Japanese Journal of Ophthalmology* **48**(3), 256–261.

Santos, A., Humayun, M. S., de Juan, E., Greenburg, R. J., Marsh, M. J., Klock, I. B. and Milam, A. H. (1997), 'Preservation of the inner retina in retinitis pigmentosa: a morphometric analysis', *Archives of Ophthalmology* **115**(4), 511–515.

Sarks, S. (1976), 'Ageing and degeneration in the macular region: a clinico-pathological study.', *British Journal of Ophthalmology* **60**(5), 324–341.

Schachter, M. J., Oesch, N., Smith, R. G. and Taylor, W. R. (2010), 'Dendritic spikes amplify the synaptic signal to enhance detection of motion in a simulation of the direction-selective ganglion cell', *PLoS Computational Biology* **6**(8), e1000899.

Schiefer, M. A. and Grill, W. M. (2006), 'Sites of neuronal excitation by epiretinal electrical stimulation', *IEEE Transactions on Neural Systems and Rehabilitation Engineering* **14**(1), 5–13.

Schierwagen, A. K. (1989), 'A non-uniform equivalent cable model of membrane voltage changes in a passive dendritic tree', *Journal of Theoretical Biology* **141**(2), 159–179.

Schierwagen, A. and Ohme, M. (2008), A model for the propagation of action potentials in nonuniform axons, *in* 'AIP Conference Proceedings', Vol. 1028, AIP, pp. 98–112.

Schmitt, O. H. (1969), Biological information processing using the concept of interpenetrating domains, *in* 'Information Processing in the Nervous System', Springer, pp. 325–331.

Schnabel, V. and Struijk, J. J. (2001), 'Evaluation of the cable model for electrical stimulation of unmyelinated nerve fibers', *IEEE Transactions on Biomedical Engineering* **48**(9), 1027–1033.

Schubert, M., Hierzenberger, A., Lehner, H. and Werner, J. (1999), 'Optimizing photodiode arrays for the use as retinal implants', *Sensors and Actuators A: Physical* **74**(1-3), 193–197.

Sekirnjak, C., Hottowy, P., Sher, A., Dabrowski, W., Litke, A. and Chichilnisky, E. (2006), 'Electrical stimulation of mammalian retinal ganglion cells with multi-electrode arrays', *Journal of Neurophysiology* **95**(6), 3311–3327.

Sekirnjak, C., Hottowy, P., Sher, A., Dabrowski, W., Litke, A. M. and Chichilnisky, E. (2008), 'High-resolution electrical stimulation of primate retina for epiretinal implant design', *Journal of Neuroscience* **28**(17), 4446–4456.

Sekirnjak, C., Hulse, C., Jepson, L. H., Hottowy, P., Sher, A., Dabrowski, W., Litke, A. M. and Chichilnisky, E. (2009), 'Loss of responses to visual but not electrical stimulation in ganglion cells of rats with severe photoreceptor degeneration', *Journal of Neurophysiology* **102**(6), 3260–3269.

Sekirnjak, C., Jepson, L. H., Hottowy, P., Sher, A., Dabrowski, W., Litke, A. M. and Chichilnisky, E. (2011), 'Changes in physiological properties of rat ganglion cells during retinal degeneration', *Journal of Neurophysiology* **105**(5), 2560–2571.

Sheasby, B. W. and Fohlmeister, J. F. (1999), 'Impulse encoding across the dendritic morphologies of retinal ganglion cells', *Journal of Neurophysiology* **81**(4), 1685–1698.

Shivdasani, M. N., Luu, C. D., Cicione, R., Fallon, J. B., Allen, P. J., Leuenberger, J., Suaning, G. J., Lovell, N. H., Shepherd, R. K. and Williams, C. E. (2010), 'Evaluation of stimulus parameters and electrode geometry for an effective suprachoroidal retinal prosthesis', *Journal of Neural Engineering* **7**(3), 036008.

Sim, S., Szalewski, R., Johnson, L., Akah, L., Shoemaker, L., Thoreson, W. and Margalit, E. (2014), 'Simultaneous recording of mouse retinal ganglion cells during epiretinal or subretinal stimulation', *Vision Research* **101**, 41–50.

Siqueira, R. C., Messias, A., Voltarelli, J. C., Scott, I. U. and Jorge, R. (2011), 'Intravitreal injection of autologous bone marrow–derived mononuclear cells for hereditary retinal dystrophy: a phase i trial', *Retina* **31**(6), 1207–1214.

Smith, J. K. and Agbandje-McKenna, M. (2018), 'Creating an arsenal of adeno-associated virus (aav) gene delivery stealth vehicles', *PLoS Pathogens* **14**(5), e1006929.

Smith, R. G. (1995), 'Simulation of an anatomically defined local circuit: the cone-horizontal cell network in cat retina', *Visual Neuroscience* **12**(3), 545–561.

Spencer, T. C., Fallon, J. B. and Shivdasani, M. N. (2018), 'Creating virtual electrodes with two-dimensional current steering', *Journal of Neural Engineering* .

Spencer, T. C., Fallon, J. B., Thien, P. C. and Shivdasani, M. N. (2016), 'Spatial restriction of neural activation using focused multipolar stimulation with a retinal prosthesis', *Investigative Ophthalmology & Visual Science* **57**(7), 3181–3191.

Steinberg, R. H., Fisher, S. K. and Anderson, D. H. (1980), 'Disc morphogenesis in vertebrate photoreceptors', *Journal of Comparative Neurology* **190**(3), 501–518.

Stett, A., Mai, A. and Herrmann, T. (2007), 'Retinal charge sensitivity and spatial discrimination obtainable by subretinal implants: key lessons learned from isolated chicken retina', *Journal of Neural Engineering* **4**(1), S7.

Stingl, K., Bartz-Schmidt, K. U., Besch, D., Braun, A., Bruckmann, A., Gekeler, F., Greppmaier, U., Hipp, S., Hörtdörfer, G., Kernstock, C. et al. (2013), 'Artificial vision with wirelessly powered subretinal electronic implant alpha-ims', *Proc. R. Soc. B* **280**(1757), 20130077.

Strettoi, E., Porciatti, V., Falsini, B., Pignatelli, V. and Rossi, C. (2002), 'Morphological and functional abnormalities in the inner retina of the rd/rd mouse', *Journal of Neuroscience* **22**(13), 5492–5504.

Surges, R., Freiman, T. M. and Feuerstein, T. J. (2004), 'Input resistance is voltage dependent due to activation of ih channels in rat ca1 pyramidal cells', *Journal of neuroscience research* **76**(4), 475–480.

Suzuki, S., Humayun, M. S., Weiland, J. D., Chen, S.-J., Margalit, E., Piyathaisere, D. V. and De Juan, E. (2004), 'Comparison of electrical stimulation thresholds in normal and retinal degenerated mouse retina', *Japanese Journal of Ophthalmology* **48**(4), 345–349.

Tabata, T. and Ishida, A. T. (1996), 'Transient and sustained depolarization of retinal ganglion cells by ih', *Journal of Neurophysiology* **75**(5), 1932–1943.

Tahayori, B., Meffin, H., Dokos, S., Burkitt, A. N. and Grayden, D. B. (2012), 'Modeling extracellular electrical stimulation: Ii. computational validation and numerical results', *Journal of Neural Engineering* **9**(6), 065006.

Tahayori, B., Meffin, H., Sergeev, E. N., Mareels, I. M., Burkitt, A. N. and Grayden, D. B. (2014), 'Modelling extracellular electrical stimulation: Iv. effect of the cellular composition of neural tissue on its spatio-temporal filtering properties', *Journal of Neural Engineering* **11**(6), 065005.

Teeters, J., Jacobs, A. and Werblin, F. (1997), 'How neural interactions form neural responses in the salamander retina', *Journal of Computational Neuroscience* **4**(1), 5–27.

Traub, R. D., Buhl, E. H., Gloveli, T. and Whittington, M. A. (2003), 'Fast rhythmic bursting can be induced in layer 2/3 cortical neurons by enhancing persistent na+ conductance or by blocking bk channels', *Journal of Neurophysiology* **89**(2), 909–921.

Tsai, D., Chen, S., Protti, D. A., Morley, J. W., Suaning, G. J. and Lovell, N. H. (2012), 'Responses of retinal ganglion cells to extracellular electrical stimulation, from single cell to population: model-based analysis', *PloS One* **7**(12), e53357.

Tsai, D., Morley, J. W., Suaning, G. J. and Lovell, N. H. (2009), 'Direct activation and temporal response properties of rabbit retinal ganglion cells following subretinal stimulation', *Journal of Neurophysiology* **102**(5), 2982–2993.

Tsai, D., Morley, J. W., Suaning, G. J. and Lovell, N. H. (2017), 'Survey of electrically evoked responses in the retina-stimulus preferences and oscillation among neurons', *Scientific Reports* **7**(1), 13802.

Tung, L. (1978), A bi-domain model for describing ischemic myocardial dc potentials., PhD thesis, Massachusetts Institute of Technology.

Twyford, P., Cai, C. and Fried, S. (2014), 'Differential responses to high-frequency electrical stimulation in on and off retinal ganglion cells', *Journal of Neural Engineering* **11**(2), 025001.

Van Essen, D. C. (2003), 'Organization of visual areas in macaque and human cerebral cortex', *The Visual Neurosciences* **1**, 507–521.

Van Geit, W., De Schutter, E. and Achard, P. (2008), 'Automated neuron model optimization techniques: a review', *Biological Cybernetics* **99**(4-5), 241–251.

Van Geit, W., Gevaert, M., Chindemi, G., Rössert, C., Courcol, J.-D., Muller, E. B., Schürmann, F., Segev, I. and Markram, H. (2016), 'Bluepyopt: leveraging open source software and cloud infrastructure to optimise model parameters in neuroscience', *Frontiers in Neuroinformatics* **10**, 17.

Van Welie, I., Remme, M. W., Van Hooft, J. A. and Wadman, W. J. (2006), 'Different levels of ih determine distinct temporal integration in bursting and regular-spiking neurons in rat subiculum', *The Journal of Physiology* **576**(1), 203–214.

Vecino, E., Rodriguez, F., Ruzafa, N., Pereiro, X. and Sharma, S. C. (2016), 'Glia–neuron interactions in the mammalian retina', *Progress in Retinal and Eye Research* **51**, 1 – 40.

Velte, T. and Miller, R. (1995), 'Dendritic integration in ganglion cells of the mudpuppy retina', *Visual Neuroscience* **12**(1), 165–175.

Velte, T. and Miller, R. (1997), 'Spiking and nonspiking models of starburst amacrine cells in the rabbit retina', *Visual Neuroscience* **14**(6), 1073–1088.

Völgyi, B., Deans, M. R., Paul, D. L. and Bloomfield, S. A. (2004), 'Convergence and segregation of the multiple rod pathways in mammalian retina', *Journal of Neuroscience* **24**(49), 11182–11192.

Wang, G.-Y., Robinson, D. W. and Chalupa, L. M. (1998), 'Calcium-activated potassium conductances in retinal ganglion cells of the ferret', *Journal of Neurophysiology* **79**(1), 151–158.

Wang, X.-J., Rinzel, J. and Rogawski, M. A. (1991), 'A model of the t-type calcium current and the low-threshold spike in thalamic neurons', *Journal of Neurophysiology* **66**(3), 839–850.

Ward, R. (1982), 'Quantitative effects of retinal degeneration in mice', *Revue Canadienne de Biologie Experimentale* **41**(2), 115–119.

Wässle, H. (2004), 'Parallel processing in the mammalian retina', *Nature Reviews Neuroscience* **5**(10), 747.

Wassle, H. and Boycott, B. B. (1991), 'Functional architecture of the mammalian retina', *Physiological Reviews* **71**(2), 447–480.

Weiland, J. D., Liu, W. and Humayun, M. S. (2005), 'Retinal prosthesis', *Annu. Rev. Biomed. Eng.* **7**, 361–401.

Weiland, J. D., Walston, S. T. and Humayun, M. S. (2016), 'Electrical stimulation of the retina to produce artificial vision', *Annual Review of Vision Science* **2**, 273–294.

Weitz, A. C., Behrend, M. R., Ahuja, A. K., Christopher, P., Wei, J., Wuyyuru, V., Patel, U., Greenberg, R. J., Humayun, M. S., Chow, R. H. et al. (2014), 'Interphase gap as a means to reduce electrical stimulation thresholds for epiretinal prostheses', *Journal of Neural Engineering* **11**(1), 016007.

Weitz, A. C., Nanduri, D., Behrend, M. R., Gonzalez-Calle, A., Greenberg, R. J., Humayun, M. S., Chow, R. H. and Weiland, J. D. (2015), 'Improving the spatial resolution of epiretinal implants by increasing stimulus pulse duration', *Science Translational Medicine* **7**(318), 318ra203–318ra203.

Werginz, P., Benav, H., Zrenner, E. and Rattay, F. (2015), 'Modeling the response of on and off retinal bipolar cells during electric stimulation', *Vision Research* **111**, 170–181.

Werginz, P., Fried, S. and Rattay, F. (2014), 'Influence of the sodium channel band on retinal ganglion cell excitation during electric stimulation–a modeling study', *Neuroscience* **266**, 162–177.

Werginz, P. and Rattay, F. (2016), 'The impact of calcium current reversal on neurotransmitter release in the electrically stimulated retina', *Journal of Neural Engineering* **13**(4), 046013.

Wiley, J. D. and Webster, J. G. (1982), 'Analysis and control of the current distribution under circular dispersive electrodes', *IEEE Transactions on Biomedical Engineering* (5), 381–385.

Wilke, R., Moghadam, G. K., Lovell, N., Suaning, G. and Dokos, S. (2011), 'Electric crosstalk impairs spatial resolution of multi-electrode arrays in retinal implants', *Journal of Neural Engineering* **8**(4), 046016.

Wilson, B. S. and Dorman, M. F. (2008), 'Cochlear implants: a remarkable past and a brilliant future', *Hearing Research* **242**(1), 3–21.

Wollner, D. A. and Catterall, W. A. (1986), 'Localization of sodium channels in axon hillocks and initial segments of retinal ganglion cells', *Proceedings of the National Academy of Sciences* **83**(21), 8424–8428.

Wong, R. C., Cloherty, S. L., Ibbotson, M. R. and O'Brien, B. J. (2012), 'Intrinsic physiological properties of rat retinal ganglion cells with a comparative analysis', *Journal of neurophysiology* **108**(7), 2008–2023.

Wong, Y. T., Chen, S. C., Seo, J., Morley, J. W., Lovell, N. H. and Suaning, G. J. (2009), 'Focal activation of the feline retina via a suprachoroidal electrode array', *Vision Research* **49**(8), 825–833.

Yamauchi, Y., Franco, L. M., Jackson, D. J., Naber, J. F., Ziv, R. O., Rizzo III, J. F., Kaplan, H. J. and Enzmann, V. (2005), 'Comparison of electrically evoked cortical potential thresholds generated with subretinal or suprachoroidal placement of a microelectrode array in the rabbit', *Journal of Neural Engineering* **2**(1), S48.

Yin, S. (2012), Computational Model of the Retinal Network, PhD thesis.

Yin, S., Lovell, N. H., Suaning, G. J. and Dokos, S. (2010), A continuum model of the retinal network and its response to electrical stimulation, *in* 'Engineering in Medicine and Biology Society (EMBC), 2010 Annual International Conference of the IEEE', IEEE, pp. 2077–2080.

Yin, S., Lovell, N. H., Suaning, G. J. and Dokos, S. (2011), Continuum model of light response in the retina, *in* 'Engineering in Medicine and Biology Society, EMBC, 2011 Annual International Conference of the IEEE', IEEE, pp. 908–911.

Yue, L., Weiland, J. D., Roska, B. and Humayun, M. S. (2016), 'Retinal stimulation strategies to restore vision: Fundamentals and systems', *Progress in Retinal and Eye Research* **53**, 21–47.

Zhou, Y. and Bell, J. (1994), 'Study of propagation along nonuniform excitable fibers', *Mathematical Biosciences* **119**(2), 169–203.

Zigmond, M. (1999), *Fundamental Neuroscience*, Academic Press.

Zrenner, E. (2002), 'The subretinal implant: can microphotodiode arrays replace degenerated retinal photoreceptors to restore vision?', *Ophthalmologica* **216**(Suppl. 1), 8–20.

Zrenner, E., Bartz-Schmidt, K. U., Benav, H., Besch, D., Bruckmann, A., Gabel, V.-P., Gekeler, F., Greppmaier, U., Harscher, A., Kibbel, S. et al. (2011), 'Subretinal electronic chips allow blind patients to read letters and combine them to words', *Proceedings of the Royal Society of London B: Biological Sciences* **278**(1711), 1489–1497.